Solution Processed Alq_3/ZnO Hybrid Thin Films and Strategy to Improve Optoelectronic Device Performance

THESIS

Submitted in partial fulfilment of the requirements for the award of the degree of

Doctor of Philosophy

In

PHYSICS

By

GNYANESHWAR DASI

(Roll No: 716054)

Under the supervision of

Dr. K. Thangaraju

DEPARTMENT OF PHYSICS

NATIONAL INSTITUTE OF TECHNOLOGY

WARANGAL - 506004, TELANGANA, INDIA

June 2022

NATIONAL INSTITUTE OF TECHNOLOGY
WARANGAL - 506004, TELANGANA, INDIA

APPROVAL SHEET

This thesis entitled **"Solution Processed Alq_3/ZnO Hybrid Thin Films and Strategy to Improve Optoelectronic Device Performance"** by **Mr. GNYANESHWAR DASI** (Roll No.: 716054) is approved for the degree of **Doctor of Philosophy**.

Prof. N. Gopalakrishnan
(External Examiner)
Department of Physics
NIT Tiruchirappalli-620 015, India

Dr. K. Thangaraju
(Research supervisor)
Associate Professor
Department of Physics
NIT Warangal, India

Prof. D. Dinakar
(Head & Chairman)
Department of Physics
NIT Warangal, India

Date: 13/06/2022
Place: NIT Warangal

DECLARATION

This is to declare that the work presented in the thesis entitled ***"Solution Processed Alq_3/ZnO Hybrid Thin Films and Strategy to Improve Optoelectronic Device Performance***" is a bonafide work done by me under the supervision of Dr. K. Thangaraju, Associate Professor, Department of Physics, NIT Warangal and was not submitted elsewhere for the award of any degree.

I declare that this written submission represents my ideas in my own words and where ever other's ideas or words have been included, I have adequately cited and referenced the originalsources. I also declare that I have adhered to all principles of academic honesty and integrity and have not misrepresented or fabricated or falsified any idea/data/fact/source in my submission. I understand that any violation of the above will be a cause for disciplinary action by the Institute and can also evoke penal action from the sources which have thus not been properly cited or from whom the proper permission has not been taken when needed.

Date: 13/06/2022
Place: NIT Warangal

GNYANESHWAR DASI
(Roll No: 716054)

NATIONAL INSTITUTE OF TECHNOLOGY WARANGAL

CERTIFICATE

This is to certify that the work presented in the thesis entitled ***"Solution Processed Alq_3/ZnO Hybrid Thin Films and Strategy to Improve Optoelectronic Device Performance"*** is a bonafide work carried out by Mr. **GNYANESHWAR DASI** under my supervision and was not submitted elsewhere for the award of any degree.

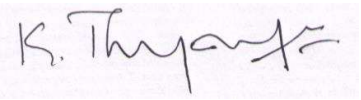

Date: 13/06/2022
Place: NIT Warangal

Dr. K. THANGARAJU
(Research supervisor)
Associate Professor

Acknowledgements

I take this opportunity to thank the people who have been involved in my efforts directly or indirectly, to complete this dissertation. The words mentioned here may not be sufficient to express my gratitude towards them.

Foremost, I would like to express my sincere heartfelt gratitude to my research supervisor, Dr. K. Thangaraju, Associate Professor, Department of Physics, NIT Warangal for his constructive guidance, relentless encouragement, and his love of research motivated me throughout my research life. I very much appreciate the freedom to pursue my research interests that he has given for completion of this research work. Moreover, he inspired to ensure the completion of this work. His expertise, availability to discuss ideas and willingness to share his knowledge were instrumental. For this, I will be eternally grateful. This thesis wouldn't have been possible without his immense support, academically and personally.

I express my sincere thanks to the Director, National Institute of Technology, Warangal, for having given me the opportunity to carry out the work and allowing me to submit the work in the form of thesis.

I express my sincere thanks to Prof. D. Dinakar, Head, Department of Physics, NITW, for his valuable suggestions and support throughout my research. I am very much indebted to Prof. D. Dinakar for his mentorship and fatherhood advice and affection which made me to submit my doctoral thesis. This thesis submission wouldn't have been possible without his immense support academically and personally. I express my sincere thanks to Former Heads of Department of Physics, NITW, for their valuable help and support.

I sincerely thank the members of the Doctorial scrutiny committee (DSC) Prof. Prof. R. L. N. Sai Prasad, Department of Physics, NITW, Dr. P. Abdul Azeem, Department of Physics, NITW, Prof. K.V. Gobi, Department of Chemistry, NITW, for their immense review and valuable suggestions at every stage of my research.

I must also extend my gratitude to my research mentors Dr. D. Paul Joseph, Dr. V. Jayalakshmi, and Dr. Kusum Kumari, Department of Physics, NIT W, for their great patience, efficient guidance. They taught research ideas of thin-film technology, and device fabrication which certainly form a concrete basis of my research knowledge, that can help me forever.

I am thankful to senior faculty members of our department, Prof. S.V.S. Ramana Reddy, Prof. Sai Sankar, Prof. L. Ramgopal Reddy, Prof. K. Venugopal Reddy, for their encouragement and support.

I take this opportunity to express my gratitude to faculty members of our department Dr. B. Sobha, Dr. T. Venkatappa Rao, Dr. P. Syam Prasad, Dr. Sourabh Roy, Dr. D. Haranath, Dr. R. Rakesh Kumar, Dr. K . Udaykumar, Dr. Vijay Kumar, Dr. Surya K. Ghosh, Dr. Hitesh Borkar, Dr. Aalu Boda, for their valuable advice, encouragement and moral support in my research career.

I express my sincere thanks to SERB, New Delhi for providing research facilities and JRF through research project (SERB/FTP/PS-162/2012). I express my sincere thanks to MHRD, New Delhi for the financial support in the form of fellowship. I express my thanks to NITW TEQIP–II for grant towards procuring thermal evaporation vacuum coating unit.

I express my sincere thanks to Prof. M. K. Mohan, Dr. P. Subhash Chandra Bose, and Mr. Ravindhar for providing the lab facilities at CAM NITW. I would like to thank Mr. Srinivas, Ms. Ramya, and Mr. Srinivas Technicians, NIT Warangal for the help in characterizations of samples. I am thankful to Taranath chemicals Warangal for suppling the chemicals in time.

I am very much thankful to Prof. R. Jayavel, Dr. M. Arivananthan, Mr. Anandh, Dr. Shivakumar and Ms. Suguna, Anna University Chennai, India, Prof. K. Asokan, Inter-University Accelerator Centre, New Delhi, India, Prof. P. Ramamurthi, Dr. Karunakaran, Madras University, Prof. A. Subrahmanyam, IIT Madras, India, Dr. R. Ramesh babu, Bharathidasan University, India, for their help in experimental measurements. I am also thankful to Dr. G. Sathiyan, Dr. Raju Kumar Gupta, Dr. Ashish Garg, IITK, Kanpur, India, Dr. M. Kovendhan, Inha University, Incheon, South Korea, S. Vijayakumar, Jae-Jin Shim, Yeungnam University, Republic of Korea for their help in experimental measurements.

With all happiness I acknowledge the cheerful assistance rendered by all my senior research colleagues Dr. K. Sowri babu, Dr. P. Kishore, Dr. P. Vengal Rao, Dr. Venkat Reddy, Dr. P.V.N. Kishore, Dr. M.N. Mallika, Dr. S. Rajkumar, Dr. V. Himamaheswara Rao, Dr. M. Mohan babu, Dr. Hari Krishna, Dr. Lal Singh, Dr. Ashish kumar, Dr. P. M. Pratheeksha for their encouragement throughout the period of my research.

I would like to express my heartfelt thanks to my lab research colleagues Dr. R. Ramarajan, Dr. N. Purusotham Reddy, Mr. Buchaiah, Mr. B. Ramesh, Mr. M. Nagaraju, Ms. T. Lavanya, Mrs. S. Suneetha, Mrs. S. P. Ramadevi, Mr. R. Muniramaiah, Mr. M S. Abdul Azeez, Mr. K. Naresh, and Mr. Soumya Ranjan, for their immense help in my experiments.

I thank all my research colleagues Dr. A. Sravanthi, Dr. T. Ramesh, Dr. Srinath, Dr. Shiva Prasad, Dr. Vishnu, Mr. VDR Pavan, Mrs. N . Manjula, Mr. Akshay Kranth, Mr. Koustav Dey, Mr. M. Krishnam Raju, Mr. M. Sattiah, Mr. A. Prasad, Mr. N. Jayaram Babu, Mr. Veera Babu, Mr. V. Nikhil, Mr. Siju Mishra, Mr. Sushil, Ms. A. Maha Lakshmi, Ms. P. Supraja, Mr. Gouranga Maharana, Mr. Poornesh and other co-research scholars for their munificent support.

I am thankful to all the non-teaching staff department of physics, NITW for their supportive help in research academic. I also thank to all the sweepers and security guards, NITW for their service to the lab maintenance.

I am happy to express my heartfelt thanks to my dear friends, Dr. N. Pavan and Dr. Kumar (OU-Physics), Dr. Sunil and Dr. Sagar (NITW-Chemistry), Dr. A. Rajesh (IITB-Physics), Dr. P. Srinivas (IITG-Physics), India, for their support in my research career. I am very much thankful to all the faculty members Department of Physics, OU Hyderabad, and my basic education teachers, Govt ZPHS Jhally, KGJC and SDC, Narsampet, Warangal, Telangana for their motivation and encouragement during the entire course of my personal life. I always remember my childhood gurus Veeraiah, Suneetha, Dr. Upendhar, and Madhav Reddy for their eminence teaching which given me the strong foundation to my education.

This thesis would not have been possible for me to enter my research journey without their motivation, cooperation and encouragement, heart goes to my beloved parents Suguna and Yadagiri, my sisters Sharada, Shailaja, Swarna, Anitha and Swapna. It wouldn't have been possible without support of my wife Anjani and also, I am delighted about my daughter Manognamanasvi for her pleasant bestowal. I would like to thank my well-wishers V. Kumaraswamy, B. Ashok kumar, for their moral support to my career. I always remember my grandparents Shyamalamba-Sarvesham and Komuramma-Bikshapathi & Komuramma for their love, moral and motivational words, which are inspiration to my career and life. I wish to thank my entire family and friends for all their support.

Date: 13/06/2022
Place: NIT Warangal.

GNYANESHWAR DASI

“The essence of science is independent thinking, hard work, and not equipment”

- Sir C. V. Raman

“Imagination is more important than knowledge. Knowledge is limited. Imagination encircles the world”

- Albert Einstein

DEDICATED TO

MY PARENTS

Suguna and Yadagiri

&

MY SUPERVISOR

Dr. K. Thangaraju

Preface

In the recent decades, the organic optoelectronic devices have achieved amazing significance over the inorganic optoelectronic devices for the commercial usage due to their long-lasting durability, higher efficiency, and other significant device performances. Mainly these are flexible and can be made on the large area. It is possible that the properties of organic semiconductors can be tuneable by modifying their structures. So, one can get the appropriate properties by simply recasting the chemical structure. There are some limitations for the commercial usage of these devices such as fabrication cost, poor stability, and lifetime. The organic light emitting diodes show the high brightness, high resolution, and large viewing angles representing the additional features in comparison with normal LEDs. Solar cell technology is the one developing area of research in the field of organic photovoltaics. It has various advantages, including its large surface area, light weight, rollable, low cost, and robustness. The main drawbacks of these organic photovoltaics are low efficiency, low ambient and thermal stability, and low strength. It is essential to surmount of these obstructions for the commercial usage of these devices. The research has been established a new concept of hybrid structures for further improvement of device performances. These hybrid structures consist of organic and inorganic parts and exhibit the properties of respective individual compounds. This thesis work explores the hybrid materials and their properties in-depth. It also explores the applications of these hybrid materials in various optoelectronic devices. The quality of the anode material is one of the several factors which directly affects the device efficiency. The indium tin oxide (ITO) is the most promising anode material used in several optoelectronic devices. This research work also describes the strategy to improve the quality of ITO film for the improved device performances of OLEDs, OSCs, and UV-photodetectors. This study finally concludes the improved optoelectronic device performances by utilising the significant features of hybrid materials and ITO anode quality.

The research work presented in this thesis is divided into nine chapters and the outline of each chapter is briefly given below,

Chapter 1: This chapter consists of introduction to the hybrid structured materials and their importance in the optoelectronic devices. It also elaborates the effect of annealed ITO anode on the optoelectronic devices performance. The brief literature review on hybrid structured materials for the solution processed hybrid thin film-based devices is presented. It presents the introduction to ZnO, preparation methods and its application in optoelectronic devices. The importance of Tris-(8- hydroxyquinoline) aluminum (Alq_3) in the application of optoelectronic devices are introduced. This chapter briefs different type of organic semiconductors in organic/ZnO hybrid structure and their applications. This chapter also introduces shift heavy ion (SHI) irradiation and its effect on thin film properties. This chapter concludes with the motivation and objectives of the research work.

Chapter 2: This chapter depicts the principle behind various experimental methods and analytical instruments used in this research work. This chapter explains preparation of hybrid thin films by sol-gel derived spin-coating method. The preparation of precursors such as ZnO sol-gel, Alq_3, solutions with different Alq_3/ZnO molar ratios for pristine ZnO and Alq_3/ZnO hybrid thin films is given in details. The molar ratio of Alq_3 to ZnO (Alq_3/ZnO) in solutions is maintained at 0.5×10^{-3} for [ZnO (80 vol.%) (0.4 M) + Alq_3 (20 vol.%) (2×10^{-4} M)], 1.3×10^{-3} for [ZnO (60 vol.%) (0.3 M) + Alq_3 (40 vol. %) (4×10^{-4} M)]; and 3×10^{-3} for [ZnO (40 vol.%) (0.2 M) + Alq_3 (60 vol.%) (6×10^{-4} M)]. This chapter contains experimental steps for the fabrication of various devices such as, hole-only devices, electron-only devices, organic light emitting diodes, organic solar cells, and UV Photodetectors.

Chapter 3: This chapter presents the optical, structural and morphological analysis of solution processed Alq_3/ZnO hybrid thin films. The hybrid thin films exhibit the good transmittance of more than 80% slightly less than that of pristine ZnO thin film. This slight decrease in transmittance is due to the adsorption of Alq_3 molecules on the ZnO grain boundaries which creates Alq_3 capped ZnO nanoparticles in the hybrid film. The X-ray diffraction studies reveal the textured crystalline property of the films with decreased crystallite size upon increasing Alq_3 content. FTIR studies confirm the increasing content of luminescent quencher (carbonyl group) formed in Alq_3 molecule for increasing Alq_3 in the films. The PL study shows a fourfold enhancement in the band-edge emission (387 nm) of ZnO upon increasing Alq_3 content in the hybrid films, attributing the energy transfer from Alq_3 molecule to ZnO when excited by 324 nm wavelength.

Chapter 4: This chapter gives the detailed analysis on structural properties of Alq_3/ZnO hybrid thin films using Raman and XPS studies. Raman studies reveal the hexagonal wurtzite structure of ZnO thin films. The XPS confirms the incorporation of Alq_3 in the hybrid thin films and corroborates that the Alq_3 molecules adsorbed onto the surface of ZnO nanoparticles (chemisorption), showing the existence of chemical interaction between Alq_3 and ZnO in the hybrid films. These studies show that the excited state energy of adsorbed Alq_3 molecule may be non-radiatively transferred to ZnO via luminescence quencher, enhancing a fourfold UV emission (387 nm) of ZnO in the hybrid thin films. The UV photodetector based on Alq_3/ZnO hybrid thin films exhibit the improved device performances compared to the pristine ZnO thin film-based devices.

Chapter 5: This chapter presents structural, optical, morphological properties, and UV photodetector properties of Ni^{7+} shift heavy ion (SHI) irradiated Alq_3/ZnO hybrid thin films. The Alq_3/ZnO hybrid thin films with the molar ratio of 0.5×10^{-3} [ZnO (0.4 M) and Alq_3 ($2x10^{-4}$ M)] were irradiated with Ni^{7+} SHI with the ion fluences of 5×10^{11}, 1×10^{12}, and 5×10^{12}

ions/cm^2. The SHI irradiation induces the defects such as oxygen vacancies and Zinc interstitials in the films. The optical properties show that the transmittance of the hybrid films decreases from 87% to 77% at 550 nm with increasing ion fluences, showing the scattering of light by SHI induced defects. The crystallite size is increased (17.7 nm for pristine, 19.34 nm for 5×10^{11} ions/cm^2, and 22.19 nm for 1×10^{12} ions/cm^2) due to the stress released in the film and it is decreased for the higher ion fluence of 5×10^{12} ions/cm^2 (14.07 nm). The gradual increase of surface roughness from 24 nm to 65 nm at 20 μm scan range ascertains the decreased transmittance for increasing ion fluences. The PL emission shows the decrease in band edge emission along with increased defective emissions (related to the oxygen vacancies and Zn interstitials), exhibiting the increased defects upon SHI irradiation. The sheet resistance decreased from 253 MΩ/□ (pristine film) to 69 MΩ/□ (1×10^{12} ions/cm^2) and then increased to 207 MΩ/□ for the highest fluence of 5×10^{12} ions/cm^2. The effect of Ni SHI irradiation on UV photodetection performance of Alq_3/ZnO thin films was studied and observed that the device with the ion fluence of 1×10^{12} ions/cm^2 exhibits the improved performance.

Chapter 6: This chapter emphasizes the improved hole injection into N,N′-Bis(3-methylphenyl)-N,N′-diphenylbenzidine (TPD) hole transport layer (HTL) by thermal annealing of ITO anode in hole-only devices (HODs). ITO anode was patterned and annealed at different temperatures (200, 300, and 400 °C) under the normal ambient. The drastic decrease of Hall carrier concentration, mobility and increase in resistivity after 300 °C is attributed to the trapping of free carriers and scattering from the chemisorbed oxygen at grain boundaries. XRD analysis shows the increasing crystallite size as annealing temperature increases. SEM images show that ITO thin film annealed at 400 °C exhibits the wrinkle kind of morphological structures. AFM studies also supported the significant changes with an increase in the surface roughness of ITO film annealed after 300 °C. The fabricated HOD (ITO/TPD/Al) based on ITO

anode annealed at 300 °C exhibited the improved hole injection than that of pristine, 200 °C, and 400 °C annealed ITO based devices. The OLEDs (ITO/TPD/Alq_3/LiF/Al) based on 300 °C also exhibit improved electroluminescence. These results show that annealing of ITO anode at 300 °C under the normal ambient improves the hole injection into TPD HTL in HODs and OLEDs.

Chapter 7: This chapter deals with the poly(3,4-ethylenedioxythiophene):poly(styrene sulfonate) (PEDOT:PSS) spin-coated on annealed indium tin oxide (ITO) (ITO/PEDOT:PSS) bilayer structure and its effect on the performance of OSCs. The ITO thin films show the improved film quality with decreased dislocation density and lattice strain as annealing temperature increases. The spin-coated PEDOT:PSS film smoothens the wrinkle kind of surface morphology of the ITO film annealed at 400 °C. The annealed ITO (400 °C) with PEDOT:PSS interlayer improves the hole-current density in the hole-only devices (HODs) having the device structure of ITO/PEDOT:PSS/TPD/Al. It enhances the efficiency of OSC [ITO (annealed)/PEDOT:PSS/P3HT:PCBM (active layer)/LiF/Al] by three times higher (1.69%) when compared to that (0.48%) of pristine ITO based device. These results show that the annealing of ITO film at the high temperature of 400 °C under the normal ambient improves the film quality and lowers the potential energy barrier at ITO/PEDOT:PSS interface for effective hole extraction process, resulting in the enhanced device electrical performances.

Chapter 8: This chapter contains the electrical properties of Alq_3/ZnO hybrid thin films and characteristics of UV photodetectors based on pure ZnO and Alq_3/ZnO hybrid thin films using pristine and annealed ITOs. The hall effect measurements reveal the increased carrier concentration and mobility with decreased resistivity for increasing Alq_3/ZnO molar ratio. The electron-only devices (EODs) were fabricated using the device structures ITO (pristine)/ZnO

or Alq_3:ZnO/Al. The EODs based on Alq_3/ZnO hybrid films exhibit the increased charge injection at lower voltages when compared to pure ZnO film-based device. The UV photodetectors were fabricated using the structure of ITO (pristine or 300 °C)/ZnO or Alq_3:ZnO/Al. In this structure ITO is used to improve the charge transport in hybrid films and Al electrodes made on the film are used for ohmic contacts. The UV photodetectors based on Alq_3/ZnO hybrid films exhibit higher device performance. The UVPDs using annealed ITOs exhibit the better performances than the devices using pristine ITOs.

Chapter 9: The final chapter presents the summary and conclusions drawn from the investigations carried out on optical, structural, morphological and electrical properties of Alq_3/ZnO hybrid thin films and the various optoelectronic devices. The strategy of annealing of ITO anode at elevated temperature under the normal ambient to further improve the UV photodetector performance is also summarized in this chapter. The suggestions and directions for the future research are sketched.

List of Symbols

Symbol	Description
α	Absorption coefficient
h	Planck's constant
ν	Frequency
E_g	Optical bandgap energy
D	Crystallite size
β	Full width at half maximum (FWHM)
θ	Diffraction angle
TC_{hkl}	Texture coefficient
I_{0hkl}	Standard peak intensity
I_{hkl}	Observed peak intensity
N	Total number of reflections
δ	Dislocation density
ε	Lattice strain
T	Transmittance
T_{av}	Average transmittance
λ	Wavelength
λ_{ex}	Excitation wavelength
V_O	Oxygen vacancy
O_i	Oxygen interstitial
V_{Zn}	Zinc vacancie
Zn_i	Zinc interstitial
O_{Zn}	Antisite oxygen
t	Film thickness

R_{rms}	Surface roughness
Φ	Surface work function
Φ_A	Anode work function
Φ_C	Cathode work function
n_c	Carrier concentration
μ	Mobility
ρ	Resistivity
σ	Conductivity
R_s	Sheet resistance
e	Charge of the electron
V	Voltage
I	Current
J	Current density
E	Electric field
Δ_e	Electron injection barrier
Δ_h	Hole injection barrier
φ	Barrier potential
Γ	Raman vibration mode
I_0	Incident light intensity
k	Boltzmann constant
V_{oc}	Open-circuit voltage
J_{sc}	Short-circuit current density
FF	Fill factor
P_{in}	Incident light power
η	Power conversion efficiency

List of Abbreviations

Abbreviation	Description
Alq_3	Tris-(8-hydroxyquinoline)aluminum
Al	Aluminum
AFM	Atomic Force Microscopy
AM	Air Mass
DI	Deionized
DL	Deep Level
EDAX	Energy Dispersive Analysis of X-rays
EIL	Electron Injection Layer
EL	Electro Luminescence
EML	Emissive Layer
ETL	Electron Transporting Layer
EOD	Electron-only Device
EQE	Electronic Quantum Efficiency
FTIR	Fourier Transform Infrared
HIL	Hole Injection Layer
HTL	Hole Transporting Layer
HOD	Hole-only Device
IPA	Iso-Propyl Alcohol
ITO	Indium Tin Oxide
JCPDS	Joint Committee on Powder Diffraction Standards
KP	Kelvin Probe
LiF	Lithium fluoride
MEA	Monoethanolamine

OLED	Organic Light Emitting Diode
OPV	Organic Photovoltaics
OSC	Organic Solar Cell
PEDOT:PSS	Poly(3,4- ethylenedioxythiophene):poly(styrene sulfonate)
P3HT	Poly(3-hexylthiophene)
PCBM	[6,6]-phenyl C61-butyric acid methylester
PL	Photoluminescence
SEM	Scanning Electron Microscope
SHI	Shift Heavy Ion
SMU	Source Measurement Unit
TPD	N,N′ -Bis(3-methylphenyl)-N,N′ -diphenylbenzidine
UV	Ultra Violet
UVPD	Ultra Violet Photo Detectors
UV-Vis-NIR	Ultraviolet-Visible-Near Infrared Spectroscopy
XRD	X-ray Diffraction
ZnO	Zinc Oxide

List of Figures

List of Tables

Content

Chapter: 1

Introduction

In recent years, the organic semiconductors become most predominant materials over inorganic semiconductors for the optoelectronic device applications because of their characteristic features such as non-toxic, environment friendly, flexibility, large-area, light-weight, good optical properties, flexibility in color tuning, and wide color gamut [1,2]. The optoelectronic devices based on organic semiconductors manifest superior improvement in device efficiency, flexibility, large area, lightness, durability, eco-friendly, and biodegradable. The required high quality of organic materials and fabrication process make the devices more expensive. The modern technology aim to reduce the environmental pollution so as to minimise the global-warming, mainly by using the organic materials which are eco-friendly and biodegradable. Thus, the aim of research in the area of organic electronics is to fabricate the organic optoelectronic devices to minimise the environmental pollution. The major drawbacks of organic semiconductors are photooxidation, environmental sensitivity, degradation under the normal ambient, aging, and less charge mobility or poor electrical properties [3–6]. The inorganic semiconductors overcome all these drawbacks of organic semiconductors with better stability and electrical properties. The combination of organic and inorganic compounds offers new properties such as mechanical strength, environmental stability, good optical and electrical properties [7,8]. The organic/inorganic hybrid structures play a key role for the improvement of optical and electrical properties and stability of optoelectronic devices. During the recent years, the extensive research is focused on the area of hybrid structures for optoelectronic device applications. Many research groups focus on various synthesis methods of hybrid structures for the cost-effective device fabrication with higher efficiency. The solution processed method is simple and easy technique for cost-effective device fabrication.

1.1. Inorganic semiconductors

Semiconductors exhibit the conductivity between conductors and insulators. Based on the carbon element, generally semiconductors are of two types inorganic and organic semiconductors. The inorganic semiconductors are of non-carbon based materials such as germanium (Ge), silicon (si), and tin (Sn) in IV(A) group, selenium (Se) and tellurium (Te) in group VI (A) of the periodic table. However, there are compound semiconductors such as Gallium arsenide (GaAs), mercury indium telluride ($HgIn_2Te_4$), aluminum gallium arsenide (AlGaAs), etc. During the 1950s germanium was the crucial semiconducting material used in many applications. The large leakage currents even at moderate temperature caused the failure of this semiconductor. Later from the 1960s silicon has become a widely used semiconductor for a large number of applications in electronics. This semiconductor exhibited the features of very less leakage currents and revealed excellent electrical properties. The silicon technology has found a very vast improvement in electronic devices and more than 95% of devices comprised of silicon. The silicon atom in the intrinsic crystalline semiconductor forms the four covalent bonds with the four neighbouring atoms. The interaction between the atoms causes the discrete energy levels which spread out into energy bands known as conduction band (CB), and valance band (VB). At absolute zero temperature the occupied energy band called valance band and the other unoccupied energy band is called conduction band. The energy gap between these two bands is called as optical bandgap and it is the region which stipulates the energies that electrons cannot possess. At higher temperatures which is capable of breaking covalent bond, the electrons jump into the CB becoming free (free electrons) and leaving the vacancy in the VB, called as hole (positive charge). Under the external electric field both electron and holes move in opposite directions and produce electric current. Generally, the semiconductors are dopped with impurities (typically one atom for million host atoms) to increase the conductivity. If one silicon atom is replaced with pentavalent impurities (arsenic-donor), the semiconductor becomes n-type containing majority of electrons and minority carriers of holes and if it is

replaced with trivalent impurity (boron-accepter), the semiconductor becomes p-type with majority charge carriers of holes and minority of electrons. By proper doping of donor and acceptor impurities one can make the pn junction diode which is the basic device in the field of inorganic electronics. Further this electronics has been vastly developed with many of the electronic devices like various types diodes, transistors, controllers, counters, microchips, integrated circuits (ICs), etc. The inorganic semiconductors have been substantially utilised in electronics for enormous applications. The inorganic semiconductors exhibit high electrical mobility (up to 1000 cm^2/Vs) at room temperature and higher stability. These materials are less appropriate for low cost and large area devices. In addition, the silicon is the indirect semiconducting material which is not quietly suitable for optoelectronic device applications like light emitting diodes, photodiodes, and solar cells. In addition to this in the beginning of the 21^{th} century a new revolution has been caused in the electronics with the use of electronic devices based on the new semiconducting materials known as organic semiconductors. The organic semiconductors are showing potential features such as mechanical flexibility, lightweight, large area coating, and fabrication of cost effective printed electronic circuits.

1.2. Organic semiconductors

The conventional semiconductors are the dominant electronic materials in the 20^{th} century. The invention of new type of semiconducting materials was started in the early of 20^{th} century. At the end of this century the microelectronics have led to the omnipresence of solid-state devices. At the very first in 1862, Henry Letheby observed partial conductivity from aniline by anodic oxidation in sulfuric acid. The conductivity and florescence properties of the organic materials was first started at the beginning of the 20^{th} century [9,10]. The photoconductivity was first observed from the anthracene by Pochettino in 1906 and Volmer in 1913 [11] . In the late 1950s and 1960s the organic materials were potentially used in photoreceptors for imaging systems [12]. In the early 1960s methylene blue has discovered as

first dye exhibits photovoltaic (PV) effect, later the PV effect was also observed in biological molecules such as chlorophylls, porphyrins and carotenes [11]. The electroluminescence was observed from the organic compounds of cellulose doped with acridine orange by Bernanose in 1953 [13]. The electroluminescence was observed from the anthracene crystals by Pope in 1963 and by Helfrich and Scheider in 1965 [14,15]. The molecular crystals of the anthracene held together by weak Vander wall forces and the compound is brittle, hence it is required that the material has to be a certain minimum thickness of about few micrometres. If it is so, the material needed high electric field of about 100 V for the charge transport processes and electroluminescence. So, it was conformed that this organic material is not useful for the applications. Further this idea was transferred to the vacuum deposited amorphous molecules and spin-coated polymers of about 100 nm film thickness which requires less operating voltage [16,17]. In the mid of 1970s Xerox and Kodak companies investigated the materials of molecularly doped polymers (MDPs) for their use in xerography and electrophotography. They invented that the polycarbonate doped with 30 wt% of optically active molecule such as triphenylamine exhibits the very low dark current and a reasonable photocurrent. In the late 1970s the high conductivity π-conjugated polymers were researched by Heeger, MacDiarmid, and Shirakawa and they awarded with Noble prize in chemistry during the year 2000. The π-conjugated polymers are hydrocarbon chains with alternative single and double bonds. In 1987, Tang and Van Slyke reported an amorphous organic molecule named as Tris(8-hydroxyquinolinato)aluminium (Alq_3) based OLED with the film thickness of 100 nm [17]. The device external quantum efficiency is about 1%, luminescence 1.5 lm/W, and brightness >1000 cd/m^2 were achieved at driving voltage below 10 V. This discovery brought a research interest for the development of new organic materials, and a lot of research has been done on the conjugated organic semiconductors during the last two decades [18]. In 2002 Philips company brought the first OLED display technology into the market through their product (Sensotec Philishave shown in Fig. 1.1(i)) and subsequently in 2003 Kodak has introduced Kodak Easy

Share LS633 digital zoom camera with an award-winning OLED display technology (Fig. 1.1(ii)). Sony introduced the first OLED TV (XEL-1) in 2007 into the market which was the world's first thinnest television of 3 mm thickness shown in Fig. 1.1(iii). It has a screen size of 11 inches with a native resolution of 960×540 and the contrast ratio is 1,000,000:1. Then till now so many companies like Samsung, LG, Apple, Motorola, etc. produced the TVs, phones, lightnings, and other electronic gadgets with OLED technology.

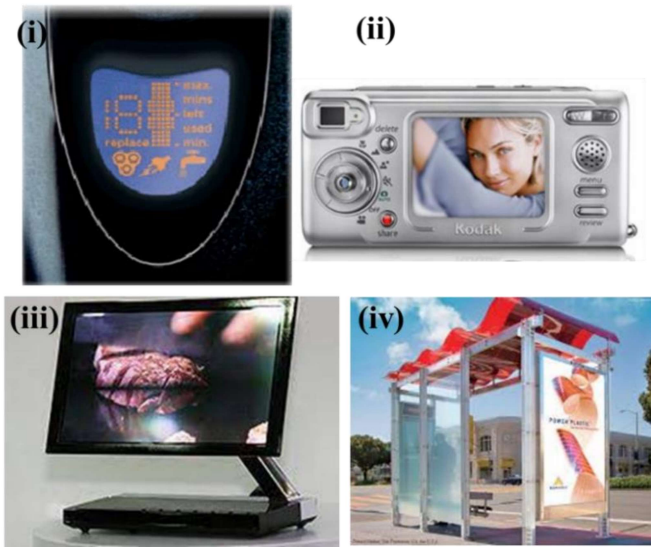

Fig. 1.1. Images of (i) first organic display in Philips trimmer, (ii) OLED display in Kodak digital camera (LS633), (iii) world's first OLED TV (XEL-1) by Sony, and (iv) first flexible OSC by Konarka Technologies.

Coming to the organic solar cells (OSCs) these are not extensively produced for the commercial use due to their low efficiency, degradation, and poor stability of the organic material under Sun light. In 2008 Konarka Technologies have started to produce fullerene based flexible OSCs (Fig. 1.1(iv)) but due to the low efficiency this was not continued for many years. During the period of 2015 – 2018 the researchers achieved 10-18% of efficiency with tandem structures of OSCs [19,20]. Still a lot of research has to be done in the area of organic electronics for the commercial use of OSCs, organic thin film transistors (OTFTs), organic photodetectors (OPDs), and other organic electronic devices.

1.2.1. Basics of organic semiconductors

Organic semiconductors are π-conjugated molecules or polymers made up of hydrocarbons and heteroatoms such as nitrogen, sulfur, and oxygen. These materials can exist in the form of molecular crystals or amorphous in nature. The optical and electrical properties of organic semiconductors can be tailored by modifying single moiety in the structure. One can synthesis the organic compounds for their desirable properties such as absorption, emission, conductivity, mechanical flexibility, and band gaps [9]. The band gap of organic semiconductors is defined as gap between the highest occupied molecular orbitals (HOMO) and lowest unoccupied molecular orbitals (LUMO) which are correspond to the valance band and conduction band in the conventional semiconductors. The organic materials are in the form of monomers, oligomers, and polymers. Monomer is the basic structure of the organic compounds consists single molecule. Oligomer is the molecule repeated with the three or four monomers. Polymer is the repeatable unit of monomers generally more than ten thousand which has the high molecular weight. The monomers and oligomers have evaporation or sublimation points where as polymers cannot be evaporated. The molecules and polymers can exist in crystalline and amorphous nature. The molecular crystals perform high charge mobility but not easily soluble e.g., acene based family like anthracene and tetracene [21]. The amorphous molecules such as Alq_3, C_{60}, phenyl-C_{61}-butyric acid methyl ester (PCBM), carbazoles, and phthalocyanine have good optical properties but low charge mobility [22]. The polymer crystals exhibit rigidity, high melting points but these are very brittle cannot be easily soluble (e.g., polyethylene, Polypropylene, Polystyrene, etc.) where amorphous polymers are soluble and have low melting points (e.g., Polyvinyl chloride, Polycarbonate, Poly-methyl methacrylate, etc.) [22,23]. The polymer crystals are the regular arrangement of large polymer chains in the form of lamellar (plate-like) crystals with the thickness of 10-20 nm. The organic molecules are bounded with the weak van-der-Waals intermolecular forces in contrast to the strong covalent bonds in inorganic crystals. These weak intermolecular forces reduce the hardness of organic

compounds and make them flexible but cause the weaker dislocations of electronic wave functions from one molecule to another which reduce the charge mobility [24]. In recent decades the organic semiconductors are playing a key role in the electronics and have been used in many applications such as Organic light-emitting diodes (OLEDs), organic solar cells (OSCs), and organic thin film transistors (OTFTs), organic photodetectors, and so on.

1.2.2. Optical and Electrical properties of Organic Semiconductors

The optical and electrical properties of the organic semiconductors are the crucial parameters for the optoelectronic device applications. The organic semiconductor requires the better optical and electrical properties for improved the device performances. Research has been focused on various aspects such as synthesis of new compounds or molecular moiety modifications, synthetic methods, growth mechanism, polymerization, film formation methods, organic doping or incorporation, etc., for the commercial applications.

Optical Properties:

Mainly the optical properties are composed of optical absorption, transmittance, optical band gap, photoluminescence (PL), PL decay, fluorescence quantum yield, and life time characteristics of the organic materials. One should achieve these properties in better way for the desirable outcome of the devices. The Jablonski diagram gives the basic mechanism of absorption and emission process using molecular energy level diagram of molecules [25]. This diagram was developed by the Polish physicist Aleksander Jablonski, for this invention in molecular florescence he is called as father of fluorescence spectroscopy. The other scientists namely Jean Baptiste Perrin and Francis Perrin (son of Jean Perrin) also contributed to Jablonski diagram by their theories. Figure 1.2 shows the schematic representation of Jablonski diagram. The horizontal black lines represent the energy levels of the molecule and bold lines represent the lowest vibrational levels of respective electronic states. Based on the spin angular momentum the electronic states are divided as singlet (S_0 - ground and S_1- first excited states

where net spin angular momentum is zero) and triplet states (T_0 - ground and T_1 - first excited states where net spin angular momentum is one). In the diagram the coloured arrows represent the various transitions. Here the radiative transitions are due to the emission of photons represented by straight arrows, non-radiative transitions are due to vibrational relaxations, internal conversion, and intersystem crossing of the molecules represented by undulating arrows [25–27]. The molecule gets excited from the ground state to the higher energy states by absorbing the photon represented by the blue arrows, it is the fast radiative transition occurs in the order of 10^{-15} seconds. At the first the excited molecule dissipates the energy through vibrational relaxation (yellow arrows) with in the intramolecular or intermolecular vibrational levels. This non-radiative transition occurs in the time scale of 10^{-12}-10^{-10} seconds. The molecules also undergo non-radiatively via internal conversion (IC) (with in the same spin multiplicity; S_2 to S_1– purple colour) and intersystem crossing (ISC) (different spin multiplicity; S_1 to T_1 – aqua colour) in the time scale of 10^{-11} - 10^{-8} s [26,27]. The intersystem conversion is the proportional dependent of spin-orbit coupling, after intersystem crossing molecule immediately undergo to the ground vibrational level of T_1 through vibrational relaxation. The two useful radiative transitions are fluorescence (S_1 to S_0 - green colour) and phosphorescence

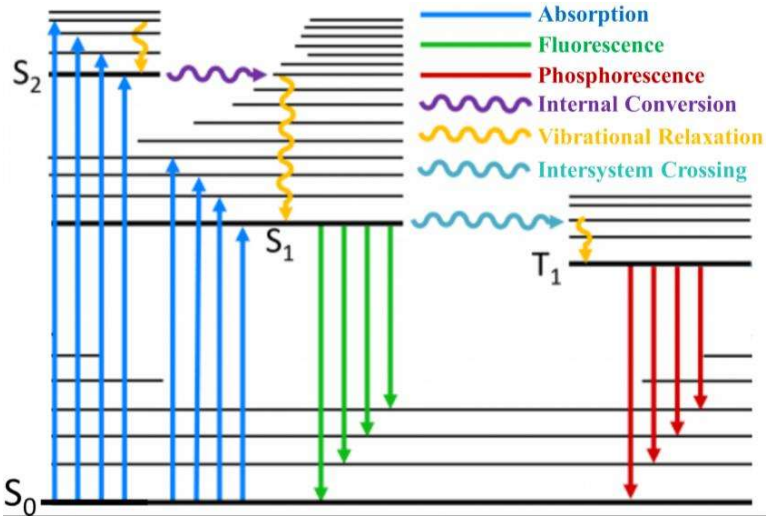

Fig. 1.2. A typical Jablonski diagram showing the possible radiative and non-radiative transitions in organic molecule.

(T_1 to S_0 - red colour) which occur in the time scale of 10^{-10} – 10^{-7} s and 10^{-6} – 10 s respectively [25,26,28,29]. The fluorescence occurs between two electronic states of same spin multiplicity after the vibrational relaxation and internal conversion processes. The phosphorescence occurs in different spin multiplicity after the vibrational relaxation and intersystem crossing. According to the Kasha's rule the luminescence (fluorescence or phosphorescence) only occurs from the lowest excited state of a given multiplicity with considerable yield. The fluorescence occurs at a longer wavelength than the absorption which is responsible for the Stokes-Shift [28,29]. Fluorescence quantum yield (FQY) and lifetime are the important properties of the fluorescent organic compounds for the OLED and OSC applications. The FQY is defines as the ratio of photons emitted by the molecule through fluorescence to photons absorbed. In other way it is the ratio of rate constant of radiative relaxation (fluorescence) to the rate constants for non-radiative relaxations.

$$\Phi_f = \frac{K_f}{K_f + \sum K_{nr}} \tag{1.1}$$

Where K_f is the rate constant for radiative relaxation ΣK_{nr} is the sum of the rate constants for non-radiative relaxations. Here the non-radiative relaxations are internal conversion, intersystem crossing, external conversion, and Forster resonance energy transfer. The relative quantum yield of the sample can be determined by comparing the absorption and PL emission spectra of the sample with the standard ones and using the following formula [30]

$$\Phi_X = \Phi_{ST}\left(\frac{Grad_X}{Grad_{ST}}\right)\left(\frac{\eta_X^{\,2}}{\eta_{ST}^{\,2}}\right) \tag{1.2}$$

where Φ_x andΦ_{st} are the quantum yield of test and standard sample. $Grad_x$ and $Grad_{st}$ are the slopes of the straight lines obtained by drawing the graph between absorption and integrated PL intensity of test and standard samples. η_x and η_{st} are the refractive index of the solvents used for test and standard samples respectively.

Life time of the molecule is defined as time taken by excited molecule to come to the ground state. Time resolved photoluminescence (TRPL) is the tool to determine lifetime of the fluorescent or phosphorescent molecules. This fluorescence lifetime can be affected by the solvent, luminescent quenchers, temperature, molecular rotation, solvation dynamics and interactions with other molecules. Therefore, the change in the lifetime can provide information about the local chemical environment, luminescent quenchers, degradation, and stability of the molecules. TRPL measurements carried out by using a method generally known as Time-Correlated Single Photon Counting (TCSPC). It works by measuring the time gap between sample excitation by a laser pulse and the arrival of the emitted photon at the detector.

Electrical Properties:

Charge conductivity, resistivity, carrier concentration, hole or electron mobility, and charge transfer mechanism are the important parameters to analyse the electrical properties of an organic semiconducting material. These properties directly affect the device performances by charge accumulations at the interfaces, charge imbalance, enhancing the barrier potentials, etc [31,32]. The charge transport mechanism in the organic semiconductors is of two types such as band- and hopping- transports. Band transport is typically observed in organic crystals (not at high temperatures) where degree of order of the charge transport is high compared to the amorphous organics. In the organic structures molecules are held together by weak van der Waals forces. These weak interactions between the molecules prevents the charge transport in delocalized HOMO and LUMO states. The disordering of organic solids creates the locally varying polarization energies, leading to a Gaussian distribution of density states for the charge transport [24]. Figure 1.3 shows the Energy levels of an isolated molecule, a molecular crystal, and an amorphous solid. Charge carriers move through hopping process among the adjacent molecules or sites in the π-conjugated polymers with statistically variable (Gaussian distribution) energies [31]. The hopping distances can also vary statistically (positional

disorder). As a consequence of the energetic broadening of the density of states (DOS) distribution, the charge mobility depends on both temperature and electric field dependent. The

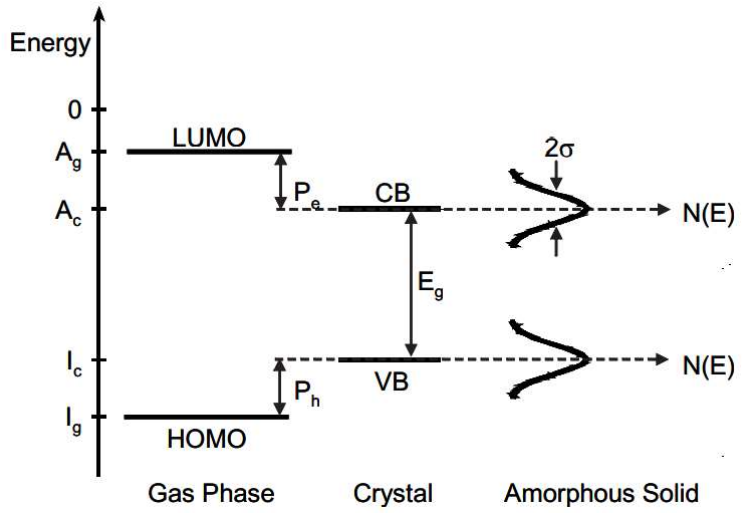

Fig. 1.3. Energy levels of an isolated molecule, a molecular crystal and an amorphous solid.

room temperature mobility of the organic crystals is in the range of 1 – 10 cm^2/Vs and it varies with the temperature following the power law as:

$$\mu = T^{-n} \quad \text{with } n = 1\ldots3\ldots \tag{1.3}$$

Since the electronic delocalization is weak in organic semiconductors the mobility is less compared to the inorganic semiconductors. The hopping transport in the delocalised states leads to the very low mobility around 10^{-3} cm^2/Vs in amorphous organic solids. Instead of power law in organic crystals, the mobility depends on activation energy and applied electric field with temperature as follows [24]

$$\mu(F,T) \propto \exp(-\Delta E/kT).\exp(\beta\sqrt{F}/kT) \tag{1.4}$$

Space charege, trapping effects, and charge injection are some of the other facters which effect the conductivity of organic semiconductors [32]. For a intresic semiconducting system the carrier density can be defined as

$$n_i = N_0 \,.\, \exp(-E_g/2kT) \tag{1.5}$$

where N_0 - effective density of states, E_g – energy gap.

Considering the typical values for pure organic semiconductor, the $E_g = 2.5$ eV and $N_0 = 1021$ cm^{-3} lead to a subpositional carrier density of $n_i = 1$ cm^{-3} at room temperature. By comparision with Si ($E_g = 1.12$ eV, $N_0 = 1019$ cm^{-3}, $n_i = 1010$ cm^{-3}), the n_i is higher orders of magnitude, which indicates that organic semiconductors have significantly low conductivity even if they are pure enough. Electro-chemical doping, photo-generation of carriers, field-effect doping, effective carrier injection from contacts, and hybridation are of the methods to improve the low mobility and carrier concentration of organic semiconductors. Based on the charge carrier mobility, the organic semiconductors are differentiated as hole transporting, electron transporting, emissive, acceptor, and donor materials. Some of the organic molecules are shown in the figure 1.4.

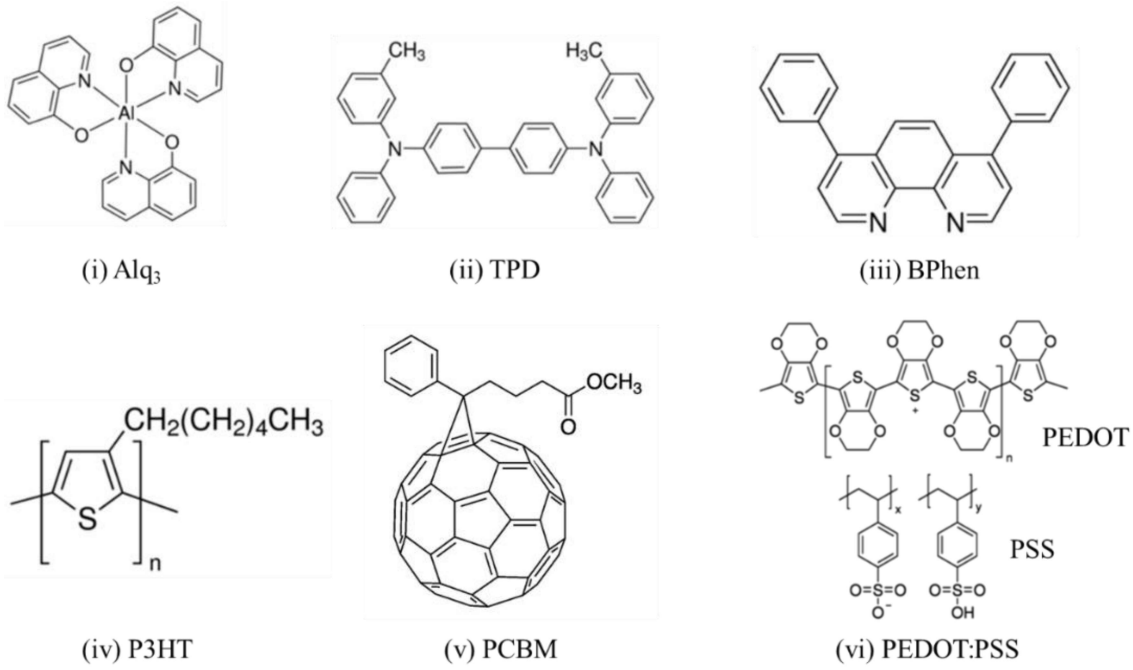

Fig. 1.4. Molecular structures of (i) Tris-(8-hydroxyquinoline)aluminum (Alq_3), (ii) N,N′-Bis(3-methylphenyl)-N,N′-diphenylbenzidine (TPD), (iii) Bathophenanthroline (Bphen), (iv) Poly(3-hexylthiophene-2,5-diyl) (P3HT), (v) Phenyl-C61-butyric acid methyl ester (PCBM), and (vi) Poly(3,4-ethylenedioxythiophene)-poly(styrenesulfonate) (PEDOT:PSS).

1.3. Organic/inorganic hybrid structures

The research on hybrid materials provides lot of opportunities and at the same time challenges. Hybrid materials exhibit superior properties compared to the individual elements. The inorganic semiconductors provide better thermal stability, high conductivity, higher refractive index, higher density, strength, and hardness, whereas the organic materials exhibit good optical properties, mechanical flexibility, connectivity networks, tuneable hydrophilic/hydrophobic nature, biochemical reactivity, biodegradable, lower refractive index, lower density, lower mobility and stability [33]. In the hybrid composite the organic material provide the mechanical flexibility and film formation ability whereas the inorganic elements contribute the thermal stability, and mobility [34]. The inorganic/organic interface, nature of bonding, surface energy, unstable bonds, and energy transfer between the individual elements play a key role on the optical, structural, electrical, and morphological properties of the hybrid composites [35]. The degree of linking or interaction of the organic and inorganic networks influence the mechanical and chemical properties of the hybrid material [36]. Based on the interaction or bonding between the organic and inorganic elements the hybrid functional materials are two types. In the class I, the organic and inorganic parts interact with weak Vander Waals forces, electrostatic forces or hydrogen bonds whereas in class II, the elements interact with covalent or ionic-covalent chemical bonds [35,37]. The materials which have the both strong and weak interface interactions are considered to be class II materials due to the significant strong chemical bonding in the final hybrid material. From these categories, the class I materials are easy to synthesis, avoid the hetero-functional metal-organic precursor, create functional architectures by self-assembly. Owing to the presence of covalent bonds, the class II materials exhibit more advantages such as deprecation of phase separation, control on the interface interactions, hydrophilic/hydrophobic balancing, better understanding of organic-inorganic interface, and stability of the organic components in the inorganic matrices. Figure. 1.5 represents the schematics of class I [(a) formation of blends due to the weak interactions,

(b) interpenetration of networks] and class II [(c) covalently connected building blocks of organic and inorganic materials, (d) interpenetration of building blocks] [38].

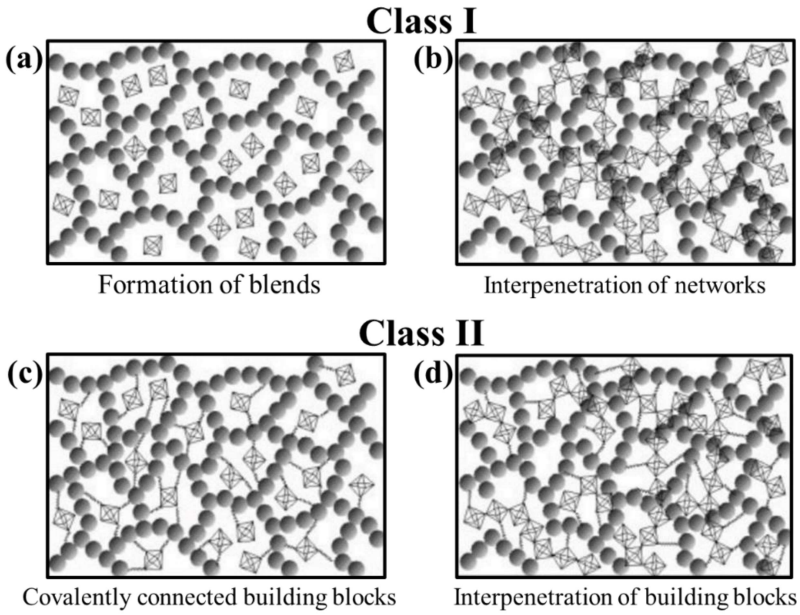

Fig. 1.5. Schematic representation of organic-inorganic interactions in hybrid materials (adopted from the book of Hybrid Materials, ISBN 978-3-527-31299-3).

The main challenge is of synthesis of hybrid structures with enhanced properties without altering the individual counterparts [35]. Most importantly the synthesis method should form the organic-inorganic nano level composites. Simply crushing and mixing of the materials consequently produce only submicron order composites [34]. The synthetic methods such as sol-gel process, hydrothermal, and solvothermal methods form nanoscale hybrids. The hybrid materials are synthesised by the in-situ formation of the components in three different methods [38]. In the first method, inorganic materials are formed in the organic materials. In this process the inorganic precursor sol-gel is prepared first and is mixed with the organic material. In the second method, the inorganic materials are treated with surfactants for enhancing the functionalization of organic materials or to compatible with the organic monomers. The third method presents the preparation of both inorganic precursor sol-gel and polymerization of

organic material simultaneously. This simultaneous preparation leads to the formation of interpenetrating networks with most homogeneity. These in-situ formations in-general are classified in to two categories (Fig. 1.6), (i) organic-in-inorganics: functionalization of inorganic materials (includes colloidal particles like nano-wires, tubes, rods) by organic molecules/polymers, and (ii) inorganics-in-organics: incorporation of inorganic components into organic matrices [38]. The sol-gel process is most advantageous method for the preparation of hybrid materials. Preparation of hybrid materials through this method includes sol-gel processing of inorganic material in presence of organic molecule (typically polymeric). In the sol-gel processing, first the particles are formed as colloids defining a sol., second the particles undergo crosslinking reactions and form the gel [39]. During the crosslinking, the particles make bonding with the functional groups of organics, leading to the growth of inorganic phase in organic matrix. The typical methods include in hybridization of materials are hydrolysis, and condensation [40,41]. The advantages of sol-gel process are formation of nanocomposites, high purity, uniformity in film formation, low temperature process, strong interactions, less porosity, structural control, pH adjustable, subtly control on morphological growth, control on the reaction parameters, and cost effective [39,41]. The type of synthesis method, amount of organic or inorganic precursor, catalyst type, time of stirring the mixture are some of the factors which affect the properties of hybrid composites [36]. Owing to the mechanical flexibility, high mobility, and thermal stability, these hybrid materials replace the organic and inorganic materials in many of the applications. These materials can be used in electronic and optoelectronic applications including light emitting diodes, solar cells, photodiodes, gas sensors, fire sensors, and field effect transistors. Hybrid materials used in coating applications such as decorative coatings, antistatic/antireflection coatings, scratch-resistive coatings, and corrosion protection coatings [33,42]. The hybrid composite also serves as electrolyte materials used in solid state lithium-ion batteries, supercapacitors, and fuel cells.

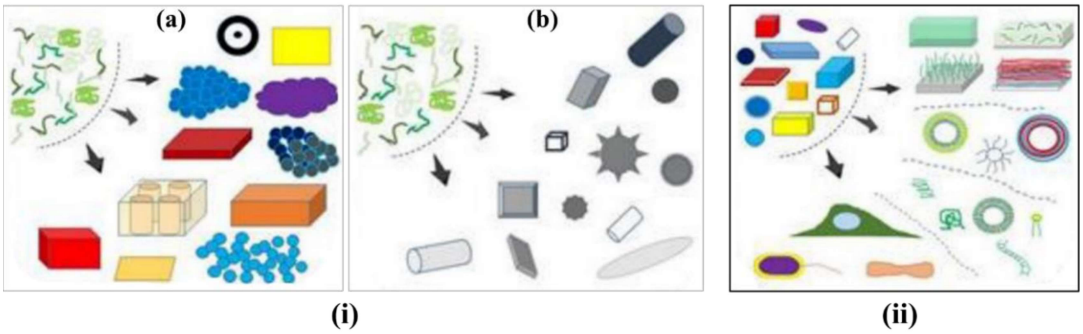

Fig. 1.6. Schematic of (i) (a) Organics-in-inorganics structure, (b) organics-in-inorganics Colloids, and (ii) inorganics-in-organics molecules/polymers. Adopted from Saveleva et al. [33].

1.4. Zinc Oxide

ZnO is an n-type degenerate inorganic semiconductor belongs to II-VI group. It is a direct and wide band-gap (3.37 eV at room temperature) semiconductor, most widely used for the photonic and optoelectronic devices. ZnO exhibits large excitation binding energy of 60 meV, which provides efficient excitonic emission in ZnO, is useful for the applications of ultraviolet light emitting diodes, and laser diodes [43]. ZnO allows easier light extraction from the optical devices due to its low refractive index of 2.05 [44]. ZnO thin films are processed using various methods such as atomic layer deposition (ALD), pulsed laser deposition (PLD), chemical vapours deposition (CVD), RF magnetron sputtering, self-assembly, epitaxial growth, sputtering technique, electrodeposition, co-precipitation, spray pyrolysis, and sol-gel method. The sol-gel method has some unique advantages from aforementioned methods such as [45].

- simple and cost-effective process.
- Better homogeneity and purity.
- low temperatures process.
- Effective control over the particle size and shape, physical and chemical properties, and chemical stoichiometry.
- uniform thin film formation.

Sol-gel method is the most useful process for synthesis of various hybrid materials. ZnO exhibits two crystalline structures, hexagonal wurtzite and cubic zincblende (Fig. 1.7). The first is the most common and stable structure at moderate temperature and pressure. At high pressures ZnO exhibits cubic structure with indirect band gap of 2.7 eV [43]. Each Zn atoms are tetrahedrally coordinate with the four oxygen atoms. The two structures exhibit perfect polar symmetry along the hexagonal axis of the ZnO. ZnO structures has no inversion symmetry results in piezoelectricity and pyroelectricity of the structures which can be applicable for piezoelectric sensors and mechanical actuators [46]. The hexagonal structure belongs to the point group of C_{6v}, and the space group of $P6_3mc$ or C_{6v}^4. The lattice constants are a = b = 3.25 Å and c = 5.2 Å; their ratio c/a ~ 1.60 is close to the ideal value for hexagonal cell c/a = 1.633 [43]. The ZnO exhibits the increased crystallite size by annealing at higher temperatures in normal ambient due to the effective substitution of O_2 atoms in Zn sites. The crystallite size

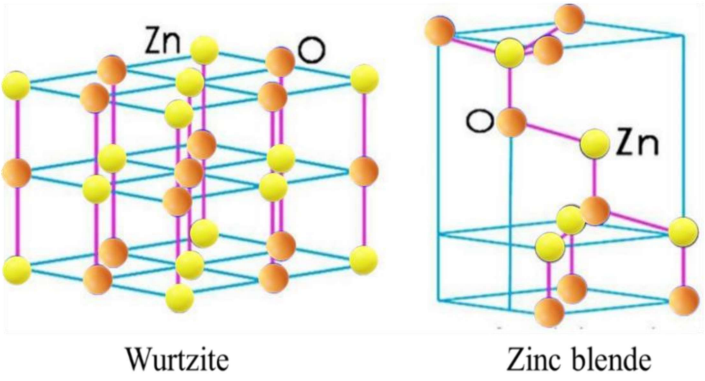

Fig. 1.7. Schematic representation of ZnO crystalline structures.

affects the mobility of the charge carriers and hence conductivity of the ZnO thin films. To enhance the electrical or optical properties, materials are doped with the suitable dopants. ZnO is intrinsically n-type materials due to the oxygen vacancies, exhibits the n-type conductivity with high mobility of 100 cm^2/Vs [44,47]. So, making the ZnO as p-type is the difficult task. There are several p-type dopant materials such as Li, Na, K, N, P, As, Cu, and Ag. Limitations of p-dopants are they hindrance the optical and electrical properties of ZnO [48]. The n-type

conductivity can be increased with doping of elements like In, Ga, B, Al, etc. These materials significantly increase the conductivity with increasing the carrier concentration [47]. Mostly, the Al is used as a dopant in ZnO for many of the applications due to the nontoxic, inexpensive, high conductance and higher transparency. ZnO nano structures exhibit superior properties than the bulk. The nano structures are in the form of nanoparticles, nanowires, nanorods, nanotubes, nanosheets, nanofibers, nanoflowers, nanocolumns, nanobelts, nanohelixes, nanocombs, nanorings, nanopropellers, nanosprings, and nanoshells [44]. All these structures are synthesised by various synthesis methods and growth mechanisms. ZnO exhibits the most interesting photonic properties in UV and visible region. The typical PL emission of ZnO reveals the two types of emissions: (i) the near-band emission (NBE) in the UV region and (ii)

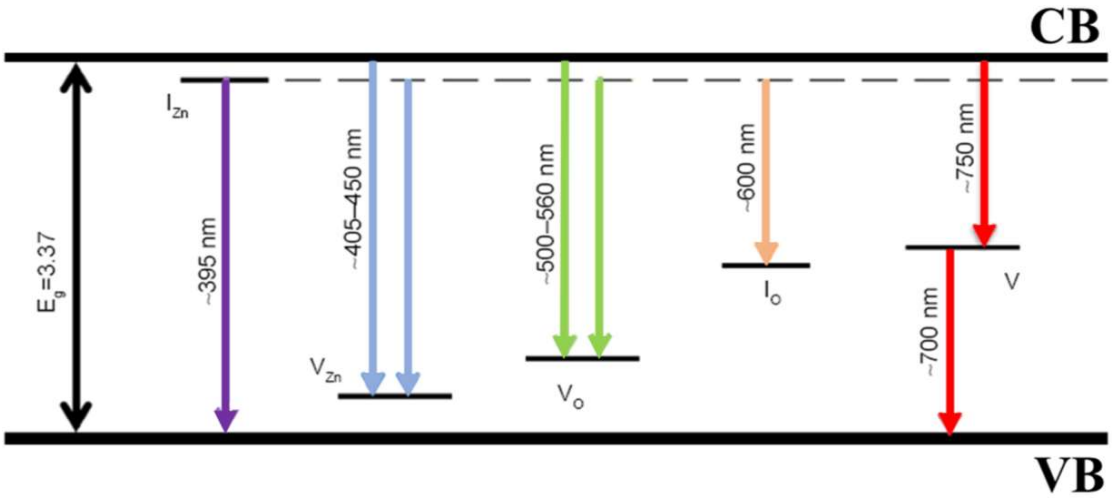

Fig. 1.8. Schematic of the radiative transitions associated with intrinsic defect states in ZnO.

the defective of deep level emissions (DLE) in the visible region. The defective emissions are due to presence of zinc vacancy (V_{Zn}), oxygen vacancy (V_O), zinc interstitial (Z_{ni}), oxygen interstitial (O_i), and other extrinsic contamination [43]. The ratio of intensity of these two emissions (I_{NBE}/I_{DLE}) indicates the optical quality of ZnO. The corresponding emissions of ZnO are shown in Fig. 1.8. Owing to its excellent optical, electrical, and mechanical properties, ZnO is used in enormous applications as mentioned in the figure 1.9.

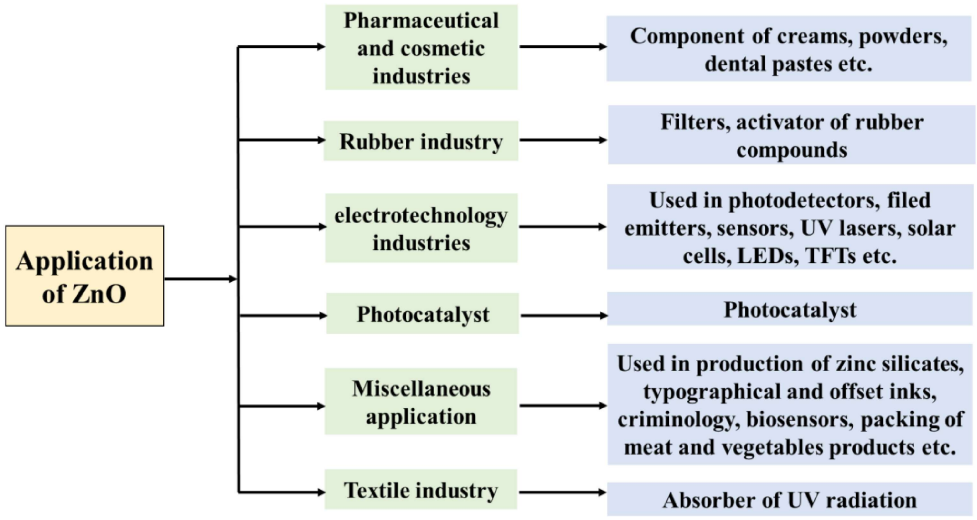

Fig. 1.9. Various applications of ZnO in different fields.

1.5. Tris(8-hydroxyquinolinato)aluminium (Alq_3)

Tris(8-hydroxyquinolinato)aluminium (Alq_3) is an organic fluorescent semiconductor frequently used in OLEDs as electron transporting as well as emissive layer. C. W. Tang and S. A. VanSlyke first reported an efficient Alq_3 based OLED with the efficiency of 1% at 5.5 V, output power of 0.1 mW/cm^2, and PCE is 0.46% [17]. Some of superior properties of Alq_3 such as cost effectiveness, easy to synthesis, highly fluorescent, tuneable properties, and non-toxic, make its commercial usage in many optoelectronic device applications. The chemical formula of Alq_3 is $C_{27}H_{18}AlN_3O_3$. It is made by the coordination of metal complex of aluminum(III) and the anion of 8-hydroxyquinoline (8-HQ). The nitrogen and oxygen atoms of 8-HQ are coordinated with the aluminum atom so that the complex takes an octahedral configuration. The HOMO and LUMO level are 5.8 eV and 3.1 eV respectively and the band gap is 2.7 eV. Alq_3 is used as an active emissive layer in green luminescent OLEDs and as electron transporting layer in other coloured OLEDs. Alq_3 has two isomers, meridional and facial as shown in Fig. 1.10 [49]. Each isomer forms multiple crystalline phases. In general, Alq_3 is amorphous in nature and is a green fluorescent material. But it exhibits different crystalline phases in various conditions. Three crystalline phases of $\propto$, β, and γ were identified by Brinkmann and co-workers

[50]. M. Colle and co-workers invented the δ-phase phase of Alq_3 by sublimation in a horizontal glass tube and they also observed the blue luminescent of Alq_3 from this phase [51]. The photoluminescence of Alq_3 can be tunable by embedding in polymer (PMMA: polymethyl methacrylate) matrix [52]. Alq_3 is efficiently used in hybrid composites and achieved improved luminescence properties with the ZnO [53,54]. The major drawback of Alq_3 is it exhibits poor stability by degradation of its optical properties. Thangaraju et al. reported the luminescence quenching of Alq_3 during the light exposure and under shift heavy ion (SHI) irradiation due to the formation of carbonyl group (C=O) which acts as a luminescent quencher [55,56]. Alq_3 also exhibits the low thermal stability, annealing at higher temperatures (T>150 °C) in normal ambient, causing the luminescent quenching [57].

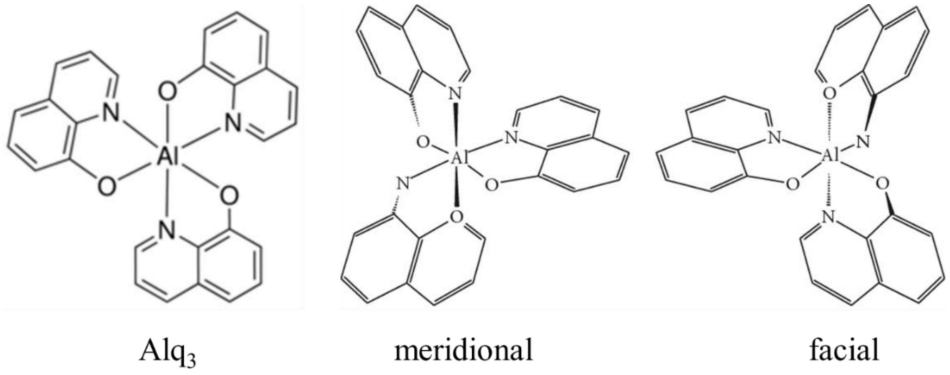

Fig. 1.10. Molecular structure of Alq_3 and its isomers (meridional and facial).

1.6. Optoelectronic devices

Optoelectronic devices are primarily transducers i.e., they can convert optical energy to electrical energy and vice versa. These devices belong to the field of optoelectronics and that use optical or electrical signal in their operation. Optoelectronics deal with the quantum mechanical effects of light on electronic materials such as semiconductors (organic or inorganic). The optoelectronic devices are light emitting diodes (LEDs), photovoltaics (solar cells, photo diodes, phototransistors, photomultipliers, and opto-isolators), photoresistors, laser diodes, etc. Coming to the organic electronics the OLEDs, OSCs, and organic photodiodes also come under optoelectronic devices which deals with the optical and electrical mechanisms.

1.6.1. Organic light emitting diodes (OLEDs)

It is a light emitting diode (LED) made by placing the series of organic thin layers in between two electrodes. The organic layers can be emissive layer (EML), electron transporting layer (ETL), hole transporting layer (HTL), electron blocking layer (EBL), hole blocking layer (HBL), electron injection layer (EIL), hole injection layer (HIL), and electron injection layer (EIL) [58]. These layers can be used and/or optimized in the optoelectronic devices for charge balancing, decreasing the barrier potentials between the layers, reducing the charge accumulation at the interfaces, the proper interface contacts, and improved the device efficiency. In 1955 Andre Bernanose and co-workers have first reported the electroluminescent from acridine derivatives (gonacrin and brilliant acridine orange E) at 2000 V AC [59]. In 1963 Martin Pope et al. has first observed the direct current electroluminescence at 400 V from anthracene crystals under vacuum [15]. In 1983 Roger Partridge reported the PLED using (poly(N-vinylcarbazole)) polymer films of 2.2 µm thickness [60]. The first efficient OLED based on Alq_3 at 2.5 V was reported by C. W. Tang and S. A. VanSlyke in 1987 [17]. Further the OLED was developed and commercialised by various companies like Kodak, Sony, LG, Samsung, etc. The basic device structure and charge transfer mechanism or emission process shown in Fig. 1.11. The device structure is consisting of sequential layers of anode, hole

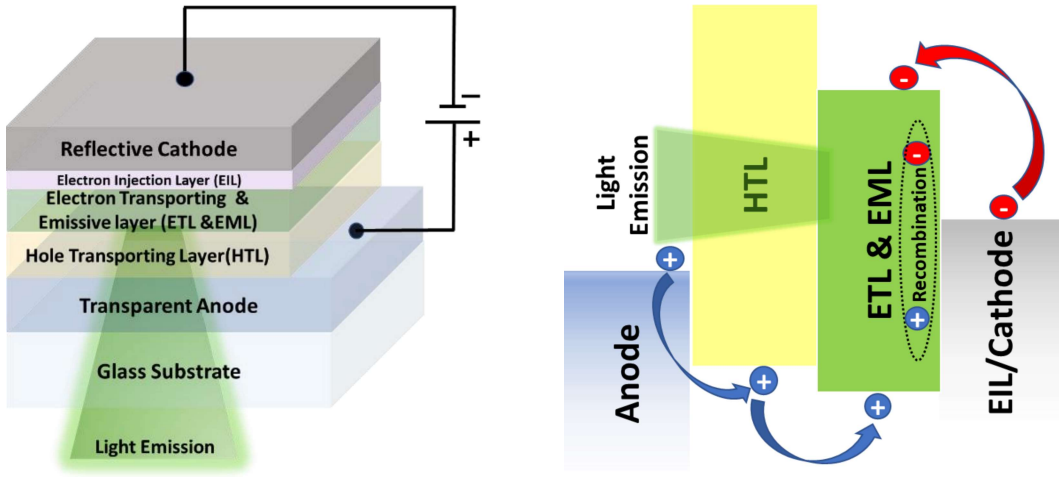

(i) (ii)

Fig. 1.11. Schematic of (i) Basic device structure of OLED and (ii) light emission process.

transporting layer, emissive layer, electron injection layer, and cathode one over the other. The anode injects the holes and cathode inject the electrons into the organic layers. HTL facilitates the injected charge carriers (holes) by the anode move towards the emissive layer (facilitates the removal of electron from the EML), EIL facilitates the charge carries (electrons) injected into the emissive layer [58]. The charge carriers move by the hoping process through the organic layers. The injected holes and electrons form the electron-hole pairs (excitons) in the emissive layer [58]. The excitons de-excite means recombine and emit the visible light. To recombine, electrons have to make transition from LUMO energy level to HOMO level of the emissive layer. In the recent years the OLEDs (display and lightning) are well commercialised and available in the market but these are expensive compared to the inorganic counterparts. High purity of organic materials, expensive fabrication process and encapsulation increase the cost of the OLEDs for commercial usage. Advantages of OLEDs over conventional LCDs and inorganic LEDs are thinner, flexible, brighter, higher contrast, faster refresh rates, and highly efficient. OLED based prototype display and lighting devices are shown in the figure 1.12. OLED have self-lit pixels, which turn off to achieve perfect black and high contrast whereas

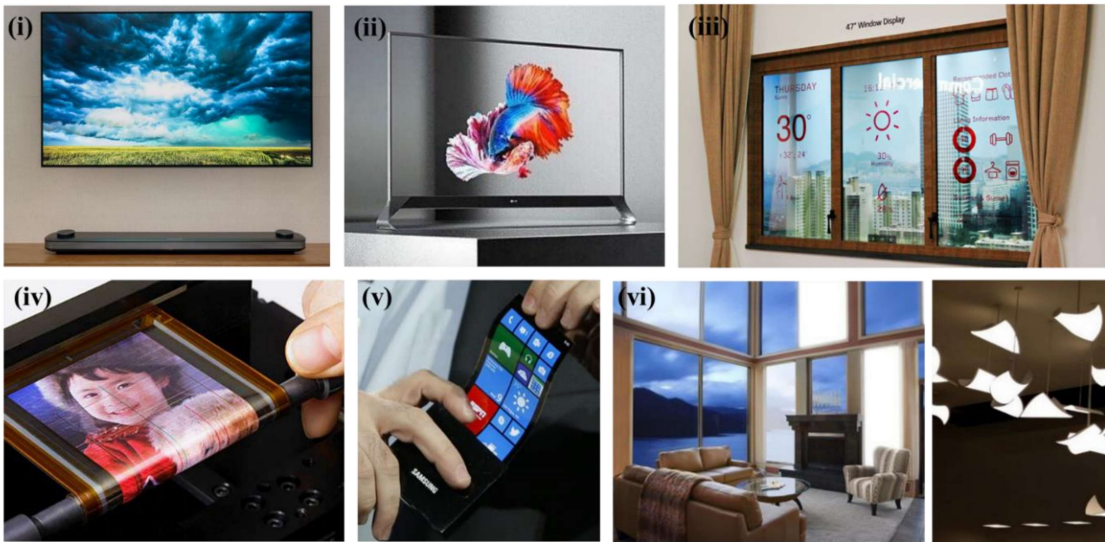

Fig. 1.12. Images of (i) LG 77" OLED TV – 2020, (ii) LG 55" Transparent OLED TV - 2021, (iii) LG 47" Window Display – 2015 (iv) Sony OTFT-driven OLED Rollable Screen – 2010 (v) Sansung OLED Curved Screen Phone - 2013, and (vi) OLED Window and Roof Lightning.

inorganic LEDs use back light so pixels are not self-emission by which perfect black cannot achieve. The self-lit pixels create the perfect black and avoid the halo effect or light bleed of the image (as shown in Fig. 1.13).

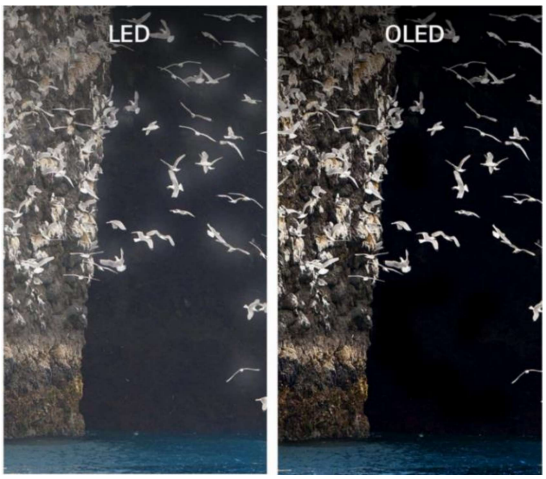

Fig. 1.13. The difference in picture quality of LED and OLED displays (Image from LG website).

1.6.2. Organic solar cells (OSCs)

Organic solar cell (OSC) is a photovoltaic device which converts electromagnetic radiation into electrical charges. It consists of a series of organic layers sandwiched between the electrodes. The organic layers are of hole transporting layer (HTL), active layers (donor and accepter), electron injection layer (EIL) [61]. When the device is exposed to the light with sufficient energy (greater than bandgap), the excitons are generated in the active layer and get dissociated by the energy difference. The acceptor transfers the donated electrons by the donor to the cathode through EIL. On the other side removal of electron (hole transfer) takes place through HTL by the anode. The conducting layers (HTL and EIL) decrease the barrier potentials at the interfaces and facilitate the diffusion of charge carriers into the electrodes without recombination [61].The charge transfer or conduction is due to the delocalisation of π-electrons by the hoping process through the conjugated organic structures [62]. The basic device structure

and working mechanism of the OSC is shown in Fig. 1.14. The key advantages of OSCs over conventional Si-based solar cells are of low-cost processing, higher solubility of materials

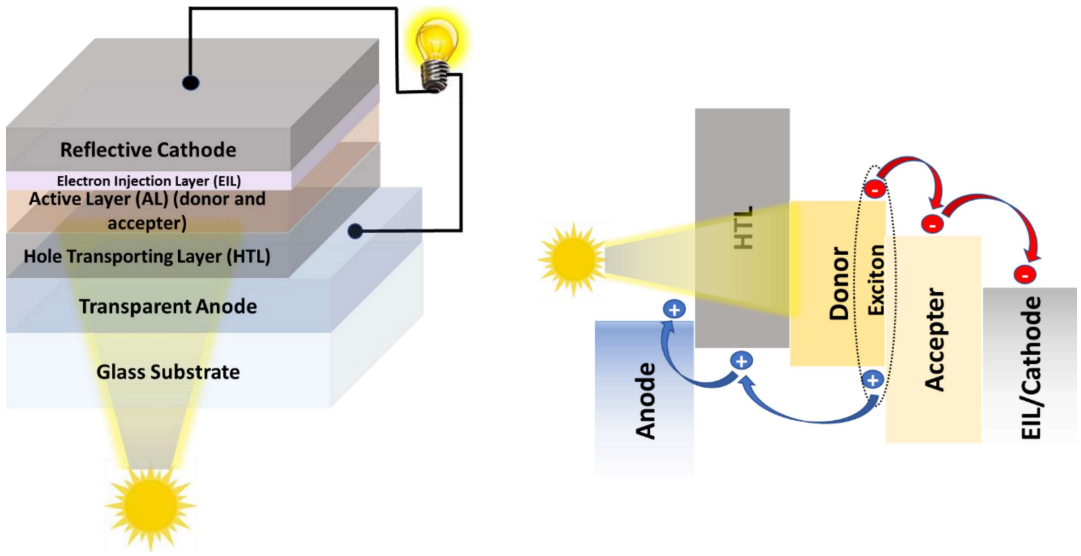

(i) (ii)

Fig. 1.14. Schematic of (i) Basic device structure of OSC and (ii) its working principle.

enabling roll to roll processing of device, earth abundance of organic materials, mechanical flexibility of device permitting a wide variety of uses, light weight, thin and large area deposition. There are drawbacks of OSCs such as low efficiency, short lifetime, lower environmental tolerance, and poor thermal stability. Atmosphere moisture, humidity, oxygen, and sunlight exposure cause a more negative effect on organics when compared to inorganic crystalline cells [63]. The low efficiency is related to the short exciton diffusion lengths and low carrier mobilities. Continuous exposure to Sunlight causes the thermal degradation of organic compounds in the device, leading to short lifetime. Current research is focusing on improving the absorber materials, developing the device architecture, improving the encapsulation, utilization of heat sinkers, and searching for alternative organic and contact materials to increase the device efficiency and lifetime [61,62]. The organic photovoltaic researchers have so far achieved the maximum efficiency of 18-20% [64,65]. The flexibility of OSCs offers to keep these devices in many applications like windows, curtains, dresses, carry bags, smart glasses, etc (example images of commercial OSCs are shown in Fig. 1.15) [66].

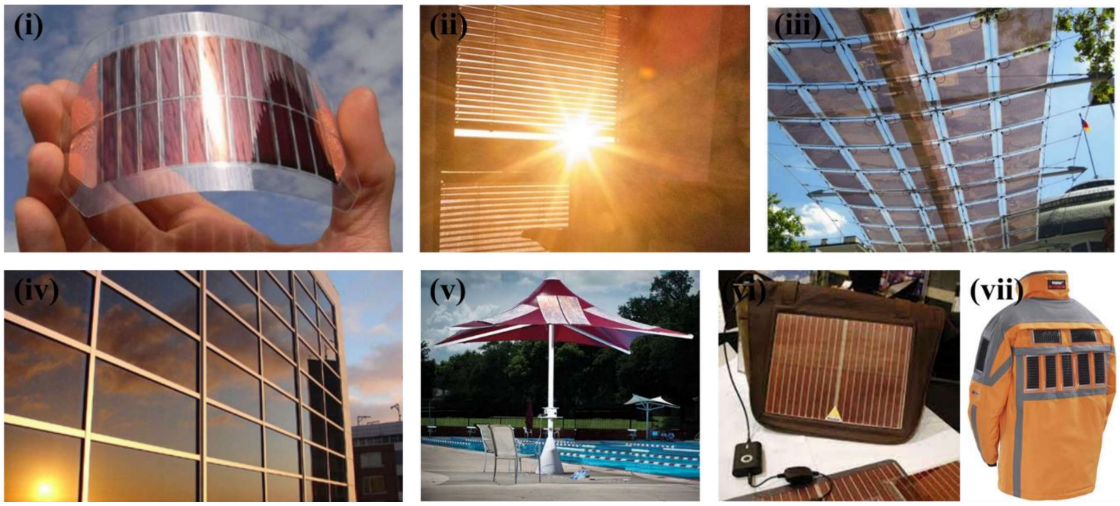

Fig. 1.15. Images of (i) flexible OSCs (ii) solar Window (iii) transparent OSC (iv) building-integrated with OSCs by Belectric company, Germany - 2014, (v) powerbrella by Konarka and Sky Shades - 2009, (vi) solar Bags by Konarka Technologies Massachusetts - 2010, and (vii) prototype of a winter outdoor jacket by Maier Sports and Institut für Physikalische Elektronik.

1.6.3. Ultra-violet (UV) Photodetectors (UVPDs)

Ultraviolet (UV) photodetectors (UVPDs) belong to a category of photosensors. A photosensor is an electronic device that detects the presence of visible light, infrared rays (IR), and ultraviolet (UV) rays. The photodetectors consist of photosensitive materials which respond to the photons and generate photocurrent conduction. A standard UV photodetector detects the UV light in the range of 195 – 370 nm and most commonly 254 nm. Based on the device structure and working mechanism, the UVPDs are classified as (i) metal-semiconductor-metal, (ii) Schottky junction, (iii) Homojunction/heterojunction-based devices [67,68]. These structure-based devices can be self-biased and/or external biased. The basic mechanism of UV photodetection includes (i) generation of excitons upon UV light illumination (energy greater than the bandgap of the semiconductor), (ii) separation of electron-hole pairs in the active layer, and (iii) collection of electrons and holes via conducting layers in the form of photocurrent by applying the external bias voltage (built-in electric field also generates the photocurrent without

external bias which are called as self-biased devices) [68]. UVPDs have been receiving large importance for the applications of environmental monitoring, forest-fire prevention, astronomical research, civilian and military fields, missile approach warning, medical analysis, etc [68,69]. In the present global warming circumstances, it is very much essential to develop the UVPDs towards large-array, fast-response, high UV sensitivity, lightweight, and low-cost production. ZnO is the highly efficient photo conducting material providing easy fabrication, high UV sensitivity, and low-cost production than the other photosensitive materials [67,70]. It works based on the oxygen adsorption and de-adsorption at the surface which plays a key role in the photoconduction.

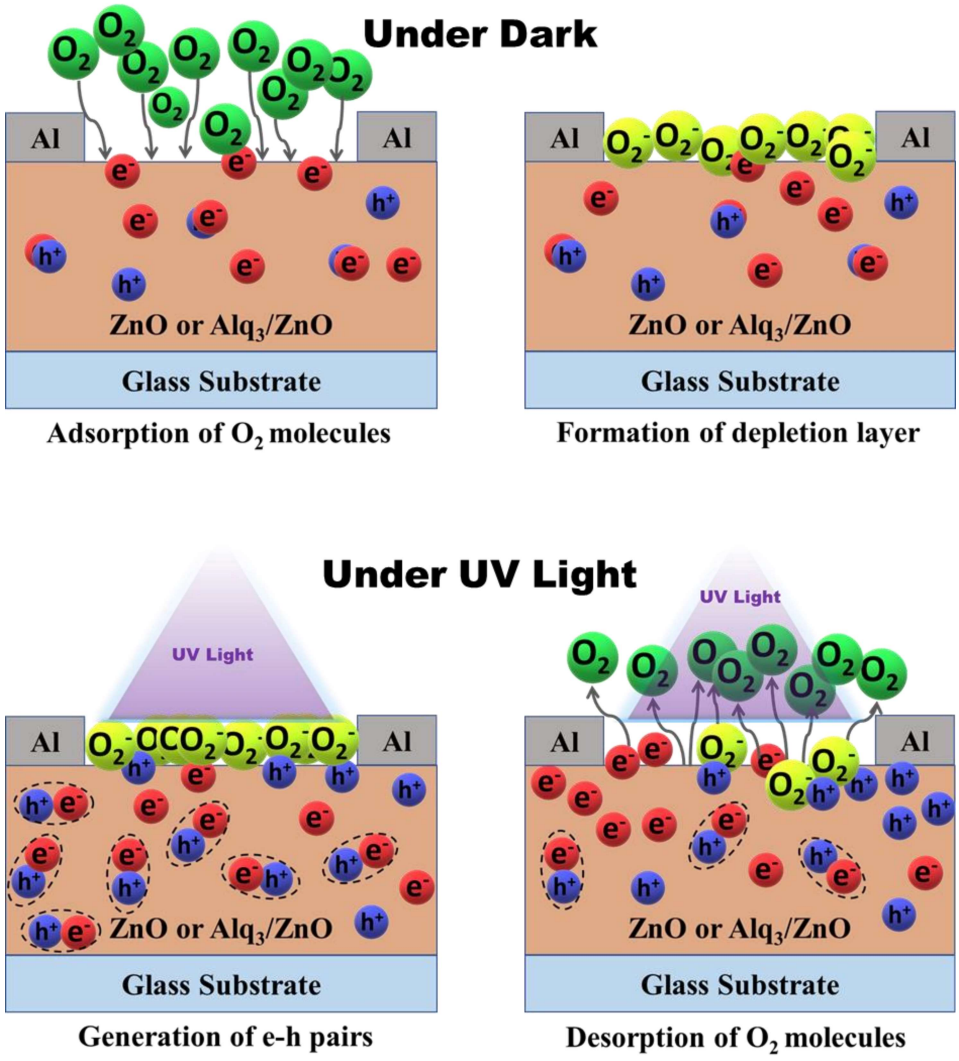

Fig. 1.16. Schematic illustrations of UV light detection process of UV photodetector.

The UV detection process (shown in Fig. 1.16) includes four steps as follows:

(i) Under the dark condition, oxygen from the atmosphere gets adsorbed onto the ZnO surface.

(ii) The adsorbed oxygen molecules captures the free electrons and forms the negatively charged depletion layer at the surface, resulting in less current.

O_2 (gas) + e^- (surface) $\rightarrow$ O_2^- (adsorption)

(iii) When UV light is illuminated the electron-hole pairs (excitons) are generated in the film.

$h\upsilon$ (UV) $\rightarrow$ e^- + h^+ (exciton)

(iv) holes migrate to the surface from the bulk and neutralize the negatively charged surface (decrease the depletion layer width or make the surface conductive) by desorbing the oxygen from the surface, simultaneously unpaired free electrons and available holes contribute to the photoconduction [71].

$h^+ + O_2^-$ (adsorption) $\rightarrow$ O_2 (gas)

The characteristic parameters of UVPD which decide the device performance are photocurrent, gain, sensitivity, responsivity, detectivity, and electronic quantum efficiency [71,72]. There are certain limitations to overcome in ZnO-based devices for better performance. ZnO consists of its characteristics native defects which create the charge traps in the film, resulting in slow charge carrier generation and recombination. In the homojunction or heterojunction-based devices, the lattice mismatch between the junctions creates the charge traps in the devices which reduces the device performance. Self-biased UV photodiodes exhibit the fast responses and high sensitivity but low photo current and responsivity. Built-in electric fields are insufficient to overcome the barriers at the interfaces/junctions resulting in less photocurrent and responsivity. Surface roughness of ZnO affects the efficient light absorption by creating the light trappings centres. Research is going on in order to overcome the native defects, homo-/hetero- junction

lattice mismatch, charge traps, light trapping effects, low mobility, and low built-in electric fields for the efficient utility of ZnO in UVPDs [67,68].

1.7. Importance of hybrid structures in optoelectronic devices

The key roles in the performance of optoelectronic devices are charge injection/extraction between electrodes and organic layers, light absorption/emission, interface interactions between the adjacent layers, charge balance, charge mobility in the conducting layers, adhesiveness and lattice mismatching between the layers, encapsulation, ambient conditions, moisture, temperature, etc. The inorganic semiconductor-based devices have high production costs especially for large-area fabrication, high processing temperature, and are not biodegradable or biocompatible. These devices offer high device efficiency, thermal stability, chemical stability, ambient stability, and high durability. Whereas organic devices possess poor stability, photo-oxidation, degradation, and short lifetime. The organic devices have the excellent features such as large-area fabrication, flexibility, improved device performances, low temperature processing, and simple fabrication method which make them as alternative to conventional inorganic devices. It is also essential to understand a new class of composite materials (hybrid) that combines the essential features of organic and inorganic, and minimise the drawbacks of respective individual based devices. The optoelectronic devices based on hybrid composites present good stability and better device performances when compared to the respective organic- or inorganic- based devices. The incorporation of inorganic nanostructures increases the stability of organic components. These nanostructures create the conducting pathways in the composites and also modulate the optical properties for optoelectronic applications [73]. Prasad et al. have reported the increased charge mobility of Polyvinylcarbazole (PVK) by incorporating the CdSe nanoparticles [74]. The enhanced photocharge generation was also observed from this hybrid nanocomposite compared to the C_{60} doped PVK. C.J. Wang et al. reported that the Poly(p-phenylene vinylene) (PPV)/silica composite glass exhibits very low optical loss when

compared to the pure PPV [75]. This composite glass presents high surface quality, easily polishable ends for end-fire coupling of light waveguides, high mechanical strength for holographic grating applications, and is capable of producing the photorefractive medium. In hybrid nanocomposites, most of the nanoparticles are in contact with the adjacent layers which increases the contact area, resulting in the efficient charge injection [73]. The hybrid compounds exhibit less film thickness compared to individual elements which induce more electric field in the device, resulting in higher current density. The LED efficiency depends upon the recombination in the active layer. The charge balance in the device increases the recombination rate which depends upon the mobility of the charge carriers (electrons/holes) in the organic materials. Mostly the organic semiconductors exhibit higher hole mobility than that of electrons whereas the inorganic semiconductors exhibit higher electron mobility [73]. The proper combination (hybrid) of these organic and inorganic counterparts enhances the charge balancing and hence improves efficiency of the devices. The highly efficient white hybrid LEDs (ITO/PEDOT:PSS (or) poly-TPD/CBP:QDs /Alq_3/Ca/Al) were reported by incorporating the CdSe/ZnS QDs in CBP and achieved the maximum electroluminescence of 1500 – 1800 cd/m^2 with the efficiency of 0.96% [76,77]. Wendy U. Huynh et al. has demonstrated the hybrid solar cell using P3HT:CdSe blend and reported the PCE of 1.7% [78]. The OSCs based on P3HT:TiO_2 and P3HT:ZnO blends also show efficient charge separation yield [73,79]. Research has been extensively carried out using ZnO as accepter or cathode buffer layer (CBL) in hybrid solar cells and achieved the better PCE with improved exciton dissociation and mobility of the charge carriers [79]. ZnO is a high photoconduction material and it is used in the applications of photodetectors [71]. ZnO in pure and doped form are widely used in UV-photodetectors as active material and achieved excellent device performance [70,71]. Owing to superior properties like thermal and chemical stability, tuneable optical properties, and balanced conductivity, hybrid materials are being used in many applications such as sensors, lasers, optical fibres, fuel cells, photodetectors, solar cells, LEDs, etc.

1.8. Scope and objective of the research work

The scope of this research work is mainly to focus on preparation and characterization of solution processed organic/inorganic hybrid thin films and fabrication of efficient optoelectronic devices. The organic compounds exhibit the good absorption and emissive properties, mechanical stability, flexibility, biocompatibility, nontoxic, and cost effective but whereas they show the poor mobility and ambient stability. The inorganic materials exhibit the good thermal, electrical properties and good chemical stability. Thus, hybrid(organic/inorganic) composite materials exhibit high thermal stability, chemical resistance, mechanical strength, good optical and electrical properties over organic and inorganic materials. The optoelectronic devices based on organic/inorganic hybrid structured materials can exhibit the better device performances with improved stability. The charge injection/extraction from the anode material is also one of the several factors which affect the optoelectronic device performances. The hybrid structure-based devices with improved film quality of ITO anode can also exhibit the higher electrical properties with efficient charge collection/extraction.

The objective of this thesis work is

(i) To deposit and optimize the sol-gel derived Alq_3/ZnO hybrid thin films by cost-effective spin-coating process for the different molar ratios of Alq_3/ZnO in the film and characterize the structural, morphological, optical and electrical properties for their solution processed optoelectronic device applications such as UV photodetectors.

(ii) To study the effect of Ni Swift heavy ions (SHI) on the structural, morphological, optical and electrical properties for their applications in solution processed Alq_3/ZnO hybrid thin film-based UV photodetectors with improved performances.

(iii) To improve the metal electrode/organic interface properties for the improved device performances, ITO coated glass substrates are to be annealed at different temperatures under the normal ambient and studied their optical and electrical properties for the efficient device performances and to understand the strategy of annealing of ITO anode at higher

temperature under the normal ambient in order to improve the hole injection/hole extraction in the OLEDs and OPVs for the efficient device performances.

(iv) The strategy of annealing of ITO anode at higher temperature under the normal ambient is to be utilized to improve the performances of Alq_3/ZnO hybrid-based UV photodetectors.

Chapter: 2

Preparation and instrumentations for characterization of Alq_3/ZnO hybrid thin films and devices

This chapter describes the preparation of Alq_3/ZnO composite thin films by solution process and basis of thin film formation using spin coating technique. It also briefs the fabrication process of various optoelectronic devices such as Hole-only devices (HODs), Electron-only devices (EODs), OLEDs, OPVs, UV photodetectors. This chapter further discusses the instrumentation details of various characterization techniques used for the study of Alq_3/ZnO hybrid thin films and devices.

2.1. Precursor preparation for Alq_3/ZnO hybrid thin films

The precursor for Alq_3/ZnO composite thin film was prepared by incorporating Alq_3 solution into ZnO precursor with different volume percentages. The sol-gel method allows powder less processing of thin films, ceramics, and glasses directly from the solution at the low processing temperature [80]. The parameters in sol-gel preparation that influence the thin film formation are the nature of precursor, solvents, additives, processing temperature, concentration, aging time, and solution filtration [80]. Various precursors have been used, such asnitrates, chloride, perchlorate, alkoxides, and acetylacetonate. Most often used precursors are nitrates and acetate. The main drawback of nitrates is contaminations or anionic species in the final product, whereas in the zinc acetate case, the contaminations are decomposed during the annealing process [81]. The zinc perchlorate instead of zinc acetate creates the coagulation of the particles rather than colloidal solution formation [80]. The ZnO thin film prepared from the zinc acetate precursor exhibits a strong c-axis orientation than the Zinc n-propoxide based films [82]. Zinc acetate dihydrate (ZAD) based ZnO thin film with a molar concentration in between 0.3 – 0.7 M presents more than 85% of transmittance, highly c-axis oriented (002) peak, and

efficient band edge emission with less defective states [83,84]. The aging time of solution influences the crystal structure of deposited film: longer aging time of 24 hrs presents the polycrystalline, and for 2 hrs, amorphous nature [85]. The low boiling point solvents will not give preferential orientation. ZAD with 2-propanol and diethanolamine (DEA) leads to the imperfect orientation, in contrary to ZAD-2-methoxyethanol (2ME)-monoethanolamine (MEA) having high boiling points, providing the strong orientation [82]. The additives also affect the film quality of ZnO, the film with MEA gives the highly crystalline and oriented films than DEA [82]. By proper selection of precursor, solvent, additive, and aging time, concentration of solution, the good quality of thin film can be achieved.

ZnO sol-gel was prepared using Zinc acetate dihydrate [$Zn(CH_3COO)_2.2H_2O$] as the precursor, 2-methoxyethanol ($C_3H_8O_2$) as the solvent, and monoethanolamine (MEA: C_2H_7NO) as the stabilizer. The ZAD was dissolved in 2-ME by adding MEA dropwise. The solution was stirred at 450 rpm for 2 hrs at 60 °C using magnetic stirrer with hot plate. The solution was prepared with the molar concentration of 0.5 M and MEA was added in 1:1 molar ratio with ZAD. In ZnO sol-gel process, at first, the Znic acetate dihydrate [$Zn(C_2H_3O_2).2H_2O$] undergoes dehydration process and transforms to mono-acetate [$Zn(C_2H_3O_2).2H_2O$] in presence of 2-ME as per the reaction given below [86]:

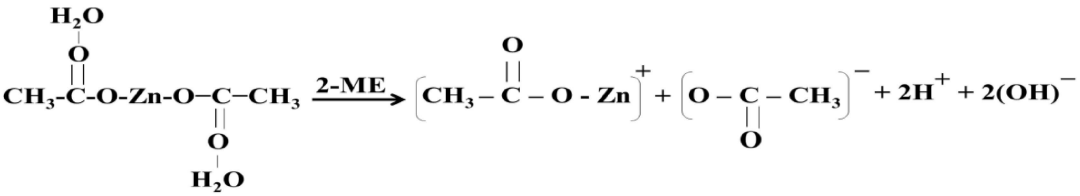

In this process, the hydrolysis and condensation of Zn (II) cation are relatively slow due to the low quantity of H_2O molecules for the formation of ZnO. The adding of additive or stabilizer (MEA: C_2H_7NO) hinders the condensation; however, it increases the pH of the solutions and promotes the formation of ZnO following as [86]:

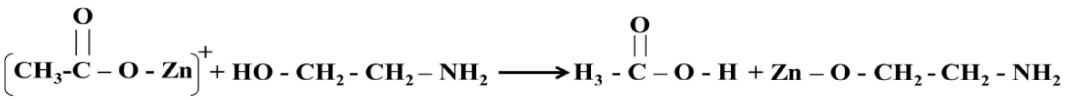

Simultaneously, Alq_3 solution of 10^{-3} M was prepared by dissolving the Alq_3 in 2-ME by stirring at 450 rpm for 2 hours under the normal ambient. Both solutions of ZnO and Alq_3 were filtered using 0.2 μm syringe filter. Alq_3 was incorporated into ZnO with different volume percentages such as 20%, 40%, and 60%. The molar ratio of Alq_3 to ZnO (Alq_3/ZnO) in the three solutions were maintained at 0.5×10^{-3} for [ZnO (80 vol.%) (0.4 M) + Alq_3 (20 vol.%) (2×10^{-4} M)], 1.3×10^{-3} for [ZnO (60 vol.%) (0.3 M) + Alq_3(40 vol.%)(4×10^{-4} M)]; and 3×10^{-3} for [ZnO (40 vol.%) (0.2 M) + Alq_3 (60 vol.%) (6×10^{-4} M)]. These solutions were aged for 24 hrs for gel formation. During the gel formation the ZnO molecules interact with the Alq_3 molecules and may covalently bond.

2.2. Substrate Cleaning

The substrate cleaning is one of the important factors for quality thin film formation. The cleaning process is done to remove oil, grease, or any other chemical contaminations (which may have formed while manufacturing) on the surface of substrate. The substrates (glass or ITO) were cut into required (2×2 cm^2) size. At first the substrates were rinsed and sonicated for 10 min in soap solution for the initial cleaning of the substrate, followed by rinsing and sonication in DI water for 10 min to remove the soap particles on the surface and dried for 10 min on hot plate at 100 °C under the normal ambient. This same process was continued in acetone, IPA and DI water respectively. Further, the substrates were high plasma cleaned for 10 min using plasma cleaner (make: Harrick plasma, model: PDC- 002) to remove the ionic contamination present on the substrates. The substrates were then exposed to the UV light for 10 min using UV light curing system (Kaivo) in order to enhance the adhesiveness and work function of ITO. The cleaned substrates were used for thin film coatings by spin coater and/or followed by thermal evaporation vacuum coating unit.

2.3. Thin film deposition methods

The thin film deposition methods are classified based on the working principle into two major categories such as physical and chemical deposition methods. Fig. 2.1 shows the various chemical and physical deposition methods, and these two methods are further sub-classified into the liquid phase, gas phase, evaporation, and sputtering [87]. In the chemical deposition method (CDM) the oxidation and reduction process will play a crucial role in film formation. In case of physical deposition method (PDM), physical phenomenon such as evaporation, ejection, condensation, and sputtering play a crucial role. However, both the methods have their own advantages and disadvantages. The high vacuum deposition methods are much useful to fabricate films for commercial devices, In the present research work, the cost-effective chemical spin-coating process and thermal evaporation methods are used for deposition of various organic and hybrid thin films for the fabrication of devices.

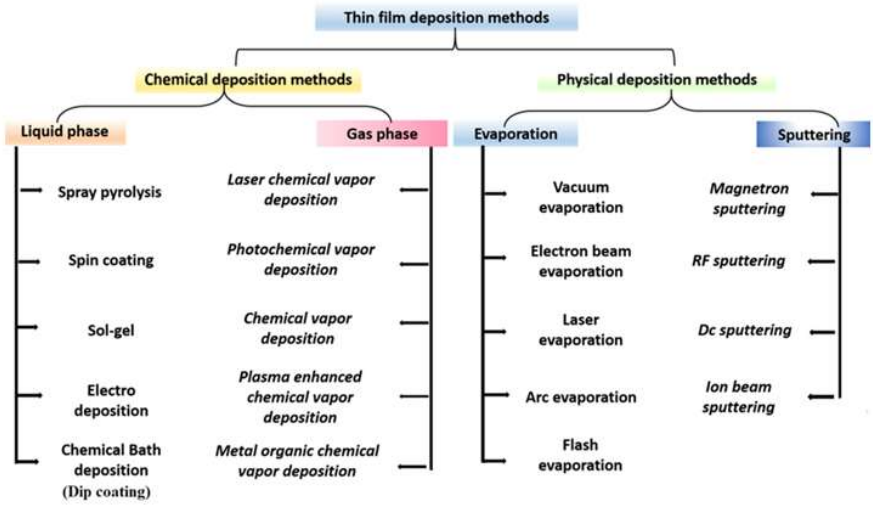

Fig. 2.1. Classification of thin film deposition methods.

2.4. Thin film formation by Spin-coating technique

It is a simple and low-cost thin-film coating technique when compared to other coating techniques. When the solution is spun on the substrate at high speed, the centrifugal force and surface tension together form the even covering of solution, and then the annealing process will

evaporate the solvent. One can form a good quality thin film by appropriately optimizing the solution preparation, spinning parameters, and pre-annealing conditions. Factors affecting the uniform film formation are solution concentration, viscosity, precursor dissolving or dispersion, spinning rpm (rotations per minute), spinning time, acceleration time, substrate cleaning, substrate type, pouring the solution onto the substrate, coating conditions, pre-annealing temperature, and annealing temperature [88,89]. There are four basic steps involved in the thin film formation using spin-coating method as followed (schematic shown in Fig 2.2) [88,90,91].

(i) Dispense: It is a stage of deposition of solution onto the substrate. This is of two types, static deposition and dynamic deposition. In the former case, the solution is deposited when the substrate is at static position, In the latter case, the fluid is deposited at the low spinning speed of the substrate commonly at 500 rpm. The static deposition requires more fluid to wet the total substrate area, it is of wasting material but it can avoid the voids in film formation and useful for poor wetting substrates.

(ii) Substrate acceleration or spin up: The substrate is given a speed from 0 to level of about 2000 rpm within 3-10 s. During spin up the solution and substrate are to rotate with different speeds. These two rotation speeds match up when flued drag force balances with the rotational acceleration force and forming the thin layer of fluid. The fast spin up rate may dissipate the solution out and spin up rate form the agglomeration of particle leads to the ununiform distribution of particles or solution.

(iii) Constant rotation: At this stage the viscous force become dominated one and solution turns into the thin film formation. Typically, this constant rotation is about 1000-6000 rpm. The thinning of film with proper atomic arrangements occurs at a constant spinning speed. Higher the spinning speed, lower the thickness of film and vice versa for a particular solution. For high viscous solution the spinning speed should be high to overcome the viscous force for uniform distribution of solution and for low viscous solution, it should be less to avoid the spilling or non-uniform distribution of solution.

(iv) Solvent evaporation: It is the process to evaporate the solvent from the spinning layer. It is of two types, first, the solvent is evaporated while spinning with constant speed at room temperature. Second, the solvent is evaporated at particular temperature (depending on the solvent) under ambient or vacuum. After the solvent evaporation the substrate is remain intact with the film. Immediate evaporation requires thorough spinning otherwise solution becomes more concentrated and viscous. In annealing case, the sudden rise in temperature will leave the cracks or agglomeration of particles. The moderate annealing is required for uniform film formation.

Thin film formation using spin-coating process has following advantages and disadvantages [88,89,92].

Advantages:

- Simple and easy process.
- Requires very less time for thin film formation.
- Able to coat less thickness even as less as 10 nm.
- Low temperature processing (Under normal ambient)
- Less material quantity.
- No need of vacuum conditions.
- Cost-effective coating.
- Fine controlling on material content and film thickness.
- Less porous and uniform film formation.

Disadvantages:

- Not suitable for large area coating and flexible substrates.
- High optimization required on solution preparation and spin-coating parameters.
- Wastage of solution during spinning, only 10% is utilised for actual film.
- Fast drying times leads to the formation of cracks in the films.

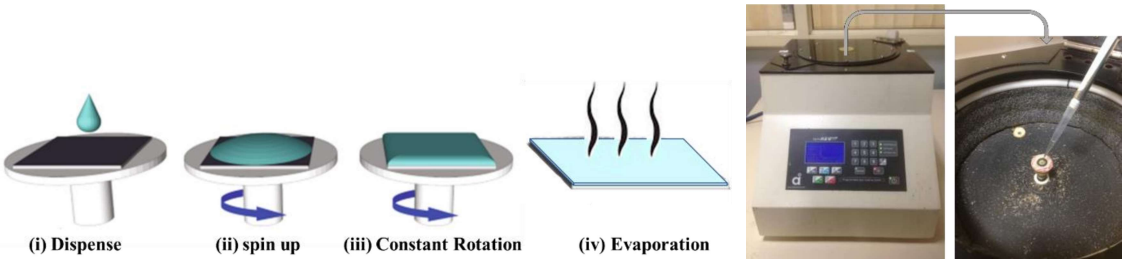

Fig. 2.2. (i) Schematic representation of thin film formation using spin-coating technique and (ii) image of spin coater.

Instrument Specifications:

Make: *Apex Instruments*; Model: *SpinNXG-P2*; Speed Range: *100-10,000 R.P.M*; Acceleration: *40-5,000 R.P.M./sec*.

2.5. Thin film Deposition by thermal evaporation method

It works on the following steps: (i) thermal evaporation of a solid material under high vacuum, (ii) the evaporated atoms/molecules hit the substrate, and (iii) the film deposition by condensing. Thermal evaporation coating unit is mainly consisting of vacuum deposition chamber and vacuum system (diffusion and rotary pumps) [93,94]. The chamber is circulated with the cooling system. Inside the chamber is consisting of electrode system at the bottom, substrate holder at the top, shutter in the middle, crystal oscillator relatively parallel to the substrate holder, and vacuum pipe at the bottom. The schematic view of chamber is shown in Fig. 2.3(i). At first the chamber is evacuated with the high vacuum ranging from 10^{-5} – 10^{-9} mbar using rotary and diffusion pumps [94]. The electrode system is used to sublimate the material by heating the filament or boat (evaporators: molybdenum, tungsten or tantalum) following the joule heating effect [$Q = I^2Rt$; I – current (10 - 100 A), R – resistance, t – time] [95]. The atoms sublimated from the source directly travel in all directions, hit the substrate and condense to form a film onto the substrate. Magnitude of the vacuum highly affects the uniformity of film (Fig. 2.3(ii)). At low vacuum (< 10^{-3} mbar), the air molecules scatter the

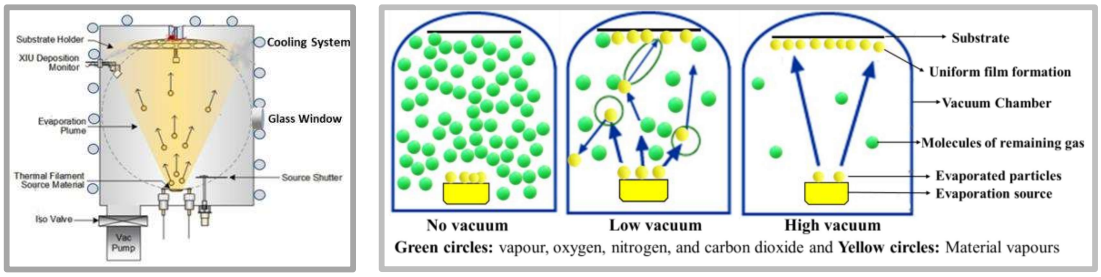

(i) **(ii)**

Fig. 2.3. Schematic representation of (i) deposition chamber of thermal evaporation vacuum coating unit and (ii) vacuum effect on thin film formation.

vapour atoms/particles (having less mean free path) leading to ununiform distribution of particles/atoms on the substrate. Under the high vacuum (> 10^{-4} mbar), the mean free path for particles/atoms is about 60 m, so under high vacuum the particles directly hit the substrate with same velocity and form the uniform film. The high vacuum avoids collisions of the particles with the foreign atoms and increases the purity of the film. The vapour particles of the material simultaneously hit the crystal oscillator, which is fixed nearly parallel to the substrate. The mechanical shocks and vibrations of the particles causes the frequency shifts of the crystal oscillator. The thickness monitor measures the thickness and rate of deposition in corelation with these frequency shifts [96]. Figure 2.4 shows (i) the schematic of thermal evaporation system and (ii) image of vacuum coating unit.

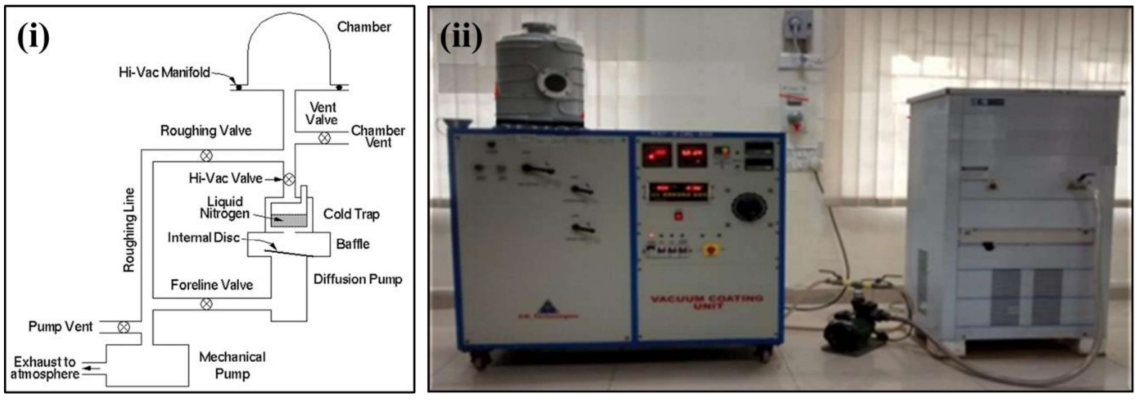

Fig. 2.4 (i) Schematic view of vacuum creating system and (ii) image of thermal evaporation vacuum coating unit with chiller system.

Thin film coating unit exhibits the following advantages and disadvantages [94,95];

Advantages:

- Control on thickness, uniformity, and adhesion strength.
- Due to the low kinetic energy of the material atoms, the substrate is protected from defect nucleation and damage.
- Easy and short time coating process (typically 1- 2 hrs).
- Cost-effective process.

Disadvantages:

- Possibility of contamination from the hot boat or filament which influences the stoichiometry of the coating material.
- Wastage of some source material which coated all around the inside walls of chamber.
- Possibility of contamination from the previous evaporated material.
- Not suitable for materials with high melting point like metal oxides.
- Limited area of coating.

Instrument Specifications:

Make: VR Technologies; Maximum Vacuum level: 1.0×10^{-6} mbar; Film Thickness: 1nm to hundreds or thousands of nm thick.

2.6. Thin Film Characterization Techniques

2.6.1. UV-Visible Spectrometer

The UV visible spectroscopy is a powerful tool to measure the optical properties (transmittance, absorption, reflectance, etc.) of samples [97]. If a material possesses higher transmittance in the visible region it clearly indicates lower absorption and reflectance. If the sample does not absorb the incident light for a given wavelength range and the incident lightintensity (I) and transmitted light intensity (I_O) are equal ($I = I_O$). However, in practice all the materials do not possess complete transmittance, Io is always lower than I ($I_O < I$). The

relation between absorption (A), and transmittance (T) is given according to Beer-Lambert's law, and the absorption of the material is expressed as follows, ($A = -\log(T) = -\log I_O/I$) [98]. The absorption of the material also depends on the film thickness and absorption coefficient of the material ($\propto$). The absorption coefficient is intrinsic property of a material. The optical band gap is estimated using the transmittance and thickness of the sample. In the semiconducting system, electrons can be excited from the valence band to conduction band during the absorption of incident light energy. In the semiconducting system, there are two types of optical transitions that can occur; direct and indirect transitions. Both transitions arise because of the interaction of the electromagnetic radiation with the crystal lattice. The estimation of direct and in direct bandgap of the samples by Tauc relation [99]. The schematic diagram of the UV-Vis-NIR spectrophotometer is shown in Fig. 2.5. In present research work, the optical properties were analysed as a function of incident wavelength using Agilent Technologies UV-Vis spectrometer.

Instrument Specifications

Model: *Cary 5000 UV-Vis-NIR spectrometer*; Lamp: *deuterium*; Detectors: *photomultiplier tube for UV−Vis, In GaAs for (NIR)*; Wavelength range: *175–3300 nm for transmission*.

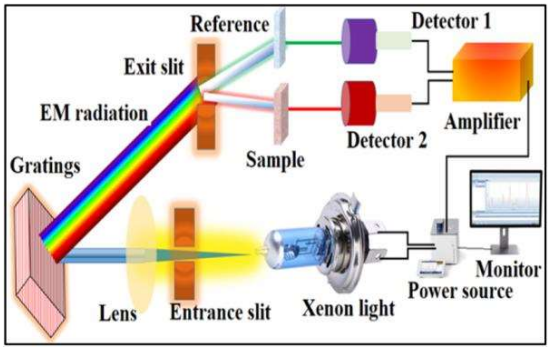

Fig. 2.5. Schematic of working mechanism of UV-visible spectrophotometer.

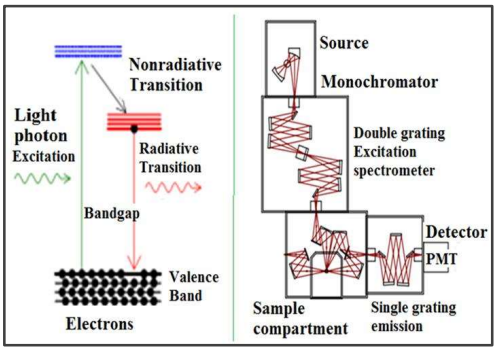

Fig. 2.6. Schematic of possible transitions in Photoluminescence emission process.

2.6.2. Photoluminescence spectroscopy

The photoluminescence (PL) spectroscopy is an effective technique to understand various electronic transitions in materials. The luminescence study is useful to identify the excitation and emission process, band gap, and impurity defect levels of materials, based on the emission spectra [100]. The PL is emission of light when the incident photon energy is equal or higher than the band gap energy. The electrons will be excited from valence band to conduction band during the absorption of light energy. The excited state is not a stable state; hence the electrons return to ground state by radiating energy as illustrated in Fig. 2.6. It is also possible for non-radioactive transition from excited state to ground state. The photoluminescence of a material is obtained because of core shall electron, valence electron, free electron, localized impurity states or defect state of the system. The electronic transitions of materials are classified into two types, i) radiative transition and ii) non-radiative transition. The radiative transition happens due to the intrinsic states formed by the impurities. There are different types of radiative transitions arise in materials such as band-to-band transition, free exciton transition, and free-to-bound transition. Non-radiative transition happens before or after the radiative transition and during the non-radiative process, no emission will be delivered [101]. In the present research work the Horiba scientific PL instrument is used for studies.

Instrument Specifications

Model: *Fluorolog3-2*; Lightsource:*450 W CW Ozone-free xenon arc lamp (250 to 2500nm)*; Monochromators: *Czerny-Turner design with plane gratings for optimized focus at all wavelengths and minimum stray light;* Sample detector: *PhotomultiplierR928P, spectralcoverage200 to 870nm*; Reference detector: *UV enhanced silicon photodiode*.

2.6.3. X-Ray diffraction

The crystalline structure, phase purity, lattice parameter, degree of crystallinity, and composition of the sample are analyzed by X-ray Diffraction (XRD) technique. It is also useful

to estimate quantitative parameters of the samples such as grain size (crystallite size), texture coefficient, and stress analysis/lattice strain of the films. For X-ray to be diffracted, the spacing in the lattice grating should be of the same order as that of the wavelength. In crystals, the typical interatomic distance is ~ 2-3 Å which is suitable for X-rays to be diffracted. X-ray diffraction is based on interference of diffracted X-rays by crystalline sample [102]. The X-ray diffraction condition is also known as Bragg's condition at $2d_{hkl}\sin\theta = n\lambda$, d_{hkl} is the inter-planar spacing of the respective hkl plane, θ is the Bragg's angle, n is the order of diffraction, and λ is the wavelength of the incident X-ray radiation. The diffracted peak pattern has non-zero width due to several factors including instrumental effect, grain size, lattice stain, etc. [103]. The Bragg's equation indicates the inter-planar distance in a given material which can be estimated from the diffracted angle and the known wavelength. Figure. 2.7 shows the schematic representation of X-ray diffraction process, and also the extended view of Bragg's plane in the inset of Fig.2.7.

Instrument Specifications

Model**:** *XPERT-PRO equipped with Cu-Kα radiation (wavelength 1.5406 Å)*, Goniometer configuration: *Horizontal goniometer (θ-θ)*; Detector: *PIXcel3D Detector;* Scan range: *3° to 136°*; Scanning angle rate: *0.01°*; Count time: *1s/step*.

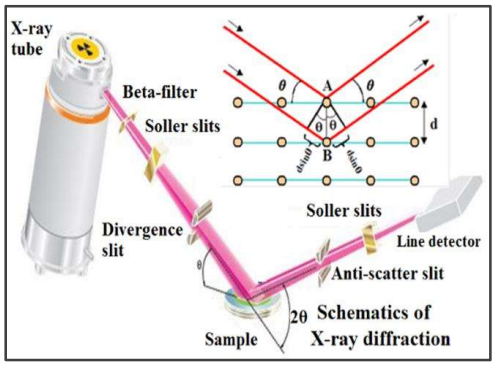

Fig. 2.7. Schematic of X-ray diffractometer and the inset is Bragg's law representation.

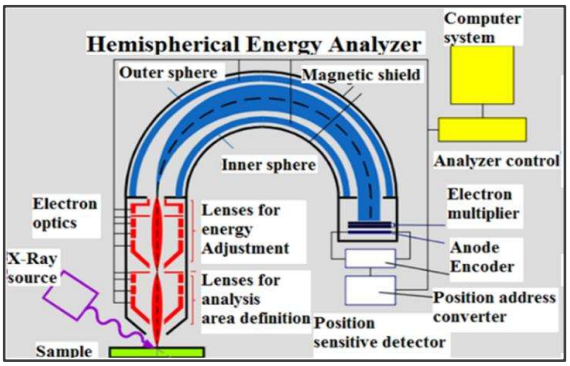

Fig. 2.8. Schematic of X-ray photo electron spectroscopy (XPS).

2.6.4. X-ray photoelectron spectroscopy (XPS)

The X-ray photoelectron spectroscopy (XPS) is a sophisticated technique to analyze the binding energy and surface oxidation of the elemental constituents of samples [104]. When the X-ray is focused on the sample, electrons absorb the X-ray energy and escape from the orbital with maximum kinetic energy of $E_k = h\nu - E_B - e\Phi$, where E_B is electron binding energy, ν is the photon frequency, and Φ is work function, which is the minimum energy essential to remove an electron from the surface of the material [105]. The X-ray radiation is continuously incident on the sample's surface, and the photoelectrons are ejected from the sample surface. The ejected photoelectron is a function of its binding energy and is characteristic of the element from which it is emitted. The energy of this conversion is adjusted by the emission of an Auger electron or a characteristic x-ray spectrum. Investigation of Auger electrons can be used in XPS measurement. The XPS is a surface sensitive technique because only those electrons generated near the surface escape and are detected. The photoelectrons of interest have relatively low kinetic energy. Due to inelastic collisions within the sample's atomic structure, photoelectrons originating more than 20 to 50 Å below the surface cannot escape with sufficient energy to be detected. The XPS instrument consists of three major parts such as photoelectron production unit, a detector unit and analyser unit as shown in Fig.2.8.

Instrument Specifications

Make: *Thermo Scientific*; Model: *The tapro be angle-resolved X-ray photo electron spectrometer (ARXPS)system*; AnalyzerType:*180°double focusing hemispherical analyzer with PARXPS detector*; X-Ray source type: *monochromatic, micro-focused AlK-Alpha, X-Ray*; Spot size:*15–400µm*; Sampling area: *maximum70×70 mm*.

2.6.5. Scanning Electron Microscopy

The scanning electron microscope (SEM) is the most extensively used technique to study the surface morphology of samples with high resolution and depth of focus [106]. The

highly accelerated electron beam interacts with sample surface in two ways; elastic and inelastic interaction. Elastic interaction results from the deflection of the incident electron beam by the sample by outer shell electrons of similar energy. Incident electrons that are elastically scattered through an angle of more than 90˚ are called backscattered electrons (BSE). Inelastic scattering take place over an interaction between the incident electrons and the sample, which results in the primary beam electron transferring substantial energy to that atom. As a result, the excitation of the specimen electrons during the ionization of specimen atoms leads to the generation of secondary electrons (SE). These two types of the electrons are used to image the surface morphology of the samples. The figure 2.9 shows the schematic of the SEM instrument. The electron beam is produced by an electron gun by field emission. The produced electron is accelerated around 300V-30kV using anode grid towards the sample surface. The accelerated electron beam is focused on the sample surface using various electromagnetic lenses and apertures. When the electron beam is scanned over the sample surface, different types of signals are obtained from the sample's surface. The emitted signal can be collected by several detectors for a particular application. The X-ray Energy Dispersive Spectroscopy (EDS) method is useful to identify the quantitative information of chemical composition of the samples, from the energy of the emitted X-ray radiation. For the present research work, surface morphology and chemical composition of the films was analysed by using a TESCAN SEM instrument with specifications given below.

Instrument Specifications

Make: *TESCAN*; Model: *VEGA-3 LMU attached with Oxford Scanning Electron Microscope*; Electron Source: *pre-centered tungsten hair pin type*; Accelerating voltage: *300V to 30 kV;* Resolution: *3.0nm*; Magnification: *5 X to 300,000 X*; Secondary electron detector: *Everhart-Thornley*; Backscattered electron detector: *Thin five-segment solid-state detector*.

2.6.6. Atomic force microscopy

The atomic force microscopy (AFM) is a very high-resolution surface scanning microscopy with established resolution of the order of nanometre. The force of attraction or repulsion between the tip and sample's surface make the cantilever to bend or deflect from the sample surface. The cantilever deflection arises due to the electrostatic force between the tip and sample and also the Vander Waals force of attraction between the inter-atomic species [107]. A detector measures the cantilever movement as a function of tips canning on the sample surface. The deflection of the cantilever monitors the surface topography. Based on the interaction between tip and sample surface, the AFM instrument work in three different modes: contact mode, non- contact mode, and tapping mode. The schematics of working principle of the AFM instrument is shown in Fig. 2.10, and it consists of three parts; laser source, cantilever part, and a detector part. When the tip is brought close to the sample surface, forces between the tip and the sample lead to a deflection of the cantilever according to Hooke's law [108]. The reflected laser light is detected by a photodiode with the respective motion of cantilever. Further, the detected light signal and the reference signal are sent to the feedback amplifier to analyse and record the surface variations on the sample. For the present research work, surface topology of the films was analysed by Park Scientific Instrument.

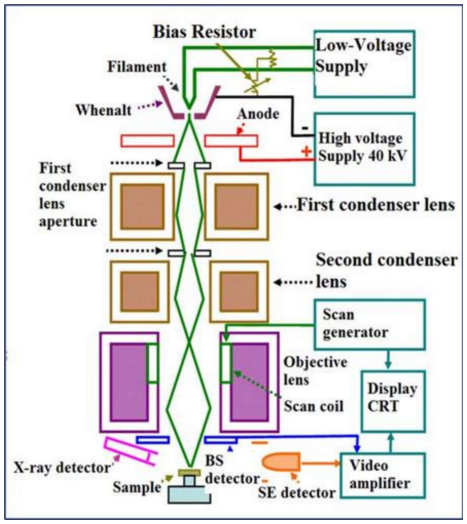

Fig. 2.9. Schematic of working mechanism of SEM.

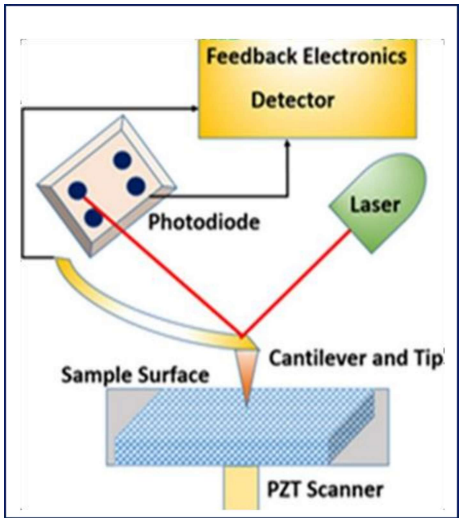

Fig. 2.10. Schematic of working mechanism of AFM.

Instrument Specifications

Model: *Park NX10*; Scanner Type: *XY Scanner Single module flexure with closed-loop control of 50 μm×50 μm*; Resolution: *0.05 nm*; XY stage travel range: *20×20 mm*; Sample size: *Open space up to 20×20 mm^2, thickness up to 20 mm^{2}in contact mode*.

2.6.7. Hall-Effect

The estimation of electrical transport properties of TCE thin film is more important from applications point of view. Investigations of the electrical transport properties of thin film indicate that it depends on thickness, structural and surface properties of the thin films. The electrical transport properties were estimated by Hall-Effect method using standard Van der pauw geometry. Hall-Effect method is a widely used techniques to distinguish the type of conduction (n-type or p-type), and to estimate the carrier concentration, mobility, conductivity of semiconducting sample accurately. The basic principle of hall-effect is, when a current (I_H) Carrying conductor is placed in a uniform perpendicular magnetic field (B), a voltage is developed in opposite to these two-plane direction which is called as Hall voltage (V_H) [109] as schematically represented in Fig. 2. 11. In present research work the Hall Effect studies were performed by using Ecopia instrument.

Instrument Specifications

Model: *HMS 3000*; Sample holder: *Spring clipboard is for use with the 0.51 Tesla magnet kit (20×20 mm^2)*; Resistivity range: *10^{-4} to 10^{7} Ω cm*; Magnet: *Permanent magnet*; Magnet fluxdensity:*0.51 Tesla nominal +/-1% of market value*; Hall voltagerange:*1μV to 2V*.

2.6.8. Four-probe measurement setup

The four-probe setup is the commonly used technique to determine the sheet resistance and resistivity of the thin film as a function of temperature or at room temperature. In four-probe method, the probes are connected in equal distance, and placed over the surface of the

sample. The sheet resistance is estimated by using equation $R_S = F\ (V/I)\ \Omega/\square$, where F = 4.532 is the correction factor, t is the thickness of the sample, V is the voltage drop across any two probes and I is the current applied between the any two probes. The temperature dependent resistivity and the sheet resistance of the films were calculated by home-made four-probe instrument equipped with power source (range 0.1 mA to 2 mA), Keithly multimeter, and controlled heater whose temperature is maintained accurately within ±1 K with the use of an NC2438 precision temperature controller. A chromelalumel thermo couple served as a temperature sensor. Temperature of the film was also externally measured by a K-type thermo couple and a DC 1010 digital volt meter. Photograph of home-made four probe unit is shown in Fig. 2.12.

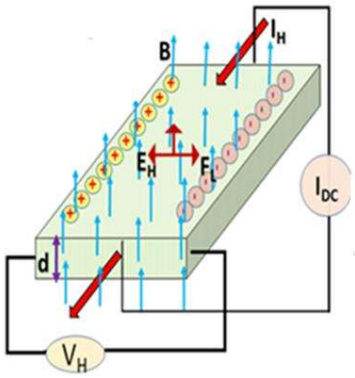

Fig. 2.11. Schematic of Hall-Effect principle

Fig. 2.12. Image of four probe resistivity measurement setup.

2.6.9. Raman spectroscopy

Raman spectroscopy first proposed by C. V. Raman in 1928, it is a non-destructive analytical method to identify functional groups present in a variety of samples [110]. Raman effect arises due to inelastic scattering of incident light by the atoms/molecules. When atoms/molecules are absorbing the light energy, it is possible to radiate or re-emit the energy through vibration or rotational motion. The energy transition by rotational/vibrational mode depends on the excited energy level. The rotational energy is lesser than the vibrational energy.

The atoms/molecules re-emit the same energy as that of incident light energy, indicating no Raman active mode to be present in the system ($\nu_o = \nu$), and this type of transition is called as Rayleigh's elastic scattering. The re-emitted photon energy lower than the incident energy indicate active Raman mode, this mode is generally called as stokes mode ($\nu_o > \nu$). When reemitted photon energy is higher than the incident photon energy, this also indicates the active Raman mode, this mode is called as anti-stokes mode ($\nu_o < \nu$) [111]. The pictorial representation of Raman modes is shown in Fig. 2.13(i). The Raman spectroscopic instrument consists of four major components, a laser source, sample illuminator, filter, and detector as shown in Fig.2.13(ii). The mono chromatic laser light source converged with a focal lens is sent via

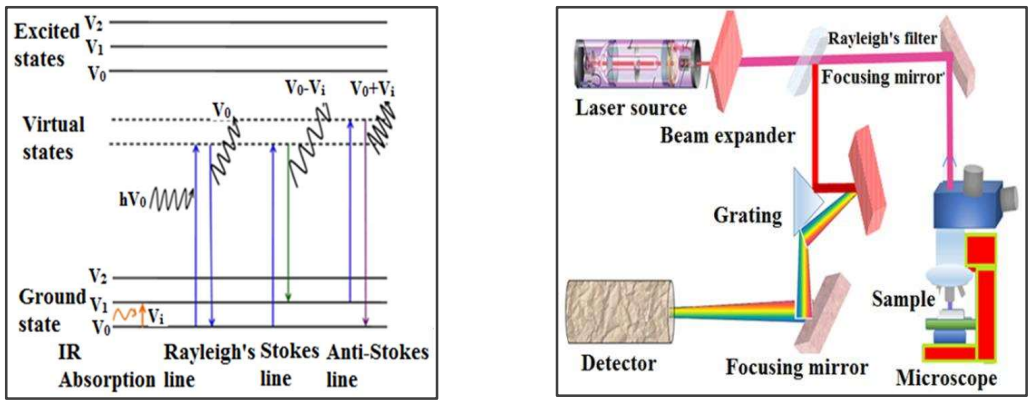

Fig. 2.13. (i) Schematics of Raman scattering effect and (ii) instrumentation of Raman spectroscopy.

interference filter to obtain the Raman spectrum. Nowadays, Raman spectrometer has more advancement in its instrumentation, in optics, laser, and other features. Raman confocal microscopy is used to investigate the surface homogeneity and uniformity of the sample. In the present research work,

Instrument Specifications

Make: *HORIBA Jobin Yvon, France*; Model: *LabRAM HR model*; Laser options: *Integrated internally–532nm CLS high brightness lasers*; Spectral range: *400 – 2200 nm*; Detector:

1024×256 TE air-cooled scientific CCD, USB control, 16 bit and up to 1.48 MHz readout speed; Confocal sampling: *Rugged confocal spatial filtering, offering maximum1×1μm lateral resolution for micron-scale Raman analysis and imaging*; Computer software: *Lab Spec6 spectral software*.

2.7. Fabrication of optoelectronic devices

The various devices such as OLEDs, OSCs, and UV photodetectors (UVPDs) are layer-by-layer structured devices, these layers are coated using spin coating and/or thermal evaporation vacuum coating techniques. The basic OLED structure consist of anode/HTL/EML and ETL/EIL/cathode. Here the ITO coated glass substrate is used as anode for the hole injection and Al as cathode for electron injection into the device. The ITO is also used for charge extraction purpose in OSCs. All the layers of OLEDs were coated using thermal evaporation vacuum coating unit. The ITO was cut into 2×2 cm^2 area using glass cutter and were patterned using zinc dust and HCl. In the patterning process the Kapton tape of strip width of 4 mm is pasted over the ITO as equidistant strips. This was placed in the petri-dish and HCl was added so as to immerse ITO. Immediately the zinc dust was dispersed onto the immersed ITO surface. Due to the chemical reaction between the zinc dust, HCl, and ITO, the exposed ITO is etched [112]. Then, the patterned ITO strips were thoroughly cleaned by following above cleaning process steps and then loaded in to the vacuum chamber of thermal evaporation unit. The HTL, EML/EML, EIL, and Al were coated using this technique at high vacuum and the devices were characterized using Keithely source meter (Source-Measurement-unit (SMU)) (Fig. 2.14) and Ocean Optics spectroradiometer (Fig. 2.15). In the OSCs fabrication process the ITO substrates were patterned and cleaned as described above. The device structure consists of ITO/HTL/Active layer (donor and acceptor)/EIL/Al. Here the HTL and active layers were coated using respective solutions by spin-coating technique and the EIL, and Al were deposited using thermal evaporation coating unit. The OSCs were characterized using SMU and solar

simulator. The UVPDs were fabricated using the structure of ITO/ZnO or Alq_3:ZnO /Al. Here, the ITO is used to enhance the charge transport where Al used for ohmic contacts. ZnO or Alq_3/ZnO composite thin films were deposited using spin coating method. The UVPDs were also fabricated (without ITO) on a glass substrate. The devices were characterized under UV light and dark using SMU. Apart from this the hole-only devices (HODs), electron-only devices (EODs) were fabricated using HTLs (TPD and PEDOT:PSS) and ETLs (ZnO and Alq_3/ZnO) respectively to study the charge transporting properties. The detailed fabrication process and their electrical characterizations of the devices will be discussed in the respective chapters.

Source-Measuring unit (SMU):

Make: *Keithley*; Model: *2450*; Voltage Ranges: *20 mV – 200 V*; Current Ranges: *10 nA – 1 A*; Accuracy: *0.012%*; Wideband Noise: *2 mV_{rms} Type*; Sweep Types: *Linear, Log, Dual Linear, Dual Log, Custom*.

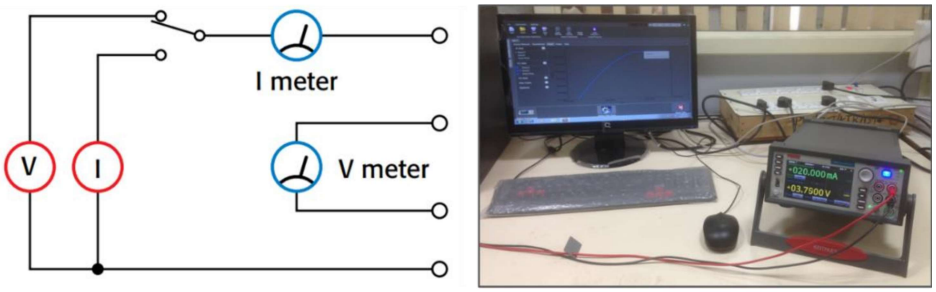

Fig. 2.14. (i) Instrument topology of SMU and (ii) photograph of Keithley 2450 SMU.

Spectroradiometer:

Make: *Ocean Optics*; Model: *USB2000+RAD*; Detector: *Sony ILX511B linear silicon CCD array*; Spectrometer Type: *Modular, Portable*; Wavelength Range: *200 - 850 nm*; Optical resolution: *~2.0 FWHM*; Signal-to-noise ratio: *250:1 (at full signal)*; A/D resolution: *16 bit*; Output Focal length: *68 mm*; Supply Voltage: *4.5 to 5.5 V*; Entrance Slit: *50 µm*;

(i) (ii)

Fig. 2.15. (i) Schematic of light measurement process (adopted from Ocean Optics Operating Manual [113]) and (ii) photograph of spectroradiometer.

UV spot light Source:

Make: *Hamamatsu*; Model: *LC8*; Emission Wavelength: 365 nm; Spectral width: ~6nm; Light Source: 200 W super-quiet mercury-xenon lamp; Maximum UV irradiance: 4500 mW/cm^2; Life Time: 4000 h; Operating temperature range: +5 ℃ to +35 ℃; Power consumption: 280 VA; Weight: ~ 6.4 kg.

(i) (ii)

Fig. 2.16. (i) Measurement setup of UV Photodetectors (ii) UV spot light Source.

2.8. Conclusion

The precursor preparation, thin-film deposition methods for Alq_3/ZnO composite thin films and the basis of thin film formation using spin coating technique were elaborated in this chapter. The fabrication procedure and device structure of various devices such as Hole-Only devices (HODs), Electron-Only devices (EODs), OLEDs, OPVs, UV photodetectors are given in detail. This chapter further discussed the instrumentation details and basic theory of various characterization techniques used for the study of Alq_3/ZnO hybrid thin films and devices.

Chapter: 3

Enhanced UV emission of solution processed highly transparent Alq_3/ZnO hybrid thin films

This chapter describes the enhanced PL emission of Alq_3/ZnO hybrid thin films. The UV emission is observed to be enhanced with the incorporation of Alq_3 in ZnO. The ZnO sol-gel and Alq_3 solution were prepared simultaneously and the Alq_3 with different volume percentages were added to ZnO sol-gel and spin-coated onto the glass substrates. The spin-coated Alq_3/ZnO thin films were characterized using various spectroscopic studies. We have achieved the high quality Alq_3/ZnO hybrid thin films. This chapter mainly focused on the optical properties of the hybrid films including with the crystalline and morphological studies.

3.1. Introduction

In the recent decades Zinc oxide (ZnO) is an extensively investigated promising semiconductor material due to their excellent optical and electrical properties for their potential applications in ultraviolet (UV)- lasers and photodetectors, light emitting diodes (LEDs), piezoelectric devices, etc. [69,114]. The ZnO is an n-type metal oxide semiconductor (due to the formation of various donor defects such as oxygen vacancies and/or Zinc interstitials) having a direct wide band gap of ~3.37 eV at room temperature, large exciton binding energy (60 meV), high electron mobility, higher thermal conductivity, high optical transmittance, and mechanical stability. It has been used as transparent electrode in solar cells and flat panel displays [114,115]. High quality crystalline ZnO thin films have been deposited using various thin film preparation methods such as laser-molecular beam epitaxy, pulsed laser deposition, metal-organic chemical vapor deposition, atomic layer deposition (ALD), ion beam deposition, electrodeposition, and radio frequency (RF)- magnetron sputtering techniques [116]. It has also been realized that the high quality crystalline ZnO thin films could be prepared by sol-gel

coating process which is the least expensive technique when compared to aforementioned methods and this cost-effective sol-gel derived ZnO thin films have the potential to be used in various solution processed optoelectronic devices [41,116,117]. In the recent years, the conjugated organic semiconductors have become an alternate material class for their utility in the electroluminescent devices because of their characteristic features such as good optical and electrical properties, high luminous efficiency, cost effective, nontoxic and environment friendly, biodegradable, flexibility, flexibility in color tuning, and wide color gamut [1,2]. The organic light emitting diodes (OLEDs) have been extensively investigated in the recent past to improve the device efficiency for their potential use in the next-generation flat-panel displays and solid state lighting by employing various technologies such as (i) highly efficient fluorescence by effective harvesting of singlet excitons, (ii) phosphorescence emission by harvesting both singlet- and triplet- excitons with 100% internal quantum efficiency using heavy metal complexes as emission materials, and (iii) thermally activated delayed fluorescence via converting the triplets to emissive singlet state [118–120]. Among the various organic semiconductors used in the devices, the highly transparent and fluorescent tris-(8-hydroxyquinoline)aluminum (Alq_3) is the most widely used electron transporting as well as green light emitting- material in the OLEDs. In general, the vacuum deposited organic molecular films show the amorphous nature due to its molecular structure and/or arrangement of molecules. The Alq_3 thin film has been deposited by sublimation process under high vacuum which leads to high device fabrication cost and influences their viability for commercial applications [4,121]. Alq_3 also exhibits poor film quality by solution process due to its low solubility and/or low gelation of the solution. The solution processed devices are much more viable for the low-cost commercial applications and large-scale production via roll-to-roll process and screen printing [122]. Tailoring the outstanding properties of both inorganic and organic conjugate molecules by making organic/inorganic hybrid composites has become a thrust area of research which reveals the extremely promising desirable characteristics for their

potential applications [123,124]. In the recent reports by combining the individual organic and inorganic desirable characteristics, the functional conjugate organic ligand anchored mesoporous silica based composite materials have been extensively studied on their efficient functionality at nanoscale due to large surface area, large pore volume, tuneable porosity, and higher stability. These sustainable composite materials are widely utilized to sense and treat the ultra-trace level of various toxic ions such as copper(II), nitrite (NO_2^-), cobalt (II), mercury(II), nickel(II), lead(II), and Arsenic(V) in the contaminated water for clean water production [125,126]. The enhanced electron transfer processes at the organic/inorganic interfaces have been studied and exploited in the hybrid electroluminescent device which exhibited the higher luminance of ~2000 cd/m^2 [127,128]. Since the study of electronic interaction and charge transfer between organic/inorganic semiconductor heterojunction at the nanoscale in the hybrid composite thin film prepared by mixing the individual components without any direct chemical interaction is highly challenging and promising, the functional organic/inorganic hybrid thin film-based solution processed organic electroluminescent devices have been of high research interest in the recent years.

In this study, an attempt is made to deposit the high quality Alq_3 incorporated ZnO (Alq_3/ZnO) hybrid thin films by cost effective sol-gel derived spin-coating process. The structural, optical, and surface morphological properties of the deposited hybrid thin films were investigated using various studies such as X-ray diffraction (XRD), UV-visible transmittance, photoluminescence (PL), scanning electron microscopy (SEM) with the energy dispersive analysis of X-rays (EDAX), atomic force microscope (AFM), and Fourier transform infrared (FTIR) spectroscopic techniques.

3.2. Experimental details

3.2.1. Materials and Precursor Preparation

The sol-gel derived spin-coated pristine ZnO and Alq_3/ZnO hybrid thin films were deposited at room temperature using the precursor solutions prepared as described below. The synthesis of ZnO precursor solution is adopted from the previous reports published elsewhere [80,129,130]. The 5.487 g (0.5 M) of zinc acetate dihydrate [$Zn(CH_3COO)_2.2H_2O$: 98.5%; SRL] as a source of Zn was firstly dissolved into 50 mL of 2-methoxyethanol ($C_3H_8O_2$: 99%; SRL) solvent and stirred at 450 rpm for 2 hrs at a temperature of 60 ºC. The 1.512 mL of monoethanolamine (MEA: 99%; SRL) stabilizer was then drop wise added to the above solution while stirring to get the ZnO precursor solution (A) with a 1:1 molar ratio of MEA to zinc acetate. This prepared solution (A) was kept under the normal ambient for 24 hrs for the gelation. Tris-(8-hydroxyquinoline)aluminum (Alq_3) precursor solution (B) was prepared by dissolving 11.48 mg (10^{-3}M) of Alq_3 ($C_{27}H_{18}AlN_3O_3$: 99.995%; Sigma Aldrich) into 25 mL of 2-methoxyethanol solvent and stirred at 450 rpm for 2 hrs under the normal ambient. The ZnO gel precursor (A) and Alq_3 solution (B) were filtered using 0.2 μm syringe filter separately. Then, the three kinds (5 mL each) of Alq_3 incorporated ZnO precursor solutions were prepared by mixing 1 mL (20 vol.%), 2 mL (40 vol.%), and 3 mL (60 vol.%) of Alq_3 solution (B) into 4 mL (80 vol.%), 3 mL (60 vol.%), 2 mL (40 vol.%) of ZnO sol-gel precursor (A) respectively with continues stirring. The nominal molar ratio of Alq_3 to ZnO (Alq_3/ZnO) in the three solutions were maintained at $0.5x10^{-3}$ for [ZnO (80 vol.%) (0.4 M) + Alq_3 (20 vol.%) ($2x10^{-4}$M)], $1.3x10^{-3}$ for [ZnO (60 vol.%) (0.3 M) + Alq_3(40 vol.%)($4x10^{-4}$M)]; and $3x10^{-3}$ for [ZnO (40 vol.%) (0.2 M) + Alq_3 (60 vol.%) ($6x10^{-4}$M)].

3.2.2. Alq_3/ZnO hybrid thin film deposition procedure

The respective ZnO sol-gel precursor (A) for the film (**a**) and the three Alq_3/ZnO sols with the Alq_3/ZnO molar ratio of $0.5x10^{-3}$for the film (**b**), $1.3x10^{-3}$ for the film (**c**), and $3x10^{-3}$

for the film (**d**), were spin-coated using programmable Spin coater (Apex Instruments, spinNXG-P2 model) on the glass substrates under the normal ambient. Prior to the coating, the glass substrates (2x2 cm^2 area) were ultrasonically cleaned for 10 min in acetone followed by isopropyl alcohol(isopropanol) and double deionized water, dried in each step at 100 ºC in vacuum oven for 10 min to remove the solvent used, finger prints and other contaminations onto the glass surface. The substrates were also finally cleaned with high power plasma using plasma cleaner (Harrick Plasma, PDC-002) at 800-micron vacuum to etch out the oxide contamination on the surface. The thin film coating process was followed by (i) the precursor sol was spin-coated on the glass substrate at 2000 rpm for 30 s, (ii) dried after each coating at 200 ºC on a hot plate under the normal ambient by covering with a glass lid, and (iii) the coating was repeated for 5 times to obtain optimal thickness of around 200 nm. The four spin-coated pristine ZnO (**a**) and Alq_3/ZnO hybrid thin films (**b - d**) were annealed (post) at 300 ºC for 2 hrs under the normal ambient to evaporate the solvents and increase the film quality.

3.2.3. Instrumentations

The thickness measurements of solution processed pristine ZnO (**a**) and Alq_3/ZnO hybrid thin films (**b - d**) were carried out using Stylus Profilometer (Bruker's DektakXT stylus) by making film step height during the spin-coating process. The UV-visible transmission spectra of the pristine (**a**) and hybrid thin films (**b - d**) were recorded using Agilent Carry 5000 UV-Vis-NIR Spectrophotometer. The PL spectra were recorded using Horiba Jobin-Yvon, Fluorolog3. The surface morphology and the elemental analysis were studied using scanning electron microscope (SEM) (TESCAN, VEGA3 LMU model) coupled with the EDAX (Oxford Instruments, INCAx-act model) with resolution at 5.9 keV: 130 eV. The SEM images of the films **(a - d)** were recorded at an operating voltage of 30 kV with the scan magnifications of 10000× (scale bar: 2 μm) and 50000× (scale bar: 500 nm), respectively. The EDAX analysis and elemental mapping of the films **(a - d)** were carried out at the operating voltage of 30 kV.

The surface topographic studies were carried out with the atomic force microscope (AFM; Park, XE-100). The X-Ray diffraction (XRD) measurements were carried out at room temperature by using X-ray diffractometer (PAN analytical Netherlands, XPERT-PRO model) with Cu K-alpha (X-ray source) radiation (wavelength (λ) of 1.5406 Å) operated at the voltage of 45 kV and current of 30 mA. XRD patterns of the films (**a - b**) were obtained using a vertical goniometer (theta - theta configuration) in the scan range of 20º - 80º with the scan step size of 0.008º and analysed analysed using X'Pert High score Plus software. FTIR spectroscopy (JASCO Co. Japan, FT/IR-6600 model) was used to the study the functional groups and its molecular bonding in the spin-coated films (**a - d**).

3.3. Results and discussion

3.3.1. Optical properties of Alq_3/ZnO hybrid thin films

The Alq_3/ZnO hybrid thin films were prepared by sol-gel spin-coating process. The optical transmittance spectra of the pristine ZnO (**a**) and Alq_3/ZnO hybrid thin films (**b - d**) are shown in Fig. 3.1(i). These films show the average transmittance (T_{av}) higher than 87% in the visible region which will be very much useful for the optoelectronic device applications. The hybrid thin film (**b**) with the Alq_3/ZnO molar ratio of $0.5x10^{-3}$ exhibits higher transparency of 90% at 550 nm which is slightly lower than that (92%) of the pristine ZnO thin film (**a**). The transparency (at 550 nm) of hybrid thin films slightly decreases (84% for film (**c**) with the Alq_3/ZnO molar ratio of $1.3x10^{-3}$, and 83% for film (**d**) with $3x10^{-3}$) for the slight increasing of Alq_3 content. This may be attributed to the fact that the incorporated Alq_3 molecules are adsorbed at the ZnO grain boundaries and acting as light scattering centers to decrease the transparency [80,131]. It is also observed that the pristine ZnO thin film (**a**) has a sharp absorption band edge in the UV region which is more and more shifted to the shorter wavelength region (blue shift) for the films (**b**) to (**d**). This is due to the shifting of Fermi level

into the conduction band as the ZnO crystallite size decreases with increasing of Alq_3/ZnO molar ratio in the hybrid films [132].

The Figure. 3.1(ii) shows the optical band gap (E_g) of the pristine ZnO (**a**) and Alq_3/ZnO hybrid thin films (**b - d**) determined by using the following Tauc relationship relation

$$(\alpha h\upsilon)^2 = A\,(h\upsilon - E_g) \qquad (3.1)$$

Where $h\upsilon$ is the photon energy (eV), α is the optical absorption coefficient of the film, and A is the constant. The plot of $(\alpha h\upsilon)^2$ as a function of the photon energy distinctly exhibits the decrease in the UV absorption upon increasing Alq_3/ZnO molar ratio in the hybrid thin films. The E_g can be obtained by extrapolation of linear portion of $(\alpha h\upsilon)^2$ against the photon energy ($h\upsilon$) plot to the point where $\alpha = 0$. The direct optical band gap energy of the pristine ZnO thin film is determined to be 3.22 eV, which is consistent with the earlier reports [129,132]. It has

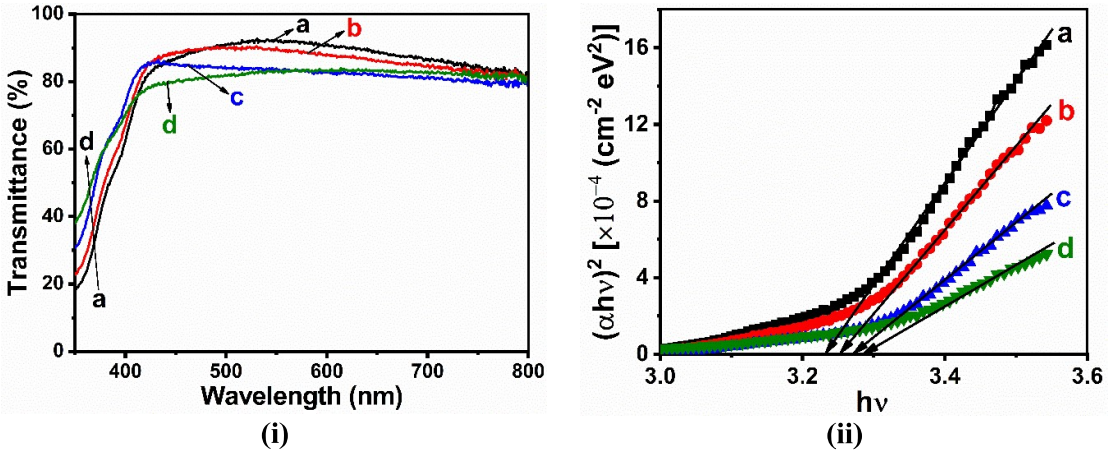

Fig. 3.1. (i) The UV-visible transmittance spectra of sol-gel derived spin-coated pristine ZnO (**a**) and Alq_3/ZnO hybrid thin films (**b - d**) with the Alq_3/ZnO molar ratio of $0.5x10^{-3}$ (**b**), $1.3x10^{-3}$ (**c**), and $3x10^{-3}$ (**d**) and (ii) the optical band gap of the films (**a - d**) estimated from the dependence of absorption coefficient on the photon energy (Tauc plot).

also been observed from the Tauc plot that the optical band-gap energy does not change significantly but slightly increases with increasing Alq_3/ZnO molar ratio in the hybrid films (3.28 eV for **d**), which is attributed to the quantum confinement effect due to the decrease in crystallite size [133]. The obtained optical and electrical properties of the pristine ZnO and Alq_3/ZnO hybrid thin films are shown in Table 3.1.

3.3.2. The XRD studies

The crystalline properties and orientation of sol-gel derived spin-coated pristine ZnO (**a**) and Alq_3/ZnO hybrid thin films (**b - d**) are studied using XRD measurements as shown in the figures 3.2 and 3.3. The texture coefficient (TC) values of the films (**a - d**) are calculated using the relation

$$TC_{hkl} = \frac{I_{hkl}/I_{0hkl}}{\frac{1}{N}\Sigma\, I_{hkl}/I_{0hkl}} \tag{3.2}$$

where I_{hkl} is the measured intensity of the hkl plane, I_{0hkl} is the standard intensity of the hkl plane from JCPDS file card No.: 89-1397, and N is the total number of reflections observed in the XRD pattern of the respective thin film. The pristine ZnO film (**a**) exhibits good crystalline properties with the XRD peaks at angle 2θ (corresponding 'hkl' plane) of 31.80º (100), 34.27º (002), 36.08º (101), and 56.66º (110) having the highly textured peak centered at 34.27º (002), which is consistent with reported data (JCPDS file: 89-1397) characterizing the hexagonal wurtzite structure [116,134]. The highly textured orientation along (002) plane of ZnO thin films prepared by various techniques such as electrodeposition, RF magnetron sputtering, ALD, and chemical vapor deposition, has widely been observed and it is attributed to the higher micro strain induced in the ZnO film enhances the growth of (002) planes [129,130]. It is also observed that the hybrid thin films (**b - d**) are showing the decreased diffraction peak intensities without any change in the peak positions for increasing Alq_3/ZnO molar ratio of $0.5x10^{-3}$ in

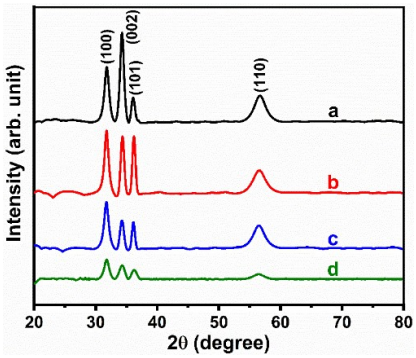

Fig. 3.2. The XRD patterns of sol-gel derived spin-coated pristine ZnO (**a**) and Alq_3/ZnO hybrid thin films (**b - d**) with the Alq_3/ZnO molar ratio of $0.5x10^{-3}$ (**b**), $1.3x10^{-3}$ (**c**), and $3x10^{-3}$ (**d**).

film (**b**), $1.3x10^{-3}$ in film (**c**), and $3x10^{-3}$ in film (**d**) when compared to the pristine ZnO thin film (**a**). This result shows that the incorporated Alq_3 has not entered into the ZnO matrix. The highly textured peak shifted to 31.80° (100) for the films (**c**) and (**d**) (Fig. 3.3(i)), attributing the fact that the incorporated Alq_3 molecules may preferably be adsorbed at the grain boundaries of ZnO crystallites along the plane (002) orientation having the higher surface energy [135]. The calculated average crystallite size of pristine ZnO (**a**) and hybrid films (**b - d**) are shown in Fig. 3.3(ii). The crystallite size of the thin films has been calculated using Debye-Scherrer's formula

$$D = k\lambda/\beta \cos\theta \qquad (3.3)$$

where D is the crystallite size, λ is X-ray wavelength (1.5406 Å), k (= 0.94) is the correction factor, β is the full width half maxima of the diffraction peak, and θ is the diffraction angle of the diffraction peak. The presence of incorporated Alq_3 molecules in the film (**b**) with Alq_3/ZnO molar ratio of $0.5x10^{-3}$may have caused the slight increase in the crystallite size. It is also observed that the calculated crystallite size is decreasing for further increasing of Alq_3/ZnO molar ratio in the hybrid films. This reveals that the incorporated Alq_3 molecules may preferably get adsorbed at the higher surface energy sites of ZnO crystallites and cap the ZnO crystallites to control its size as the Alq_3/ZnO molar ratio increases.

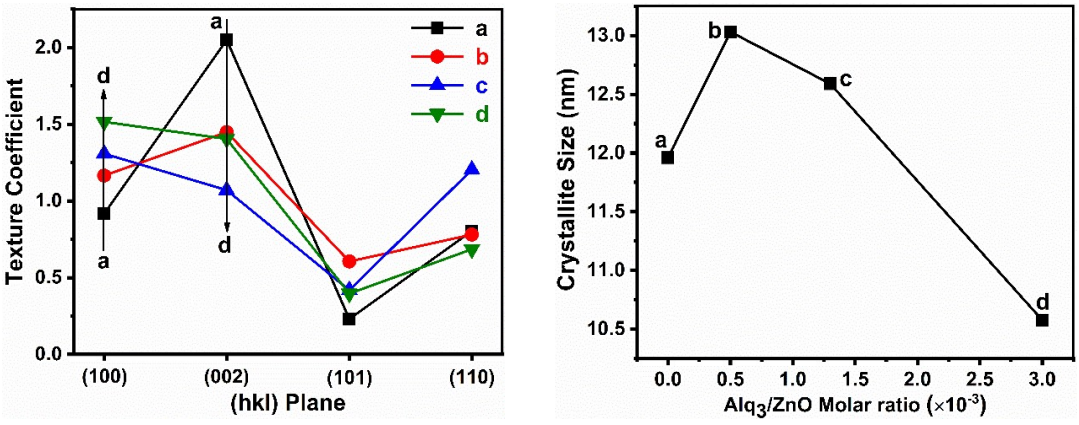

Fig. 3.3. (i) The texture coefficients of various diffraction (hkl) planes, (ii) the average crystallite size determined from the diffraction peaks of sol-gel derived spin-coated pristine ZnO (**a**) and Alq_3/ZnO hybrid thin films (**b - d**).

3.3.3. Morphological and elemental analysis

The surface morphological features of the sol-gel derived spin-coated pristine ZnO (**a**) and Alq_3/ZnO hybrid thin films (**b - d**) were examined by using analysed from SEM images as shown in Fig. 3.4. From the figure 3.4(a), it is observed that the pristine ZnO thin film exhibits a systematic root-like wrinkled surface morphology throughout the region. This is attributed to the fact that the film undergoes a large amount of stress due to substantial loss of precursor solvent during annealing and gives rise not only to the bending of the film but also to the contraction of the skeletal network, resulting in such a wrinkled surface morphology [136,137]. The incorporation of Alq_3 in the hybrid film (**b**) with Alq_3/ZnO molar ratio of $0.5x10^{-3}$reduces the thickness of root-like structure [Fig. 3.4(b)] and the same trend is also evident in the film (**c**) with increased molar ratio of $1.3x10^{-3}$. The SEM image of the film (**c**) exhibits very thin root-like wrinkled structure along with particulates which are distinctly visible between the root-like stripes as shown in the inset of Fig. 3.4(c). For the further increasing of Alq_3/ZnO molar ratio to $3x10^{-3}$ in the film (**d**), the wrinkled morphology is diminished and the flower-like particulates [Fig. 3.4(d)] are predominantly observed with uniform distribution over the entire

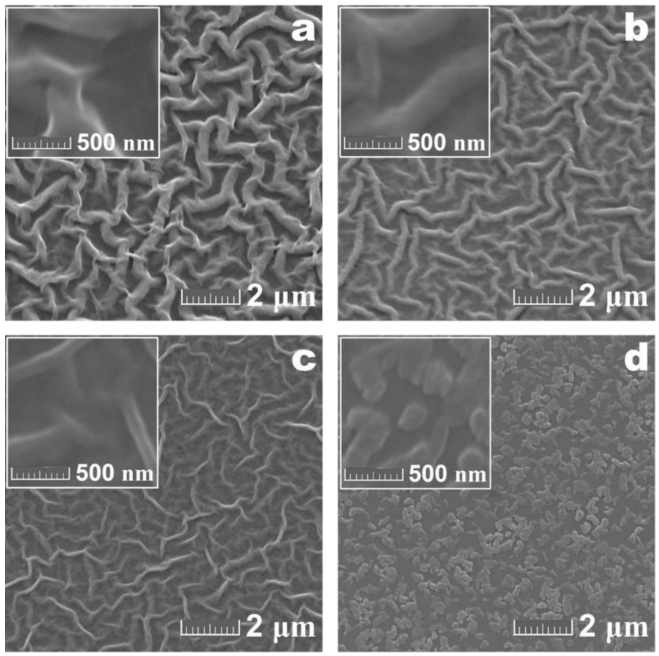

Fig. 3.4. SEM morphological images sol-gel derived spin-coated pristine ZnO (**a**) and Alq_3/ZnO hybrid thin films (**b - d**).

surface, which is consistent with the formation of flower-like structure by pure Alq_3 reported elsewhere [138]. The observed particle morphology in the hybrid thin film ascertains the adsorption of Alq_3 molecules at the grain boundaries of ZnO and formation of Alq_3 complex molecules capped ZnO nanoparticles. The change in the morphological features of hybrid thin films with increasing Alq_3/ZnO molar ratio is in support of decreasing crystallite size in the XRD studies.

The EDAX measurements for surface elemental analysis of the films (**a - d**) were carried out to confirm the incorporation of Alq_3 molecules in the hybrid thin films and the results are shown in Fig. 3.5. The pristine ZnO thin film shows the atomic concentrations (atomic percentage; at.%) of main constituent elements Zn (18 at.%) and O (56 at.%) with the presence of Si (18 at.%) originated from the glass substrate and C (8 at.%) due to handing under the normal ambient. The hybrid thin film (**b**) with Alq_3/ZnO molar ratio of $0.5x10^{-3}$ exhibits the increased atomic concentration of C (19 at.%) with the presence of N (4 at.%) along with Zn (17 at.%), O (57 at.%) and Si (3 at.%). The change in the atomic percentage ratio of C atoms (major constituent element of Alq_3 molecule ($C_{27}H_{18}AlN_3O_3$)) with respect to Zn atoms is calculated as a measure to study the incorporation of Alq_3 molecules in the hybrid thin films.

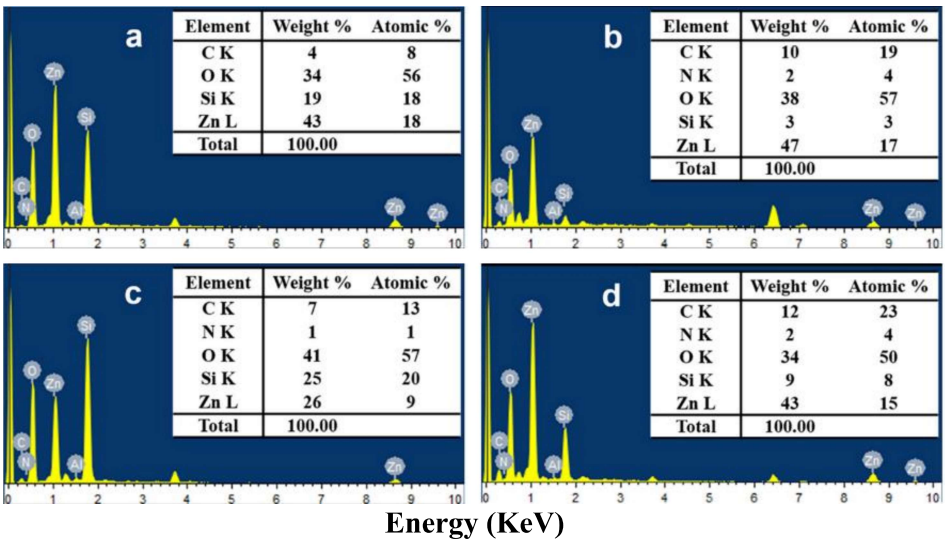

Fig. 3.5. EDAX analysis of sol-gel derived spin-coated pristine ZnO (**a**) and Alq_3/ZnO hybrid thin films (**b - d**).

The ratio (C/Zn = 1.12) is significantly increased in the film (**b**) when compared to that (C/Zn = 0.44) of film (**a).** This ratio is also increased (1.44 for the film (**c**) with Alq_3/ZnO molar ratio of $1.3x10^{-3}$ and 1.53 for the film (**d**) with molar ratio of $3x10^{-3}$) upon further increase of Alq_3 content, which ascertains the incorporation of Alq_3 molecules in the hybrid thin films.

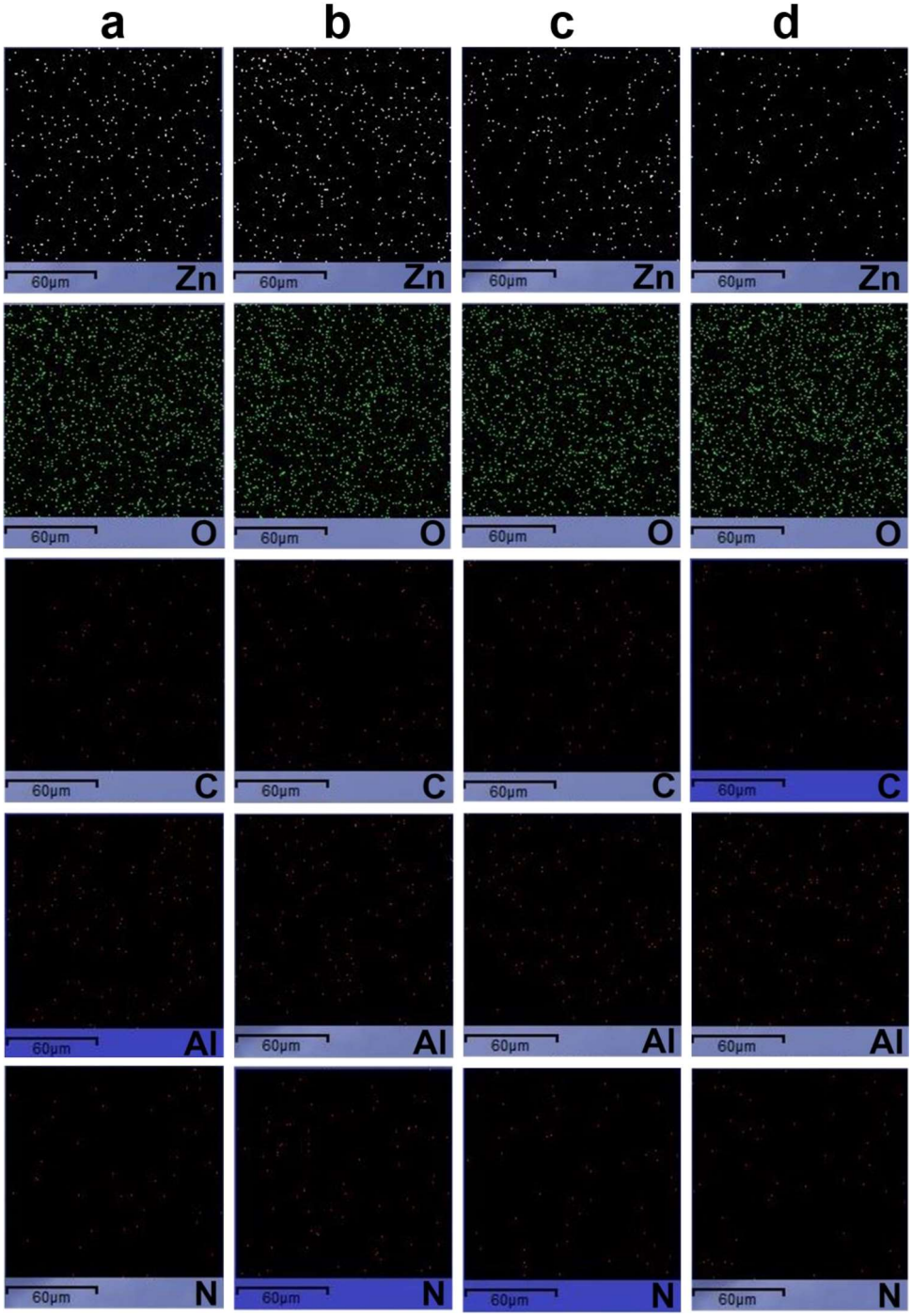

Fig. 3.6. The EDAX elemental mapping of constituent elements (Zn, O, C, Al, and N) of sol-gel derived spin-coated pristine ZnO **(a)** and Alq_3/ZnO hybrid thin films **(b - d)**.

The EDAX elemental mapping of the films (**a - d**) exhibits the uniform dispersion of constituent elements (Zn, O, C, Al, and N) over the entire surface area as shown in Fig. 3.6. The decreasing density with uniform distribution of Zn element and increasing density of the other elements (O, C, Al, and N) for increasing Alq_3 content evident the incorporation and uniform distribution of Alq_3 molecules in the Alq_3/ZnO hybrid thin films.

Table 3.1. The optical and electrical properties of pristine ZnO and Alq_3/ZnO hybrid thin films.

Films	Content (ZnO, Alq_3) (M)	The nominal molar ratio of Alq_3 to ZnO	Optical transmittance at wavelength (nm) (%)			E_g (eV)	Surface Roughness (R_{rms}) at 5 μm² area (nm)
			350	400	550		
a	(0.5, 0)	0 (Pristine)	18.26	62.28	92.37	3.22	28.6
b	(0.4, $2x10^{-4}$)	$0.5x10^{-3}$	22.78	66.91	90.13	3.24	15.6
c	(0.3, $4x10^{-4}$)	$1.3x10^{-3}$	30.72	73.26	83.89	3.26	2.9
d	(0.2, $6x10^{-4}$)	$3x10^{-3}$	37.99	70.15	83.12	3.28	2.4

3.3.4. Topographic studies

The surface topography of pristine ZnO film (**a**) and Alq_3/ZnO composite films (**b-d**) was recorded using AFM, over the scanning area of 5 μm^2 as shown in Fig.3.7. The pristine ZnO film shows the wrinkle or root-like pattern. The evaporation of the solvent in sol-gel derived ZnO thin films in the annealing process create compressive stress in the film due to the difference in thermal expansion coefficient between ZnO thin film and substrate. This compressive stress induces the volumetric strain leading to the nucleation of grains, resulting in the wrinkled kind morphological of ZnO thin film [136,137]. The incorporated Alq_3 molecules significantly changed the surface morphology of Alq_3/ZnO composite films. The

Alq_3 molecules converted the wrinkle pattern into densely packed well defined ZnO crystalline grains, which are grown perpendicular to the substrate surface with uniform distribution. The dopant element modifies the wrinkle kind morphology of ZnO thin film with uniform distribution of pointed type grains perpendicular to the substrate surface [139]. The conversion of wrinkles into the uniform grain-like structure improves the film quality with good crystalline properties [140]. The film (**b**) exhibits the more or less uniform distribution of pointed like grains with completely disappearing wrinkles, which indicates that the Alq_3 molecules are predominantly present on the surface. The film (**c**) partially exhibits the wrinkle kind structure with the presence of grains with less growth. This may be due to the more amount of Alq_3 molecules entered into the grain boundaries of the ZnO crystal lattice. The high-density uniform distribution of grains with even less growth for the film **d** shows that the Alq_3 molecules effectively adsorbed into the grain boundaries of ZnO. From the AFM images of Alq_3/ZnO composite films, it is observed that ZnO grain size and growth are reduced with the incorporation of Alq_3 which ascertains the decreased crystallite size from XRD [141]. The surface roughness of the Alq_3/ZnO hybrid films (**b-d**) is observed to be drastically decreased with the incorporation of Alq_3 in ZnO compared to the pristine ZnO film (**a**) (shown in Table 3.1). A few amount of incorporated Alq_3 molecules make disappearance of the wrinkle gaps of ZnO in film b with the molar ration of 0.5×10^{-3} and exhibit the decreased roughness of 15.57 nm compared to the pristine ZnO film (**a**) roughness of 28.67 nm. The roughness is also observed to be decreased to 2.88 nm for the film c with the molar ratio of 1.3×10^{-3} due to the adsorption of Alq_3 molecules onto the grain boundaries of ZnO. The film **d** with the molar ratio of 3.0×10^{-3} still shows the reduced roughness of 2.44 nm due to the effective adsorption of Alq_3 molecules onto the grain boundaries of ZnO thin film. The dopant element entered into the grain boundaries of ZnO and apply the compressive stress along the c-axis of the ZnO crystalline plane resulting in controlling the grain size and growth or crystallite size with reduced roughness [130,141,142]. The impurity-doped ZnO thin film exhibits more smoothness with

uniform distribution of grain-like structure than the wrinkle like structured pure ZnO thin film [137,140]. The smooth surface of the Alq_3/ZnO films gives the proper interface contact to the adjacent layers, which can avoid the accumulation of charge carriers at the interface and enhance the charge transporting property in the optoelectronic devices [131].

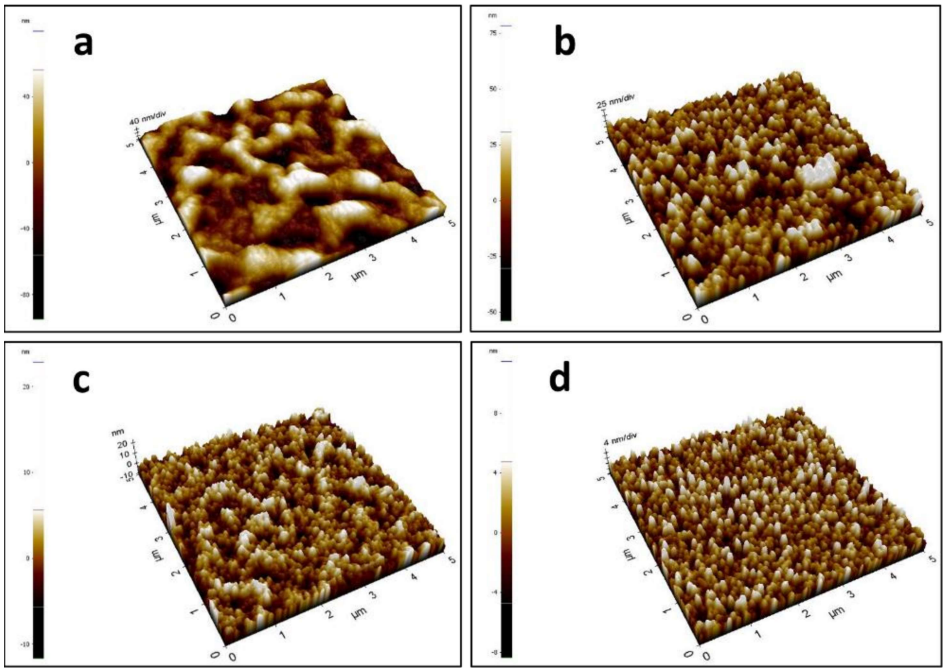

Fig. 3.7. The AFM images of sol-gel derived spin-coated pristine ZnO **(a)** and Alq_3/ZnO hybrid thin films **(b - d)**.

3.3.5. The structural analysis

The figure 3.8 shows the FT-IR spectra of the pristine ZnO (**a**) and hybrid thin films (**b - d**) in the range 400 to 3500 cm^{-1}. From the figure 3.8, the characteristic broad infrared absorption band around 400 - 600 cm^{-1}corresponding to Zn-O stretching vibration is observed in the pristine ZnO thin film (**a**). The small absorption band around 1216 cm^{-1} is assigned to C-O stretching, 1366 cm^{-1} to C-H stretching, and 1736 cm^{-1} to the carbonyl group (C=O stretching) residue formed from the precursor solutions [138,143]. The incorporation of Alq_3 in the hybrid films is confirmed by presence of the aromatic stretching (1650 - 1400 cm^{-1}) and aromatic amine resonances (1370 - 1200 cm^{-1}) with increasing IR absorption intensity for

increasing Alq_3/ZnO molar ratio in the hybrid films (**b - d**) [4,144]. The carbonyl group (C=O) stretching vibrational band intensity near 1736 cm^{-1} increases as the Alq_3/ZnO molar ratio increases in the hybrid films, confirming the formation of substantial number of carbonyl groups (C=O) in Alq_3 molecules. It has been reported that among the three 8-hydroxyquinoline (HQ) units in Alq_3 molecule, one HQ unit undergoes structural changes/chemical modifications during the light exposure under the normal ambient and forms the carbonyl group (C=O) in the affected unit. It has also been found that the number of carbonyl units is limited to a few and acting as luminescence quencher [4,121].

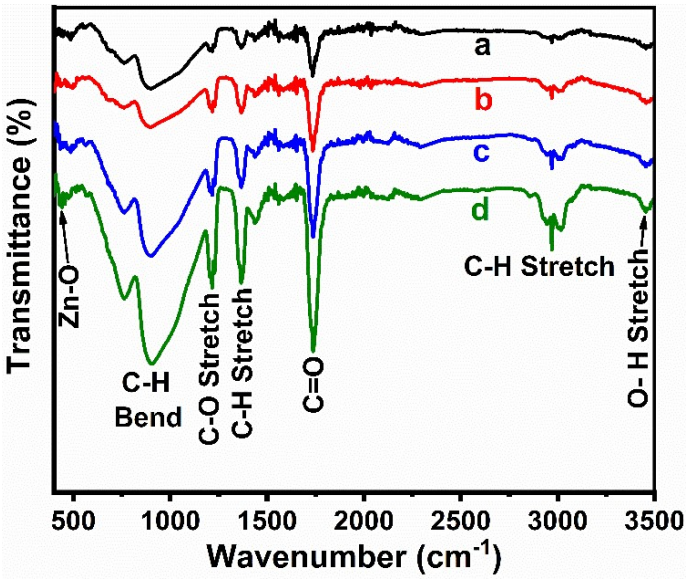

Fig. 3.8. The FT-IR transmittance spectra of sol-gel derived spin-coated pristine ZnO (**a**) and Alq_3/ZnO hybrid thin films (**b - d**).

3.3.6. Photoluminescence (PL) studies

The figure 3.9 shows the room temperature PL spectra of pristine ZnO (**a**) and Alq_3/ZnO hybrid thin films (**b - d**). These films are excited at the characteristic ZnO excitation wavelength (λ_{ex}) of 324 nm [145], the Alq_3 excitation wavelength of 380 nm [4], and common excitation wavelength of 360 nm. The pristine ZnO film (**a**) when excited under 324 nm wavelength has emitted a strong characteristic ultraviolet emission (UV-PL) around 387 nm (band edge

excitonic emission) with an additional weak defect-related emission in the visible region (Fig. 3.9(i)) [146,147]. The broad defect emission in the visible region is commonly observed in ZnO. The defect emission in green-yellow band is associated with oxygen vacancies or oxygen interstitials due to recombination of delocalized electrons near the conduction band with the deeply trapped holes in the singly ionized oxygen vacancy and its blue-green band emission is related to the energy level of oxygen vacancies in the ZnO energy gap [134]. Lv et al. [148] has observed the enhanced defect-related visible emission from electrodeposited ZnO thin films and concluded that the defect concentration is increasing as annealing temperature increases, thereby increasing the green emission (540 nm) which is attributed to oxygen vacancy (V_o)-related defects and the yellow emission (610 nm) related to oxygen interstitials in agreement with the other reports [145,148]. When excited with λ_{ex} = 360 nm, the film (**a**) showed the same UV-PL intensity around 387 nm with increased defect emission intensity (visible region) as shown in Fig. 3.9(ii). For λ_{ex} = 380 nm, it showed a broad excitation wavelength dependent near band emission (NBE) around 445 nm with low intense defect related broad emission around 680 nm (red-edge effect) due to slow rate of excited state relaxation process (Fig. 3.9(iii)) [147,149]. From the near-edge X-ray absorption fine structure spectra of Alq_3 thin films, it has been reported that the electronic transitions from the C 1s electrons to unoccupied molecular orbitals of π^* and σ^* occur at the broad UV wavelength range around 307 nm [150]. It is also observed that the UV excitation (λ_{ex} = 340 nm) of Alq_3 thin film shows the characteristic PL emission at 515 nm which is consistent with the earlier report [4].

The Alq_3/ZnO hybrid thin film (**b**) with the molar ratio of $0.5x10^{-3}$ exhibits the increased UV-PL intensity at 387 nm (for λ_{ex} = 324 nm) when compared to that of the film (**a**) without any Alq_3 characteristic emission around 515 nm, attributing the energy transfer from Alq_3 to ZnO in the film (**b**). When the film (**b**) is excited with 360 nm wavelength, the UV-PL and defect-related visible emission intensities are significantly decreased. The decreasing of broad NBE emission (around 445 nm wavelength) intensity is observed for λ_{ex} = 380 nm as well. The

PL emission (shoulder) band around 515 - 530 nm wavelength (for λ_{ex} = 380 nm) is attributed to the characteristic emission of Alq_3 in the hybrid thin films. The same kind of PL trend is also observed in the film (**c**) (with the Alq_3/ZnO molar ratio of $1.3x10^{-3}$) for all the three excitations. The PL peak intensity (compared with peak intensity percentage) plot of the hybrid thin films excited under 324 nm wavelength is shown in Fig. 3.9(iv). A fourfold increase in the ultraviolet emission (UV-PL) intensity (band edge emission) of ZnO around 387 nm (for λ_{ex} = 324 nm) is observed for the film (**d**) with the Alq_3/ZnO molar ratio of $3x10^{-3}$. The overall decrease in the NBE and defect-related visible emission intensities of ZnO in the films with increasing Alq_3/ZnO molar ratio reveals that the energy transfer from Alq_3 to ZnO is inefficient when the films are excited at λ_{ex} = 360 and 380 nm.

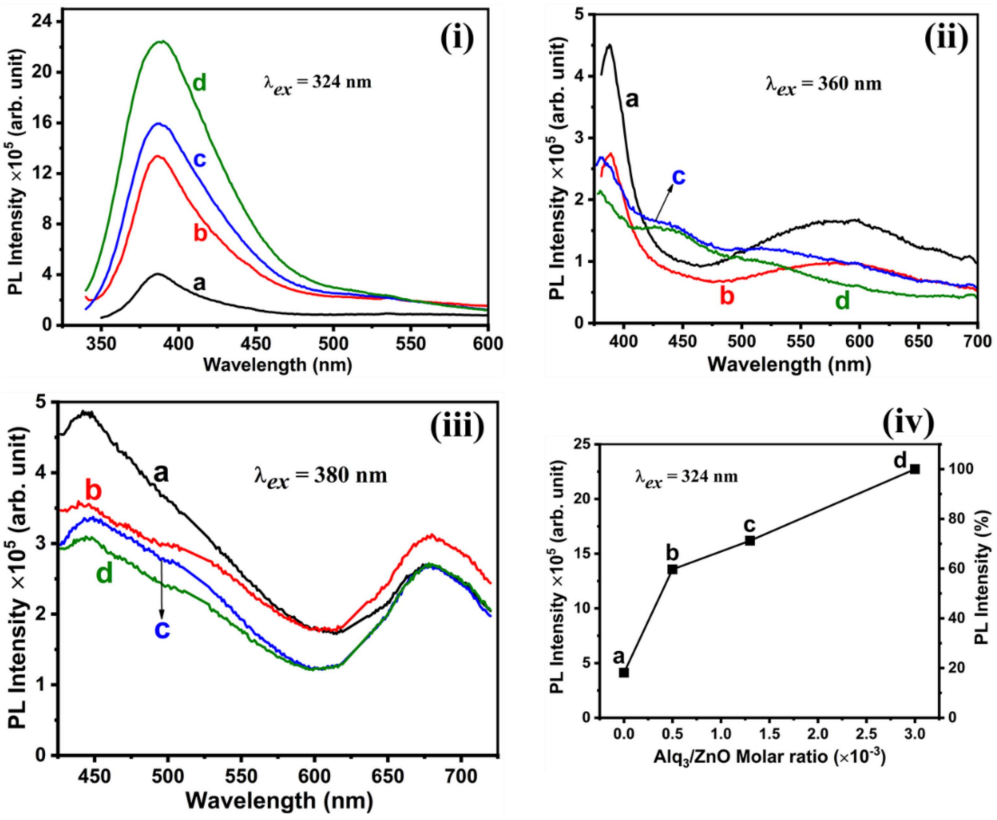

Fig. 3.9. The PL spectra of sol-gel derived spin-coated pristine ZnO (a) and Alq_3/ZnO hybrid thin films (b - d) at excitation wavelengths (λ_{ex}) of (i) 324 nm, (ii) 360 nm, and (iii) 380 nm. (iv) The PL peak intensity (in comparison with peak intensity percentage) plot of the films (a - d) at λ_{ex} = 324 nm.

In this study, it is observed that upon increasing the Alq_3/ZnO molar ratio in the hybrid thin films, the carbonyl group (C=O) formed in Alq_3 molecule is substantially increasing as evident from FTIR studies and it is acting as a luminescent quencher of Alq_3 molecule as reported elsewhere [4]. When Alq_3/ZnO hybrid thin film is excited with 324 nm wavelength, both ZnO and Alq_3 molecules are excited simultaneously. In the process of excitation, the C 1s electrons of Alq_3 molecule absorb the energy and make a transition to LUMO orbitals (π^* and σ^*) in the Alq_3 molecule (becoming energetically excited molecule). The excited state energy of Alq_3 molecule can be absorbed by the luminescent quencher and in turn the absorbed energy may eventually be non-radiatively transferred to ZnO, giving rise to a fourfold increase in ultraviolet emission (band edge emission) of ZnO in the hybrid thin films. The schematic representation of the above energy transfer process in the Alq_3/ZnO hybrid thin films is shown in Fig. 3.10. These results imply that the Alq_3/ZnO hybrid thin film may be useful as electron transporting material in the solution processed electroluminescent devices and UV photodetector.

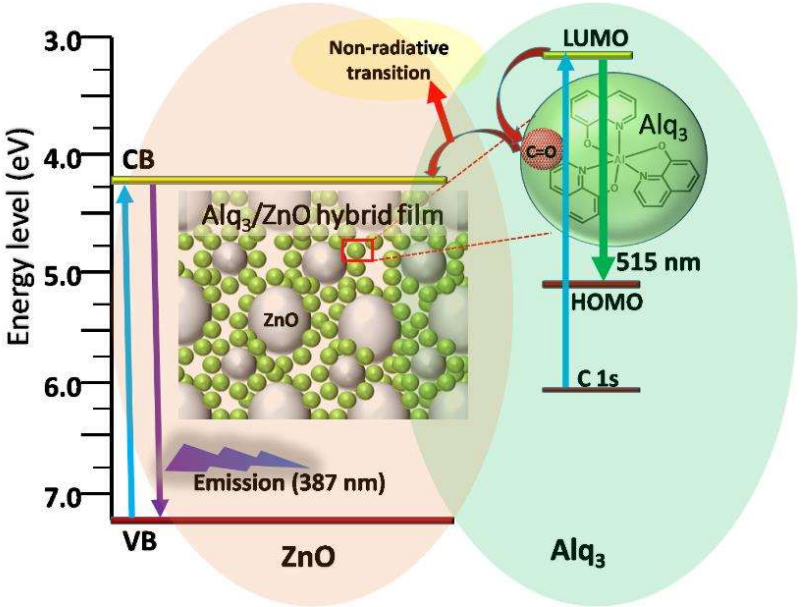

Fig. 3.10. The schematic representation of the energy transfer process in the Alq_3/ZnO hybrid thin films at λ_{ex} = 324 nm.

3.4. Conclusion

The Alq_3/ZnO hybrid thin films deposited by sol-gel spin-coating process exhibit the higher transparency of 90% at 550 nm and it slightly reduced to 83% for increasing Alq_3/ZnO molar ratio due to the adsorbed Alq_3 molecules at the grain boundaries of ZnO. The PL study shows a fourfold increase in ultraviolet band-edge emission (387 nm) of ZnO upon increasing Alq_3/ZnO molar ratio in the hybrid films, attributing the energy transfer from Alq_3molecules to ZnO. The SEM images reveal the formation of ZnO nanoparticles with increasing molar ratio in the hybrid films by adsorption of Alq_3 molecules at the grain boundaries of ZnO. The decreased crystallite size upon subsequent incorporation of Alq_3 in the hybrid films ascertains the capping of Alq_3 molecules to control the ZnO particle size. The luminescence quencher (carbonyl group, C=O) formed in Alq_3 molecule is substantially increasing with Alq_3 content in the hybrid films. These studies show that when excited at 324 nm, the excited state energy of Alq_3 molecules is non-radiatively transferred to ZnO via luminescent quencher and giving rise to a fourfold ultraviolet emission (387 nm) of ZnO in the hybrid films.

Chapter: 4

Raman, X-ray photoelectron spectroscopic investigation and UV-photoresponse of solution processed Alq_3/ZnO hybrid thin films

This chapter contains the detailed analysis on Raman and X-ray photoelectron spectroscopic (XPS) studies of solution processed tris-(8-hydroxyquinoline)aluminum(Alq_3)/ZnO hybrid thin films. It also deals with the UV Photoresponses of Alq_3/ZnO hybrid thin films. Raman studies reveal the sol-gel derived spin-coated ZnO thin film has hexagonal wurtzite structure. The incorporation of Alq_3 molecules in the hybrid film results in the formation of bonding onto the surface of highly crystalline ZnO nanoparticles. The XPS confirms the incorporation of Alq_3 in the hybrid thin films and corroborates that the Alq_3 molecules may be adsorbed onto the surface of ZnO nanoparticles (chemisorption), showing the existence of chemical interaction between Alq_3 and ZnO in the hybrid films. The sheet resistance is observed to be deceased with the incorporation of Alq_3 in ZnO revealing the improved electrical properties Alq_3/ZnO thin films. The Alq_3/ZnO hybrid thin films exhibit the better UV light measurements and fast photoresponses when compared to that of pure ZnO. These studies support that the chemisorbed Alq_3 molecules onto the ZnO nanoparticles may facilitate the charge transfer (non-radiative) between Alq_3 and ZnO in the hybrid thin films which improves the UV photoresponses of the hybrid films.

4.1. Introduction

In the recent years, the investigation on multifunctional nanostructured thin films has been exponentially expanding particularly in the semiconductor technology due to their advantages such as attainment of better chemical, optical, and physical properties for improved device efficiencies [151–153]. Nowadays, the novel smart devices are way out for the cost-effective commercial applications which are made possible by using multifunctional

semiconductor thin films owing to reduction in the raw materials, leading to miniaturization of the devices. In the recent decades, Zinc oxide (ZnO) has been a promising third generation semiconducting material which is extensively investigated for their potential applications in the area of optoelectronics, chemical and biological sensing, and renewable energy such as light emitting diodes (LEDs) for displays and solid state lightings, laser diodes, ultraviolet (UV)-lasers and photodetectors, photovoltaic devices, photocatalysts, gas sensors, humidity sensors, thin film transistors, spintronic devices, piezoelectric devices, water splitting, etc [47,79,115,116,154]. The n-type metal oxide ZnO semiconductor has the fascinating optical and electrical properties [79,143,155]. The highly crystalline pure/doped ZnO thin films can be deposited by cost effective sol-gel coating process which are widely used in aforementioned devices and also have the potential to be used in the upcoming solution processed optoelectronic devices [134,156]. The ZnO has also been widely utilized in various structures such as ZnO/metal/ZnO multilayers, ZnO/metal and ZnO/metal oxide nano-scale heterostructures, graphene oxide (GO)/ZnO nanocomposites, etc. to alter and/or improve certain important properties such as transmittance, optical dispersion, reflection, and electrical conductivity for their optoelectronic device and photocatalytic applications [70,157].

In the recent decades, the chemical, physical, optical and electrical (optoelectronic) properties of organic semiconductors (conjugated organic molecules) have been intensively investigated for their extensive use in the organic optoelectronic devices [16,62,119,120]. The high quality amorphous organic semiconductor thin films have most widely been deposited by using vacuum sublimation process (Thermal evaporation method). It increases the manufacturing cost of the devices which is not viable for the commercial usage. More recently, the highly crystalline solution processed inorganic/organic artificial multifunctional composite thin films have attracted enormous attention worldwide due to their promising desirable features manifested by combining the unique characteristic properties of both inorganic and organic candidates for the next generation highly efficient device applications. Zou et al. has

investigated the spin-coated ZnO nanoparticles (NPs) incorporated polyfluorene composite thin films for their potential use as an electroluminescent material in OLEDs and reported that the prepared nanocomposite thin films exhibit the high stability and improved PL emission (peak at 554 nm) due to incorporation of ZnO NPs into polymer, facilitating the energy transfer between ZnO NPs and Polymer in the films [143]. Dhara et al. has studied the surface modification of organic anthracene capped vertically aligned ZnO nanowires in the ZnO/organic heterostructured film and demonstrated a six-fold improvement in the UV photosensitivity with much faster photoresponse time of 1.5 s and reset time of 1.6 s [158]. The hybrid ZnO/polyacrylic acid (PAAX; X = H or Na) nanocomposites synthesized via sol-gel method have exhibited the increased photoluminescence (PL) in the visible region (above 450 nm) with stable PL quantum yield of 70%. This intense visible emission and suppressed UV emission have been corroborated based on the effect of surface modification of ZnO nanoparticles (NPs) surrounded by polymers in the ZnO/PAAH composites [159]. In our recent study, Dasi et al. has prepared tris-(8-hydroxyquinoline)aluminum (Alq_3)/ZnO hybrid thin films by sol-gel spin coating process [156]. Alq_3 is one of the most widely used electron transporting as well as green-light emitting molecules in the OLEDs [4,121,160]. It has been reported that the incorporation of Alq_3 controls ZnO particle size and transfers the energy to ZnO, resulting in fourfold enhancement of the UV emission in the Alq_3/ZnO hybrid thin films. Hybrid (organic/inorganic) composite materials exhibit high thermal stability, chemical resistance, mechanical strength, good optical and electrical properties over organic and inorganic materials [8,117,161,162]. Organic/ZnO hybrid film-based UV-photodetectors show good advantages as high gain, sensitivity, and responsivity with low- cost fabrication [163–165]. Hence, it is highly beneficial and important to understand the structural and chemical environment at the hybrid organic/ZnO interface for their potential applications in UV photodetectors.

In this study, we report on structural, chemical and compositional properties of the high quality Alq_3/ZnO hybrid thin films deposited by spin-coating process using Raman and X-ray

photoelectron spectroscopic (XPS) results. We also report the enhanced photoresponse of UV photodetectors based on Alq_3/ZnO hybrid thin films.

4.2. Experimental details

4.2.1. Alq_3/ZnO hybrid thin film preparation and Instrumentation

The procedure for the preparation of pristine ZnO and Alq_3/ZnO hybrid thin films by using sol-gel spin-coating process was followed as-such from our earlier report published elsewhere [156]. The zinc acetate dihydrate [$Zn(CH_3COO)_2.2H_2O$: 98.5%; SRL] of 5.487 g (0.5 M) was firstly dissolved into 50 mL of 2-methoxyethanol ($C_3H_8O_2$: 99%; SRL) solvent and stirred at 450 rpm for 2 hrs at 60ºC. The ZnO precursor solution (A) was obtained by drop wise addition of monoethanolamine (MEA: 99%; SRL) (1.512 mL) for 1:1 molar ratio of MEA to zinc acetate and allowed it for gelation by keeping it under the normal ambient for 24 hrs. Alq_3 ($C_{27}H_{18}AlN_3O_3$: 99.995%; Sigma Aldrich) (11.48 mg) was dissolved in 2-methoxyethanol solvent (25 mL) (10^{-3} M) and stirred (450 rpm) for 2 hrs [solution (B)]. The 0.2 μm syringe filter was used to filter the ZnO sol-gel precursor (A) and Alq_3 solution (B) separately. Using these, the three (5 mL each) Alq_3 incorporated ZnO precursor solutions were prepared with the nominal molar ratio of Alq_3 to ZnO (Alq_3/ZnO) as $0.5x10^{-3}$ [4 mL of ZnO (80 vol.%) (0.4 M) + 1 mL of Alq_3 (20 vol.%) ($2x10^{-4}$ M)] for film (**b**), $1.3x10^{-3}$ for [3 mL of ZnO (60 vol.%) (0.3 M) + 2 mL of Alq_3 (40 vol.%) ($4x10^{-4}$ M)] for the film (**c**); and $3x10^{-3}$ [2 mL of ZnO (40 vol.%) (0.2 M) + 3 mL of Alq_3 (60 vol.%) ($6x10^{-4}$ M)] for film (**d**). The glass substrates [Blue star (PIC-2) micro slides, Polar Industrial corporation, Mumbai, India] were thoroughly cleaned prior to the coating using acetone, isopropyl alcohol (isopropanol) and double ionized water as per the cleaning steps reported elsewhere [156]. Finally, substrates were plasma cleaned using Harrick Plasma, PDC-002. The pristine ZnO film (**a**) using the sol-gel precursor (A) and Alq_3/ZnO hybrid thin films (**b - d**) by above three respective precursor sols were deposited on clean glass substrates using Spin coater (Apex Instruments, spinNXG-P2 model) under the

normal ambient. Each thin film was having the optimal thickness of around 200 nm [156]. The four thin films (**a - d**) were then post-annealed at 300 ºC (for 2 hrs) under the normal ambient. The Raman spectra of solution processed pristine ZnO (**a**) and Alq_3/ZnO hybrid thin films (**b - d**) were recorded at room temperature using Raman spectrometer (HORIBA Jobin Yvon, France, LabRAM HR model) with an Argon laser excitation wavelength of 488 nm (2.54 eV) and power of ~47 mW at the sample. These spectra were collected through a confocal optical microscope coupled with a holographic grating (600 gr/mm) and a CCD camera detector. The surface elemental compositional analysis of the hybrid films was carried out using X-ray photoelectron spectroscopy (XPS, Thermo Scientific) having a monochromatized X-ray source of Al Kα (hν = 1486.6 eV) with spot size of 400 μm. The wide survey spectra of the films were recorded in the binding energy range of 0 to 1300 eV with analyzer pass energy of 200 eV and energy step size of 1 eV. The binding energy of C 1s peak (284.3 eV) of pristine ZnO film (**a**) is used as a charge reference and energy-scale calibration (charge correction) for all spectra of Alq_3/ZnO hybrid thin films was carried out with reference to C 1s peak at 284.3 eV. The narrow scan core level (Zn, 2p, O 1s, C 1s, and Al 2p) spectra were measured with analyser pass energy of 50 eV and energy step size of 0.1 eV. The sheet resistance was measured by four probe method using Keithley source measurement unit (SMU). The UV photodetectors were fabricated based on pure ZnO and Alq_3/ZnO hybrid thin films following the below procedure.

4.2.2. Fabrication process of UV-Photodetectors

To study the ultraviolet-photoresponse of the pristine ZnO and Alq_3 incorporated ZnO hybrid films, UV-Photodetectors were fabricated based on the films (**a - d**). The four glass substrates were cut into 2×2 cm^2 area and were cleaned by following the above procedure. The glass substrates were also plasma cleaned in high power plasma at 800-micron vacuum for 10 min. The prepared and filtered pristine ZnO and three Alq_3 incorporated ZnO solutions were spin-coated at 2000 rpm for 30 sec separately onto the four cleaned glass substrates and pre-

annealed at 200 °C for 10 min on the hot plate in normal ambient to evaporate the solvent. The coating process was repeated for 5 times for the required thickness. The UV-photodetectors were fabricated by depositing the two aluminium (Al) layers (120 nm) as ohmic contacts onto the spin-coated films using thermal evaporation vacuum coating unit under the vacuum of ~5×10^{-6}mbar. The Al electrodes were deposited with a gap of 2 mm by covering with the metal mask (device area = 2×4 mm^2). The fabricated UV-photodetectors having the structure of glass "substrate/pristine ZnO film (device **A**) or Alq_3/ZnO hybrid films with the molar ratio of $0.5x10^{-3}$ (device **B**), $1.3x10^{-3}$ (device **C**) and $3x10^{-3}$ (device **D**)/Al". The current density (J)-voltage (V) characteristics of the four fabricated UV-photodetectors were measured using the source measurement unit (SMU: Keithley, 2450 model) in dark and under the UV-spot light illumination (wavelength: 365 nm, Spectral width: ~6nm) in normal ambient. The time-dependent UV responses of the devices were measured by ON/OFF the UV illumination onto the device in regular intervals of 30 sec. The ON/OFF for UV illumination was controlled by the in-built semi-automatic shutter provided in the UV light source system, where the UV light source is continuously kept in the ON state until the measurements get over.

4.3. Results and discussion

4.3.1. Raman spectroscopic studies

Raman spectroscopy is a powerful technique to study various parameters such as chemical components, purity/crystal quality, crystal structure, microscopic structural features, crystal defects, distortion of lattices, and their vibrational properties of the bulk crystals and nanostructured thin films [166]. Raman spectra of sol-gel derived spin coated pristine ZnO (**a**) and Alq_3/ZnO hybrid thin films (**b - d**) were shown in Fig. 4.1. The wide band gap n-type metal-oxide semiconductor ZnO crystallizes commonly in the hexagonal wurtzite structure with the space group of C_{6v}^4 ($P6_3mc$) [167]. According to group theory prediction, at the Γ (k = 0) point of the Brillouin zone, the following optical phonon normal modes are expected:

$\Gamma_{opt} = A_1 + E_1 + 2B_1 + 2\,E_2$

where the two B_1 (B_1^{low} and B_1^{high}) symmetry modes are silent/forbidden modes (Raman & infrared (IR) inactive); the A_1 and E_1 phonon modes are polar and both Raman & IR active vibrational modes, whereas the doublet E_2 phonon mode with two phonon frequencies (E_2^{low} and E_2^{high}) is non-polar (IR inactive) and Raman active only. In addition, the two polar modes A_1 and E_1 (their vibrations polarize the unit cell and result in the generation of a long-range electrostatic field) split into longitudinal optical (LO) and transverse optical (TO) components as A_1(TO), E_1(TO), A_1(LO), and E_1(LO) [168].

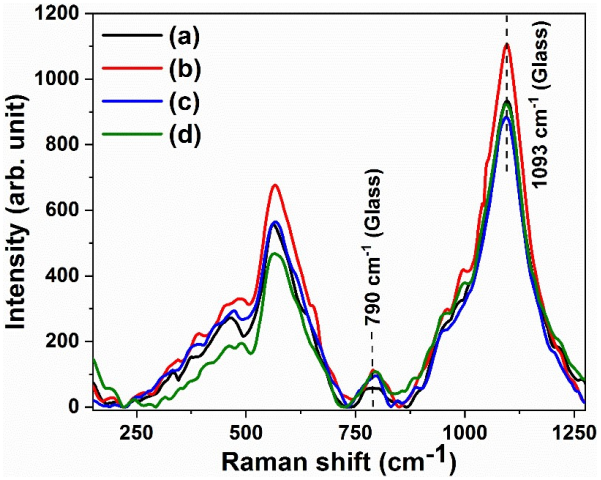

Fig. 4.1. The Raman spectra of spin-coated pristine ZnO (**a**) and Alq_3/ZnO hybrid thin films (**b - d**) with the Alq_3/ZnO molar ratio of $0.5x10^{-3}$ (b), $1.3x10^{-3}$ (**c**), and $3x10^{-3}$ (**d**).

The Raman spectrum of pristine ZnO thin film (**a**) exhibited the vibrational modes at 375, 410, 443, 563, and 591 cm^{-1} corresponding to A_1(TO), E_1(TO), E_2^{high}, A_1(LO), and E_1(LO) phonon modes, respectively (Fig. 4.2) [167]. The E_2^{high} vibration mode (443 cm^{-1}) shows the characteristic wurtzite phase of ZnO. The relatively strong intensity of E_2^{high} and A_1 (LO) modes show the sol-gel derived spin-coated pristine ZnO film is highly (002) plane c-axis oriented [169]. The E_1(LO) phonon mode (positioned at 591 cm^{-1}) is attributed to the formation of defects such as Zinc interstitials (Zn_i), oxygen vacancy, and lack of free carriers [170]. The

additional vibrational bands present with the frequencies of 205 and 333 cm^{-1} are attributed to the second-order Raman processes [171]. The vibrational peaks observed at 790 and 1093 cm^{-1} are corresponding to the glass substrate [170,172]. The observed vibrational phonon modes and their assignments of constituent compounds in the hybrid thin film are given in Table 4.1.

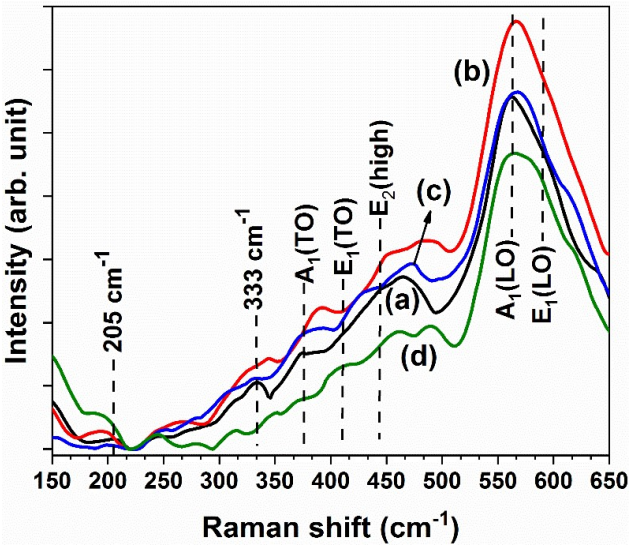

Fig. 4.2. The Raman spectra of hybrid thin films (**a- d**) in the range of 150 - 650 cm^{-1}.

In Fig. 4.3, the Raman spectrum of Alq_3/ZnO hybrid thin film (**b**) with Alq_3 to ZnO molar ratio of $0.5x10^{-3}$ shows the oxine (8-hydroxyquinoline; 8HQ) C-H out-of-plane bending modes with strong relative intensity at 748, 781, 818 cm^{-1} which are ascribed to characteristic frequency of 8HQ in tris-(8-hydroxyquinoline)aluminum (Alq_3) molecule [173]. The respective Raman bands observed in the hybrid thin films (**b - d**) are assigned to incorporated Alq_3 molecule (Table 4.1) based on the reported Raman studies of Alq_3 thin films published elsewhere [173]. The vibrational mode (shoulder) observed at 758 cm^{-1} can be assigned to the breathing mode of 8HQ moiety and the strong relative band at 800 cm^{-1} assigned to 8HQ Ring deformation mode. The reported Raman bands of Alq_3 at 404 cm^{-1} (assigned to Ring deformation + Al-O stretching mode), 428 cm^{-1} (Ring deformation), 456 cm^{-1} (C-H torsion), 577 cm^{-1} (Ring deformation + Al-O-C bending mode), and 596 cm^{-1} (C-H torsion) may also be correlated with the shifts of observed modes of ZnO in the Alq_3/ZnO hybrid thin films. The

E_2^{high} mode (443 cm^{-1}) of wurtzite ZnO is blue shifted to a higher frequency closer to the reported C-H torsion mode (456 cm^{-1}) of Alq_3, showing the Alq_3/ZnO hybrid film (**b**) is under compressive pressure as the ZnO crystallites are surrounded by the incorporated Alq_3 molecules in the film [169]. A shift of A_1(TO) phonon mode to a higher frequency in the hybrid film (**b**) may also corroborate the incorporation of Alq_3 molecules in the film (**b**). The increased peak intensity of A_1(LO) (569 cm^{-1}) phonon mode along with a weak E_1(LO) (591 cm^{-1}) shoulder peak (which is closer to the reported C-H torsion mode (596 cm^{-1}) of Alq_3) when compared to that of film (**a**) may indicate that the ZnO crystallites possess the preferred c-axis orientation and become more crystalline with low density of defects in the presence of Alq_3 in the hybrid film. Zamiri et al. has also reported the higher Raman peak intensity of E_1(LO) phonon mode in ZnO/Ag nanostructure and explained by using a chemical theory; the formation of charge transfer complexes/species which have formed a bond with the surface of ZnO, causes the enhancement [174]. The enhanced intensity of the longitudinal optical phonon modes reveals that the incorporated Alq_3 molecules do not enter into the ZnO matrix and may be surrounded on the highly (002) plane c-axis oriented ZnO crystallites in the Alq_3/ZnO hybrid thin film as supported by the earlier report published elsewhere [156].

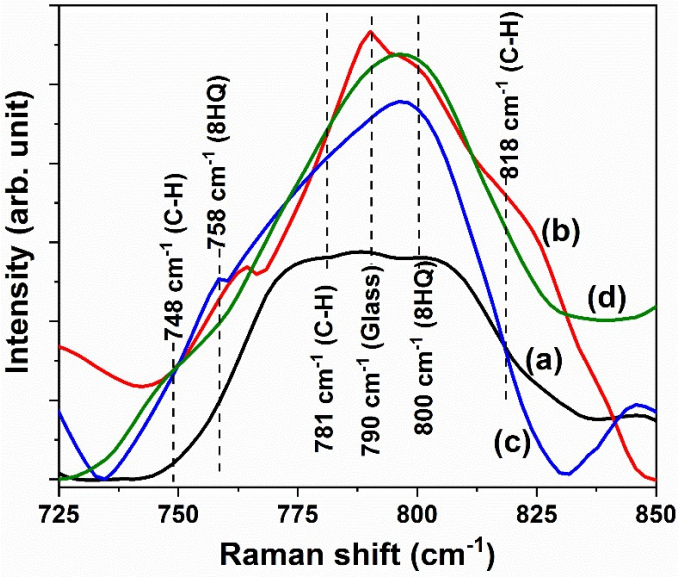

Fig. 4.3. The Raman spectra of hybrid thin films (a- d) in the range of 725 - 850 cm^{-1}.

Table 4.1. Raman active mode frequencies and assignments of pristine ZnO and Alq_3/ZnO hybrid thin films.

Mode frequency (cm^{-1})	**Symmetry / Assignments**		**compound/ Molecule**
205, 333	Second order Raman processes		ZnO
375	A_1(TO)	Transverse optical mode	
410	E_1(TO)	Transverse optical mode	
443	E_2^{high}	Preferred c-axis orientation	
563	A_1(LO)	Preferred c-axis orientation	
591	E_1(LO)	Formation of defects	
790, 1093	Glass Substrate		
404	Ring deformation + Al-O stretching mode		Alq_3
428	Ring deformation		
456, 596	C-H Torsion		
577	Ring deformation + Al-O-C bending mode		
758, 781, 818	Oxine (8-hydroxyquinoline, 8HQ)		
758	Breathing mode of 8HQ moiety		
800	8HQ Ring deformation mode		

From the Raman spectrum of Alq_3/ZnO hybrid thin film (**c**) with increased Alq_3/ZnO molar ratio of 1.3 $x10^{-3}$, it is obvious to observe the overlapping features of Alq_3 and ZnO in the Raman shifts of hybrid Alq_3/ZnO structures. The slight decrease in the intensity of the characteristic E_2^{high} and A_1 (LO) vibrational modes associated with ZnO without any significant change in

the Raman shift when compared to that of film (**b**) may be attributed to the presence of increased Alq_3 molecules surrounded onto the ZnO particles in the bulk of the film also. There is no significant change in the intensity of Raman peaks associated with Alq_3 in the film (**c**) which in turn relates the increased Alq_3/ZnO ratio. In our recent report, Dasi et al. has demonstrated that the incorporated Alq_3 molecules do not enter into the ZnO matrix and instead control the particle size by effective capping of Alq_3 molecules onto the ZnO particles

in the Alq_3/ZnO hybrid thin films [156]. The considerable decrease in the intensity of characteristic Raman bands of ZnO in the Alq_3/ZnO hybrid thin film (**d**) supports the size-controlled ZnO particles capped by Alq_3 molecules. A slight increase in the intensity of characteristic vibrational modes of Alq_3 when compared to that of film (**c**) corroborates the decreasing ZnO particle size due to the highest Alq_3/ZnO ratio of 3 $x10^{-3}$ and by effective capping of Alq_3 molecules in the hybrid film (**d**). This Raman study of Alq_3/ZnO hybrid thin films supports to report that the incorporation of Alq_3 favors the formation of a bond with the surface of highly crystalline c-axis oriented ZnO particles in the hybrid thin film.

4.3.2. X-ray photoelectron spectroscopic (XPS) analysis

In order to analyze the surface elemental composition and chemical state of different elements in the pristine ZnO (**a**) and Alq_3/ZnO hybrid thin films (**b - d**), the XPS measurements were carried out and the wide survey spectra of the films in the binding energy (BE) range of 0 to 1300 eV are shown in Fig. 4.4. It reveals the existence of various elements such as zinc (Zn), oxygen (O), carbon (C), and aluminium (Al) in the films. The relative surface atomic concentrations (%) of the elements [Zn (2s, 2p, 3s, 3p, 3d), O (1s), C (1s), and Al (2s, 2p)] in the films are given in Table 4.2. The narrow scan core level (Zn 2p, O 1s, C 1s, and Al 2p) XPS spectra of the films (**a - d**) are shown in the figures 4.5 – 4.8 and the respective BE peak positions (eV) are given in Table 4.2. The Zn 2p core level spectrum (Fig. 4.5) of pristine ZnO film (**a**) shows the presence of two BE peaks centered at 1020.8 eV and 1043.9 eV

corresponding to doublets Zn $2p_{3/2}$ and Zn $2p_{1/2}$ respectively with the atomic concentration of 64%, confirming the existence of Zn atoms in the oxidized state (Zn^{2+} ion in Zn-O bond) in the film [175]. The asymmetric peak (observed at 529.8 eV with the atomic concentration of 16%) of O 1s core level spectrum (Fig. 4.6) of the pristine film (**a**) is deconvoluted by using Gauss fitting, showing the peak at 529.5 eV (O_I) and the shoulder peak at 531.0 eV (O_{II}). The dominant

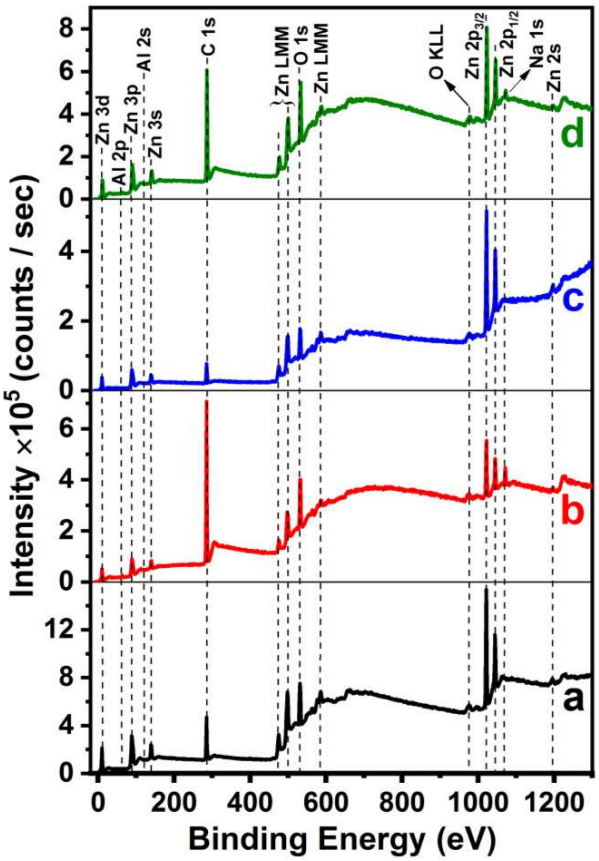

Fig. 4.4. The wide survey X-ray photoelectron (XPS) spectra of spin-coated pristine ZnO (**a**) andAlq_3/ZnO hybrid thin films (**b - d**) with the Alq_3/ZnO molar ratio of $0.5x10^{-3}$ (**b**), $1.3x10^{-3}$ (**c**), and $3x10^{-3}$ (**d**).

peak centered at 529.5 eV (O_I) is attributed to the oxygen (O^{2-}) ion surrounded by Zn^{2+} ions (Zn-O bonds) [176,177]. The higher BE peak (O_{II}) is usually attributed to chemisorbed or dissociated oxygen or hydroxyl group or carbonyl group on the surface of the ZnO film [145]. In the figure 4.7, the BE peak centered at 284.3 eV (with atomic concentration of 20%) is assigned to adventitious carbon (C 1s core level) atoms formed onto the surface of the film (**a**)

during the coating under the normal ambient [145,175]. The C 1s binding energy (284.3 eV) of the pristine ZnO is used as a charge reference. The core level spectra (Zn 2p, O 1s, C 1s, and Al 2p) of respective hybrid film are calibrated with respect to the observed shift of its C 1s peak for being aligned with reference C 1s peak (284.3 eV) of pristine ZnO film (**a**). The Alq_3/ZnO hybrid thin film (**b**) (with molar ratio of $0.5x10^{-3}$) exhibits a slight peak shift towards the higher binding energy in the core level spectra of Zn 2p (1020.9 eV; 27%) and O 1s [deconvoluted peaks O_I (529.6 eV) and O_{II} (530.9 eV) with the atomic concentration of 11%] with reference to C 1s (284.3 eV; 60%) when compared to that of pristine film (**a**). An additional symmetric BE peak centered at 62.9 eV (atomic concentration; 2%) in the film (**b**) is assigned to Al 2p core level (Fig. 4.8). The presence of a weak BE energy peak at ~1072 eV corresponding to Na 1s is not part of the thin films (it may possibly be a surface contaminant occurred during handling films for the measurements) and hence it is not considered for the analysis. Wang et al. has reported the core level XPS spectra of C 1s (284.4 eV), O 1s (531.3 eV) and Al 2p states corresponding to the Al-O-C bond in the pristine Alq_3 thin film in agreement with other reports published elsewhere [178–180]. As shown in the above figures, the observed BE peaks of C 1s (284.3 eV), O 1s (O_{II}: 530.9 eV), and Al 2p (62.9 eV) core level spectra distinctly confirm the Al-O-C bonds of the incorporated Alq_3 molecules in the hybrid film (**b**). The change in the BE state of Zn (Zn $2p_{3/2}$:1020.9 eV and Zn $2p_{1/2}$: 1044.0 eV) also suggests the presence of incorporated Alq_3 molecules in the film (**b**). The observed increased BE peak intensity and atomic concentrations of C, O (O_{II}) with a BE peak of Al along with the decreased intensity and concentration of Zn in the hybrid film (**b**) (Table 4.2) reveal the relative concentration of incorporated Alq_3 molecules on the surface of the film. The schematic representation of incorporated Alq_3 in the film (**b**) is given in Fig. 4.9. The possible contribution of excess carbon atoms (a surface contaminant which may be formed during handling the films for the measurements) to the increased relative surface atomic concentration of C in the hybrid film (**b)** is not completely ruled out but may be considered to be substantially low.

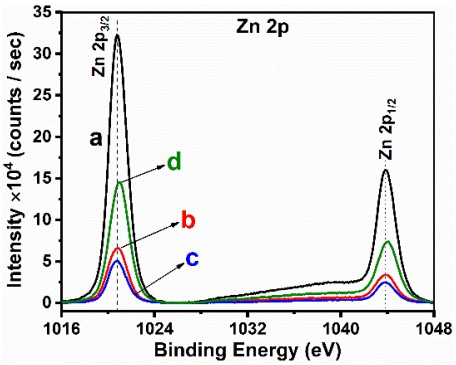

Fig. 4.5. The narrow scan Zn 2p core level XPS spectrum of hybrid thin films (**a- d**).

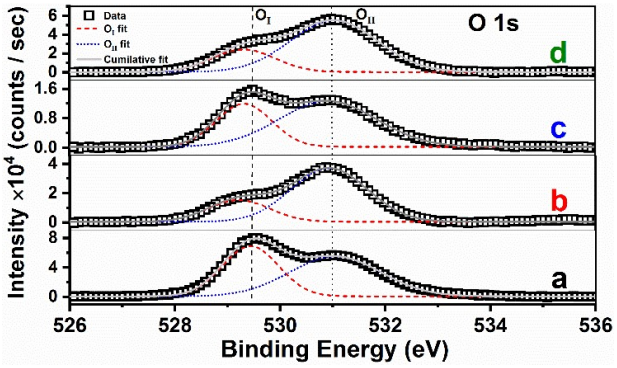

Fig. 4.6. The narrow scan O 1s core level XPS spectrum of hybrid thin films (**a- d**).

The core level XPS spectra (Fig. 4.5) of Zn 2p [Zn $2p_{3/2}$ (1020.8 eV) and Zn $2p_{1/2}$ (1043.9 eV) with atomic concentration of 63%], C 1s (284.3 eV; 19%), O 1s [deconvoluted peaks O_I (529.5 eV) and O_{II} (530.9 eV) with the atomic concentration of 17%], and Al 2p (62.8 eV; 1%) states of the hybrid thin film (**c**) are showing the BE peaks without any change in its position when compared to that of the above films. These spectra also show a significant decrease in the BE peak intensity of C 1s, O 1s (O_{II}) and Al 2p and their atomic concentrations along with an increase in the surface atomic concentrations of Zn and O (Table 4.2). These results may reveal that the incorporated Alq_3 molecules (with Alq_3/ZnO molar ratio of $1.3x10^{-3}$) may be adsorbed at the grain boundaries of ZnO crystallites in bulk of the film (**c**) and facilitating the formation of Alq_3 capped ZnO nanoparticles as reported in the earlier studies (Fig. 4.9) [156]. In the Alq_3/ZnO hybrid thin film (**d**) with increased molar ratio of $3x10^{-3}$, the BE peaks of Zn 2p [Zn $2p_{3/2}$ (1021.0 eV) and Zn $2p_{1/2}$ (1044.1 eV) with atomic concentration of 43%], C 1s (284.3 eV; 42%), O 1s [deconvoluted peaks O_I (529.6 eV) and O_{II} (531.0 eV) with the atomic concentration of 14%], and Al 2p (62.8 eV; 1%) core level spectra are consistent in the binding energy shift when compared to above films. The BE peak intensities of C 1s, O 1s (O_{II}) and Al 2p states corresponding to Al-O-C bonds of Alq_3 molecule and that of Zn 2p (Zn-O) are substantially increased with respect to atomic concentrations. It may be corroborated

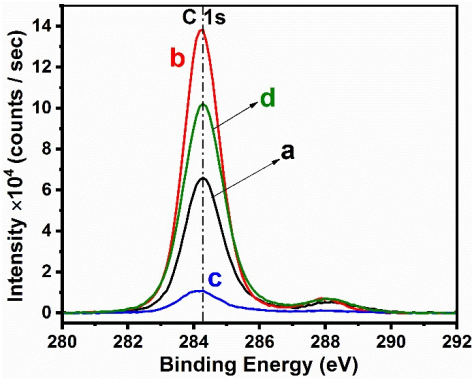

Fig. 4.7. The narrow scan C 1s core level XPS spectrum of hybrid thin films (**a- d**).

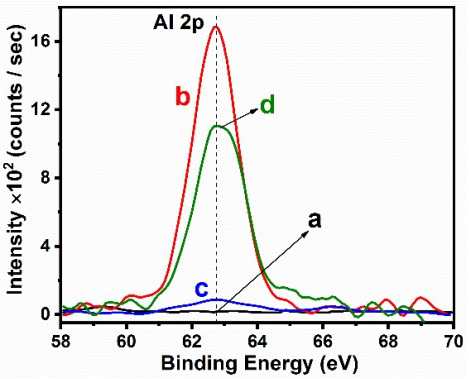

Fig. 4.8. The narrow scan Al 2p 1s core level XPS spectrum of hybrid thin films (**a- d**).

with the effective coverage/capping of Alq_3 molecules onto the ZnO particles and thus controlling the ZnO nanoparticle size in the film (**d**) (Fig. 4.9) [156]. The BE peak shift of Zn 2p and O 1s (O_I) corresponding to Zn-O bonds and that of C 1s, O 1s (O_{II}) and Al 2p states corresponding to Al-O-C bonds in Alq_3 molecule ascertain the existence of chemical interaction via non-covalent bonds (chemisorption) and/or charge transfer species between Alq_3 and ZnO in the hybrid thin films [156]. The observation of existence of chemical interaction and/or charge transfer in the hybrid thin films is in good agreement with the recent literature reports on the organic/inorganic mesoporous silica based composite materials. Awual et al. has reported the strong binding of the organic ligand molecules to mesoporous silica via hydrogen or non-covalent bonding in the composite material used for detection of copper(II) ions in the contaminated water [126]. The anchoring of sulfur donor containing organic ligand molecule onto the silica has been based on non-specific interactions via hydrogen bonding, reversible covalent bond, and Van der Waals forces [125]. The formation of the non-covalent affinity (hydrogen bonding) between the abundant hydroxyl groups of surface silicates and organic ligand heteroatoms has also been reported in the ligand functionalized conjugate mesoporous silica composites for the detection of NO_2^- ions from the waste water [181]. These results show that the incorporation of Alq_3 molecules favours the formation of preferred c-axis oriented ZnO nanoparticles and ascertains the existence of chemical interaction via non-covalent bonds

(chemisorption) and/or charge transfer complexes between Alq_3 and ZnO in the Alq_3/ZnO hybrid thin films. The entire sequential representation of formation of Alq_3 capped ZnO nanoparticles in sol-gel derived spin-coated Alq_3/ZnO hybrid thin films is depicted in Fig 4.9.

Table 4.2. The XPS parameters of the elements present in pristine ZnO(**a**) and Alq_3/ZnO hybrid thin films (**b - d**).

Element	Photoelectron Line	Binding Energy (BE) peak position* (eV)				Relative surface atomic concentration of elements (%)			
	Film	**a**	**b**	**c**	**d**	**a**	**b**	**c**	**d**
Zn	Zn 2p**	1020.8	1020.9	1020.8	1021.0	64	27	63	43
	$Zn\ 2p_{3/2}$	1020.8	1020.9	1020.8	1021.0				
	$Zn\ 2p_{1/2}$	1043.9	1044.0	1043.9	1044.1				
O	O 1s***	529.8	530.9	529.9	530.9	16	11	17	14
	O 1s (O_I)	529.5	529.6	529.5	529.6				
	O 1s (O_{II})	531.0	530.9	530.9	531.0				
C	C 1s	284.3	284.3	284.3	284.3	20	60	19	42
Al	Al 2p	---	62.9	62.8	62.8	---	2	1	1

*The core level spectra (Zn 2p, O 1s, C 1s, and Al 2p) of respective hybrid film are calibrated with respect to the observed shift of its C 1s peak for being aligned with reference C 1s peak (284.3 eV) of pristine ZnO film (**a**).

**Zn 2p core level spectrum shows the presence of two BE peaks corresponding to doublets $Zn\ 2p_{3/2}$ and$Zn\ 2p_{1/2}$.

***The asymmetric peak of O 1s core level spectrum is deconvoluted by using Gaussian fitting, showing two BE peaks O_I and O_{II}.

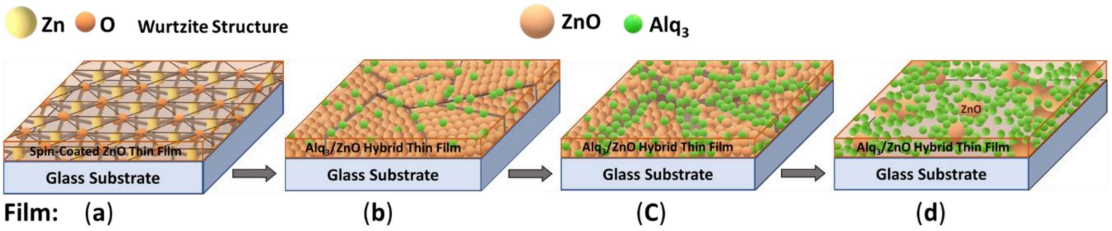

Fig. 4.9. Schematic representation of formation of Alq_3 capped ZnO nanoparticles in sol-gel derived spin-coated Alq_3/ZnO hybrid thin films (**a- d**).

4.3.3. Sheet resistance (R_s)

The sheet resistance values of the sol-gel derived spin-coated pristine ZnO (**a**) and Alq_3/ZnO hybrid thin films (**b - d**) have been obtained (Fig. 4.10) by the four-point collinear probe technique using the relation

$$R_s = [\pi/\ln 2]\,(V/I)\,k \qquad (4.1)$$

Where R_s is the sheet resistance, V is the voltage measured (between probes 2 and 3), I is the source current (between probes 1 and 4), and k (= 1) is the correction factor. The pristine ZnO thin film (**a**) shows the higher sheet resistance of 5075 MΩ/□ and it is significantly decreasing for increasing Alq_3/ZnO molar ratio in the hybrid films (**b**: 2401, **c**: 1359, and**d**:951MΩ/□). It is attributed to the adsorption of Alq_3 molecules at the grain boundaries of ZnO creates Alq_3 capped ZnO nanoparticles with improved crystalline properties which reduces the sheet resistance of the Alq_3/ZnO hybrid films. It supports the energy transfer from Alq_3 to ZnO in hybrid films results in decreased sheet resistance. From the PL spectra it is observed that the emission corresponding to the Zinc interstitials (390 – 420 nm) is increased with the incorporation of Alq_3. The Zn interstitials may increase the free carriers for conductivity and hence decrease the sheet resistance.

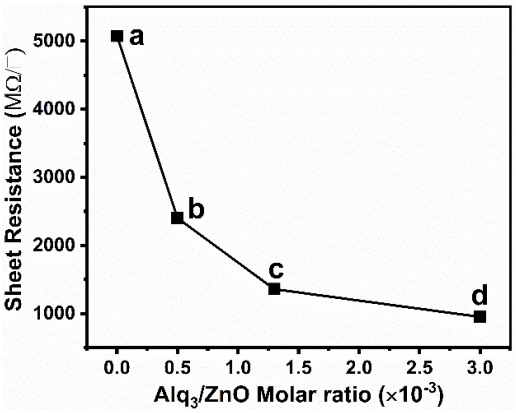

Fig. 4.10. The sheet resistance of Alq_3/ZnO hybrid thin films (**a - d**).

4.3.4. UV photodetector

To further investigate the photoelectric performances of pristine ZnO and Alq_3/ZnO hybrid thin films, UV-photodetectors were fabricated. Two Al electrodes were deposited onto the pristine ZnO film for device **A** and Alq_3/ZnO hybrid films for the device **(B - D)** as ohmic contacts using thermal evaporation vacuum coating unit at a high vacuum of 5.0×10^{-6} mbar. The Al electrode contacts were deposited with a gap of 2 mm by covering with a metal mask such that the device area is 0.08 cm^2. Fig. 4.11 shows the Schematic structure of fabricated UV-photodetectors and energy level diagram. The fabricated devices structures are as follows:

Device A: Glass substrate/pristine ZnO (~200 nm)/Al (120 nm).

Device B: Glass substrate/(Alq_3/ZnO-$0.5x10^{-3}$) (~200 nm)/Al (120 nm).

Device C: Glass substrate/(Alq_3/ZnO-$1.3x10^{-3}$) (~200 nm)/Al (120 nm).

Device B: Glass substrate/(Alq_3/ZnO-$3x10^{-3}$) (~200 nm)/Al (120 nm).

It is known that oxygen adsorption or desorption play the important role in controlling the photoconductivity of ZnO in bulk or thin films [182]. In the dark, oxygen molecules adsorbed onto the ZnO thin film surface as negatively charged ions by capturing the free electrons from n-type ZnO, thereby creating a depletion layer which induces a barrier with low conductivity near the thin film surface [68,182].

O_2 (gas) + e^- → O_2^- (adsorbed)

Upon exposure to UV-light, the electron-hole pairs will be photogenerated.

$h\nu \rightarrow e^- + h^+$ (exciton)

Holes migrate to the surface and discharge the adsorbed oxygen ions through surface electron-hole recombination:

$h^+ + O_2^-$ (adsorbed) → O_2 (gas)

At the same time, the photo-generated electrons significantly increase the conductivity of the ZnO thin film by decreasing the width of the depletion layer and barrier height [68,183].

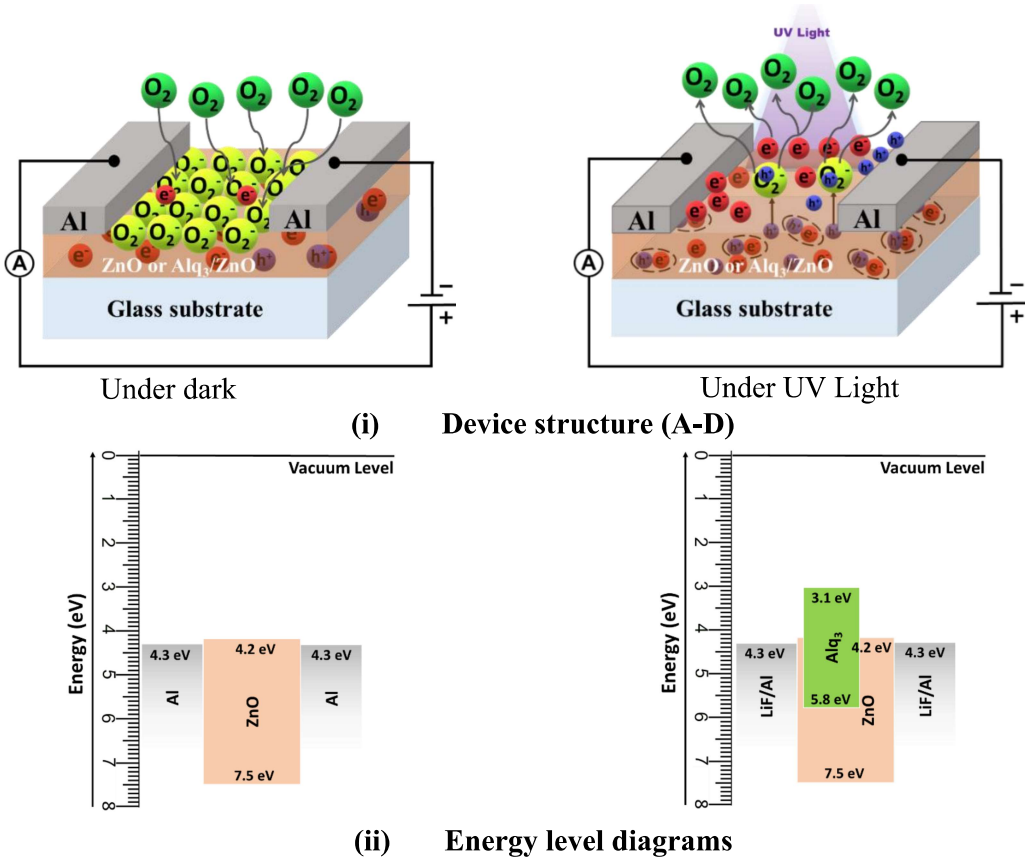

Fig. 4.11. The Schematic of (i) device structure and (ii) energy level diagrams of constituent elements of UV-photodetectors based on pristine ZnO (device **A**) or Alq_3/ZnO hybrid thin films (devices **B-D**)

The current density (J)-voltage (V) characteristics were performed using voltage/current source/measure unit (Keithley, 2450 model) in dark and under the UV-spot light illumination

(wavelength: 365 nm) with bias voltage from -8 V to +8 V in normal ambient. Fig. 4.12(i) shows the semi-log plots of J-V characteristics. It is observed that under UV light, devices exhibit the photocurrent several orders of magnitude higher than the dark currents, attributed to the good UV response of pristine ZnO (device **A**) and Alq_3/ZnO hybrid thin film-based devices (**B – D**). The current density is observed to be increased for the devices **B - D** with Alq_3/ZnO molar ratios of $0.5x10^{-3}$, $1.3x10^{-3}$, and $3.0x10^{-3}$ respectively compared to device **A** based on pristine ZnO film in dark as well as under UV light. The less current for device **A** is due to the high sheet resistance of film **a** when compared to hybrid films. The increase in dark current for the devices (**B – D**) with the incorporation of Alq_3 is may be due to the decreased sheet resistance attributed by the increase in Zn interstitials (free carriers) in hybrid films (**b – d**). The device **D** exhibits slightly the less current density than device **C** in dark and it increased more under UV light compared to the other devices. The possible reasons for slight decrease in the dark current in device **D** may be i) the drastic decrease in the crystallite size of film **d** which may alter the charge conductivity, ii) the excess incorporation of Alq_3 in ZnO creates the charge trap states in the films which reduces the free carriers in the film, and iii) the more content of Alq_3may create the depletion layer in between Al contact and ZnO due to the more barrier potential (1.2 eV) between Alq_3 and Al contact than between ZnO and Al (0.1 eV). The hybrid film-based devices (**B – D**) exhibit the increased current under UV light compared to the pristine film-based device (**A**), which increases with the incorporation of Alq_3. The improved current is the resultant of free charge carriers present in the hybrid film and energy transfer from Alq_3 to ZnO. The excited electrons in Alq_3 under the UV light of 365 nm (near to the Alq_3 characteristic excitation of 380 nm) non-radiatively transferred to the ZnO via carbonyl group (C=O) resulting in increased charge carriers and hence increased current density attributed to the enhanced PL emission [4,156]. It has been reported that the excitons from the organic material transfer to the ZnO, resulting in improved photo responses [164,184].

Photocurrent, gain, responsivity, and detectivity are the main parameters to characterize a UV photodetector [68,183]. These parameters were calculated for 1 V bias and 1mW/cm^2 UV light power using the following formulae [68,134]. The values are given in Table 4.3.

Photocurrent gain (G) = I_{light}/I_{dark} (4.2)

Sensitivity(S) = I_{ph}/I_{dark} (4.3)

Responsivity(R) = I_{ph}/ P.A (4.4)

Detectivity(D) = $(I_{ph}/E)\ (2qI_{dark})^{1/2}$ (4.5)

where I_{dark} - dark current, I_{light}– current under UV light, I_{ph} (I_{light}- I_{dark}) – photocurrent, P - power of UV light, A - effective area of device, and q - electron charge.

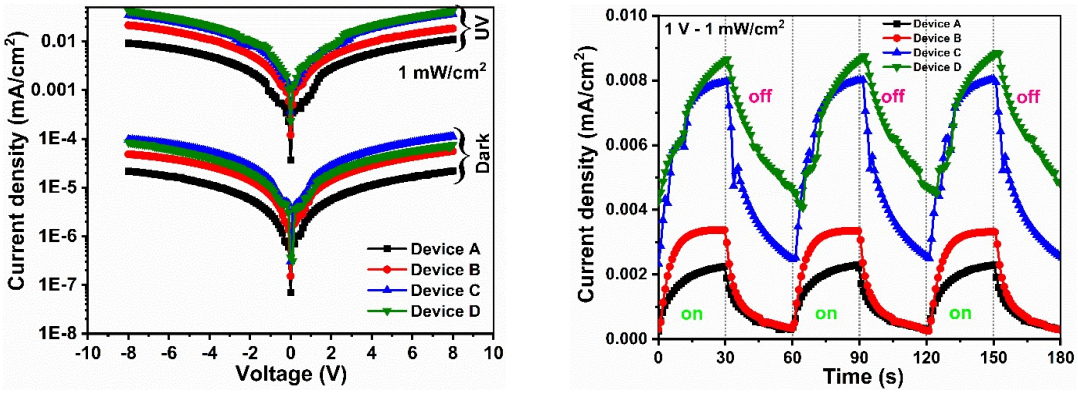

Fig. 4.12. (i) Current density–voltage (J–V) and (ii) time-dependent photoresponse characteristics of fabricated UV-photodetectors [devices (**A – D)** based on Alq_3/ZnO hybrid films (**a – d**)].

The photocurrent of the devices is mainly due to the excitons generated by the UV illumination. The photocurrent and responsivity are the proportional factors. The subsequent increase of photocurrent with the incorporation of Alq_3 in ZnO, ratifies the increase of exciton generation in ZnO by the energy transfer from Alq_3. The substantial improvement in photocurrent for device **D** compared to the other devices is due to the higher energy transfer from Alq_3 to ZnO in film **d**. The higher energy transfer is due to the more content of Alq_3 in film **d**, supporting the four-fold enhancement in PL emission [156]. The current gain,

sensitivity, and detectivity are the proportional factors, which are effectively altered by the dark current. The hybrid film-based devices exhibit the improved current gain and photo detectivity than the device **A**. The device **D** exhibits the higher detectivity compared to the other devices, due to its low dark current and higher light current means high current gain. The incorporation of Alq_3 controls the growth of crystallites which means it reduces the ZnO particle size [156]. The reduced particle size enhances the large surface to volume ratio which plays a key role in the photodetection process [185]. The large surface to volume ratio facilitates the oxygen adsorption and desorption resulting in the enhanced photocurrents or gain. The incorporation of Alq_3 provides more surface-active sites by reducing the ZnO particle size, resulting in improved device performances (gain, sensitivity, and detectivity) of hybrid films. XPS studies reveal that films **c** and **d** have the more surface atomic concentration of Zinc which increases the surface to volume ratio and hence improves photo responses of devices **C** and **D** [185]. The possible reasons for the better photoresponses of device **D** could be i) the excess incorporation of Alq_3 in ZnO in film **d** activates the oxygen adsorption and desorption due to its ambient sensitivity [186], ii) the incorporated Alq_3 is an electron transporting material which facilitates the transport of electrons and results in improved performance of UV photodetector [68,121,186], iii) the reduced crystallite or particle size for film **d** which is smaller than the Debye length (~ 18 nm) allows for the high density of electron trapped states on the surface resulting in increased photocurrent [187], and iv) the reduced particle size also enhances the surface to volume ratio which activates the oxygen adsorption and desorption effectively by increasing the hole-trap states on the surface [185].

Response speed and repeatability are the two important factors to know the photoresponse of the UV photodetectors. Figure 4.12 (ii) shows the time-dependent response characteristics of UV photodetector by modulating UV light source (incident optical power of 1 mW/cm^2), at 1 V bias with the interval of 30 sec. When the UV illumination is ON the current of pristine ZnO and Alq_3/ZnO thin film-based devices increased rapidly and when the UV

illumination is OFF, the current decreased drastically to its initial level, revealing the stability and reproducibility of all the devices **(A - D)**. The growth time τ_r and decay time τ_d, (defined as the time required for the photocurrent to increase from 10% to 90% and drop from 90% to 10% of the maximum current) were calculated from the response plots (Table 4.3) [164]. All the devices exhibit the slow decay time than the growth time. The slow decay time is due to the more photo persistent current (PPC) (the current present in the device even after the UV light off). The presence of charge trapped states in the film increases the rise time. The higher rise time of devices **C** and **D** compared to devices **A** and **B** may be due to the more presence of Alq_3 in ZnO grain boundaries which may create the charge traps. The device **B** exhibits the decreased time constants when compared to all other devices **(A, C,** and **D)**. The incorporated Alq_3 molecules with Alq_3/ZnO molar ratio of $0.5x10^{-3}$ predominantly present on the ZnO surface (more carbon atomic % form XPS studies) which may decrease the charge trapped states and PPC in the film **b,** resulting in fast responses of the device **B** than the other devices [69,156,188]. From the UVPD characteristics of all the devices it is observed that the device **D** exhibits the high current gain, responsivity, and detectivity whereas device **B** exhibits the fast response than the other devices.

Table 4.3. Device characteristics of UV photodetector (**A-D**) based on ZnO (**a**) and Alq_3/ZnO (**b-d**) hybrid thin films at 1V bias and UV light power of 1 mW/cm^2.

Device	Molar ratio of Alq_3/ZnO	Photocurrent density (J_{ph}) ($\mu A/cm^2$)	Current gain (G)	Responsivity (R) ($\times10^{-3}$ A/W)	Detectivity (D) ($\times10^{10}$)	Response time (s)	
						growth	decay
A	0 (Pristine)	1.01	330	1.01	3.24	4.8	17.2
B	$0.5x10^{-3}$	2.51	384	2.51	5.48	6.5	13.9
C	$1.3x10^{-3}$	3.93	636	3.93	6.31	16.8	19.0
D	$3x10^{-3}$	5.33	706	5.33	10.74	15.7	20.1

4.4. Conclusion

We deposit solution processed sol-gel derived Alq_3/ZnO hybrid thin films and Raman and XPS techniques were used to study their structural properties, and surface elemental composition & chemical state of different constituent elements. The pristine ZnO thin film exhibits the hexagonal wurtzite structure. From the Raman studies, it is corroborated that the incorporated Alq_3molecules make bonding onto the surface of highly oriented crystalline ZnO nanoparticles in the hybrid films. The XPS studies have supported that the incorporated Alq_3 molecules may be adsorbed on the surface of ZnO nanoparticles (chemisorption), showing the existence of chemical interaction between Alq_3 and ZnO in the hybrid films. These results are in support of the fact that the chemisorbed Alq_3 molecules onto the ZnO nanoparticles facilitate the non-radiative energy transfer between Alq_3 and ZnO in the hybrid thin films which enhance their optical and electrical properties, resulting in improved UV photodetectors performances.

Chapter: 5

Influence of Ni^{7+} swift heavy ion (SHI) irradiation on Alq_3/ZnO hybrid thin film for UV photodetector applications

This chapter describes the influence of Ni swift heavy ion (SHI) irradiation on Alq_3/ZnO hybrid thin film having the molar ratio of 0.5×10^{-3}. It gives the detailed analysis on optical, structural, and morphological properties of Ni SHI irradiated Alq_3/ZnO thin films. It also deals the effect of Ni SHI irradiation on photoresponse of UV photodetectors based on Alq_3/ZnO hybrid thin films. The Alq_3/ZnO hybrid thin films were irradiated with 120 MeV Ni^{+7} SHIs with the ion fluences of 5×10^{11}, 1×10^{12}, and 5×10^{12} ions/cm^2. These films were characterized and the results were compared with the pristine Alq_3/ZnO hybrid thin film. The UV photodetectors were also fabricated based on these irradiated films and the UV detection properties were analysed.

5.1. Introduction

In the present years the organic optoelectronic devices like OLEDs, OSCs, laser diodes, optical sensors, and UV photodetectors are developed for their commercial use. Out of these, the OLEDs are commercialized in lighting and display technology due to their extraordinary performances. Especially the display technology of OLEDs has been achieving fast growth for their wide usage. Current research on organic semiconductor based optoelectronic devices is to improve their stability, device efficiency, and durability. Using hybrid (organic/Inorganic) materials is one of the ways for better optoelectronic device performances [124,187]. Researchers have synthesized various hybrid materials and achieved improved performances of the devices [79,117,124]. The synthesis of hybrid materials has the incorporation of organic materials in inorganic and vice versa. The hybridization of material has to be done in such a way that one should achieve the new beneficial properties without altering the individual's

properties. Not only the hybridization, but in any doping process also the dopant element should not affect the actual properties of the host, and the properties should be in enhanced way. One can tune the host material properties for their requirements by doping with the other elements in a controlled way. But doping with the other elements changes the stoichiometry of the host which may affect its original characteristics. During the thin film formation of composites, the dopant may not be uniformly distributed or it may alter the atomic arrangement of the host material. The composite materials cannot be coated as a thin film using evaporation or vapour deposition process due to the difference in evaporation temperature of individual elements. The solution process is a good method for the thin-film formation of hybrid or other composites, which requires fine-tuning and a high degree of optimization in solution preparation and uniform film formation [41,117]. Even though the solution process is a simple, easy, and cost-effective method there are some disadvantages like the creation of charge traps, barriers at the boundaries, and less conductivity. It is quite difficult to achieve the solution-processed thin films with all desired qualities. Swift heavy ion (SHI) irradiation is one method which is used for tailoring the properties of thin film [189]. In this method, the thin films are irradiated with the different ionic states of elements with various ion fluences. The elements can be Au, Ni, H, Ni, Ag, Li, etc with different ionic states. One can tailor the properties of thin films with this process by controlling the ion energy and fluences. Researchers have been utilising this method for acquiring the better optical, structural, and electrical properties of the thin films and also for stability measurements of thin films and devices [189–191]. In the irradiation process an energetic ion hits the target with high velocity, travel through the material and loses its energy. It loses the energy in two processes i) direct transfer of energy to atoms in the target through elastic collision in low energy regime of up to ~ 10 KeV/amu known as nuclear energy loss (S_n), ii) electronic excitation and ionization of target atoms through inelastic collision in high energy regime of ~ 1 MeV/amu and above known as electronic energy loss (S_e) [189,192]. If the ion energy is from few KeV to 1 MeV, it hits target atom and partially transfers the energy

to the atom and displace it. The displaced or recoiled atom hits the neighbouring atoms through elastic collision resulting in collision cascade. The high energy ions whose velocity is equal to the Bohr electron velocity or more passes through the target very swiftly through inelastic collision and excite or ionise the atoms along its path [192]. These high energy ions are called swift heavy ions (SHI). The formation of ion tracks happens in insulators and semiconductors but not in metals (create only defects) except (Fe, Ti, Bi, etc.) [192]. The SHI irradiation leads to the creation of defects in the sample or anneal the sample by creating the ion tracks results in modulating properties [192,193]. The low energy ions implanted in the target by creating the point/columnar defects whereas high energy ions create the defective ion tracks without implanting [189,192,194]. The ion tracks not only create the defects but also rearrange the disordered atoms (due to the foreign elements doping or during the process of synthesis) in a regular way.

ZnO thin film is vastly using to tune its properties with the SHI irradiation process due to its high thermal stability and mechanical strength [189,191,193]. Sahoo et al. reported the surface morphological changes (smoothening of surface), increased crystalline and conducting properties of Al doped ZnO thin films with H^+ irradiation by varying the ion fluences [190,195]. S. Mal et al. reported the induced ferromagnetism in undoped ZnO thin films by creating the lattice disorder leading to the enhancing of Zinc and oxygen vacancies (produce magnetic moments) with high energy (300 MeV) Ag^{9+} SHI irradiation [193]. Kumar et al. achieved the drastic decrease in resistivity and increased carrier concentration in ZnO thin films irradiated with electronic stopping power of 120 MeV Au ions [191]. K. Thangaraju et al. analysed the stability of organic semiconducting material (Alq_3) with SHIs of 40 MeV Li^{3+} irradiation and reported the quenching of PL emission with the ion fluences [56,196]. H. A. Khawal and B. N. Dole reported that the Mn doped ZnO thin films exhibit the enhanced crystallite size, PL emission and conductivity with 160 MeV Ni^{7+} SHI irradiation [194]. Zn is very suitable for ion radiation due to its potential creation of Zn interstitials and O vacancies. In this study, we have

made an attempt to tune the properties of solution processed Alq_3/ZnO hybrid thin by 120 MeV Ni^{7+}SHI irradiation for their optoelectronic applications.

5.2. Experimental details

5.2.1. Preparation and SHI irradiation of Alq_3/ZnO hybrid thin films

The Alq_3/ZnO hybrid thin films were prepared following our previous reports [156,197]. Out of the three Alq_3/ZnO hybrid films (**b – d**), film **b** was chosen for the ion irradiation due to its advantageous film properties such as improved crystalline properties and optical transmittance, considerable decrease in the sheet resistance, enhanced PL emission, fast response in UV photodetector due to predominantly presence of Alq_3 molecules on the film surface. To further improve film characteristics and UV photoresponses, the film **b** with Alq_3/ZnO molar ratio of 0.5×10^{-3} was irradiated with the Ni^{7+} SHI irradiation.

The hybrid films were prepared with Alq_3/ZnO molar ratio of 0.5×10^{-3} [ZnO (80 vol.%) (0.4 M) + Alq_3 (20 vol.%) (2×10^{-4} M)] following the procedure mentioned in the chapter 3 and 4. The films coated on glass substrates were cut into 1×1 cm^2 area for three different ion influences. The three Alq_3/ZnO films were irradiated with 120 MeV Ni^{7+} SHI with the ion fluences of 5×10^{11}, 1×10^{12}, and 5×10^{12} respectively at room temperature. It was observed from the SRIM (Stopping Range of Ions in Matters) calculations that there is no implantation of Ni ions in irradiated films [198]. Since the films are irradiated with electron stopping power of 120 MeV the ions create the ion tracks and loses their energy through electronic excitation (electronic energy loss: S_e) or ionization of atoms in the film. The optical, structural, morphological, and electrical properties of pristine and irradiated Alq_3/ZnO hybrid films were characterized using various characterization techniques. Further to investigate the Ni^{7+} SHI irradiation effect on UV light detection of Alq_3/ZnO hybrid thin films, the UV photodetectors were fabricated. The fabrication process was followed by coating the two Al contacts for the ohmic contacts using thermal evaporation vacuum coating unit at a high vacuum of ~ 5×10^{-6}

mbar. The current -voltage (I-V) characteristics were carried out under dark and UV light using SMU (Keithley, 2450). The response characteristics were also measured by alternatively varying the UV light illumination in ON/OFF states for each 30 s.

5.2.2. Instrumentation and irradiation process of SHI

The 15 UD pelletron is a versatile, heavy ion tandem type of electrostatic accelerator. In this accelerator, negative ions are produced and pre-accelerated to ~300 keV in the ion source and injected into strong electrical field inside the accelerator tank filled with insulating gas, sulphur hexa fluoride (SF6). At the centre of the tank, there is a terminal shell maintained at a high voltage of ~15 MV. The negative ions on traversing through the accelerating tubes from top of the tank to the positive terminal get accelerated. On reaching the terminal, they pass through a stripper, which removes some electrons from the negative ions, thus transforming the negative ions into positive ions. These positive ions are then repelled away from the positively charged terminal and are accelerated to ground potential to the bottom of the tank. The positive ions exit from the tank are bent into horizontal plane by analysing magnet, which also selects a particular beam of ion. The switching magnet diverts the high energy ion beams into various

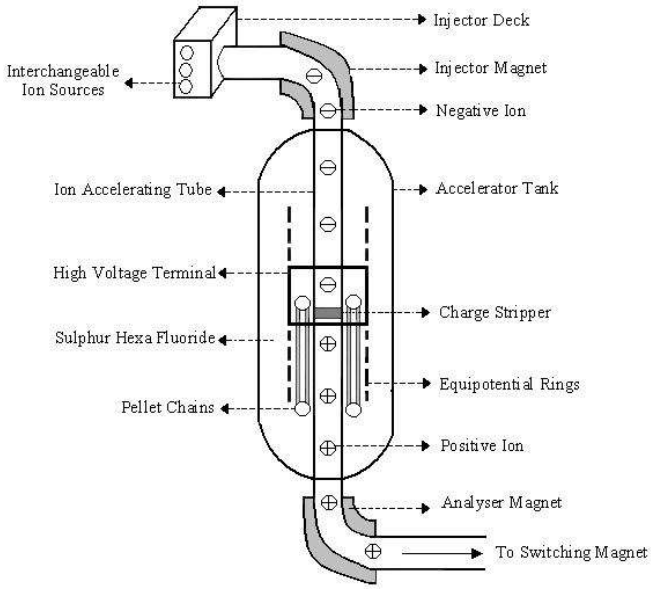

Fig. 5.1. Schematic of 15 UD pelletron, a heavy ion tandem type of electrostatic accelerator.

beam lines for the different experiments. Beamlines provide the facility to perform swift heavy ion beam irradiation experiments (Kanjilal et al 1993). The schematic of 15 UD pelletron accelerator at the Inter-University Accelerator Centre (IUAC), New Delhi is shown in the figure 5.1 SHI irradiation chamber is shown in Fig 5.2.

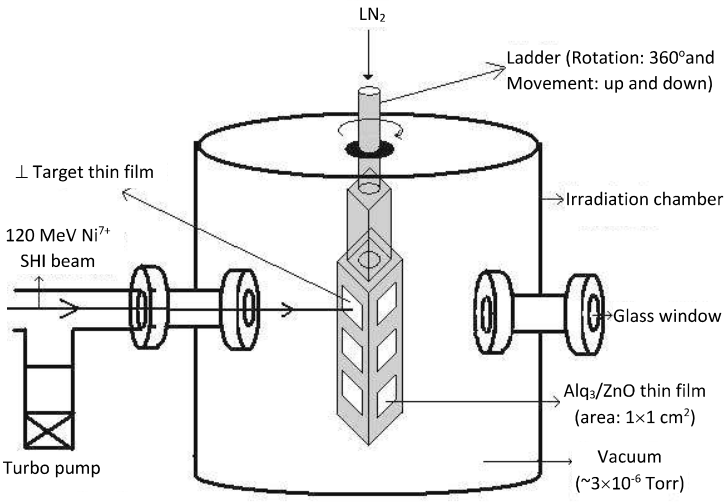

Fig. 5.2. Schematic of SHI irradiation chamber.

5.3. Results and discussion

5.3.1. Optical properties

The optical transmittance was recorded at room temperature using UV-Vis spectroscopy instrument in order to determine the irradiation effect on the transmittance of Alq_3/ZnO hybrid films. The Fig. 5.3(i) shows the transmittance spectra of Alq_3/ZnO hybrid films irradiated with the ion fluences of pristine, 5×10^{11}, 1×10^{12}, and 5×10^{12} ions/cm^2 in the wavelength range of 300 – 900 nm. The transmittance values in the UV region at 365 nm were tabulated in Table 5.1, the transmittance is observed to be decreased with the ion fluences which reveals the increase of absorption in the UV region at 365 nm, this will be the advantageous property for the UV photodetector applications. The films also exhibit the decreased transmittance in the visible region with increasing the ion fluences. With reference to earlier reports, it is assumed

that the decrease in transmittance is probably due to the scattering of light photons by the defects or ion tracks created during irradiation [192,195]. The optical bandgap (direct bandgap) (E_g) of the SHI irradiated Alq_3/ZnO hybrid thin films was estimated from the transmittance data using the following formula:

$$(\propto h\upsilon)^2 = A(h\upsilon - E_g), \quad (5.1)$$

where hυ is the photon energy, α (α = 2.303(1/T)/t, T - Transmittance, t - Thickness of the film) is the optical absorption coefficient of the film, and A is the constant. Figure 5.3(ii) reveals the tauc plot drawn between hυ and $(\propto h\upsilon)^2$ in order to estimate the optical band gaps by extrapolating the linear portion of $(\propto h\upsilon)^2$ against to the hυ plot to the point where $\propto = 0$. There is no much change in the band gap with the ion fluences, revealing that the ion fluence is not much affecting the band gap. The slight decrease in the band gap with the ion fluence is due to the quantum confinement effect [54,133].

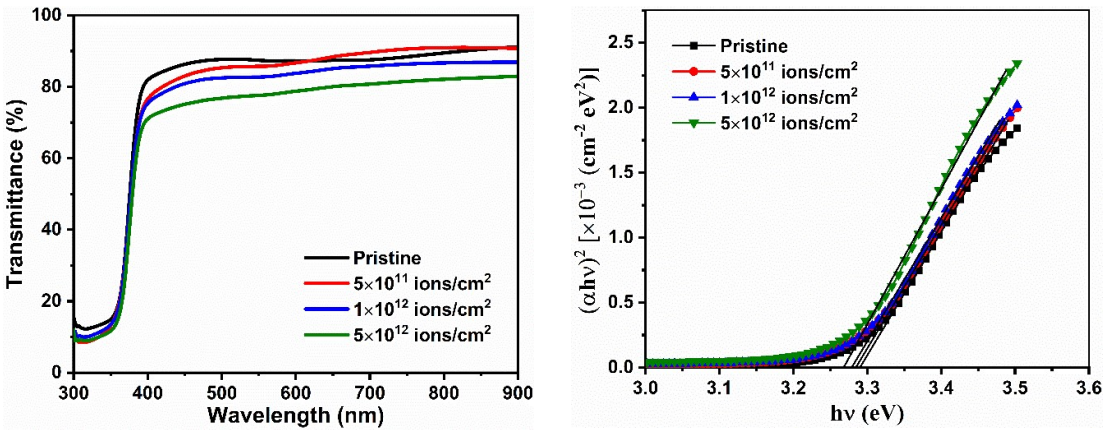

Fig. 5.3. (i) Optical transmittance and (ii) band gap estimation Tauc plot of pristine and Ni^{7+} SHI irradiated Alq_3/ZnO hybrid thin films with the ion fluences of **5×10^{11}, 1×10^{12}, and 5×10^{12} ions/cm^2**.

5.3.2. Crystalline properties

The SHI irradiation alters the crystalline properties of thin films immensely. The hit ions create the ion tracks or latent tracks which order or disorder the atomic arrangement. In order to understand the irradiation effect on crystalline properties, the XRD-characterization

was recorded at room temperature the diffraction angle in the range of 10° - 80° with step angle of 0.0083° using Cu K-Alpha X-Rays. The Fig. 5.4 (i) represents the XRD spectra of pristine and irradiated Alq_3/ZnO hybrid thin films. The XRD patterns show that pristine ZnO film exhibits the diffraction peaks at 31.78° (100), 34.36° (002), and 36.35° (101) consistent with the JCPDS Card Nos.: 36-1451and 75-0576, exhibiting the good crystalline properties with hexagonal wurtzite structure and space group of P63mc [134,139]. The irradiated films also exhibit the reflect the diffraction peaks at the same position reveals the no phase change. All the films exhibit the highly textured along the (0 0 2) plane compared to the other hkl planes conveying the c-axis orientation perpendicular to the substrate surface [80,129,139]. The c-axis orientation is due to the highest density of Zn atoms with preferential growth along (0 0 2) plane [80,130]. The c-axis orientation with hexagonal wurtzite structure exhibits the higher stability than cubic structure and perform the improved photo detecting responses [47,134]. The achieved single-crystalline ZnO thin film with the simple spin-coating technique is the best fit for the fabrication of low-cost UV photodetectors and other optoelectronic device application. The crystallite size for the films at (0 0 2) plane has been estimated by the following Debye-Scherrer's formula and the values were mentioned in Table 5.1

$$D = 0.94\lambda / \beta \cos\theta, \quad (5.2)$$

where D is the crystallite size, λ is the X-ray wavelength (1.5046 Å), β is the full-width half maxima (FWHM) and θ is the diffraction angle. The crystallite size of Alq_3/ZnO thin films is observed to be increased with the ion fluences of 5×10^{11}, 1×10^{12} ions/cm^2 and it is considerably decreased for the highest ion fluence of 5×10^{12} ions/cm^2. The SHI irradiation creates the ion tracks in the film which may order or disorder the atomic arrangements depending on the ion fluences. The Alq_3 incorporation with the Alq_3/ZnO molar ratio of 0.5×10^{-3} may create the stress by disordering the atomic array. The SHI irradiation with the ion fluences of 5×10^{11}, 1×10^{12} ions/cm^2 release the stress, resulting in increased crystallite size [189,192]. The stress increased in the atomic array due to heavy ion fluences of 5×10^{12} ions/cm^2 leads to the decreased

crystallite size. The textured coefficients of the films were calculated using the following formula from the XRD data,

$$TC = \frac{I_{hkl}/I_{0hkl}}{\frac{1}{N}\Sigma I_{hkl}/I_{0hkl}} \quad (5.3)$$

where I_{hkl} is the measured intensity, I_{0hkl} is the standard intensity from JCPDS file, and N is the total number of reflections observed in the XRD pattern of the respective thin film. The Fig. 5.4 (ii) represents the variation of texture coefficients of hkl planes with the ion fluences. All the films highly textured along the (002) plane representing the c-axis orientation perpendicular to the substrate surface. The TC of (002) plane is increased up to the ion fluence of 1×10^{12} ions/cm^2 and decreased for the high ion fluence of 5×10^{12} supporting the variation of crystallite size with the ion fluences. The dislocation density and lattice strain are the important parameters used to estimate the magnitude of defects. The dislocation density (δ) is defined as the length of dislocation lines per unit volume of crystal. It is calculated for pristine and irradiated hybrid films using the following equation [194,199]. The estimated values are given in Table 5.1

$$\delta = n / D^2 \ (3) \quad (5.4)$$

where δ is the dislocation density, n (=1 for minimum dislocation density) is the factor, and D is the crystallite size. The strain induced in the lattice sites due to the lattice mismatch in the crystalline material is called as lattice strain (ε) and it is estimated from the Williamson-Hall equation [199,200].

$$\varepsilon = \beta_{hkl}/4 \tan\theta \quad (5.5)$$

The dislocation density and lattice strain are decreased till the ion fluences of 1×10^{12} ions/cm^2 and a drastic hike is observed for 5×10^{12} ions/cm^2 attributing the stress release to some extent of ion fluence. Based on the XRD results we endorse that the stress due to the incorporation of Alq_3 is released with increasing the regularity of atom for the ion fluences of 5×10^{11}, 1×10^{12} ions/cm^2. The more ion fluence of 5×10^{12} ions/cm^2 may create the irregularities in atomic order leading to the more stress and decreased crystallite size [189,192].

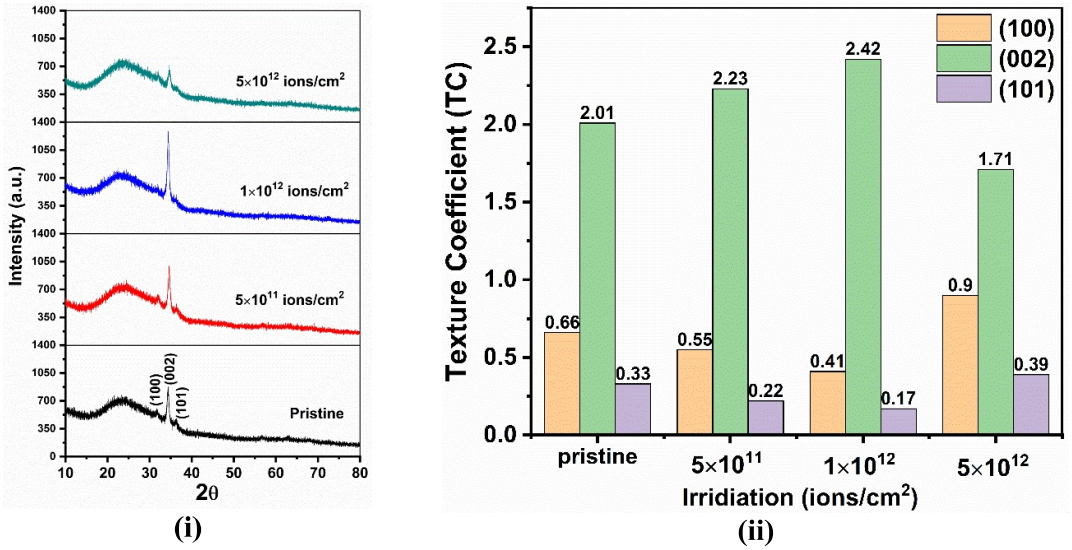

Fig. 5.4. (i) XRD Spectra and (ii) variation of texture coefficient with respect to ion fluences of pristine and irradiated Alq_3/ZnO hybrid thin films.

5.3.3. Topography studies

The three-dimensional surface topography of pristine and irradiated Alq_3/ZnO composite films was recorded at room temperature using AFM over the scanning area of 5 and 20 μm^2as shown in Fig. 5.5 (i) and (ii). Generally, the sol-gel spin coated ZnO thin film exhibits the wrinkle kind (root like) morphology [137]. The pointed like structure perpendicular to the substrate surface of all the films is due to incorporation of Alq_3 molecules into ZnO. The Alq_3 molecules convert the wrinkle pattern into densely packed well defined ZnO crystalline grains grown perpendicular to the substrate surface with uniform distribution. The dopant element modifies the wrinkle kind morphology of ZnO thin film with uniform distribution of pointed type grains perpendicular to the substrate surface [139,140,201]. The point-like structure instead of root like structure is attributing the predominantly presence of Alq_3 molecules over the ZnO as observed from XPS studies given in the previous chapter 4. The Alq_3/ZnO hybrid thin films with the ion fluences of 5×10^{11}, 1×10^{12} ions/cm^2 exhibit the agglomeration of point-like structures with small grain growth leading to the slight increase in the root-mean-square roughness (R_{rms}) [194,201]. During the irradiation the ion beam generates the local heat in the

collision process, this local rise in temperature is sufficient for the grain growth resulting in increased crystallite size [190,194,195]. The agglomeration of these microstructural grains is attributing the rearranging of atoms due to the ion tracks created by SHI ion irradiation [194]. The film with 5×10^{12} ions/cm^2 fluence exhibits the agglomeration of grains and its growth with increased rate leading to the ununiform distribution of grains resulting in high surface roughness [190,194]. The massive agglomeration of grains increases the grain boundaries and hence surface roughness ascertains the decreased crystallite size from XRD studies. The root-mean-square surface roughness values were mentioned in Table 5.1.

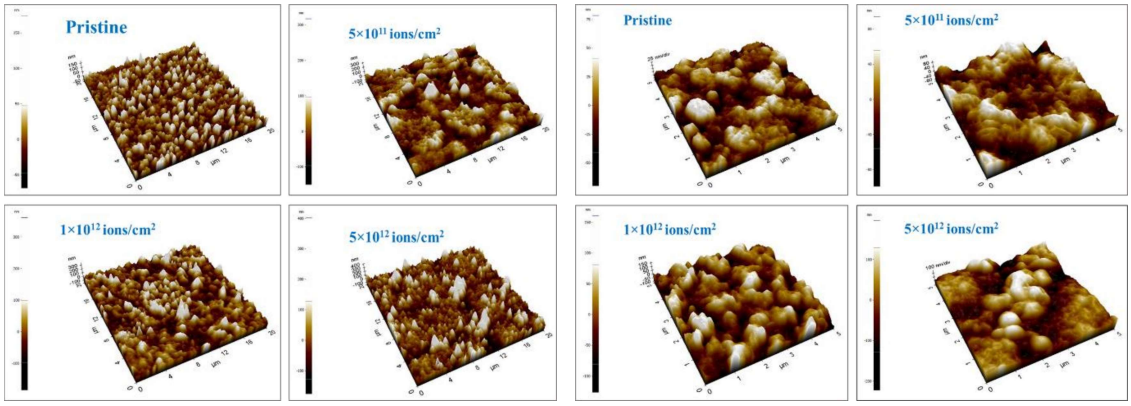

Fig. 5.5. AFM topography of pristine and irradiated Alq_3/ZnO hybrid thin films at (i) 20 µm and (ii) 5 µm scanning area.

5.3.4. Photoluminescence studies

In our previous report (chapter 3) we described that the PL emission (near band edge) is observed to be enhanced with the incorporation of Alq_3 in ZnO due to the energy transfer from Alq_3 to ZnO via carbonyl (C=O) group [156]. This chapter describing the irradiation effect on Alq_3/ZnO hybrid thin films. Majorly the SHI ion irradiation creates the defects in the film leading to the defect related emission [192,194]. The PL emission is the crucial characterization in order to study the various defect related emissions. The Fig. 5.6 shows the PL spectra of pristine Alq_3/ZnO and Ni^{7+} SHI irradiated Alq_3/ZnO films with the ion fluences of 5×10^{11}, 1×10^{12}, and 5×10^{12} ions/cm^2. The PL spectra were recorded at room temperature by exciting

the films with 340 nm wavelength using xenon lamp. All the films exhibit the ZnO characteristic near band edge emission (NBE) in the UV region and defect emission or deep level (DL) emission in the visible region. The NBE emission is related to free-exciton recombination and DL emission is related to the defects present in the film [149,154]. The crystal defects in ZnO are due to the interstitials oxygen (O_i), oxygen vacancies (V_O), interstitials Zinc (Zn_i), Zinc vacancies (V_{Zn}), and antisite oxygen (O_{Zn}) [139,145,202]. From the spectra (Fig. 5.6) it is observed that the NBE is decreased with enhanced DL emission up to the ion fluences of 5×10^{11} ions/cm^{2}conveys the creation of defects due to the SHI irradiation. The enhanced defect emissions are related to the V_O (~520 – 565 nm), O_i (~580-620 nm), O_{Zn} (~620 – 640 nm) [202,203]. The broadening of NBE emission with decreased peak intensity represents the increase of Zn_i (~395-435) states. For the high ion fluence of 5×10^{12} ions/cm^2, the NBE is drastically suppressed with a slight enhance in the DL emission in comparison with pristine Alq_3/ZnO hybrid thin film. The PL spectra manifests that the V_O and Zn_i are enhanced with the ion fluences of 5×10^{11}, 1×10^{12} ions/cm^2 and get diminished for 5×10^{12} ions/cm^2. The V_O and Zn_i enhance the free carriers so, it is expected that the ion fluences of 5×10^{11}, 1×10^{12} ions/cm^2 heightens the carrier density and hence conductivity of the films which will be efficacious for optoelectronic device applications [152,204]. Further the ion fluence of 5×10^{12} ions/cm^2 drastically declines the PL emission supporting the decreased crystallite size from XRD. The decreased crystallite size due to the structural defects may causes the non-radiative transitions which decreases the PL emission [189,205,206]. The ion irradiation is highly influencing the Alq_3, which quenches the PL emission by generating the unstable cationic spices in the film [196,207]. Alq_3 enhance the NBE of ZnO due to the energy transfer from Alq_3 to ZnO [156]. Hence, the Alq_3 also plays a role in affecting the NBE of ZnO. The NBE of Alq_3/ZnO film with ion fluence of 5×10^{11} ions/cm^2 is not altered revealing that the Alq_3 molecules are influenced at this ion fluence and the increased DL emission is related to the defects created in ZnO. The

two ion fluences of 1×10^{12} and 5×10^{12} ions/cm^2 may affect the Alq_3 in Alq_3/ZnO hybrid thin film which also a considerable reason for decreased NBE.

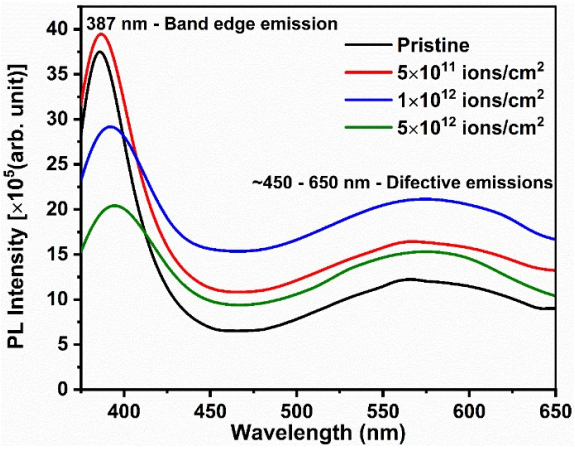

Fig. 5.6. Photoluminescence spectra of pristine and irradiated Alq_3/ZnO hybrid thin films.

5.3.5. Sheet Resistance

Sheet resistance measurement using four probe method is a simple and easy process in order to estimate the electrical properties of thin films. The sheet resistance of pristine and irradiated Alq_3/ZnO hybrid thin films was measured using Keithley SMU by four probe method at room temperature using the relation

$$R_s = [\pi/\ln 2]\,(V/I)\,k \qquad (5.6)$$

Where R_s is the sheet resistance, V is the voltage measured (between probes 2 and 3), I is the source current (between probes 1 and 4), and k (= 1) is the correction factor. The measured sheet resistance values are tabulated in Table 5.1 and the corresponding graphs also shown in Fig. 5.7. It is observed that the sheet resistance is decreased for Alq_3/ZnO hybrid thin films irradiated with the ion fluences of 5×10^{11}, 1×10^{12} ions/cm^2 and it is increased for 5×10^{12} ions/cm^2 [191]. The enhanced carrier density and mobility decrease the sheet resistance. From the PL spectra it is clear that the transitions corresponding to the Zn_i and V_O are increased which enhances the free carrier density and hence enhances the mobility [145,189]. The increased sheet resistance of Alq_3/ZnO composite film with ion fluence of 1×10^{12} attributed to the

diminished PL emission and crystallinity. The high ion fluence create the damages at the nano level in the film which alters the mobility of charge carriers and increase the sheet resistance [190,195]. Thus, with supporting of these characteristics it is ascertained that the conducting properties of Alq_3/ZnO hybrid thin films with the ion fluences of 5×10^{11}, 1×10^{12} ions/cm^2 are improved.

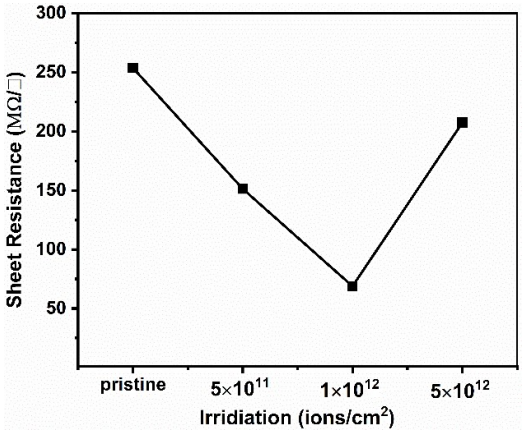

Fig. 5.7. Sheet resistance of pristine Alq_3/ZnO and Ni^{7+} SHI Irradiated Alq_3/ZnO hybrid thin films with the ion fluences of 5×10^{11}, 1×10^{12}, and 5×10^{12} ions/cm^2.

Table 5.1. Optical, structural, morphological, and electrical characteristics of pristine and 120 MeV Ni^{7+} SHI irradiated Alq_3/ZnO (molar ratio of $0.5x10^{-3}$) hybrid thin films.

Ni SHI Fluences (ions/cm^2)	Optical transmittance (%) at wavelength (nm)			E_g (eV)	Crystallite size (nm)	Dislocation density ($\times10^{14}$ lines/m^2)	Lattice Strain ($\times10^{-2}$) no unit	Surface Roughness at area (μm^2)		Sheet Resistance (MΩ/□)
	365	450	550					5	20	
Pristine	24	86	87	3.28	17.73	31.79	0.39	21.0	24.2	253
5×10^{11}	23	83	85	3.27	19.34	25.60	0.35	23.2	38.0	151
1×10^{12}	22	80	82	3.26	22.19	20.24	0.31	41.3	49.9	69
5×10^{12}	19	75	77	3.24	14.07	50.50	0.49	65.8	65.3	207

5.3.6. UV photodetector characteristics

With the motivation of above encouraging characteristics of SHI ion irradiated films, it is aimed to understand the UV light detection responses in the devices. The UV photodetectors were fabricated based on pristine and Ni^{7+} SHI irradiated Alq_3/ZnO hybrid thin films with the ion fluences of 5×10^{11}, 1×10^{12}, and 5×10^{12} ions/cm^2. Two Al layers were coated onto the pristine and irradiated Alq_3/ZnO hybrid thin films as ohmic contacts using thermal evaporation vacuum coating unit at high vacuum of 5×10^{6} mbar. The Al thin films were coated with the thickness of 120 nm by covering with a metal mask so as to fabricate the device with the area of 0.08 cm^2. The schematic device structure of UVPDs based on irradiated Alq_3/ZnO hybrid films is shown in Fig 5.8. The fabricated device structures are as follows:

Device A: Glass substrate/pristine (Alq_3/ZnO)/Al

Device B: Glass substrate/(Alq_3/ZnO film irradiated with Ni SHI fluence of 5×10^{11})/Al

Device C: Glass substrate/(Alq_3/ZnO film irradiated with Ni SHI fluence of 1×10^{12})/Al

Device B: Glass substrate/(Alq_3/ZnO film irradiated with Ni SHI fluence of 5×10^{12})/Al

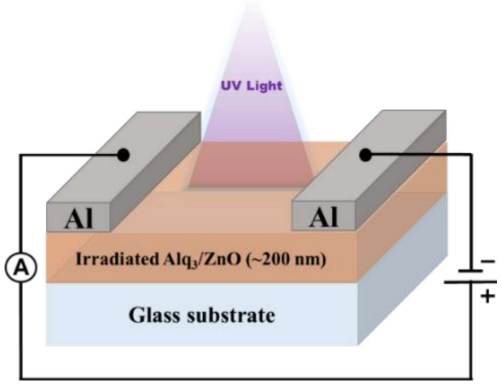

Fig. 5.8. Schematic of UVPD device structure based irradiated Alq_3/ZnO hybrid thin films.

The current density (J)-voltage (V) characteristics were performed using voltage/current source measure unit (SMU: Keithley, 2450 model) in dark and under UV-spot light illumination (wavelength: 365 nm, power: 1 mw/cm^2) biasing from -8 V to +8 V under the normal ambient. The Fig. 5.9(i) shows the semi-log plots of J-V characteristics. It is observed that, devices

exhibit the several orders of light current higher than the dark currents, attributed to the good UV responses of pristine and irradiated Alq_3/ZnO hybrid thin films. The response of the devices is same on both the sides of the voltage biases (-Ve to +Ve) revealing the ohmic nature of devices. The devices exhibit the same trend in both dark and UV light conditions showing the increased current density for the ion fluences of 5×10^{11} (device B) and 1×10^{12} ions/cm^2 (device C) and it is decreased for the high influence of 5×10^{12} ions/cm^2 (device D) compared to the pristine based device. The enhanced current density for the devices B and C compared to the device A is predominantly due to the increase in Zn_i and V_O (each provide the two free electrons) which enhance the free carriers enormously in ZnO based thin films [190,195,205]. The increased crystallite size is also supporting for the same which facilitate the mobility of the charge carriers [190]. The enhancement of conducting properties is supported by decreased sheet resistance for the two ion fluences of $5\times10^{11}$and 1×10^{12}ions/cm^2 ascertaining the increased current density of device B and C [190,195]. The decresed current density of device D is due to the nano level damages (defects) in the film because of swift heavy ion fluence of 5×10^{12} ions/cm^2, attributed to reduced crystallite size and increased sheet resistance [192,208].

The photocurrent, gain, responsivity, and sensitivity are the important parameters for the characteristic analysis of UV photodetector [68,183]. These parameters were calculated at 1 V bias and 1mW/cm^2 UV illumination intensity following below formulae [68,134]. Values are tabulated in Table 5.2.

$$\text{Photocurrent gain (G)} = I_{light}/I_{dark} \quad (5.7)$$

$$\text{Sensitivity(S)} = I_{ph}/I_{dark} \quad (5.8)$$

$$\text{Responsivity(R)} = I_{ph}/\text{ P.A} \quad (5.9)$$

$$\text{Detectivity(D)} = (I_{ph}/E)\,(2qI_{dark})^{1/2} \quad (5.10)$$

where I_{dark} - dark current,I_{light}– current under UV light, I_{ph} (I_{light}- I_{dark}) – photocurrent, P - power of UV light, and A - effective area of device.

The photocurrent (I_{light}- I_{dark}) is due to the excitons generated by the UV illumination whereas the dark is due to the free carriers present in the film. The enhanced photo current for the devices B and C reveals the good response of Alq_3/ZnO hybrid films with the ion fluences of $5\times10^{11}$and 1×10^{12} ions/cm^{2}to the UV light. The creation of large nano level damages in the film may obstruct the exciton generation for the device D with the ion fluences of 5×10^{12} ions/cm^2. Current gain and sensitivity are propositional parameters which are observed to be enhanced for the devices (B and D) up to the ion fluences of 1×10^{12} ions/cm^2 (gain: 543.34) compared to the pristine Alq_3/ZnO based device (A) (gain: 351.41). The device D exhibits less gain (260.28) compared to the other devices. The current gain (I_{light}/I_{dark}) of the devices are increased at low dark and/or high light currents [134,187]. In the devices B and C, they are not exhibiting the low dark currents compared to the pristine film-based device (A) but due to the high improvement in the light current the gain is increased. Device D is exhibiting the low dark current and less light current, showing less current gain when compared to the other devices. Responsivity (I_{ph}/ P.A) is defined as the photocurrent per unit area and light intensity [134]. Since it is a proportional factor to the photocurrent it is varying accordingly with the photocurrent. It is enhanced for the devices with ion fluences of 5×10^{11} (4.14 mA/W) and 1×10^{12} ions/cm^2 (7.51 mA/W) and reduced for 5×10^{12} ions/cm^2 (2.39 mA/W) compared to the pristine film-based device A (12.72 mA/W).

Response speed and repeatability are the two important parameters in order to know the photoresponse of the UV photodetectors. The Fig. 5.9 (ii) shows the current density variations with respect to the UV light (1 mW/cm^2) illumination ON and OFF states following the regular intervals of time of 30 sec at constant bias of 1 V. In the ON state the devices exhibit the high current and OFF state low current revealing the stability and reproducibility of all the devices **(A-D)**. In Fig. 5.9 (ii), the anomaly in the current densities during the first two cycles is due to the lower electric fields, since the devices were measured at 1V. For the third cycle it is diminished due to the formation of proper carrier tracks during the first two cycles. The growth

time τ_g and decay time τ_d, (defined as the time required for the photocurrent to increase from 10% to 90% and drop from 90% to 10% of the maximum current) were calculated from the response plots, values are mentioned in the Table 5.2. The ion irradiation films-based devices (**B-D**) exhibit the fast responses with less τ_g and τ_d compared to the pristine Alq_3/ZnO film-based device (**A**). The delay in the growth and decay times may be due to the charge trapped states present in the films and also the presence of photo-persistent current (PPC-existent of current even after the light is OFF) in the devices [69,187,209]. The large τ_g and τ_d are relating the presence of large charge trapped states in the pristine Alq_3/ZnO film-based device (**A**). The ion irradiation may collapse the charge trapped states in the collision process to some extent which may lead to the fast responses of the devices [69,187]. Even the better crystallinity of films for devices **B** and **C** also reduce the charge trapped states resulting in the fast responses than device **A**. For the device **D** case even though the crystallinity is less due to the high ion fluence the charge traps may get diminished resulting in less time constants. With this it is confirmed that the Ni^{7+} SHI irradiation on Alq_3/ZnO hybrid thin films improve the UV photo detecting properties of UVPDs for the ion fluences of 5×10^{11} and 1×10^{12} ions/cm^2. The ion fluence of 1×10^{12} ions/cm^2 is considered as the threshold influence of Ni^{7+} SHI for the better crystallinity, photoluminescence, electrical, and UV photoresponses.

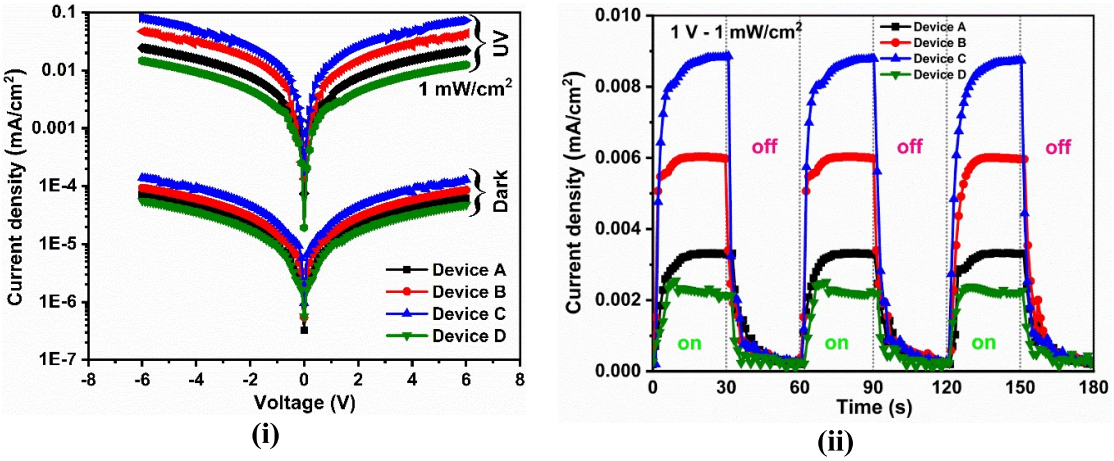

Fig. 5.9. (i) Current density–voltage (J–V) and (ii) time-dependent photo response characteristics of fabricated UV-photodetectors based on pristine Alq_3/ZnO (device **A**) and Ni^{7+} SHI irradiated Alq_3/ZnO (devices **B -D**) hybrid films.

Table 5.2. Device characteristics of UV photodetectors based on pristine Alq_3/ZnO (device **A**) and Ni^{7+} SHI irradiated Alq_3/ZnO (devices **B -D**) hybrid thin films at 1V bias and UV light power of 1 mW/cm^2.

Device	Ni SHI influence Ions/cm^2	Photocurrent density (J_{ph}) (μAcm^2)	Current gain (G)	Responsivity (R) (×10^{-3} A/W)	Detectivity (D) (×10^{10})	Response time (s)	
						growth	decay
A	Pristine	0.33	351.41	4.14	0.05	9.04	12.1
B	5×10^{11}	0.60	477.59	7.51	0.11	2.49	8.08
C	1×10^{12}	1.02	543.34	12.72	0.10	4.67	5.81
D	5×10^{12}	0.19	260.28	2.39	0.22	3.75	6.63

5.4. Conclusion

Based on the pristine and Ni^{7+}SHI irradiated Alq_3/ZnO hybrid thin films it is confirmed that the transmittance is slightly decreasing with the ion fluences by the scattering of light photons at the ion tracks created by the SHI irradiation. The crystallite size is increased up to the ion fluence of 1×10^{12} ions/cm^2 which may be due to the reordered of atomic array in the film. The PL emission is improved with gradual enhancement in the defect level emissions related to the Zn_i and V_O which enhance the free carriers. The decrease in sheet resistance up to the ion fluence of 1×10^{12} ions/cm^2 attributed to the increased crystallite size. The Ni^{7+} SHI irradiation with the ion fluences of 5×10^{11} and 1×10^{12} ions/cm^2 facilitating the UVPD responses with improved photocurrents, gain, and fast responses. We conclude that the Ni^{7+} SHI irradiation of Alq_3/ZnO hybrid thin films with the threshold influence of 1×10^{12} ions/cm^2 will be fruitful for UV photodetector applications.

Chapter: 6

Strategy to improve the performance of organic light emitting diode by annealing of ITO anode at higher temperature

This chapter describes the annealing effect on optical, structural, electrical, and morphological properties of ITO thin film. The ITO substrates were annealed at 200 ℃, 300 ℃, and 400 ℃ and were characterized using various characterization techniques. This chapter gives the detailed analysis on improved quality of annealed ITO at higher temperature. The improved quality of ITO film is utilised in order to improve OLED device performances. Before the utilising it in OLEDs the hole injection property of ITO is studied by fabricating the hole-only devices (HODs) with the device structure of ITO (pristine of annealed ITO)/TPD/Al, where the N,N′-Bis(3-methylphenyl)- N,N′-diphenylbenzidine (TPD) is used as a highly efficient hole transporting material. The HODs revealed that the annealed ITO at 300 ℃ is efficiently injecting the holes into the devices, improving the device current density.

6.1. Introduction

Organic light-emitting diodes (OLEDs) have widely been used in the recent past for their potential use in the next generation flat-panel displays, solid-state lighting, and other applications due to its self-emission, high luminous efficiency, ease of large area device fabrication, low cost, high color contrast ratio, fast response time, and wide color gamut [210–214]. Achieving the higher efficiency of OLEDs of different colors is the most important for the OLEDs to be used in the next-generation commercial organic electronic devices [213–215]. One of the several factors causing the decay in the efficiency and failure of organic electronic devices is the surface quality and/or bulk properties of indium tin oxide (ITO) films (anode electrode) in the devices [216–218]. ITO, one of the most commonly used transparent conducting oxides (TCOs), is an n-type degenerate semiconductor material and, due to its high

electrical conductivity and transparency to visible light, it is used as transparent electrode in OLEDs, OPVs, photo-transistors, lasers, and transparent coatings for solar energy heat mirrors. Because of its high work function, ITO is used as the anode contact for hole-injection into organic material in the OLEDs [219,220]. Since the organic thin film is in direct contact with ITO film, the surface properties of the ITO thin film are expected to directly affect the hole-injection characteristics in the OLEDs [221]. The as-deposited ITO thin-film anode has been reported to be less efficient for hole injection in OLEDs, resulting in hole-limited device [221–223]. It has widely been reported that the surface-modified ITO films by gas plasma- or UV-ozone-treatments have exhibited the enhanced hole injection/transport in the OLEDs [221,224–226]. Kim et al. have studied the thermal behaviour of ITO thin films deposited by RF magnetron sputtering by annealing in the air, because the thermal effect of ITO anode in the electronic devices is expected under high electric field conditions during the device operation [219]. It has been reported using Hall-effect measurements that the diffusion of oxygen into oxygen interstitials and oxygen vacancies decrease the carrier concentration blow 250 °C and the chemisorption of oxygen into grain boundaries causes the decrease in the carrier concentration and carrier mobility above 250 °C. Therefore, it is very important to understand the thermal effect of ITO thin film on its surface properties to affect the hole-injection properties at ITO/organic interface in the organic electronic devices, such as OLEDs.

6.2. Experimental details

Indium-tin-oxide (ITO) (~200 nm thick) coated glass substrates (TECHINSTRO, ITO-TIX005) were ultrasonically cleaned in acetone for 10 min followed by isopropyl alcohol (IPA) and deionized water, dried in each step at 100 °C in vacuum oven for 10 min to remove the solvent used, finger prints, and other contaminations onto the ITO surface. ITO coated glass substrates were annealed under the normal ambient for 60 min at 200, 300, and 400 °C, respectively. The optical transmittance of pristine and annealed ITO films was measured using

UV–visible spectrophotometer (LABINDIA Analytical Instruments Pvt. Ltd., UV-3092 model). The sheet resistances of the ITO films were measured under the ambient condition using Keithley's SMU instrument (2450 model) by four-point collinear probe method. The electrical properties, such as charge carrier concentration, mobility, and resistivity, were determined using Hall-effect measurement setup (ECOPIA-HMS 3000) at room temperature. The surface morphology and surface roughness of pristine and annealed ITO films were studied using scanning electron microscope (SEM; TESCAN, VEGA3 LMU model) and atomic force microscopic (AFM; Park Systems XE-70 model) techniques. The X-ray diffraction (XRD; PANanalytical, X'Pert PRO model) experiments were carried out at room temperature to study the crystalline quality of ITO films after annealing at different temperatures. The work functions of the pristine and annealed ITO films were measured by obtaining the contact potential difference (CPD) using ultrahigh vacuum compatible reed-type Kelvin Probe setup with a sensitivity of better than 0.1 mV (the work function of the reference gold electrode is assumed to be 5.1 eV) [227]. ITO thin films were patterned by chemical etching (zinc powder and HCL) with a strip width of 5 mm and cleaned thoroughly by the same procedure to be used as anode in the devices. The hole-only devices (HODs) having the structure of the patterned ITO (Pristine and annealed)/N,N′-Bis(3-methylphenyl)-N,N′-diphenylbenzidine (TPD) (Sigma-Aldrich, Catalogue No.: 443263) as hole transport layer (HTL) (60 nm)/Al (120 nm) were fabricated by thermal evaporation process under a vacuum of ~5×10^{-6} Torr. Al electrode was deposited using a metal mask so as to have the device area of 5 mm^2. The current density–voltage (J–V) characteristics of the fabricated HODs were measured using the current/voltage source/ measure unit (Keithley's SMU unit 2450 model) at room temperature.

6.3. Results and discussion

6.3.1. Optical Transmittance

ITO thin films coated on glass substrates were annealed at different temperatures (200, 300, and 400 °C) under the normal ambient for 60 min. The optical transmittance spectra of pristine and annealed ITO thin films in the wavelength range of 300–800 nm are shown in Fig. 6.1(i). The pristine ITO film shows the good transparency in the visible region. The transparency of the ITO film annealed at 200 °C is slightly increased to 80% (at 550 nm) when compared to that (75% at 550 nm) of pristine film, showing the improved film quality upon annealing. As the annealing temperature increases further, the transparency of the films decreases (72% at 550 nm for 300 °C; 66% at 550 nm for 400 °C) below that (75%) of the pristine film, which is attributed to the formation of light absorbing/scattering centers upon annealing at higher temperatures [219].

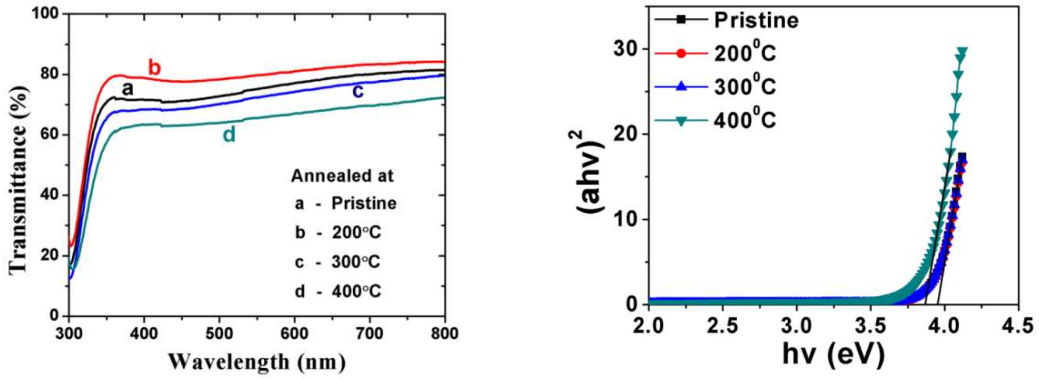

Fig. 6.1. (i) Optical transmission spectra, and (ii) Tauc plot for band gap estimation of pristine and annealed ITO thin films at different temperatures (**200, 300, and 400 °C**) under the normal ambient.

The optical bandgap (E_g) of the direct band gap semiconductor ITO thin films is determined by the following formula:

$$(\propto h\upsilon)^2 = A(h\upsilon - E_g), \quad (6.1)$$

where hυ is the photon energy, α is the optical absorption coefficient of the film, and A is the constant. The figure 6.1(ii) shows the plot of $(\alpha h\upsilon)^2$ as a function of the photon energy (hυ).

The optical band gap (E_g) can be obtained by extrapolation of linear portion of $(\alpha h\upsilon)^2$ against the photon energy ($h\upsilon$) plot to the point where $\alpha = 0$. According to the reports published, the direct optical bandgap energy of the ITO has been in the range of 3.5–4.5 eV due to the degeneracy of the semiconductor oxides [228,229]. The pristine ITO thin film shows the optical band gap energy (E_g) of 3.95 eV (Fig. 6.1(ii)). It has also been observed from the graph that there is no significant decrease in the optical energy band gap (E_g = 3.95 eV) of the ITO thin films up to annealing at 300 °C but a slight decrease to 3.87 eV at 400 °C, which is attributed to increase in crystallite size due to the quantum confinement effect [230,231].

6.3.2. Electrical Properties

The sheet resistance values of pristine and annealed ITO thin films have been obtained (Fig. 6.2) by the four-point collinear probe technique using the relation.

$$R_s = [\pi/\ln 2]\,(V/I)\,k \qquad (6.2)$$

where σ is the sheet resistance, V is the voltage measured (between probes 2 and 3), I is the source current (between probes 1 and 4), and k (=1) is the correction factor. The pristine ITO film shows the sheet resistance of 92 Ω/□ and the film annealed at 400 °C film exhibits the highest value of 185 Ω/□ with a slight increase up to the annealing at 300 °C, as shown in Fig. 6.2, which is supported by the Hall-effect measurements.

The charge carrier concentration, mobility, and resistivity of pristine and annealed ITO thin films measured at room temperature by Hall-effect measurements in van der pauw configuration are shown in Fig. 6.2. All ITO films showed the Hall coefficients to be negative which confirms the n-type conductivity of the films. The pristine ITO film shows the Hall carrier concentration of 19.46×1020 cm^{-3}, and mobility of 248 $cm^2/(V\ s)$, whereas the lowest values of the carrier concentration (4.13×1020 cm^{-3}) and mobility [29.35 $cm^2/(V\ s)$] were obtained for the film annealed at 400 °C with a slight decrease of values up to the annealing at 300 °C as given in Table 6.1 (Fig. 6.2). ITO thin film annealed at 400 °C showed the highest

resistivity of 5.685×10^{-4} Ω cm when compared to that (1.46×10^{-4} Ω cm) of pristine ITO film, because the conductivity (the reciprocal of resistivity) is a function of the carrier concentration and the mobility. This result is consistent with the earlier reports published elsewhere, showing the increase in the resistivity of ITO thin films annealed in air or oxygen [232,233]. The slight decrease in the carrier concentration and mobility (which is mainly dominated by scattering of free electrons by charged donors, such as ionized tin impurities and oxygen vacancies) of ITO films as the annealing temperature increases up to 300 °C under the normal ambient can be attributed to the diffusion of oxygen into oxygen interstitials and oxygen vacancies (each vacancy donates two electrons) in the ITO thin film [219,234,235]. Frank et al. reported that the free electrons in the reduced state (at higher carrier concentration) are scattered by charged donors, such as ionized tin impurities and oxygen vacancies, whereas in the oxidized state (at lower carrier concentration), free electron scattering is caused by charge-neutral impurities [234]. Minami et al. have showed that as the carrier concentration of ITO thin film decreases upon the heat treatment in the air due to suppression of further oxygen diffusion because of the increase in the oxygen interstitials and the decrease in oxygen vacancies, the mechanism of scattering of free electrons by charged donors, such as ionized tin impurities and oxygen vacancies, changes to grain boundary scattering (scattering of free electrons at grain boundaries), which becomes the most dominant due to the oxygen atoms adsorbed (chemisorption) onto the grain boundaries and the surface [236]. In the oxygen adsorption model, Adachi et al. have reported that the oxygen atoms adsorbed onto the surfaces (oxygen chemisorption, which is more dominant in the thinner films) of ITO films cause the trapping of free electrons at the surfaces, resulting in a decrease in the charge carrier concentrations [237]. Kim et al. have also studied the thermal degradation behaviour of rf magnetron sputter deposited ITO thin film (550 nm thick) over the temperature range of 100–400 °C in the air and reported the similar kind of observations that the carrier concentration and carrier mobility decreased upon the heat treatment with a sharp decrease of mobility above 275 °C, suggesting

the changeover from ionized impurity scattering to grain boundary scattering [219]. Hence, the observed drastic decrease in charge carrier concentration and mobility of ITO film annealed at 400 °C (Fig. 6.2) may be attributed to a significant change in the grain boundaries and/or surface morphology, which facilitate oxygen adsorption or chemisorption, of the ITO thin films upon annealing at higher temperatures.

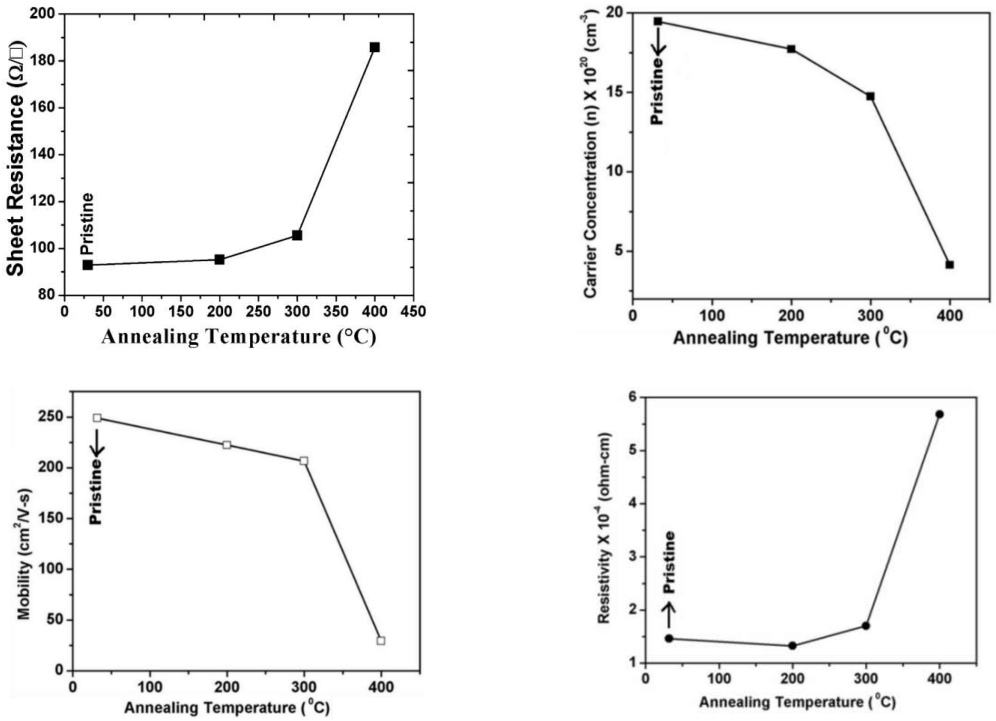

Fig. 6.2. Dependence of the electrical properties (Sheet resistance, hall carrier concentration, carrier mobility, and resistivity) of pristine and annealed ITO thin films.

Table 6.1. The Optical and electrical properties of pristine and annealed ITO thin films.

ITO Film	Optical Transmittance (%) @ 550 nm	(E_g) (eV)	Sheet Resistance (Ω/□)	Hall measurement values			Work function (eV)
				Resistivity ×10^4 (Ω-cm)	Carrier concentration ×10^{20} (cm^{-3})	Mobility [cm^2/(Vs)]	
Pristine	75	3.95	92	25.06	0.54	8.3	4.95
200 °C	80	3.95	95	22.90	0.51	8.4	4.97
300 °C	72	3.95	105	19.43	0.47	8.9	4.94
400 °C	66	3.87	185	17.33	0.44	30.8	4.98

6.3.3. Crystalline studies

To study the crystalline properties of ITO thin films upon annealing at different temperatures, the X-ray diffraction (XRD) measurements were carried out at room temperature on pristine and annealed ITO thin films and theXRD patterns are shown in Fig. 6.3(i). XRD pattern of pristine ITO film shows the good crystalline properties with diffraction peaks at 2θ (corresponding 'hkl' plane) = 30.66° (222), 35.69° (400), 50.95° (440), and 60.46° (622), consistent with reported data (JCPDS card No.: 06-0416), and it is also shown that all annealed ITO thin films are exhibiting the good crystalline properties without any change in the peak positions. The calculated full width at half maximum (FWHM) and crystallite size of pristine and annealed ITO films for (222) diffraction peak are shown in Fig. 6.3(ii). The crystallite size of pristine and annealed ITO thin films has been calculated using Debye–Scherrer's formula.

$$D = 0.94\lambda / \beta \cos\theta, \quad (6.3)$$

where D is the crystallite size, λ is X-ray wavelength (1.5406 Å), k = 0.94 is the correction factor, β is the FWHM of the diffraction peak (222), and θ is the diffraction angle of the diffraction peak (222). From Fig. 6.3(ii), it has been observed that the FWHM of the diffraction peak (222) of annealed ITO thin films is decreasing as annealing temperature increases, and thus, crystallite size is increased accordingly for the increasing annealing temperatures, which shows the improved film quality due to aggregation of native grains into the larger clusters upon annealing of ITO thin films under the normal ambient [238,239].

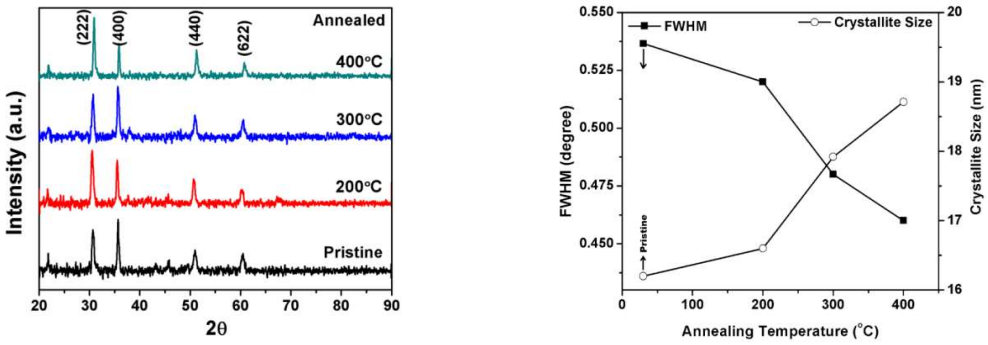

Fig. 6.3. (i) XRD patterns and (ii) full width at half maximum (FWHM) and crystallite size calculated from (222) diffraction peak of pristine and annealed ITO thin films.

6.3.4. Surface morphological studies

To examine the surface morphological features and surface roughness of ITO films upon annealing at different temperatures, SEM and AFM studies were carried out on pristine and annealed ITO thin films at different temperatures under the normal ambient. Figure 6.4(i)

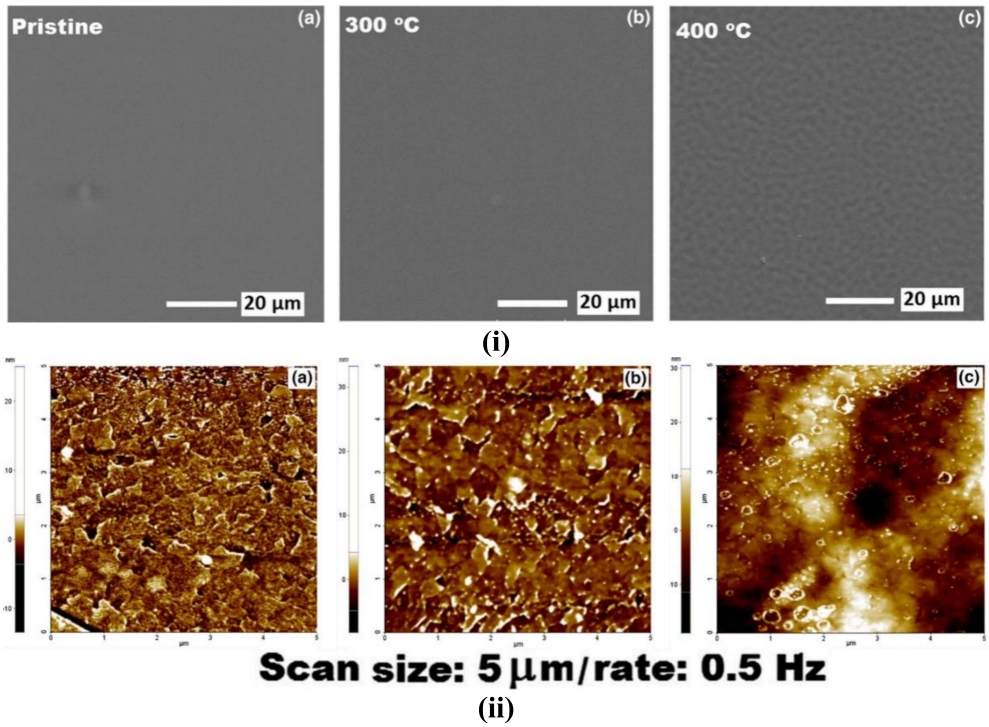

Fig. 6.4. (i) Scanning electron microscopic (SEM) images and (ii) Atomic force microscopic (AFM) topography of (a)pristine and annealed ITO thin films at different temperatures (b) 300 °C, and (c) 400 °C under the normal ambient.

shows the SEM micrographs of pristine and annealed ITO thin films. The smooth surface morphology has been observed for pristine as well as 300 °C annealed ITO thin films, whereas 400 °C annealed ITO film exhibited the wrinkle kind of surface morphology. Figure 6.4(ii) shows the AFM topography of pristine and annealed ITO thin films. It has been observed that microstructural grains observed on pristine ITO film grow with increasing annealing temperature, which is in agreement with the increase of crystallite size from XRD analysis for the increasing annealing temperatures. The root-mean-square roughness (R_{rms}) of the pristine ITO film (R_{rms} = 1.8 nm) slightly increases as the annealing temperature increases (R_{rms} = 2.3 nm for 300 °C annealed film). The observed increase of surface roughness

(R_{rms} = 5.8 nm) for 400 °C annealed ITO film when compared to that (R_{rms} = 2.3 nm) of 300 °C annealed film also supports the change in the surface morphology of 400 °C annealed ITO film, as is observed in the SEM analysis. The formation of wrinkling may be due to the fact that the film suffers a large amount of stress during annealing at higher temperature, giving rise not only to the bending of film but also to the contraction of the skeletal network, leading to wrinkle kind of formation [240].

6.3.5. Hole-only devices (HODs)

To study the effect of annealing of ITO thin films at different temperatures under the normal ambient on the charge injection into N,N′-Bis(3-methylphenyl)-N,N′- diphenylbenzidine (TPD), which is widely used as one of the low cost, efficient hole transport layers (HTL) in organic light-emitting diodes (OLEDs), "Hole-only" devices (HODs) having the structure of ITO/TPD as HTL (60 nm)/Al (120 nm) were fabricated using pristine and annealed ITO coated glass substrates as anode. The molecular structure of TPD HTL, device structure, and energy level diagram of the HODs are shown in fig. 6.5(i), (ii), and (iii)respectively. The HOMO (5.5 eV) and LUMO (2.3 eV) values of TPD HTL and work functions (Φ) of ITO anode (Φ_A: 4.7 eV) and Al cathode (Φ_C: 4.2 eV) materials are taken from the reports [214,241]. Based on the energy level diagram of HODs (Fig. 6.5(iii)), the hole injection barrier from the cleaned ITO anode can be estimated to $\Delta h \approx 0.8$ eV and the electron injection barrier of $\Delta e \approx 1.9$ eV from Al cathode. In the HODs devices, hole injection is expected to be significantly more efficient and dominant when compared to the electron injection because of its higher barrier height (1.9 eV) (electron injection can be neglected). The work functions (Φ) of pristine and annealed (300–400 °C) ITO thin films were measured at room temperature in the air using ultrahigh vacuum compatible reed-type Kelvin Probe setup. The work function of the reference gold electrode is assumed to be 5.1 eV [227]. The Φ value of 4.95 eV is estimated for pristine ITO thin films, as given in Table 6.1. It is also observed that there is no considerable change in

the work function (Φ = 4.94 eV for 300 °C and Φ = 4.98 eV for 400 °C) of ITO thin films upon annealing at different temperatures under the normal ambient, showing that the injection of holes into TPD HTL is based on the ITO/TPD interface properties in the devices.

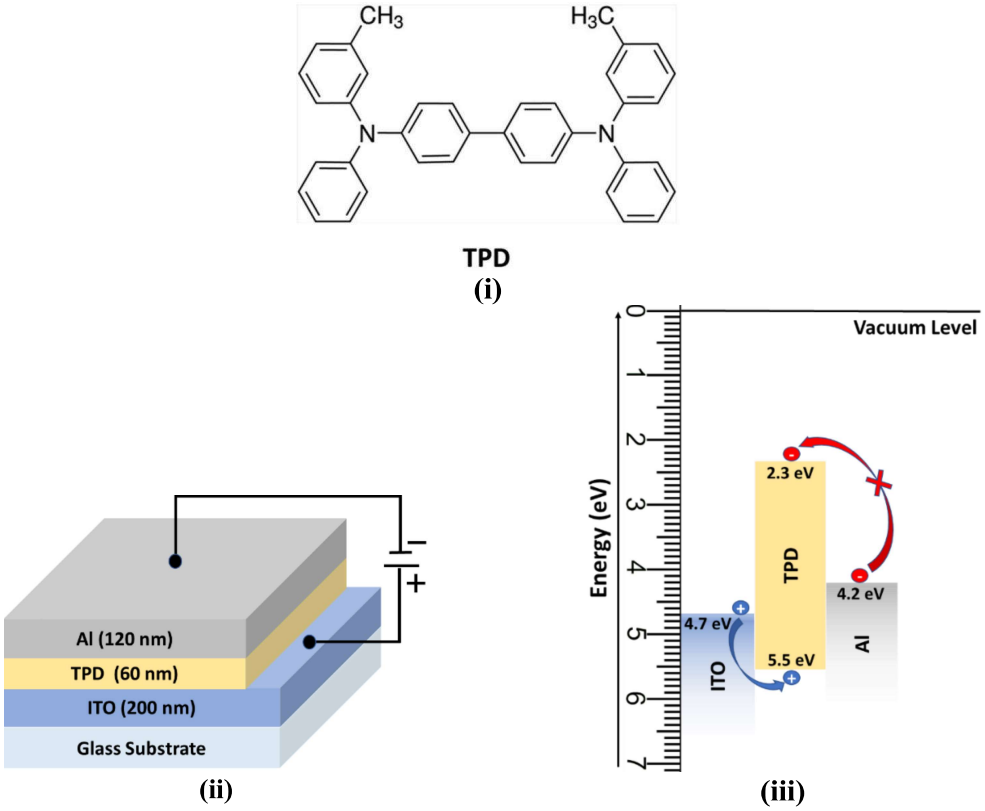

Fig. 6.5. (i) Molecular structure of TPD, (ii) device structure, and (iii) energy level diagram of the materials used in HODs.

The current density–voltage (J–V) characteristics of the fabricated HODs are shown in Fig. 6.6. In the HODs from the J–V characteristics of devices, it is observed that the hole injection on-set of pristine ITO anode-based HOD is around 0.5 V and it is also seen that the leakage current domination is hindering the on-set at around 0.5 V in the annealed (200 and 300 °C) ITO-based devices. Hence, it is to say that the hole carrier injection regime can be considered above the drive voltage of 0.5 V, below which the injection current can barely be extracted due to the leakage current domination [222,241]. From the J–V characteristics of HODs, it has been observed that HOD based on ITO anode annealed at 300 °C exhibited higher hole current density of 93.7 mA/cm^2 at 2 V and 333.8 mA/cm^2 at 4 V when compared to that

of pristine (13.3 mA/cm^2 at 2 V and 69.5 mA/cm^2 at 4 V) and 200 °C (51.1 mA/cm^2 at 2 V and 201.9 mA/cm^2 at 4 V) annealed ITO anode-based HODs. The hole current density of HOD based on ITO annealed at 400 °C is drastically decreased to 10.6 mA/cm^2 at 2 V and 36.2 mA/cm^2 at 4 V. This result thus shows that the hole injection from ITO film into TPD HTL is significantly improved as annealing temperature increases upto 300 °C, and afterwards, it is drastically decreased at 400 °C annealing.

From the experimental data described in this present work, we report that (1) the improved hole injection of the annealed ITO thin films up to 300 °C in the devices may be due to the improved ITO film quality with increasing crystallite size upon annealing under the normal ambient, which improves the ITO/TPD interface properties and hence enhancing the hole injection, and (2) the decrease in the hole injection of 400 °C annealed ITO film in the device may be due to a significant change in the grain boundaries and/or surface morphology of 400 °C annealed ITO film, which alters the surface chemical properties and affects the hole injection at the ITO/TPD HTL interface in the device. This study suggests that the annealing of ITO thin film (anode) under the normal ambient upto 300 °C improves the hole injection in the device, and thus, it will be useful to enhance the hole injection/transport in the OLEDs in addition to the various ITO treatments and to balance the charge carriers in OLEDs based on TPD HTL to improve the device efficiencies.

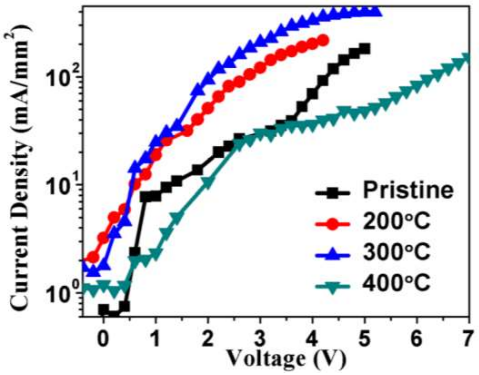

Fig. 6.6. Current density–voltage (J–V) characteristics of Hole-only devices (HODs) based on pristine or annealed (at different temperatures 200, 300, and 400 °C under the normal ambient) ITO thin film (anode) in the device structure of ITO/TPD/Al.

6.3.6. Organic light emitting diodes (OLEDs)

In order to verify the improved hole injection property of annealed ITOs, OLEDs have been fabricated based on pristine and annealed ITOs as anode using Alq_3 as the electron transporting as well as emissive layer. The Alq_3 molecular structure and basic OLED structure are shown in Fig 6.7. The detailed fabricated device structures are as follows

Device A: ITO(pristine)(200 nm)/TPD(60 nm)/Alq_3(60 nm)/LiF(5 nm)/Al(120 nm)

Device B: ITO(300 °C)(200 nm)/TPD(60 nm)/Alq_3(60 nm)/LiF(5 nm)/Al(120 nm)

Device C: ITO(400 °C)(200 nm)/TPD(60 nm)/Alq_3(60 nm)/LiF(5 nm)/Al(120 nm)

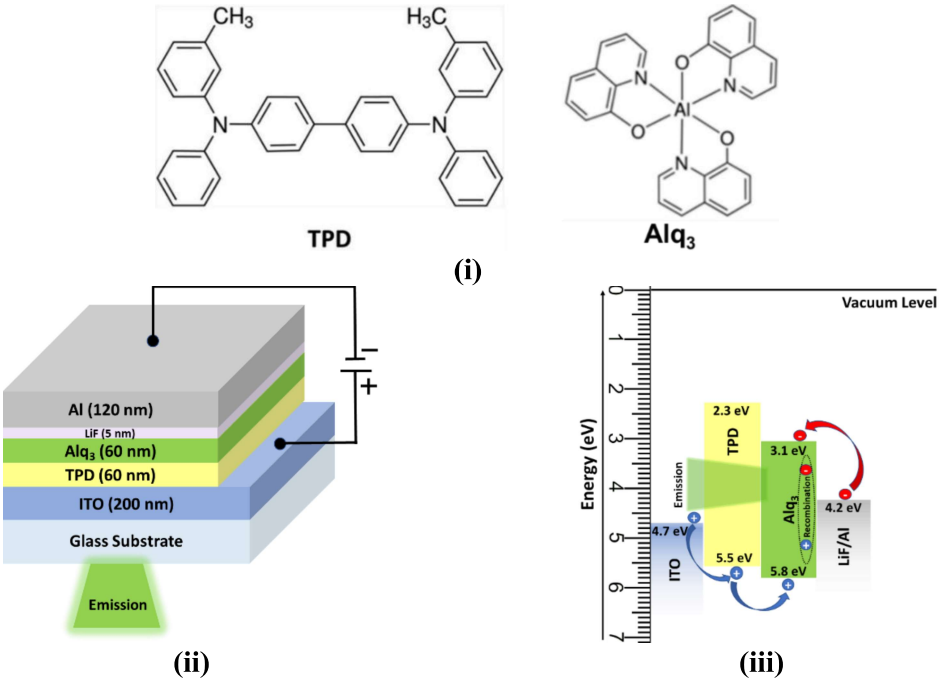

Fig. 6.7. (i) Molecular structure of TPD and Alq_3, (ii) device structure, and (iii) energy level diagram of the materials used in OLEDs.

The J-V characteristics of OLEDs (Device **A-C**) were measured at room temperature using Keithley SMU which are shown in Fig. 6.8 (i). It is observed that OLED (Device **B**) based on ITO anode annealed at 300 °C exhibited the higher current density of 94 mA/cm^2 at 8 V when compared to that (82 mA/cm^2 at 8 V) of pristine ITO based device **A**. The current density of the device **C** based on ITO annealed at 400 °C is drastically decreased to 17 mA/cm^2 at 8V. The electroluminescence (EL) of OLEDs is measured at normal ambient using

spectroradiometer. The EL spectra of devices **A-C** confirming the green emission from the Alq_3 emissive layer (Fig. 6.8 (ii)). Device **B** showed the higher EL emission peak intensity when compared to that of the device A and a drastic decrease in EL intensity is observed for the device **C**. The results show that the annealing of ITO thin films under the normal ambient upto 300 °C improves the ITO film quality and enhances the hole injection into the OLED device which in turn improves the charge balances, resulting in the higher EL emission in the device **B** whereas in the device C based on ITO anode annealed at 400 °C, the change in the surface morphology (wrinkle structure) of ITO film affects the ITO/TPD interface properties and thus decreasing the hole injection which imbalances the charge carriers in the device, resulting in the decreased EL emission of the device **C**.

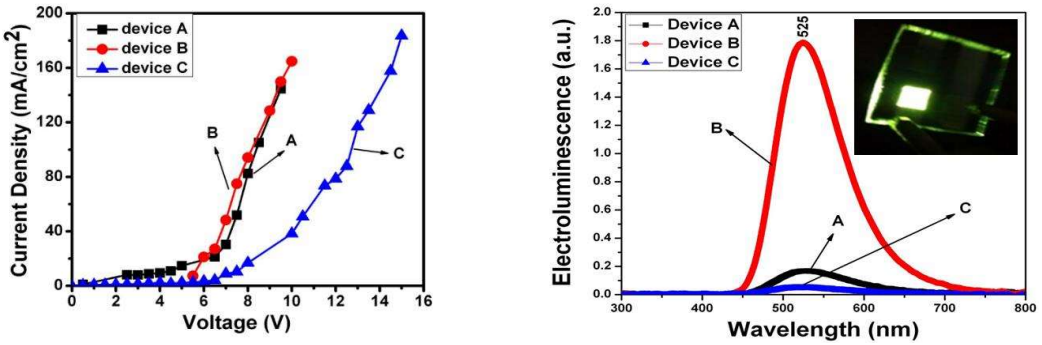

Fig. 6.8. (i) J-V Characteristics and (ii) Electroluminescence spectra of OLEDs based on pristine (Device **A**) and annealed ITO anode at 300 °C (Device **B**) and 400 °C (Device **C**). Inset shows the image of the fabricated OLED device glowing green.

6.4. Conclusion

We demonstrated the improved hole injection into TPD HTL in the HODs using thermal annealed ITO films (anode) under the normal ambient. ITO film annealed at 400 °C shows the highest sheet resistance and the Hall resistivity with a drastic increase after 300 °C annealing. As the annealing temperature of ITO film increases up to 300 °C, the Hall carrier concentration and mobility slightly decrease due to the diffusion of oxygen into oxygen interstitials and oxygen vacancies, and the decreasing of scattering centers, such as ionized impurities and

oxygen vacancies, respectively. The drastic decrease of later above 300 °C is attributed to the dominant scattering of free carriers at chemisorbed grain boundaries, whereas that of former is due to the trapping of free electrons by oxygen chemisorbed. XRD analysis shows the improved ITO film quality with an increasing crystallite size for the increasing annealing temperatures. SEM studies showed that the observed smooth film surface morphology upto 300 °C annealing is turned to wrinkle kind of surface morphological structures at 400 °C, which is supported by AFM studies showing the increase in the surface roughness of ITO thin film annealed at 400 °C. HOD based on ITO anode annealed at 300 °C exhibited the improved hole injection when compared to that of pristine and 200 °C annealed ITO anode-based HODs, this may be due to the improved ITO film quality upon annealing up to 300 °C under the normal ambient, which improves the ITO/TPD interface properties and hence enhancing the hole injection. The drastic decrease in the hole injection of HOD based on ITO annealed at 400 °C may be attributed to a significant change in the grain boundaries and/or surface morphology of 400 °C annealed ITO film, which alters the surface chemical properties and affects the hole injection at the ITO/TPD HTL interface in the device. The results show that the annealing of ITO substrates under the normal ambient up to 300 °C improves the hole injection in the device and also this will be useful to balance the charge carriers in OLEDs based on TPD derivatives as HTL to improve the device efficiencies. The higher hole-current density of HOD based on ITO annealed at 300 °C ascertains the improved film quality of ITO film and/or ITO/TPD interface properties, which enhances the hole injection and balancing the charge carriers in the OLEDs, resulting in the improved EL emission intensity. The change in the surface morphology (wrinkle structure) of ITO anode may affect the ITO/TPD interface properties and thus decreasing hole injection leading to imbalanced charge carriers in the OLED device and resulting in the decreased EL emission intensity. This strategy could be useful to improve the OLED device performances despite the other ITO anode surface treatments.

Chapter: 7

Strategy to improve organic solar cells using PEDOT:PSS interlayer coated onto high temperature annealed ITO anode

This chapter describes the use of ITO annealing strategy in improving the OSC performances using the anodic electrode as "poly(3,4-ethylenedioxythiophene):poly(styrene sulfonate) (PEDOT:PSS)" spin coated onto the annealed indium tin oxide (ITO). Since the PEDOT:PSS is very widely used in OSCs as hole injection layer (HIL) this chapter is decided to study the properties of bilayer structure of PEDOT:PSS spin-coated onto the pristine and/or annealed ITO. It studies the optical, structural, electrical, and morphological properties of ITO(pristine or annealed)/PEDOT:PSS bilayer film. It also deals with the OSCs fabricated based on ITO(pristine or annealed)/PEDOT:PSS bilayer anodic electrode. The hole transporting property of ITO/PEDOT:PSS were verified by fabricating the hole-only devices (HODs) having the device structure of ITO/PEDOT:PSS/N,N'-Bis(3-methylphenyl)-N,N'-diphenylbenzidine as hole-transporting layer/Al. The annealed ITO (400 °C) with PEDOT:PSS interlayer improves the hole-current density and it enhances the efficiency of organic photovoltaic devices [ITO (annealed) /PEDOT:PSS/P3HT:PCBM (active layer)/LiF/Al] by three times higher (1.69%) when compared to that (0.48%) of pristine ITO based OPV device. These results show the strategy that the annealing of ITO film at the high temperature of 400 °C under the normal ambient improves the film quality and lowers the potential energy barrier at ITO/PEDOT:PSS interface for effective hole injection/extraction process, resulting in the enhanced device electrical performances.

7.1. Introduction

The recent technological developments and commercial applications of organic optoelectronic devices such as organic light emitting diodes (OLEDs) and organic photovoltaic

cells (OPVs) have sparked wide research interest in order to improve the device efficiency and device durability for their potential use in the next generation flat panel displays, solid state lighting, and renewable solar energy harvesting owing to its ease of large area device fabrication by roll-to-roll printing, light weight, the possibility to fabricate flexible device, and cost effectiveness [4,119,120,214,242–244]. One of the several factors affecting the higher device efficiency and causing the failure of organic optoelectronic devices after continuous operation is the surface quality and/or bulk properties of indium tin oxide (ITO) film (anodic electrode) [221,245,246]. ITO is the n-type transparent conducting oxide (TCO) material most commonly used as thin anodic electrode in various electronic and/or optoelectronic devices such as transparent coatings for solar energy heat mirrors, liquid crystal flat-panel displays, OLEDs, OPVs, photo-transistors, and lasers, due to its excellent surface adherence, hardness, chemical inertness, wide band gap, higher transparency in the visible region, good electrical conductivity, high infrared reflectance, and tuneable high work function [119,120,221,243–246]. The as-deposited ITO film is found to be less efficient for hole injection in OLEDs and hole collection or extraction process in the OPVs [247].

Since the ITO film is in direct contact with the organic thin film in the devices, the surface properties of ITO anodic electrode directly affect the hole injection/extraction process at ITO/organic interface and electrical properties of the devices [212,223]. Thus, the surface of ITO anode substrate has been modified by various methods such as chemical (Aquaregia, RCA), plasma (O_2, Ar, H_2), and UV-ozone treatments in order to improve the device efficiencies [221,248].The post-deposition thermal annealing of ITO films prepared by various techniques such as direct current (dc) and radio frequency (rf) magnetron sputtering, electron beam evaporation, pulse laser method, spray pyrolysis, and the sol-gel method, has exhibited improved structural, optical and electrical properties. Maurya et al. has studied the post-thermal treatment of rf reactive sputtered ITO films and reported the improved crystalline structure with minimum resistivity of 8.3 x 10^{-4} Ω-cm and higher transparency of 90% in the visible region

for the films annealed at 400 ºC [249]. Cho et al. have reported that the as-deposited amorphous ITO film prepared by electron beam evaporation system exhibited the crystalline structure with lower sheet resistance and higher transmittance over 85% in the visible region after post-annealing at 300 ºC in an oxygen environment [250]. In contrary, the post-annealing (under the normal ambient, air) of rf magnetron sputtered ITO films caused slight increase of resistivity upto 250 ºC which is attributed to free electron scattering by inoized impurities, whereas the resistivity abruptly increased above 250 ºC because of the change in the free electron scattering mechanism by chemisorbed oxygen atoms adsorbed at grain boundaries [251].

In support of the above results, our earlier studies on ITO substrates annealed at different temperatures under the normal ambient revealed that as annealing temperature increases upto 300 °C, the ITO film quality improves with slight increase in the sheet resistance (92 Ω/□ for pristine and 105 Ω/□ for 300 °C), enhancing the hole injection properties at the ITO/organic interface in hole-only devices, whereas the annealing of ITO at 400 °C forms the wrinkle kind of surface morphology with higher sheet resistance of 185 Ω/□, limiting the hole current through the interface in the device [131]. These reports show that the film quality (bulk), surface chemical and morphological properties of ITO thin film are the important parameters to make it more efficient to be used as anodic electrode in the optoelectronic devices. In the recent years, a polymer poly(3,4-ethylenedioxythiophene):poly(styrene sulfonate)(PEDOT:PSS) has been most extensively studied for their wide use in conductive layers, capacitors, antistatic coatings, and organic optoelectronic devices due to its high conductivity, high transparency, easy film deposition, and mechanical flexibility [252,253]. When the solution processed PEDOT:PSS layer is introduced in light emitting diodes and organic solar cells as buffer layer, it facilitates the hole transport and hole injection/extraction process at the interface, thus enhancing the efficiency and lifetime of the devices [254,255].

In this report, we study the optical, structural, and morphological properties of the bilayer structure of PEDOT:PSS film coated onto pristine and annealed (200, 300, 400 °C) ITO

films using various techniques such as X-ray diffraction (XRD), UV-visible transmittance, scanning electron microscopy (SEM), and four-probe method. We fabricate the hole-only devices (HODs) based on PEDOT:PSS coated pristine or annealed ITO film (anodic electrode) to study the hole injection/extraction characteristics of the structure in the devices. This bilayer structure is also utilized in the OPVs for the improved device performances.

7.2. Experimental details

7.2.1. Preparation of ITO/PEDOT:PSS bilayer structure

ITO coated glass substrates (TECHINSTRO, ITO-TIX005) with the thickness of ~200 nm were cut into 2×2 cm^2 area and were annealed at 200, 300, and 400 °C in the tubular furnace under the normal ambient for 1 hour. The pristine and annealed ITO films were rinsed and ultrasonically cleaned in soap solution, deionized water, acetone, isopropyl alcohol (IPA) and finally in deionized water for 10 minutes, and dried for 10 minutes at 120 °C in each step using vacuum oven to evaporate the solvents used, fingerprints and other oil contaminations on the ITO surface. These ITO substrates were cleaned using plasma cleaner (Harrick Plasma, PDC-002) under the ambient pressure of 800 micron for 10 min to remove the unwanted ions on the ITO surface and followed by UV light treatment for 10 minutes under the normal ambient using UV light curing system (Kaivo, UV-1318) to increase the work function and/or adherence of ITO films. The PEDOT:PSS solution (Sigma-Aldrich, Catalog No.: 739316) was filtered using 0.45μm syringe filter and spin-coated onto the cleaned pristine and annealed ITO films at 5500 rpm for 60 seconds using programmable spin-coating unit (Apex Instruments, spinNXG-P2 model) and dried at 120 °C for 10 minutes. The thickness of spin-coated PEDOT:PSS film was measured to be around 45 nm using stylus profilometer (Bruker's DektakXT stylus). The optical transmittance spectra of the bilayer structure of PEDOT:PSS film coated onto the pristine and annealed ITO films were measured using ultraviolet -visible (UV-vis) spectroscopic technique (Agilent, Carry 5000). The measurements of sheet resistance of the bilayer structure were

carried out using the current/voltage source/measure unit (Keithley SMU, 2450 model) by four-point collinear probe method at room temperature. The X-ray diffraction spectra were recorded using XRD (PANanalytical Netherlands, XPERT-PRO model) with Cu K-alpha (X-ray source) radiation (wavelength (λ) of 1.5406 Å). The surface morphological studies were carried out using SEM (TESCAN, VEGA3LMU model).

7.2.2. Fabrication of Hole-Only devices (HODs)

The pristine and annealed (200, 300, and 400 °C) ITO films were patterned for the device area of 4 mm^2 by chemical etching process using hydrochloric acid (HCl) and zinc dust, and thoroughly cleaned by the above substrate cleaning procedure. The Hole-only devices (HODs) were fabricated with the device structure: Pristine or annealed (200, 300,400 °C) ITO substrate (anodic electrode)/PEDOT:PSS as hole injection layer (HIL) (45 nm)/*N*,*N*′-Bis(3-methylphenyl)-*N*,*N*′-diphenylbenzidine (TPD) (Sigma-Aldrich, Catalogue No.: 443263) as hole transport layer (HTL) (60 nm)/Al as cathode (120 nm). The TPD HTL and Al electrode were deposited using organic and metal mask for the device area of 4 mm^2 by thermal evaporation unit under the vacuum of ~6×10^{-6} Torr. The current density - voltage (*J* - *V*) characteristics of the fabricated HODs were measured using the voltage/current source/measure unit (Keithley SMU, 2450 model) under the normal ambient.

7.2.3. Fabrication of Organic Photovoltaic Cells (OPVs)

The 15 mg/mL of P3HT and PCBM each with the volume ratio of 1:1 were dissolved in chlorobenzene solvent and stirred at 600 rpm at 50 °C in glove box under the N_2 ambient for 12 hours followed by filtration using 0.45 μm syringe filter (Solution A). The PEDOT:PSS solution filtered using 0.45 μm syringe filter (Solution B) was spin-coated onto the cleaned pristine or annealed ITO films as a buffer layer at 5500 rpm for 60 sec and dried at 120 °C for 10 minutes on hot plate. The P3HT:PCBM (active) layer was spin-coated using solution A onto

the PEDOT:PSS layer at 800 rpm for 60 sec and dried at 150 °C for 10 minutes on hot plate. Lithium fluoride (LiF) as electron injection layer (EIL) and aluminum (Al) as cathodic electrode were deposited using metal mask for the device area of 4 mm^2 by thermal evaporation process at ~5×10^{-6}Torr. The structure of fabricated OPVs is of ITO (pristine or annealed at 200, 300, 400 °C)/PEDOT:PSS (45 nm)/P3HT:PCBM (100 nm)/LiF (1 nm)/Al (120 nm). The fabricated OPVs were characterized using current/voltage source measurement unit (Keithley's SMU unit, 2450) and the photocurrent was measured under AM 1.5 solar simulator source of 100 mW/cm^2.

7.3. Results and discussion

7.3.1. Optical transmittance

The bilayer structure of PEDOT:PSS layer spin-coated onto the pristine and annealed (200, 300, and 400 °C) ITO films is characterized by using various studies. The Fig. 7.1(i) shows the optical transmittance spectra of PEDOT:PSS coated pristine and annealed (200, 300, and 400 °C) ITO films. It is observed that the PEDOT:PSS/pristine ITO bilayer structure is having good transparency (96% at 550 nm) in the visible region without any significant change for increasing annealing temperature of ITO film (95% for 200 °C and 96% for 300 °C at 550 nm). It has been reported that annealing the bare ITO film under the normal ambient forms the light absorbing/scattering centers in the film and slightly decreases the transparency in the visible region [131]. The transmittance of PEDOT:PSS/annealed (400 °C) ITO bilayer structure is considerably decreased in the UV region (33% at 325 nm) when compared to other films (58% for pristine, 61% for 200 °C and 57% for 300 °C at 325 nm) without any significant change in its transmittance in the visible region (97% for 400 °C at 550 nm), which may be attributed to the significant change in the ITO film and/or in the ITO/PEDOT:PSS interface properties upon annealing of ITO at high temperature of 400 °C [131,251].

The direct optical bandgap energy (E_g) of PEDOT:PSS/pristine or annealed ITO bilayer structure is determined from transmittance spectra using the following formula;

$$(\alpha h\upsilon)^2 = A(h\upsilon - E_g) \quad (7.1)$$

Where, α (α = 2.303(1/T)/t, T - transmittance, t - total film thickness) is the absorption coefficient, hυ is the photon energy, and A is the constant. The Fig. 7.1(ii) shows the plot of $(\alpha h\upsilon)^2$ versus hυ, and the optical band gap (E_g) energies were obtained by extrapolating the linear portion of $(\alpha h\upsilon)^2$ against to the photon energy (hυ) where the absorption coefficient (α) is equal to zero. The PEDOT:PSS coated pristine ITO film exhibited the band gap energy (E_g) of 3.75 eV which is consistent with the reported values [131,246]. No significant change in the optical band gap (3.73 eV for 200 °C and 3.67 eV for 300 °C) is observed for annealing of ITO film upto 300 °C in the bilayer structure and the similar trend has been reported in the case of bare annealed ITO film below300 °C [131]. The PEDOT:PSS/annealed (400 °C) ITO bilayer structure showed a slight decrease in the optical band gap (3.43 eV), attributed to the quantum confinement effect due to increase in crystallite size upon annealing [230,231]

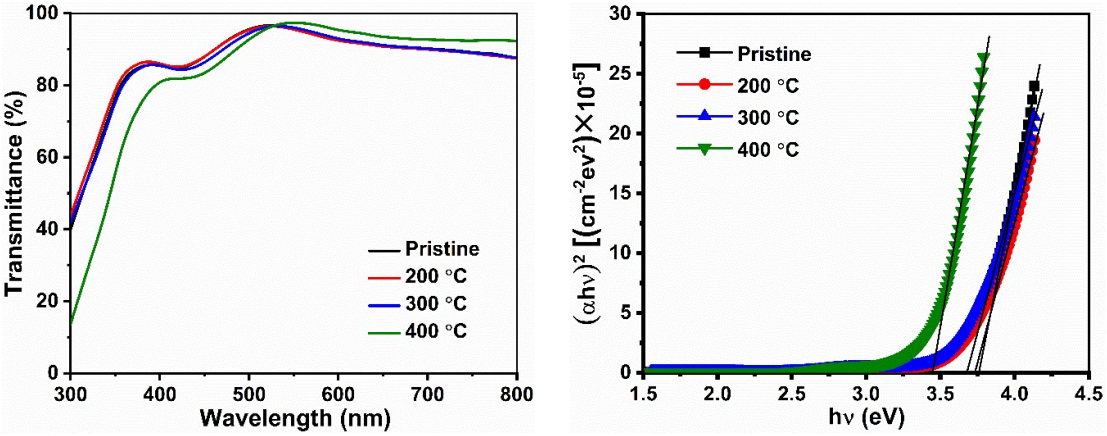

Fig. 7.1. (i) Optical transmittance spectra and (ii) Tauc plots of the bilayer structure of PEDOT:PSS layer coated onto pristine or annealed (**200 °C, 300 °C, and 400 °C**) ITO films under the normal ambient.

7.3.2. Crystalline properties

The XRD patterns of PEDOT:PSS/pristine or annealed (200, 300, and 400 °C) ITO bilayer structure are obtained at room temperature and shown in the figure 7.2(i). The

PEDOT:PSS/pristine ITO bilayer exhibits the diffraction peaks corresponding to ITO [2θ (corresponding hkl plane): 21.39° (211), 30.35° (222),35.28° (400), 50.60° (440), and 60.19° (622), consistent with the JCPDS data (Card No.: 39-1058)], showing the good crystalline properties of ITO film. The PEDOT:PSS/annealed ITO bilayer showed the similar diffraction pattern without any change in the peak positions with increased diffraction peak intensities for increasing annealing temperature of ITO film. The crystallite size of PEDOT:PSS/pristine or annealed (200, 300, and 400 °C) ITO bilayer has been calculated using Debye-Sherrer's formula.

$$D = 0.94\lambda/\beta\cos\theta \qquad (7.2)$$

Where D is the crystallite size, λ is the X-ray wavelength (1.5046 Å), β is the full width half maxima and θ is the diffraction angle. It is observed that the average crystallite size is increasing as annealing temperature of ITO film in the bilayer increases (Fig. 7.2(ii)), which is attributed to combining of native crystalline grains into large size upon annealing under the normal ambient and resulting in the improved ITO film quality [131].

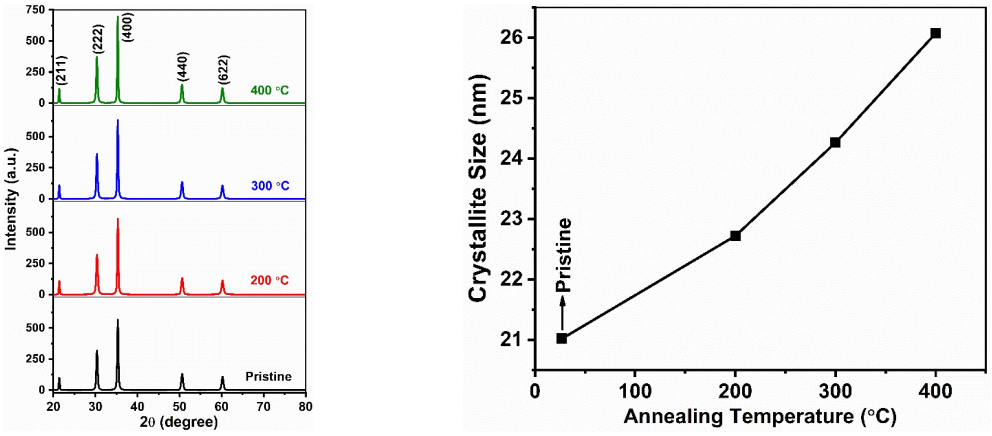

Fig. 7.2. (i) XRD patterns and (ii) Crystallite size estimated from the XRD data of the bilayer structure of PEDOT:PSS layer coated onto pristine or annealed (**200 °C, 300 °C, and 400 °C**) ITO films under the normal ambient.

The dislocation density (δ) is defined as the length of dislocation lines per unit volume of the crystal [199]. It is calculated for PEDOT:PSS/pristine or annealed (200, 300, and 400 °C) ITO bilayer using the following equation. The estimated values are given in Table 7.1 and shown in Fig. 7.3(i).

$$\delta = n/D^2 \quad (7.3)$$

Where δ is the dislocation density, n (=1 for minimum dislocation density) is the factor, and D is the crystallite size. The strain induced in the lattice sites due to the lattice mismatch in the crystalline material is called as lattice strain (ε) and it is estimated from the Williamson-Hall equation [199,200].

$$\varepsilon = \beta_{hkl}/4\tan\theta \quad (7.4)$$

Where ε is the lattice strain, β is the FWHM, θ is the diffraction angle. From the figure 7.3(ii), the trend of decreasing lattice strain with increase of annealing temperature of ITO film in the bilayer structure is attributed to the observed decrease of dislocation density contributed by decreasing of grain boundaries due to growing crystallites [256].

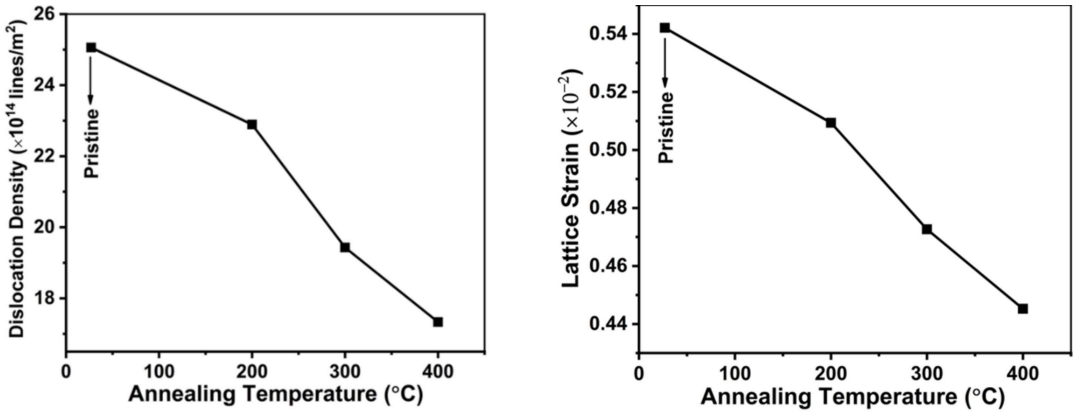

Fig. 7.3. (i) The estimated dislocation density and (ii) lattice strain for the bilayer structure of PEDOT:PSS layer coated onto pristine or annealed (200 ℃, 300 ℃, and 400 ℃) ITO films under the normal ambient.

7.3.3. Morphological studies

The figure 7.4 shows the SEM morphological images of PEDOT:PSS film coated pristine or annealed (200, 300, and 400 °C) ITO bilayer structure in comparison with that of bare pristine or annealed ITO film, respectively. It is observed that the surface morphology of spin-coated PEDOT:PSS film coated onto pristine or annealed (200 and 300 °C) ITO film is smooth and uniform as similar to that of bare pristine or annealed ITO films. The bare ITO film annealed at higher temperature (400 °C) exhibited the wrinkle kind of surface morphological features, which may be attributed to the bending and contraction of skeletal network caused by large amount of stress induced in the film during annealing [131,137]. Interestingly, the spin-coating of PEDOT:PSS film onto the wrinkle surface leads to the smooth and uniform surface morphology of the bilayer structure with increased PEDOT:PSS/ITO interfacial surface area.

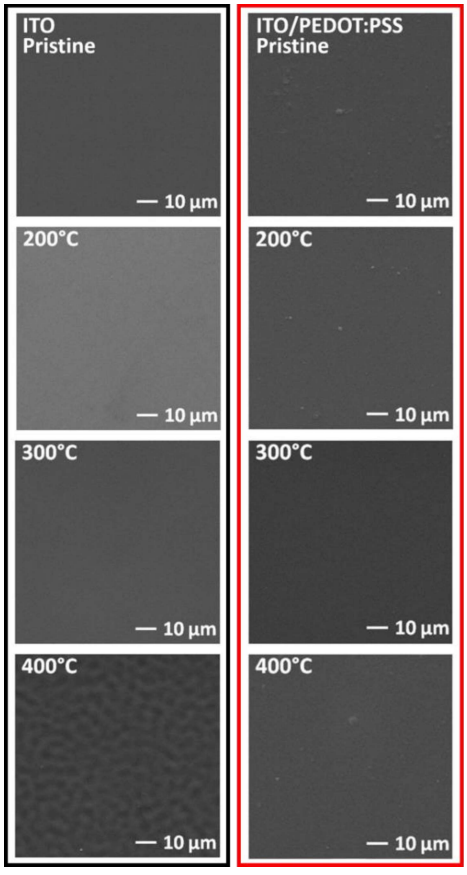

Fig. 7.4. The scanning electron microscopic (SEM) images of PEDOT:PSS layer coated pristine or annealed (200 ◦C, 300 ◦C, and 400 ◦C) ITO films under the normal ambient in comparison with that of bare ITO films (pristine and annealed).

7.3.4. Sheet Resistance

The sheet resistance (R_s) values of PEDOT:PSS coated pristine or annealed ITO bilayer and pristine or annealed ITO films have been estimated using the collinear four-probe technique with the relation

$$R_s = [\pi/\ln.2].(V/I).k \quad (7.5)$$

Where I is the current measured between the probes 1 and 4, V is the voltage measured between the probes 2 and 3, and k (=1) is the correction factor. The observed higher sheet resistance of 30.86 Ω/□ for ITO film annealed at 400 °C with slight increase upto 300 °C (8.3 Ω/□ for Pristine ITO film, 8.4 Ω/□ for 200 °C, 8.9 Ω/□ for 300 °C) is consistent with the earlier report and attributed to a significant change in the grain boundaries and/or surface morphology of the films upon annealing at higher temperature [131]. The coating of PEDOT:PSS film onto the pristine or annealed ITO films shows no significant decrease in the sheet resistance upto 300 °C, whereas the PEDOT:PSS/annealed (400 °C) ITO bilayer exhibited lower sheet resistance of 23.56 Ω/□ compared to that of bare ITO film annealed at 400 °C (Fig. 7.5). The observed decrease in sheet resistance may be related to the improved film quality and/or significant enhancement in the charge conduction at ITO/PEDOT:PSS interface upon annealing of ITO film at 400 °C.

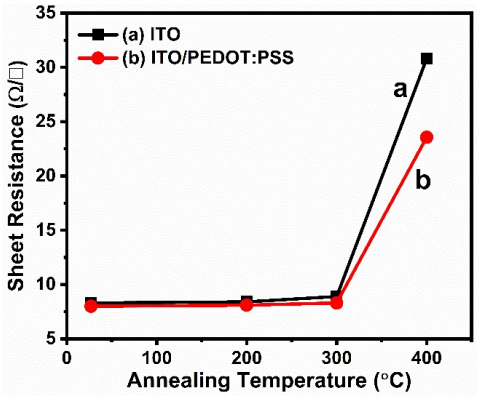

Fig. 7.5. Sheet resistance values of PEDOT:PSS layer coated pristine or annealed (200 °C, 300 °C, and 400 °C) ITO films under the normal ambient in comparison with that of bare ITO films (pristine and annealed).

Table 7.1. The optical, electrical, and crystalline parameters of the PEDOT:PSS layer coated pristine and annealed ITO films.

Film	Optical Transmittance (%) @ nm		Optical band gap energy (E_g) (eV)	Average Crystallite size (nm)	Dislocation density ($\times 10^{14}$ lines/m^2)	Lattice Strain ($\times 10^{-2}$) (no unit)	Sheet Resistance (Ω/□)	
	325	550					ITO	ITO/ PEDOT:PSS
Pristine	58	96	3.75	21.01	25.06	0.54	8.3	8.0
200 °C	61	95	3.73	22.72	22.90	0.51	8.4	8.1
300 °C	57	96	3.67	24.26	19.43	0.47	8.9	8.3
400 °C	33	97	3.43	26.07	17.33	0.44	30.8	23.5

7.3.5. Hole-only devices (HODs)

The hole-only devices (HODs) were fabricated using the structure of PEDOT:PSS interlayer coated onto the pristine or annealed ITO electrode with the device structures as follows:

HOD - A: ITO (pristine)(200 nm)/PEDOT:PSS(45 nm)/TPD(60 nm)/Al(120 nm)

HOD - B: ITO (200 °C)(200 nm)/PEDOT:PSS(45 nm)/TPD(60 nm)/Al(120 nm)

HOD - C: ITO (300 °C)(200 nm)/PEDOT:PSS(45 nm)/TPD(60 nm)/Al(120 nm)

HOD - D: ITO (400 °C)(200 nm)/PEDOT:PSS(45 nm)/TPD(60 nm)/Al(120 nm)

where TPD has been most widely used hole-transporting layer (HTL) in OLEDs with improved device efficiencies. The Fig. 7.6 shows the molecular structures, device structure, and energy level diagram of the materials used in the fabricated HODs. The energy level diagram indicates (i) lower hole injection barrier (Δ_h) of 0.3 eV at ITO/PEDOT:PSS and 0.5 eV at PEDOT:PSS/TPD interfaces for significantly efficient and dominant hole current, and (ii) the higher electron injection barrier (Δ_e) of 2.0 eV at TPD/Al interface for almost negligible electron current in the devices. The Fig. 7.7(i) shows the current density-voltage (*J - V*) characteristics of the HODs. The HOD - A based on pristine ITO exhibits the on-set of hole

injection above 0.5 V below which the leakage current dominates and hence the hole injection current can barely be extracted [241]. It is also observed that the hole injection on-set is hindered at around 0.5 V for other HODs (B - D) due to the leakage current domination. The hole current density of HOD - C at lower bias voltage is observed to be slightly less (45 μA/cm^2 at 1 V, 0.28 mA/cm^2 at 3 V, and 3.67 mA/cm^2 at 6 V) when compared to that of HOD - A (83 μA/cm^2 at 1 V, 0.28 mA/cm^2 at 3 V, and 2.80 mA/cm^2 at 6 V) and HOD - B (97 μA/cm^2 at 1 V, 0.34 mA/cm^2 at 3 V, and 3.24 mA/cm^2 at 6 V) without any significant change in hole current density at higher deriving voltages as shown in Fig. 7.7(i). The HOD - D exhibited a drastic increase in hole current density (0.7 mA/cm^2 at 1 V, 6.52 mA/cm^2 at 3 V, and 38.21 mA/cm^2 at 6 V) when compared to other HODs (A - C). The surface chemical and/or morphological features of ITO film annealed at 400 °C may play a critical role in favor of improved hole injection and transport through ITO/PEDOT:PSS interface.

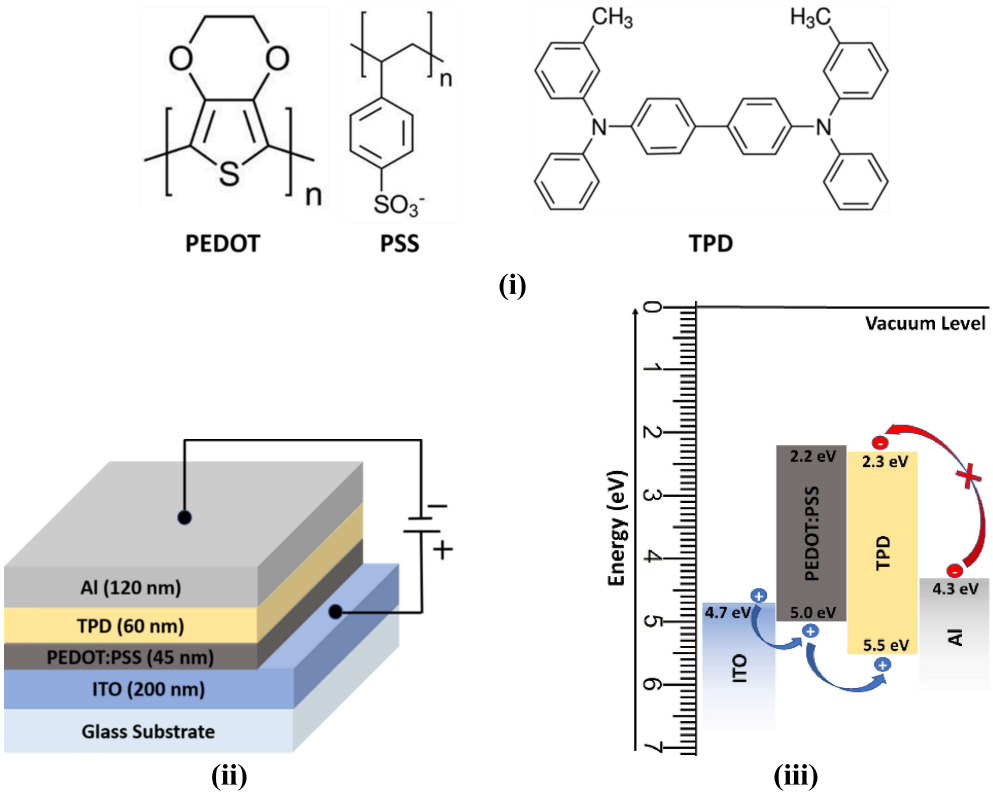

Fig. 7.6. (i) Molecular structure of PEDOT:PSS and TPD, (ii) device structure, and (iii) energy level diagram of the materials used in HODs.

The interface barrier potentials of the HODs (A - D) were estimated from the Fowler-Nordheim (F-N) plots ($Ln(J/E^2)$ verses 1/E) drawn from the *J-V* characteristics of the devices as shown in the figure 7.7(ii). The slope of linear region is directly proportional to $\phi^{3/2}$, where ϕ is the barrier potential for charge injection by tunneling at the interface in the devices [257]. The slope of pristine ITO based HOD – A is found to be 6.6×10^{-4} and is increasing as annealing temperature increases upto 300 °C (10.7×10^{-4} for HOD - B and 16.4×10^{-4} for HOD – C). It is also observed that the slope of HOD – D is drastically decreased to 3.1×10^{-4}, showing the decreased barrier potential for charge injection in the device. These results reveal that annealing of ITO thin film at higher temperature of 400 °C under the normal ambient improves the ITO/PEDOT:PSS surface interface properties and lowers the barrier potential for charge injection, resulting in the higher hole current density in the HODs.

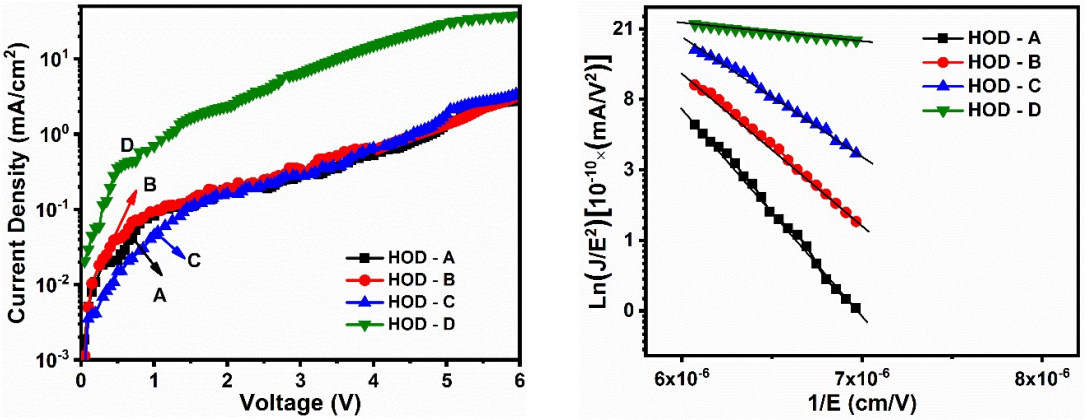

(i) (ii)

Fig. 7.7. (i) The Current density–voltage (J–V) characteristics and (ii) the Fowler-Nordheim (F–N) tunneling plots extracted from the J-V characteristics of the HODs using the bilayer structure of PEDOT:PSS layer coated onto pristine (HOD – **A**) or annealed (at 200 °C for HOD - **B**, 300 °C for HOD - **C**, and 400 °C for HOD - **D**) ITO anodic films under the normal ambient.

7.3.6. Organic solar cells

In order to examine the effect of annealing of ITO thin film at ITO/PEDOT:PSS interface on the device performance of organic photovoltaic cells (OPVs), we fabricate the OPVs with the device structures as follows:

Device A: ITO(pristine)/PEDOT:PSS/P3HT:PCBM/LiF/Al

Device B: ITO(200 °C)/PEDOT:PSS/P3HT:PCBM/LiF/Al

Device C: ITO(300 °C)/PEDOT:PSS/P3HT:PCBM/LiF/Al

Device D: ITO(400 °C)/PEDOT:PSS/P3HT:PCBM/LiF/Al

The molecular structures (PEDOT:PSS and P3HT:PCBM), energy level diagram of the materials used in the organic photovoltaic cells (OPVs), and its device structure are shown in Fig.7.8. The current density – voltage ($J-V$) characteristics of the devices (**A – D**) are shown in Fig. 7.9 and the estimated device parameters are given in the Table 7.2. The device **A** with pristine ITO exhibited the low open circuit voltage (V_{oc}) of 0.28 V with the short-circuit current density (J_{sc}) of 6.48 mA/cm^2, fill factor (FF) of 0.26, and the efficiency (η) of 0.48%. It is observed that the $V_{oc}$is increasing with increasing FF and η as the annealing of ITO film

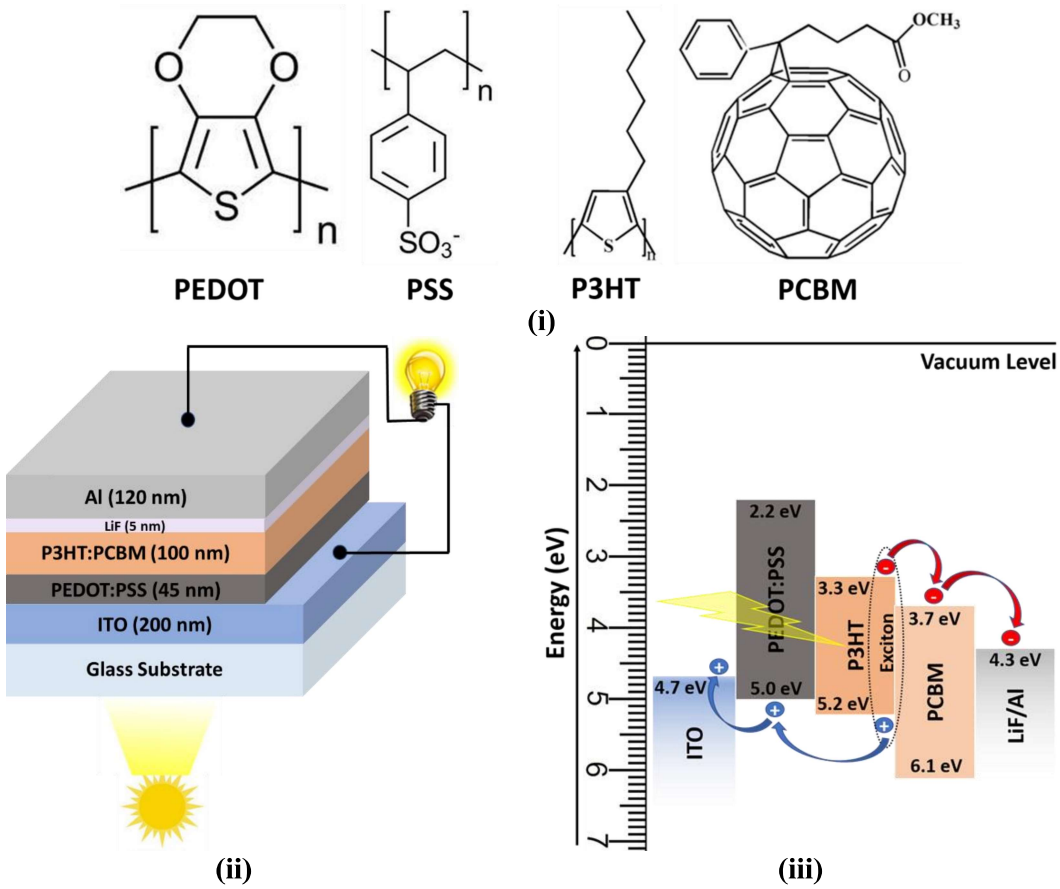

Fig. 7.8. (i) Molecular structure of PEDOT:PSS and P3HT:PCBM, (ii) device structure, and (iii) energy level diagram of the materials used in organic photovoltaic cells (OPVs).

increases (V_{oc} = 0.36 V, FF = 0.29, and η = 0.57% for device B (200 °C); V_{oc} = 0.50 V, FF = 0.35, and η = 0.60% for device C (300 °C); and V_{oc} = 0.54 V, FF = 0.42, and η = 1.69% for device D (400 °C)), which may be attributed to the fact of decreasing charge trap levels at the PEDOT:PSS/active layer interface due to improved molecular orientation of PEDOT:PSS film upon annealing of ITO film under the normal ambient [258]. It is also observed that the J_{sc} of devices is decreasing upon annealing of ITO film upto 300 °C (5.30 mA/cm^2 for device **B** (200 °C) and 3.39 mA/cm^2 for device C (300 °C)), which may be associated with the increasing barrier potential at the annealed ITO/PEDOT:PSS interface. The J_{sc} of device **D** using annealed ITO film at 400 °C is drastically increased to 7.40 mA/cm^2 with increased device parameters (V_{oc} = 0.54 V, FF = 0.42, and η = 1.69%) when compared to other devices (**A – C**). These results show that annealing of ITO film at high temperature of 400 °C under the normal ambient may alter the energy levels and/or interface properties of the ITO/PEDOT:PSS interface, enhancing the hole collection/extraction and resulting in the higher efficiency of OPVs.

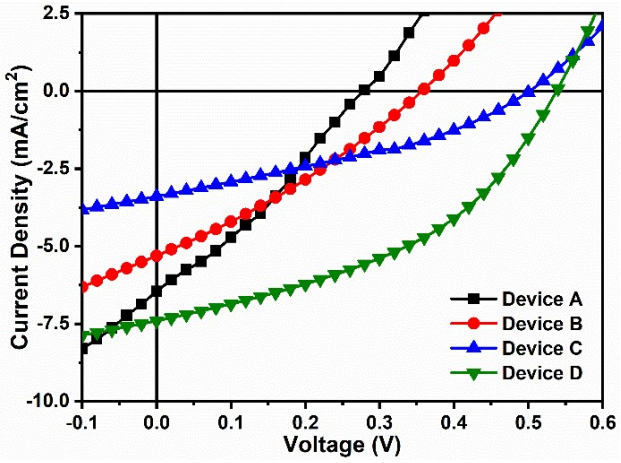

Fig. 7.9. The current density–voltage (J–V) characteristics of the OPVs using the bilayer structure of PEDOT:PSS layer coated onto pristine (Device A) or annealed (at 200 ◦C for Device B, 300 ◦C for Device C, and 400 ◦C for Device D) ITO anodic films under the normal ambient.

Table 7.2. The estimated device parameters of OPVs using the bilayer structure of PEDOT:PSS layer coated onto pristine or annealed ITO films.

Device	J_{sc} (mA/cm^2)	V_{oc} (V)	Fill Factor	Efficiency (%)
A	6.48	0.28	0.26	0.48
B	5.30	0.36	0.29	0.57
C	3.39	0.50	0.35	0.60
D	7.40	0.54	0.42	1.69

7.4. Conclusion

The annealing of ITO film at 400 °C reveals higher transparency in the visible region and improves the film quality upon aggregation of native grains into large crystallites, resulting in decreased dislocation density and lattice strain, and leaving the wrinkle kind of surface morphology. The spin coating of PEDOT:PSS film onto the wrinkle kind of surface morphology smoothens the surface and absorbs the UV light significantly. The higher hole current density of the HODs based on ITO annealed (400 °C)/PEDOT:PSS interlayer may be associated with decreased potential barrier at the ITO/PEDOT:PSS interface for hole injection process into the device due to improved interfacial (energy levels and/or surface area) properties. The OPV using the annealed (400 °C) ITO/PEDOT:PSS buffer layer exhibits the efficiency three times higher (η = 1.69%) than that (η = 0.48%) of pristine ITO based device. These results show that the ITO film (annealed at 400 °C)/PEDOT:PSS interface favors the effective hole injection/extraction process in the devices for the improved performances. The spin coating of PEDOT:PSS layer onto the annealed (400 °C) ITO anodic electrode could be an effective way to improve the device performances of OLEDs and OPVs for the commercial applications.

Chapter: 8

Improved performance of Alq_3/ZnO hybrid thin film-based UV photodetectors using strategy of annealed ITO film

This chapter describes the improved photoresponse of Alq_3/ZnO hybrid thin film-based UV photodetectors by using the strategy of annealing of ITO electrode film at higher temperature as seen in the earlier chapters. The annealed ITO film in the device is used in order to enhance the charge transport in the hybrid films. The electron-only devices (EODs) based on Alq_3/ZnO hybrid thin films were fabricated and characterized. The analysis of Hall-effect measurements (carrier concentration, mobility, and resistivity) of Alq_3/ZnO hybrid thin films is compared with pristine ZnO thin film. This chapter deals with the UV photoresponses of the Alq_3/ZnO hybrid thin films by using the pristine and/or annealed ITO film as a strategy to improve the device performances.

8.1. Introduction

In recent decades Ultraviolet (UV) photodetectors have been receiving large importance in the applications of environmental monitoring, forest-fire prevention, astronomical research, civilian and military fields, missile approach warning, medical analysis, etc [67–69]. The development of UV photodetector is working towards large-array, fast-response, high performance, lightweight, and low-cost production [67,68,164,183]. UV-photodetectors based on silicon are the most common devices, exhibiting some limitations such as the requirement of visible and infrared light filters, degradation of devices upon exposure to UV light for a long time, required to be cooled to reduce the dark current, and inaccuracy for high sensitivity applications [68,185]. ZnO is recognized as a very promising optoelectronic material to fabricate high sensitivity UV photodetectors, due to its better properties such as direct wide-bandgap (3.36 eV), high exciton binding energy (60 meV), non-toxicity, high radiation stability,

and higher transparency in the visible region [68,164,185]. Tris-(8-hyroxyquinoline)aluminum (Alq_3) is a well-known highly fluorescent organic semiconductor widely used as an electron-transporting and emissive layer in organic light-emitting diodes (OLEDs) [4,17]. Alq_3 can be used in many other optoelectronic device applications in pure or doped in host to enhance the electrical conducting properties. The drawbacks of Alq_3 are the degradation of optical and electrical properties upon environmental aging and light exposure [4,6,196,207]. Hybrid (organic/inorganic) composite materials exhibit the high thermal stability, chemical resistance, mechanical strength, good optical and electrical properties over organic and inorganic materials [33,123,161]. Organic-Inorganic hybrid film-based UV-photodetectors show good advantages such as high gain, sensitivity, and responsivity for cost-effective applications [164,184,259,260].

Indium tin oxide (ITO) coated glass substrates are the most widely used TCO anode in optoelectronic devices due to its high work function, higher electrical conductivity and transparency to the visible light [239,261]. The surface quality and/or bulk properties of ITO anode is one of the several factors affecting optoelectronic device efficiencies because of the deposited organic layer is in direct contact with ITO surface [241,246,247,262]. The surface modifications of ITO anode by plasma cleaning and UV ozone treatments have been widely demonstrated for the improved optoelecronic device efficiencies [225,238,263]. The thermal behaviour of ITO thin films deposited by RF sputtering method has been studied by annealing of ITO thin film at different temperature in air [239,249]. The sudden decrease in the charge carrier mobility and carrier conductivity occurs above 300 °C annealing, attributed to the chemisorption of oxygen into grain boundaries (which absorbs the free electrons and in turn reduces the scattering of free carriers at the boundary) and no further diffusion of oxygen into bulk due to no more donor oxygen vacancies (two electrons donated by each vacancy) [131,219,237]. Since the ITO film is in direct contact with the organic thin film in the devices, the surface properties of ITO anodic electrode directly affect the hole injection/extraction

process at ITO/organic interface and electrical properties of the devices [241,262]. Hence, it is highly beneficial to study the effect of annealing of ITO thin film to improve the device performances of UV photodetectors.

8.2. Experimental work

8.2.1. Solution preparation

The procedure for the preparation of pristine ZnO and Alq_3/ZnO hybrid thin films by using sol-gel spin-coating process was followed as-such from our earlier report published elsewhere [156]. The ZnO sol-gel was prepared with the molar concentration of 0.5 M by dissolving the zinc acetate dihydrate [$Zn(CH_3COO)_2.2H_2O$: 98.5%; SRL] in 2-methoxyethanol ($C_3H_8O_2$: 99%; SRL) solvent and stirred at 450 rpm for 2 hrs at 60ºC. The ZnO precursor solution (A) was obtained by drop wise addition of monoethanolamine (MEA: 99%; SRL) for 1:1 molar ratio of MEA to zinc acetate and allowed it for gelation by keeping it under the normal ambient for 24 hrs. Alq_3 ($C_{27}H_{18}AlN_3O_3$: 99.995%; Sigma Aldrich) was dissolved in 2-methoxyethanol solvent and stirred (450 rpm) for 2 hrs for the preparation of 10^{-3} M Alq_3solution (B). The 0.2 µm syringe filter was used to filter the ZnO sol-gel precursor (A) for film **(a)** and Alq_3 solution (B) separately. Using these, the three (5 mL each) Alq_3 incorporated ZnO precursor solutions were prepared with the nominal molar ratio of Alq_3 to ZnO (Alq_3/ZnO) as $0.5x10^{-3}$ [4 mL of ZnO (80 vol.%) (0.4 M) + 1 mL of Alq_3 (20 vol.%) ($2x10^{-4}$ M)] for film (**b**), $1.3x10^{-3}$ for [3 mL of ZnO (60 vol.%) (0.3 M) + 2 mL of Alq_3 (40 vol.%) ($4x10^{-4}$ M)] for the film (**c**); and $3x10^{-3}$ [2 mL of ZnO (40 vol.%) (0.2 M) + 3 mL of Alq_3 (60 vol.%) ($6x10^{-4}$ M)] for film (**d**).

8.2.2. Thin film formation

The glass substrates were cut into 2x2 cm^2 area and thoroughly cleaned by rinsing and sonicating in soap solution, DI water, acetone, IPA, and finally in DI water each for 10 min. Before changing the cleaning agent, the substrates were vacuum dried for 10 min at 120 ºC to

evaporate the solvent. This cleaning process is utilised to remove any stains and oil or chemical contaminations. The substrates were also cleaned in high plasma at 800-micron vacuum using plasma cleaner (Harrick Plasma, PDC-002). The prepared four solutions (pure and Alq_3/ZnO hybrid) were spin-coated at 2000 rpm for 30 sec and pre annealed at 180 ℃ for the preparation of thin films (**a – d)**. The coating process was repeated for 5 times for the required thickness (~200 nm). The spin-coated thin films (**a - d**) were post annealed at 300 ℃ for 2 hr under the normal ambient using tubular furnace to enhance the film quality. The electrical properties (carrier concentration, mobility, and resistivity) of these films were measured using hall-effect measurement setup.

8.2.3. Fabrication of Electron-only devices (EODs)

The pure ZnO and Alq_3 are well-known electron transporting materials. Thus, it is to analyse the electron transporting properties of Alq_3/ZnO hybrid thin films by fabricating EODs based on pristine ZnO and Alq_3/ZnO hybrid thin films. The ITO coated glass substrates (TECHINSTRO, ITO-TIX005) with the thickness of ~200 nm were cut into 2 × 2 cm^2 area. The ITOs were patterned for the device area of 4 mm^2 by chemical etching process using hydrochloric acid (HCl) and zinc dust. The patterned ITOs were cleaned following the same substrate cleaning procedure and followed by plasma cleaning and UV light curing for 10 min. The prepared four solutions were spin-coated onto the four cleaned patterned ITO at 2000 rpm for 30 sec and pre-annealed at 180 ℃ to evaporate the solvent. Prior to the pre-annealing the span solution was wiped off at the edges for the bottom ITO anode contact. This coating process is repeated for 5 times for the appropriate thickness of ~200 nm. Further the ITO substrates with deposited ZnO or Alq_3/ZnO hybrid thin films were loaded into the vacuum chamber of thermal evaporation vacuum coating unit to coat the Al electrode. This cathode contact is coated using metal mask for the effective device area of 4 mm^2 under the high vacuum of ~ 5×10^{-6}

mbar. The current density-voltage (J-V) characteristics of the fabricated EODs were measured at room temperature using Keithley 2450 SMU.

8.2.4. Fabrication of UV photodetectors (UVPDs) based on Alq_3/ZnO hybrid thin films using pristine or annealed ITO film

The UVPDs discussed in chapter 4 are fabricated based on Alq_3/ZnO hybrid thin films on glass substrates and Al electrodes as ohmic contacts. For utilizing the improved quality of ITO film, the UVPDs were fabricated based on the Alq_3/ZnO hybrid thin films using the ITO film. The ITO substrates were cut into 2x2 cm^2 area of eight pieces (two sets) and patterned using Zinc dust and HCl with 4mm strip width. The first set of four ITOs (set-I) were considered as pristine ITOs and the another set of four ITOs (set-II) are annealed at 300 ℃ for 1 hr in tubular furnace under the normal ambient. The ITO electrode substrates of set-I (for pristine ITO) and set-II (for annealed ITO) were cleaned thoroughly following the regular cleaning process. The pristine ZnO and Alq_3/ZnO (with three different molar ratios as above mentioned for the films **b - d**) solutions were spin coated on the two set of ITO substrates at 2000 rpm with the continuous spin of 30 sec. Immediately after spun the solution was wiped off along the ITO strip such that the film is remain on the ITO only and they were pre-annealed at 180 ℃ on hot plate by covering with glass lid. The coating process was repeated for five time to get the film thickness of ~200 nm. The spin-coated films were annealed at 300 ℃ in normal ambient to improve the film quality. Further the ZnO and Alq_3/ZnO films coated ITO substrates (set-I and set-II) were loaded into the vacuum chamber and Al electrodes were coated at high vacuum of ~5×10^{-6} mbar with the strip width of 2 mm perpendicular to the bottom ITO strip. Here the bottom ITO is used to enhance the charge transport in Alq_3/ZnO hybrid film and the top Al strips are used for ohmic contacts. The fabricated UVPDs were characterized using Keithley SMU and UV spot light.

8.3. Results and discussion

8.3.1. Hall-effect measurements

The charge carrier concentration, mobility, and resistivity of pristine ZnO (**a**) and Alq_3/ZnO hybrid thin films (**b-d**) were measured at room temperature by Hall-Effect measurements in the van der Pauw method and are given in Table 8.1. From Fig. 8.1, it is observed that the resistivity is decreased whereas mobility and electron carrier concentrations are increased with increasing the Alq_3/ZnO molar ratio in hybrid films (**b-d**) when compared to the pristine ZnO film **a**. The incorporated Alq_3 molecules adsorbed onto the grain boundaries and may create the space charge region between the ZnO grains which facilitates the charge carriers to move across ZnO grains, resulting in enhanced mobility for the hybrid films **b-d** with decreased resistivity [264,265]. The adsorption of Alq_3 molecules onto the grain boundaries of ZnO decreases the grain boundary scattering of free charge carriers resulting in enhanced mobility in the composite films [156]. The highest mobility for the film **d** when compared to the other films may be due to the increased Alq_3 content. The PL spectra (Fig 3.9 (i) from chapter 3) distinctly show the enhanced peak intensity with broadening of band edge emission and slight enhancement at defective emission leading to the increased Zn_i (~395 – 435 nm) and V_O (~520 – 565 nm) with the incorporation of Alq_3 in the hybrid films. Thus, the increase in the carrier concentration in the hybrid films with increasing Alq_3 content may be due to the presence of Zn_i and V_O (each vacancy creates two electrons) [47,185,241]. The Zn_i and V_O are

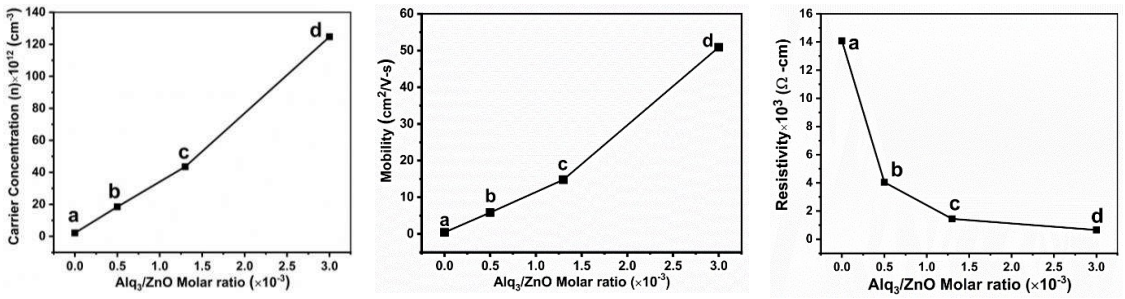

Fig. 8.1. The hall effect measurements (electron carrier concertation, mobility, and resistivity) of pristine ZnO (**a**) and Alq_3/ZnO hybrid thin films (**b - d**)

easily got ionized in ZnO thin films and produce free charge carrier [185]. The increase in the carrier concentration is also led to a decrease in the optical transmittance (Fig. 3.1 from chapter 3) for the films **b-d** because of the increase in free carrier absorption [266].

Table 8.1. The hall effect measurements of pristine ZnO and Alq_3/ZnO hybrid thin films.

Film	Molar ratio of Alq_3/ZnO	Hall effect measurements		
		Carrier Concentration (n_c) ($\times 10^{12}/cm^3$)	Mobility (μ) ($cm^2/V\text{-}s$)	Resistivity (ρ) ($\times 10^3/\Omega\text{-}cm$)
a	0 (Pristine)	2.14	0.45	14.08
b	$0.5x10^{-3}$	18.47	5.83	4.04
c	$1.3x10^{-3}$	43.51	14.8	1.44
d	$3x10^{-3}$	124.7	50.92	0.65

8.3.2. Electron-only devices (EODs) characteristics

The EODs were fabricated based on pristine and Alq_3/ZnO hybrid thin films and the device structures are as follows:

EOD-A (film **a**): ITO/ZnO(molar concentration of 0.5 M)/LiF/Al

EOD-B (film **b**): ITO/Alq_3:ZnO(molar ratio of 0.5×10^{-3})/LiF/Al

EOD-C (film **c**): ITO/Alq_3:ZnO(molar ratio of 1.3×10^{-3})/LiF/Al

EOD-D (film **d**): ITO/Alq_3:ZnO(molar ratio of 3×10^{-3})/LiF/Al

The current density-voltage (J-V) characteristics were performed using Keithley SMU at room temperature. The figure 8.2 shows device structure and energy level diagram with charge transferring process of EODs and Fig. 8.3 shows the semi-log plots of J-V characteristics of four EODs (EOD A-D). The EODs (A-D) exhibit the current densities at 4 V: 134.4, 31, 50, and 174 mA/cm^2; and at 8V: 132.6, 376.2, 560.7, and 619 mA/cm^2. It is clearly observed that the two devices (EOD-B and EOD-C) exhibit the charge injection with distinctly shooting

current density. The charge injection for the EOD–B starts at 4-5 V and for the EOD–C at 2-3 V revealing that for increasing Alq_3 content in ZnO up to the molar ratio of 1.3×10^{-3} the charge injection is taking place at lower voltages. In the EOD-D, even though there is no distinct charge injection but it is exhibiting the enhanced current density than the other devices. The improved current density for the Alq_3/ZnO based devices is attributed to the enhanced carrier concentration and mobility of the hybrid thin films. The energy level diagram shows the lower electron injection barrier (Δ_e) of 0.1 eV at Al/ZnO interface and the higher hole injection barrier (Δ_h) of 2.6 eV at ITO/ZnO interface. This reveals that the current in the devices is majorly due to electrons and the hole current is almost negligible. From the energy level diagram of EODs (B-D), the Δ_e at Al/Alq_3 is 1.2 eV which is higher than Δ_e (0.1 eV) at Al/ZnO indicating that the electrons are injected into the ZnO only. The incorporated Alq_3 molecules are adsorbed at the grain boundaries of ZnO and create the space charge region facilitating the enhanced current

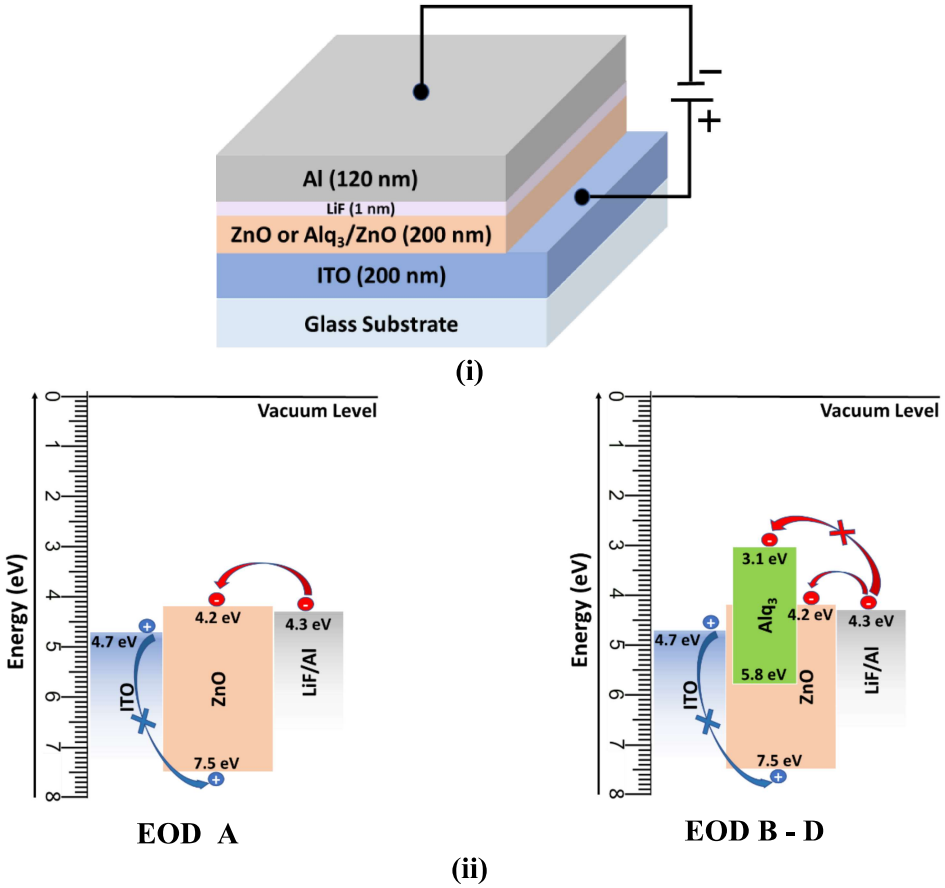

Fig. 8.2. (i) EOD structure and (ii) energy level diagram of the materials used in EODs.

density of EODs [10,156]. The adsorbed Alq_3 molecules create the Alq_3 capped ZnO nanoparticles with improved crystalline properties which may also enhance the electron transporting properties in EODs [156].

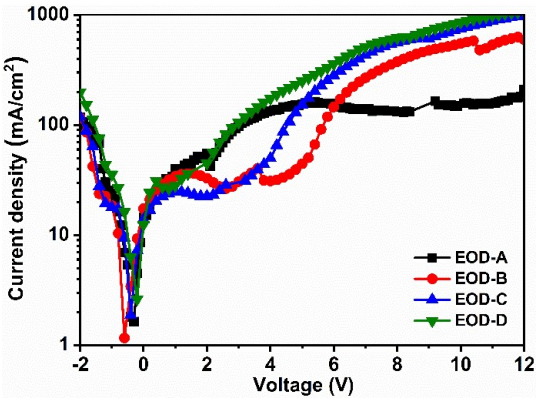

Fig. 8.3. Current density - Voltage (J-V) characteristics of EODs (**A-D**).

8.3.3. UV photodetectors (UVPDs) characteristics

Two sets of Alq_3/ZnO hybrid thin film based UVPDs were fabricated using pristine ITO film (Set-I) and annealed ITO film (Set-II), the device structures are as follows (the schematic representations of the respective devices are shown in Fig 8.4).

Set-I

Device A (based on film **a**): ITO (pristine)/ZnO/Al

Device B (based on film **b**): ITO (pristine)/ Alq_3:ZnO(molar ratio of 0.5×10^{-3})/Al

Device C (based on film **c**): ITO (pristine)/ Alq_3:ZnO(molar ratio of 1.3×10^{-3})/Al

Device D (based on film **d**): ITO (pristine)/ Alq_3:ZnO(molar ratio of 3×10^{-3})/Al

Set-II

Device E (based on film **a**): ITO (300 °C)/ZnO/Al

Device F (based on film **b**): ITO (300 °C)/ Alq_3:ZnO(molar ratio of 0.5×10^{-3})/Al

Device G (based on film **c**): ITO (300 °C)/ Alq_3:ZnO(molar ratio of 1.3×10^{-3})/Al

Device H (based on film **d**): ITO (300 °C)/ Alq_3:ZnO(molar ratio of 3×10^{-3})/Al

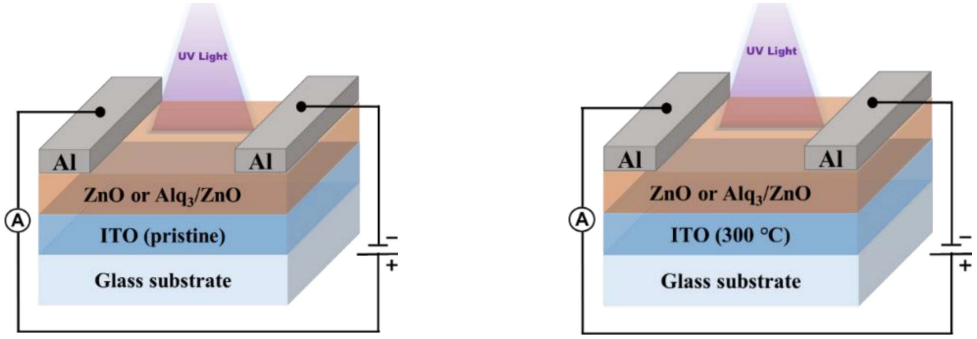

Fig. 8.4. Schematic diagrams of fabricated UVPDs based on pristine ZnO and Alq_3/ZnO hybrid thin films using pristine ITO (set I: devices A-D) and annealed ITO (set II: devices E-H)

In the fabricated UVPD devices, pristine ZnO or Alq_3/ZnO hybrid thin films are spin coated onto ITO films for the thickness of ~200 nm and Al contacts were made over with 120 nm. The ITO films are used to enhance the charge transporting in pristine ZnO or Alq_3/ZnO hybrid thin films. The current density-voltage (J-V) characteristics of the devices were performed using voltage/current source measure unit (SMU: Keithley, 2450 model) under the dark and UV-spot light illumination (wavelength: 365 nm, power: 1 mw/cm^2) with biasing from -4 V to +4 V under the normal ambient. The figures 8.5(i) and 8.5(ii) show the semi-log plots of J-V characteristics of ZnO or Alq_3/ZnO hybrid thin film based UVPDs using pristine ITO film and/or annealed ITO film respectively. The UVPDs based on films **a-d** using ITO substrates (pristine and/or annealed) exhibit the higher current densities when compared to that of UVPDs made-on glass substrates (UVPDs from chapter **4**). This is revealing that the ITOs enormously increase the electric field in the films leading to the drastic enhancement in the current densities than the glass substrate-based devices [68,267,268]. The devices based on pristine ITO and annealed ITO exhibit the JV characteristics with nearly same trend under dark and UV light. This is revealing that the ITO annealing does not affect the characteristic UV response of pristine ZnO and Alq_3/ZnO hybrid thin films. The UVPDs based on film **b** (device **B** and **F**) and film **c** (device **C** and **G**) exhibit the increased dark and light currents when

compared to the film **a** (device **A** and **E**) based devices in both pristine ITO and annealed ITO cases. This enhancement in current density for the devices based on film **b** and **c** supports the results of the devices made on glass substrate. The improved Hall effect parameters and EOD characteristics also supports the enhanced current density. The energy transfer from Alq_3 to ZnO in hybrid films ascertains the increased light current [156]. The film **d**-based devices (**D** and **H**) exhibit the lower dark current and higher light current when compared to the remaining devices. The higher concentration of Alq_3 in ZnO for film **d** may create the charge trap-states in ZnO which reduce the current density in dark [269,270]. On the other hand, the potential barrier at ITO/Alq_3 is 1.8 eV which is higher than that of 0.7 eV at ITO/ZnO, hence the higher concentration of Alq_3 in film **d** may affect the supportive electric field by the ITO in devices **D** and **H** leading to decreased dark current [271,272]. Under the UV illumination, there is a distinct energy transfer from Alq_3 to ZnO increasing the light current drastically, supporting the enhanced PL emission of hybrid films as discussed in chapter **3** [156]. The UV illumination onto the Alq_3/ZnO film-based devices enhances the energy transfer from Alq_3 to ZnO leading to the distinct increment of currents, whereas under dark the increment in the current density is considerably less.

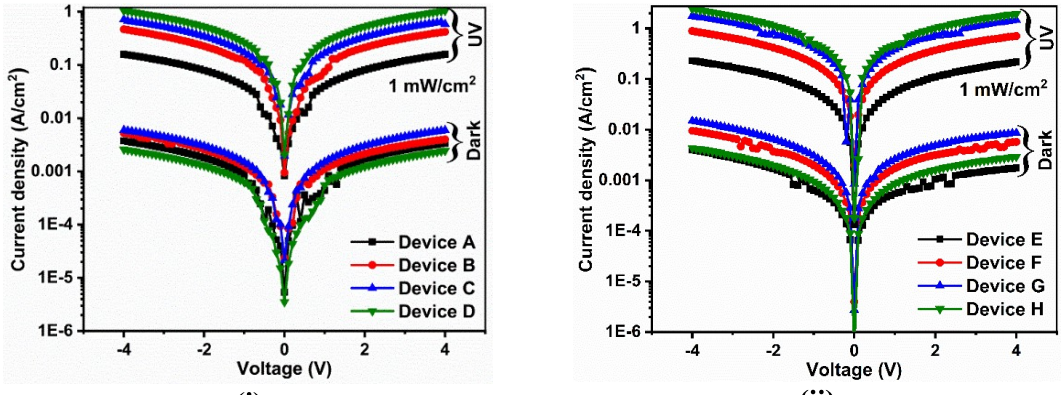

Fig. 8.5. J-V characteristics of pure ZnO and Alq_3/ZnO hybrid thin film based UVPDs using (i) pristine ITO (Devices **A-D**) and (ii) annealed ITO (Devices **E-H**)

Photocurrent, gain, responsivity, and detectivity are the essential parameters in order to estimate the UV photo detecting responses [68,183]. These parameters were calculated at bias

of 1 V and 1mW/cm^2 UV light intensity and are show in in Table 8.2 (devices **A-D**) and Table 8.3 (devices **E-H**) [68,134].

Photocurrent gain (G) = I_{light}/I_{dark} (8.1)

Sensitivity(S) = I_{ph}/I_{dark} (8.2)

Responsivity(R) = I_{ph}/ P.A (8.3)

Detectivity(D) = $(I_{ph}/E)\ (2qI_{dark})^{1/2}$ (8.4)

where I_{dark} - current under dark, I_{light}– current under UV light, I_{ph} (I_{light} - I_{dark}) – photocurrent, P - power of UV light, and A - effective area of the device.

The responsivity and sensitivity proportionately vary with the photocurrent and gain respectively. The photocurrent (I_{light} - I_{dark}) is due to the excitons generated by the UV illumination whereas the dark current is due to the free carriers present in the film. In both the sets of devices (using pristine and annealed ITO), the photocurrent and gain are observed to be increased with the incorporation of Alq_3 in comparison with the results of the UVPDs fabricated on glass substrate. The enhancement of photocurrent in all devices (using glass substrate, pristine ITO, and annealed ITO) is assumed mainly due to the energy transfer from Alq_3 to ZnO in hybrid films (**b-d**). Since the current gain is the ratio of light current to dark current (I_{light}/I_{dark}), low dark current and high light current gives the high current gain. The devices (**D** and **H**) based on film **d** exhibiting the high current gain than the other devices due to their low dark and high light current [67,134]. The increasing of Alq_3 in ZnO for film **d** generate the high density of charge trapped states resulting in low dark currents in devices **D** and **H** whereas under the UV illumination this excess content of Alq_3 facilitates the higher energy transfer from Alq_3 to ZnO leading to the drastic enhancement in the light current [188,192,267]. The response characteristics were measured by modulating the UV light source (incident optical power of 1 and 3 mW/cm^2), at 0 and 1 V bias with the interval of 30 sec. The figures 8.6 and 8.7 show the time-dependent response characteristics of pure ZnO or Alq_3/ZnO hybrid thin film-based UV photodetector using pristine ITO and annealed ITO respectively. The current density is

observed to be increased and then decreased with respect to the UV light illumination ON/OFF states in regular intervals of time, revealing the stability and reproducibility of all the devices **(A-H)**. At 0 bias the devices are exhibiting the currents in micro amperes during the ON state whereas at 1 V bias the currents are in ampere revealing that even at small bias the electric field generated by the ITO is more. The anomaly in the current densities is due to the lower electric fields because less voltage (1 V). The growth time τ_g (time required for the current to increase from 10% to 90% of maximum current when UV illumination ON) and decay time τ_d (time required for the current to decrease from 90% to 10% of maximum current when UV illumination OFF) were calculated from the response plots and shown in Table 8.2 and Table 8.3 [164]. The devices are exhibiting the nearly same τ_g and τ_d at different UV power (1 and 3 mW/cm^2) and at different voltages (0 and 1 V) revealing that the τ_g and τ_d are independent of power and bias voltage. The mentioned τ_g and τ_d values in the tables are average times of response plots at 0V-1mW/cm^2, 0V-3mW/cm^2, 1V-3mW/cm^2, and 1V-3mW/cm^2.The devices exhibit fast growth and slow decay responses. In general, the drawback of ZnO based UV photodetectors is slow decay current due to the presence of more photo persistent current (PPC-the current present in the device even after the UV light off) [69,187]. The films **c** and **d**-based devices (**C**, **D**, **G**, and **H**) exhibiting the slow growth and decay times compared to film **a** based devices (**A** and **E**). The slow growth may be due to the presence of charge trapped states due to the Alq_3 and slow decay is related to photo persistent current [69,269,273]. The devices (**B** and **F**) based on film **b** showing the fast responses (growth and decay) than that of the other devices. The incorporated Alq_3 molecules with Alq_3/ZnO molar ratio of $0.5x10^{-3}$ predominantly present on the ZnO surface (evident from EDAX and XPS) which may decrease the charge trapped states and PPC in the film **b** resulting in the fast responses of the devices **B** and **F** than that of the other devices [69,156,188]. From the UV photoresponses of the devices, it is observed that the hybrid films with Alq_3/ZnO molar of 0.5×10^{-3} (film **b**) are preferable for the fast UV responses whereas the hybrid films with molar ratio of 3×10^{-3} (film **d**) are useful for large

photocurrents and current gains. It is observed that interestingly the devices are responding even at 0V (no bias) which are called self-powered UVPDs [68,268]. Without any bias the devices are exhibiting the currents in micro-ampere under the UV illumination even at low power.

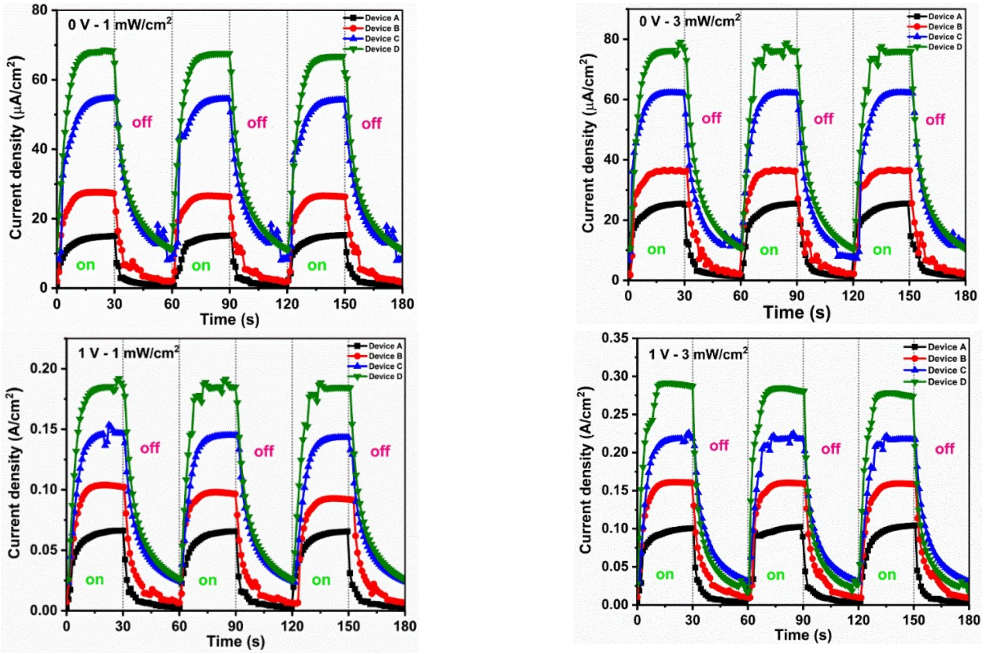

Fig. 8.6. Time-dependent photoresponse characteristics of UV-photodetectors based on pure ZnO (device **A**) and Alq_3/ZnO (devices **B-D**) hybrid thin films using pristine ITO.

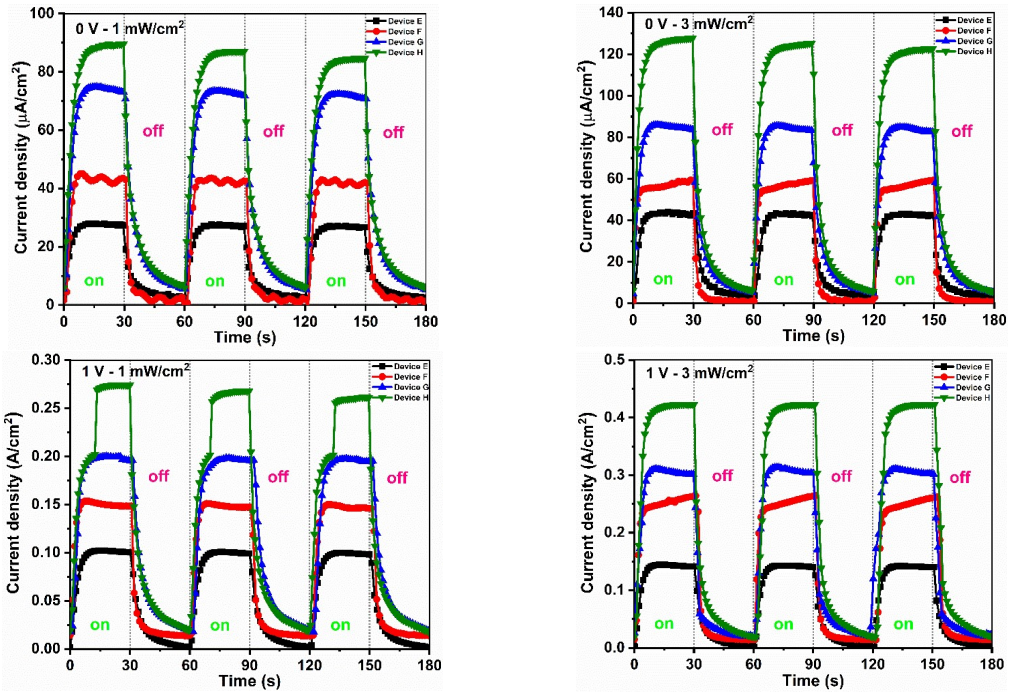

Fig. 8.7. Time-dependent photoresponse characteristics of UV-photodetectors based on pure ZnO (device **E**) and Alq_3/ZnO (devices **F-H**) hybrid thin films using annealed ITO.

Table 8.2. Characteristics of UV photodetectors (**A-D**) based on ZnO (**a**) or Alq_3/ZnO (**b-d**) hybrid thin films using pristine ITO films.

Device	Molar ratio of Alq_3/ZnO	Photocurrent density (J_{ph}) (mA/cm^2)	Current gain (G)	Responsivity (R) (A/W)	Detectivity (D) ($\times 10^{12}$)	Response time (s)	
						growth	decay
A	0 (Pristine)	39.8	91.1	39.8	6.73	6.73	10.56
B	$0.5x10^{-3}$	102.8	85.2	102.8	5.17	5.48	8.35
C	$1.3x10^{-3}$	166.5	111.3	166.5	0.23	8.51	15.98
D	$3x10^{-3}$	265.0	480.7	265.0	19.79	7.36	14.54

Table 8.3. Characteristics of UV photodetectors (**E-H**) based on ZnO (**a**) or Alq_3/ZnO (**b-d**) hybrid thin films using annealed ITO films at 300 °C.

Device	Molar ratio of Alq_3/ZnO	Photocurrent density (J_{ph}) (mA/cm^2)	Current gain (G)	Responsivity (R) (A/W)	Detectivity (D) ($\times 10^{12}$)	Response time (s)	
						growth	decay
E	0 (Pristine)	54.7	101.7	54.7	8.26	5.41	10.43
F	$0.5x10^{-3}$	188.1	110.7	188.1	6.60	3.05	4.78
G	$1.3x10^{-3}$	383.3	148.4	383.3	8.71	5.25	12.47
H	$3x10^{-3}$	471.3	560.6	471.3	23.49	7.68	11.71

In order to study the effect of annealing of ITO film in ZnO or Alq_3/ZnO based UV photodetectors, the J-V plots (corresponding to the dark and UV light) were drawn with respect to the ITO and annealed ITO. The Fig. 8.8 and Fig. 8.9 show the semi-log plots of J-V characteristics under dark and UV light representing the variation in the current density due to annealing of ITO film. In all the graphs, black color graphs represent the current density of pristine ITO based devices and red color graphs represent the current density of annealed ITO based devices. From the Fig. 8.8 and Fig 8.9, it is clearly observed that the devices using

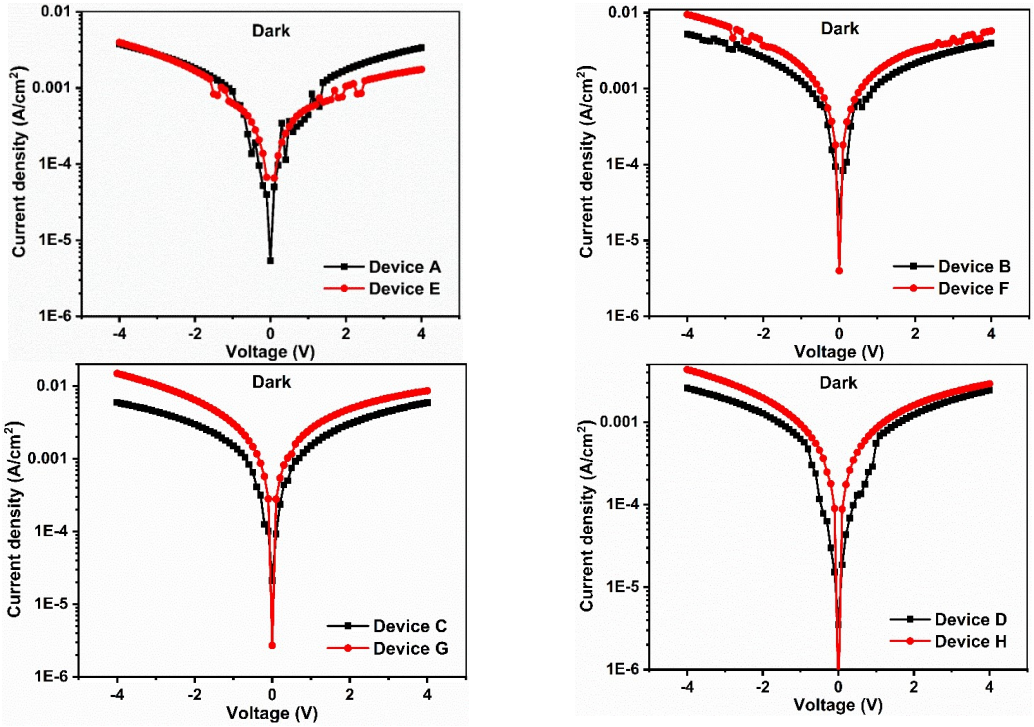

Fig. 8.8. J-V characteristics of pure ZnO and Alq_3/ZnO hybrid thin film based UVPDs using pristine ITO and annealed ITO under dark condition.

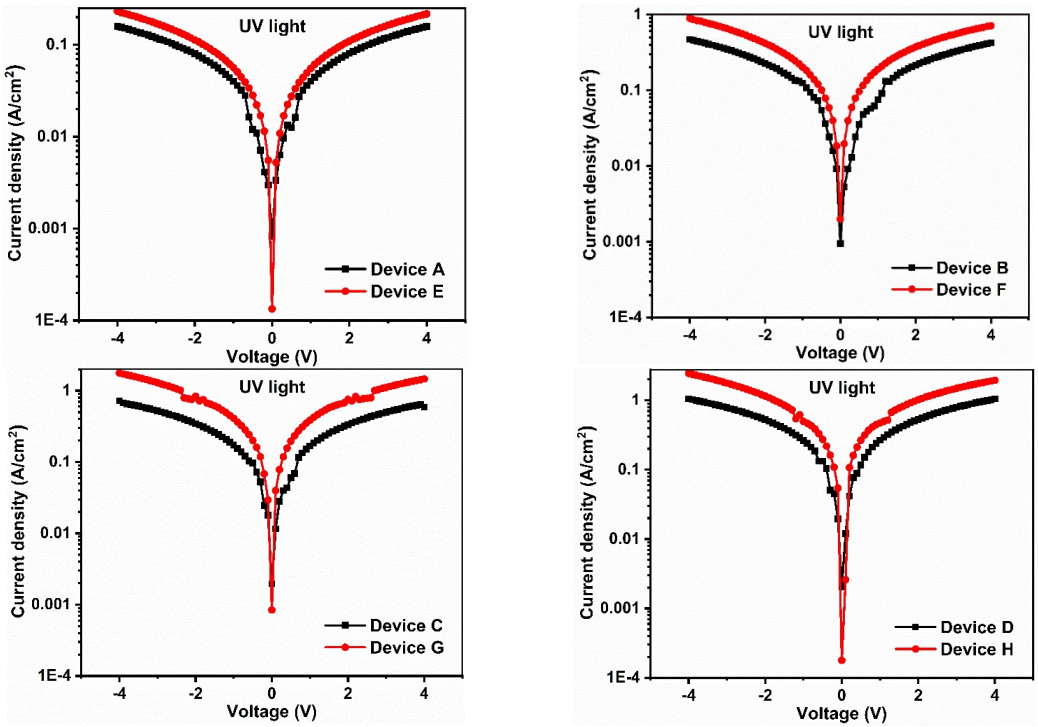

Fig. 8.9. J-V characteristics of pure ZnO and Alq_3/ZnO hybrid thin film based UVPDs using pristine and annealed ITO under UV light.

annealed ITOs exhibit the improved current density than that of devices using pristine ITO. As discussed in the earlier chapters the annealing of ITO up to 300 ℃ the quality of ITO film is observed to be increased without affecting its surface and electrical properties [131]. The crystallinity of the ITO film is increased with increasing the annealing temperature. There is a distinct change in the surface morphology of ITO film annealed at 400 ℃ showing the grain-like structure with increased roughness. The improved hole injection was also observed by annealing of ITO film up to 300 ℃ under the normal ambient [131]. Thus, it is observed that the improved ITO film quality (annealed at 300 ℃) enhances the current densities and device performances in pure ZnO or Alq_3/ZnO hybrid films based UVPDs [131,267,274]. The improved crystallinity of ITO film at 300 ℃ may enhance the charge transport in ZnO and Alq_3/ZnO films, resulting improved photoresponses of UVPDs. The 300 ℃ annealed ITO film may form the proper interface contact with the spin coated hybrid films, resulting in enhanced charge transport and hence current densities in the UVPDs [241,263]. The UVPDs using annealed ITOs also exhibit the fast growth and decay times when compared to that of UVPDs using pristine ITOs (Table 8.2 and 8.3). The annealed ITO film may decrease the charge-trap states in the films due to the large electric fields resulted in fast growth of current density [147,267]. In the decay process the enhanced electric fields forcing the charge carriers for the fast collection by the electrodes leading to the less photo persistent current and resulting in fast decay time. It is observed that Alq_3/ZnO hybrid thin films exhibit the improved photoresponses than that of pure ZnO thin film-based devices.

8.4. Conclusion

The UVPDs based on spin-coated Alq_3/ZnO hybrid thin films using annealed ITO at 300 ℃ improves the UV light detection when compared to that of UVPDs using pristine ITO. The UVPDs using annealed ITO film exhibit the enhanced current density with increased charge transport in the hybrid films. The annealed ITO film supports for fast responses (less growth

and decay times) by decreasing charge trapped states in the hybrid films. The Alq_3/ZnO hybrid films exhibit the improved electrical properties with increased carrier concentration and mobility upon the incorporation of Alq_3 molecules in ZnO. The electron-only devices (EODs) based on hybrid films reveal the effective electron injection with distinct rise in current density. The UVPDs based on Alq_3/ZnO hybrid films using annealed ITOs exhibit the improved photoresponses for simple and cost-effective fabrication of UV photodetector devices to serves as self-powered UVPDs.

Chapter: 9

Summary, Conclusion and Perspectives for Future Work

This chapter summarizes and concludes all the results discussed on Alq_3/ZnO hybrid thin films and their application in UV photodetectors. It also summarizes the effect of annealing of ITO film on hole injection/extraction in OLEDs/OSCs. It concludes on ITO annealing strategy to improve the optoelectronic device performances. This chapter summarizes the UV photodetectors based on Alq_3/ZnO hybrid thin films coated on glass, pristine ITO, and annealed ITO substrates.

9.1. Summary of the Research work

This doctoral thesis research work has been carried out to explore the Alq_3/ZnO hybrid thin films and ITO annealing strategy for their application to improve the optoelectronic device performances. The solution processed Alq_3/ZnO hybrid thin films have been prepared by using cost effective sol-gel derived spin-coating method. The Alq_3 solution was incorporated in ZnO sol-gel precursor with 20, 40, and 60 vol.% to make 5 mL solution each and the corresponding Alq_3/ZnO molar ratios are 0.5×10^{-3} (film **b**), 1.3×10^{-3} (film **c**), and 3×10^{-3} (film **d**) and pure ZnO (film **a)**. The thin films were coated using cost effective spin-coating technique. The preparation methods, coating parameters, and annealing conditions were well optimized for high quality uniform thin films. The Alq_3/ZnO hybrid thin films exhibit the higher transmittance of more than 80% in the visible region which is most advantageous property required for optoelectronic devices. The incorporated Alq_3 molecules get adsorbed onto the grain boundaries of ZnO along the (002) hkl plane, forming the Alq_3 capped ZnO particles. This capping of Alq_3 controls the ZnO growth and form the ZnO nanoparticles with improved crystalline properties. The increased optical band gap of ZnO with the incorporation of Alq_3 supports the formation of ZnO nanoparticles attributed to the quantum confinement effect. The

pristine ZnO and Alq_3/ZnO hybrid thin films exhibit hexagonal wurtzite structure with highly textured c- axis orientation along (002) plane perpendicular to substrate. These highly textured films were achieved using simple spin coating technique with proper optimization. The width of the wrinkles on the surface of sol-gel derived ZnO thin films is observed to be decreased upon incorporation of Alq_3 making the surface smooth with decreased roughness. This smooth surface will make a proper interface contact with the adjacent layers which facilitates the charge injection in the devices. The EDAX and XPS reveal that the Alq_3 molecules predominantly present on the surface of film **b**. The XPS studies conform the incorporation of Alq_3 in ZnO and corroborate that the Alq_3 molecules may be adsorbed onto the surface of ZnO nanoparticles (chemisorption), showing the existence of chemical interaction between Alq_3 and ZnO in the hybrid films. Raman studies reveal the sol–gel derived spin-coated ZnO thin film has hexagonal wurtzite structure. The FTIR also conforms the incorporation of Alq_3 in ZnO by showing the increase in carbonyl group (C=O) upon Alq_3 incorporation. Importantly, the incorporation of Alq_3 enhances the band edge emission of ZnO. There is an energy transfer from Alq_3 to ZnO via Carbonyl group in hybrid thin films by exciting the films with the wavelength from UV region (324 nm). The increase in carbonyl group with the incorporation of Alq_3 facilitate the energy transfer from Alq_3 to ZnO. The conductivity of the hybrid thin films was estimated using Hall effect measurements and four probe setup and observed the increased conductivity of hybrid thin films upon the incorporation of Alq_3. The electron-only devices (EODs) were fabricated to study the electron transporting properties of Alq_3/ZnO hybrid thin films. The charge injection in EODs is observed to be enhanced with the incorporation of Alq_3 in ZnO. It is conformed that the Alq_3 incorporated ZnO thin films exhibit the improved electron transporting properties which can be used as alternative electron transporting materials in the optoelectronic device applications. Based on the enhanced PL emission in the UV region the UV photoresponses of Alq_3/ZnO hybrid thin films were verified by fabricating the UV photodetectors. For the comparison of UV photoresponses the UVPDs were fabricated using

glass substrate with simple device structure of glass substrate/ZnO or Alq_3:ZnO/Al where the Al electrodes are used for ohmic contacts. The UVPDs based on Alq_3/ZnO hybrid thin films exhibit the improved devices performances than the pristine ZnO based UVPDs. The current gain, external quantum efficiency (EQE), and time constants are compared in Table 9.1. The UVPD based on film **b** (Alq_3/ZnO molar ratio – 0.5×10^{-3}) is showing the fast responses with less growth and decay times.

The film **b** is chosen for Ni^{7+} SHI irradiation to further improve the UVPDs performance. The thin films were irradiated with the Ni^{7+} SHI ion fluences of 5×10^{11}, 1×10^{12}, and 5×10^{12} ions/cm^2 and the results are compared with the pristine (unirradiated) Alq_3/ZnO film. The film exhibits the decrease in transmittance with increasing ion fluences due to the scattering of light photons by the ion tracks. The ion influence is not affecting the band gap, there is a slight decrease at the higher ion fluence of 5×10^{12} ions/cm^2 attributing the quantum confinement effect. The crystallite size is observed to be increased up to the ion fluence of 1×10^{12} ions/cm^2 due to the release in stress in the crystalline planes with decreased dislocation density and lattice strain. The ion fluence increases the roughness of the films by creating the ion tracks. The defect level (DL) emission is enhanced with decreased near band edge emission for increasing the ion fluences. The V_O and Zn_i enhance the charge carrier density in the films. The sheet resistance is decreased up to the ion fluences of 1×10^{12} ions/cm^2 revealing the improved conducting properties of the Alq_3/ZnO hybrid films with Ni SHI irradiation. The UVPDs also exhibit the enhanced device performances up to the ion fluences of 1×10^{12} ions/cm^2 with fast responses (Table 9.1).

In order to further improve the optoelectronic devices performances of OLED, OSC, and UVPDs, the ITO annealing strategy is utilized. The ITO highly affects the charge injection/extraction in the devices. We achieved the enhanced charge injection/extraction in the devices and hence device performances by annealing the ITO anode film at higher temperature. The ITO films were annealed at 200 °C, 300 °C, and 400 °C under the normal ambient for 1 hr.

The quality of the ITO film is observed to be improved up to the annealing of 300 °C. Annealing at 400 °C is highly affecting the ITO quality which decreases the transmittance, carrier concentration, mobility, increases the roughness, resistivity and sheet resistance. Upto the annealing at 300 °C the transmittance and crystalline properties improve without affecting the electrical and surface properties much. The hole-only devices (HODs) were fabricated based on annealed ITOs using the structure of ITO (pristine or annealed)(200 nm)/TPD(60 nm)/Al(120 nm). The enhanced current density or hole injection was observed upto the 300 °C and then decreased for 400 °C annealing. The OLEDs were also fabricated based on annealed ITOs using the device structure of ITO(pristine or annealed)(200 nm)/TPD(60 nm)/Alq_3(60 nm)/LiF(1 nm)/Al(120 nm). It exhibits the enhanced electroluminescence (EL) emission upto the annealing at 300 °C and it is drastically diminished for 400 °C annealed ITO.

In order to confirm the ITO annealing effect on OSCs, the OSCs were fabricated based on annealing ITOs using the structure of ITO(pristine or annealed)/PEDOT:PSS(45 nm)/P3HT:PCBM(100 nm)/LiF(1 nm)/Al(120 nm). The ITO annealing characteristics were studied by spin-coating the PEDOT:PSS onto the annealed ITOs as ITO/PEDOT:PSS bilayer structure. The ITO/PEDOT:PSS bilayer films were exhibited the good transmittance of about 95% in the visible region and it is not affected by the ITO annealing. There is drastic decrease in transmittance (increased absorption) in the UV region at 325 nm for 400 °C annealed ITO revealing the decrease in band gap attributed to the quantum confinement effect. The crystallite size of ITO/PEDOT:PSS bilayer structure was observed to decrease with decreased dislocation density and lattice strain. There is no considerable change in sheet resistance by annealing the ITO upto 300 °C and is increased at 400 °C. The spin coated PEDOT:PSS film onto the 400 °C annealed ITO suppresses the wrinkle kind morphology and makes the surface smooth. The hole injection properties of ITO/PEDOT:PSS bilayer structure were characterized by fabricating the HODs using the device structure of ITO(pristine or annealed)(200 nm)/PEDOT:PSS(45 nm)/TPD(60 nm)/Al(120 nm). The current density is observed to be increased by annealing the

ITO at higher temperatures. The increased crystallite size, smooth surface morphology, and enhanced hole transporting properties attributed the improved interface properties of ITO(400 °C)/PEDOT:PSS bilayer structure. Even though the annealed ITO at 400 °C gives the lowest performance in OLEDs it is giving the best performance in OSCs with bilayer structure. The spin-coated PEDOT:PSS covers the wrinkle gaps by properly aligning with the 400 °C annealed ITO surface which is enhancing the interface properties for charge extraction of charge carrier resulting in improved performance of HODs and OSCs.

It is conformed that the annealing of ITO at higher temperatures (300 °C) gives the improved performance of the devices. Further an attempt is made to improve the UV photodetection performances of Alq_3/ZnO hybrid thin films by utilising the ITO annealing strategy. The UV photodetectors were fabricated by spin-coating of pure ZnO or Alq_3/ZnO precursors onto the pristine or annealed ITO film. The UVPDs were fabricated using the structure of ITO (pristine or annealed ITO at 300 °C)(200 nm)/ZnO or Alq_3/ZnO(~200 nm)/Al(120 nm). The ITO film is used to enhance the charge transport in pure ZnO or Alq_3/ZnO hybrid thin films. The UVPDs using ITOs (pristine or annealed) exhibit the several orders of increased responsivity, detectivity, and EQE when compared with that of UVPDs without ITO film (Table 9.2). On the other hand, the current gain of these devices is decreased when compared to UVPDs without ITOs which is due to the higher dark current density of UVPDs with ITO film. It is important that UVPDs using ITOs act like self-biased devices (giving the responses at 0V) where the UVPDs using glass substrates are not respond at 0V. The UVPDs using ITOs exhibit the fast responses than the devices made on glass substrates which may be due to the decreased charge-trap states by ITOs.

Table 9.1. Characteristics of UV photodetectors based on ZnO or Alq_3/ZnO hybrid thin films using pristine and Ni^{7+} SHI irradiated Alq_3/ZnO hybrid thin films.

Device	Molar ratio of Alq_3/ZnO	UVPDs based on ZnO or Alq_3/ZnO hybrid films on glass substrates				UVPDs based on pristine and Ni^{7+} SHI irradiated Alq_3/ZnO hybrid film (b)				
		Gain	EQE (%) $\times 10^{-3}$	Growth/Decay Time (s)		SHI Fluences (ions/cm^2)	gain	EQE (%) $\times 10^{-3}$	Growth/Decay Time (s)	
				τ_g	τ_d				τ_g	τ_d
A	**0 (Pristine)**	330	3.46	4.8	17.2	**Pristine**	351	14.1	9.04	12.1
B	**0.5x10^{-3}**	384	8.54	6.5	13.9	**5×10^{11}**	477	25.5	2.49	8.08
C	**1.3x10^{-3}**	636	13.4	16.8	19.0	**1×10^{12}**	543	43.2	4.67	5.81
D	**3x10^{-3}**	706	18.1	15.7	20.1	**5×10^{12}**	260	8.13	3.75	6.63

Table 9.2. Characteristics of UV photodetector based on ZnO or Alq_3/ZnO hybrid thin films using pristine ITO and annealed ITO thin films.

Device	Molar ratio of Alq_3/ZnO	UVPDs based on ZnO or Alq_3/ZnO hybrid films using pristine ITO films				Device	UVPDs based on ZnO or Alq_3/ZnO hybrid films using annealed (300 ℃) ITO films			
		Gain	EQE (%)	Growth/Decay Time (s)			Gain	EQE (%)	Growth/Decay Time (s)	
				τ_g	τ_d				τ_g	τ_d
A	0 (Pristine)	91	135	6.73	10.56	**E**	101	186	5.41	10.43
B	0.5x10^{-3}	85	349	5.48	8.35	**F**	110	640	3.05	4.78
C	1.3x10^{-3}	111	568	8.51	15.98	**G**	148	1300	5.25	12.47
D	3x10^{-3}	480	901	7.36	14.54	**H**	560	1600	7.68	11.71

9.2. Conclusion of the research work

It has been concluded that the UV photodetection properties of Alq3/ZnO hybrid thin film were found to be enhanced by incorporating the Alq_3 molecules in ZnO thin film. The Alq_3 molecules in Alq_3/ZnO hybrid thin film transfer the absorbed UV energy to ZnO, resulting in the enhanced NBE emission. The incorporated Alq_3 molecules adsorbed onto the grain boundaries of ZnO and are forming the Alq_3 capped ZnO nanoparticles. The conducting properties (carrier density and mobility) of ZnO thin film are observed to be enhanced upon incorporation of Alq_3. The EODs show augmented current density for Alq_3 incorporated ZnO film, revealing the efficient electron transporting properties in Alq_3/ZnO hybrid thin films. The Ni^{7+} SHI irradiated Alq_3/ZnO hybrid thin film exhibits the enhanced PL emission related to the V_O and Zn_i which increase free charge carriers in the film. The SHI irradiation decreased the sheet resistance of thin films upto the ion fluence of 1×10^{12} ions/cm^2. The UVPDs based on Ni^{7+} SHI irradiation reveal the enhanced device characteristics with increased current gain, responsivity, detectivity, EQE, and fast growth and decay currents when compared with that of unirradiated film based UVPDs. It is also concluded that the annealing strategy of ITO anode film at higher temperatures improves the optoelectronic devices performance. The ITO annealing at higher temperature enhances the hole injection in OLEDs, hole extraction in OSCs, and charge transport in UVPDs. The annealing of ITO upto 300 °C improves the film quality with enhanced crystallite size and conducting properties without altering the optical transmittance. The improved ITO film quality forms the proper interface contact with the adjacent layers, resulting in improved charge injection in OLEDs. The spin-coated PEDOT:PSS solution onto the 400 °C annealed ITO aligned with the wrinkles and make the smooth surface. The wrinkles increase the area of contact with the spin-coated PEDOT:PSS film which leads to the proper alignment of ITO/PEDOT:PSS bilayers, resulting in effective charge extraction in OSCs. The fabricated HODs based on annealed ITO film conform improved charge injection/extraction in the devices with reduced barrier potentials at the interfaces. The UVPDs

based on ZnO or Alq_3/ZnO hybrid thin films made on ITO film show the higher current density in the order of amperes whereas the devices made on glass substrate exhibit milliampere currents. The drastic enhancement in the current density is due to the improved charge transport in hybrid thin films made on ITO film. The devices using ITO film also exhibit the fast UV responses which may be due to the decreasing of charge traps at high electric fields. The UVPDs have been used as self-powered devices which work at zero bias. The annealing of ITO at higher temperature may improve the interface properties at ITO/Alq_3:ZnO, leading to further strengthening of electric fields for enhanced current densities. This suppresses the charge traps effectively resulting in much fast responses of device using annealed ITO film. Hence, it is concluded that the Alq_3/ZnO hybrid thin films serve as alternative and cost-effective electron transporting materials in hybrid material based optoelectronic devices certainly. The ITO annealing strategy is found to be one of the best methods to improve the anodic properties and also optoelectronic device performances. The UVPDs based on Alq_3/ZnO hybrid thin films could be the cost-effective devices for the improved UV light detector applications.

9.3. Future research work

It is to be further continued as future research work that utilizing Alq_3/ZnO hybrid thin films as alternative electron transporting layer in OLEDs and OSCs and achieving the improved device performances. Further to optimize the Alq_3/ZnO hybrid thin films for developing solution processed OLEDs and OSCs for commercial applications. It is proposed to utilize the strategy of ITO annealing for improved performances of Alq_3/ZnO hybrid thin film based optoelectronic devices for the improved device performances. It is suggested to explore the novel organic/ZnO or organic/inorganic compounds for efficient energy transfer and charge transport for their applications in the future cost-effective solution processed optoelectronic devices.

References

[1] M.A. Baldo, M.E. Thompson, S.R. Forrest, High-efficiency fluorescent organic light-emitting devices using a phosphorescent sensitizer, Nature, 403 (2000) 750–753, https://doi.org/10.1038/35001541.

[2] M.A. Baldo, D.F. O'Brien, Y. You, A. Shoustikov, S. Sibley, M.E. Thompson, S.R. Forrest, Highly efficient phosphorescent emission from organic electroluminescent devices, Nature, 395 (1998) 151–154, https://doi.org/10.1038/25954.

[3] K. Thangaraju, R. Kumaran, K. Asokan, P. Ramamoorthy, D. Kanjilal, J. Kumar, Photoluminescence of Tris-(8-hydroxyquinoline)aluminum thin films and influence of swift heavy ion irradiation, Polym. Plast. Technol. Eng., 47 (2008) 479–482, https://doi.org/10.1080/03602550801952003.

[4] K. Thangaraju, J. Kumar, P. Amaladass, A.K. Mohanakrishnan, V. Narayanan, Study on photoluminescence from tris-(8-hydroxyquinoline)aluminum thin films and influence of light, Appl. Phys. Lett., 89 (2006), https://doi.org/10.1063/1.2338566.

[5] K. Thangaraju, R. Kumaran, T. Mohanty, K. Asokan, P. Ramamurthy, D. Kanjilal, J. Kumar, Swift heavy ion irradiation-induced modifications of tris-(8- hydroxyquinoline)aluminum thin films, Radiat. Eff. Defects Solids, 161 (2006) 695–700, https://doi.org/10.1080/10420150600909604.

[6] K. Thangaraju, P. Amaladass, K.S. Bharathi, A.K. Mohanakrishnan, V. Narayanan, J. Kumar, Studies on influence of light on fluorescence of Tris-(8-hydroxyquinoline)aluminum thin films, Appl. Surf. Sci., 255 (2009) 5760–5763, https://doi.org/10.1016/j.apsusc.2008.12.079.

[7] A. Antonello, G. Brusatin, M. Guglielmi, A. Martucci, V. Bello, G. Mattei, P. Mazzoldi, G. Pellegrini, Hybrid organic-inorganic ZnS-loaded nanocomposite films for stable optical coatings, Thin Solid Films, 518 (2010) 6781–6786, https://doi.org/10.1016/j.tsf.2010.06.013.

[8] S. Ummartyotin, N. Bunnak, J. Juntaro, M. Sain, H. Manuspiya, Hybrid organic-inorganic of ZnS embedded PVP nanocomposite film for photoluminescent application, C. R. Phys.13 (2012) 994–1000, https://doi.org/10.1016/j.crhy.2012.09.008.

[9] L. Valkunas, Electronic processes in organic systems, Chem. Phys., 404 (2012) 1, https://doi.org/10.1016/j.chemphys.2012.06.010.

[10] K. Walzer, B. Maennig, M. Pfeiffer, K. Leo, Highly efficient organic devices based on electrically doped transport layers, Chem. Rev, 107 (2007) 1233–1271, https://doi.org/10.1021/cr050156n

[11] H. Spanggaard, F.C. Krebs, A brief history of the development of organic and polymeric photovoltaics, Sol. Energy Mater. Sol. Cells, 83 (2004) 125–146, https://doi.org/10.1016/j.solmat.2004.02.021.

[12] A.R. Melnyk, D.M. Pai, Organic photoreceptors: an overview, Hard Copy and Printing Materials, Media, and Processes, 1253 (1990) 141, https://doi.org/10.1117/12.19809.

[13] A. Bernanose, Electroluminescence of organic compounds, Br. J. Appl. Phys., 6 (1955), S54, https://doi.org/10.1088/0508-3443/6/S4/319.

[14] W. Helfrich, W.G. Schneider, Recombination radiation in anthracene crystals, Phys. Rev. Lett. , 14 (1965) 229–231. https://doi.org/10.1103/PhysRevLett.14.229.

[15] M. Pope, H.P. Kallmann, P. Magnante, Electroluminescence in organic crystals [16], J. Chem. Phys., 38 (1963) 2042–2043, https://doi.org/10.1063/1.1733929.

[16] J.H. Burroughes, D.D.C. Bradley, A.R. Brown, R.N. Marks, K. Mackay, R.H. Friend, P.L. Burns, A.B. Holmes, Light-emitting diodes based on conjugated polymers, Nature, 347 (1990) 539–541, https://doi.org/10.1038/347539a0.

[17] C.W. Tang, S.A. Vanslyke, Organic electroluminescent diodes, Appl. Phys. Lett., 51 (1987) 913–915, https://doi.org/10.1063/1.98799.

[18] P.F. Seidler, J.M. Shaw, Organic electronics: Introduction by, IBM J. Res. Dev., 45 (2001) 3–9, https://doi.org/DOI:10.1147/rd.451.0003.

[19] J. You, L. Dou, K. Yoshimura, T. Kato, K. Ohya, T. Moriarty, K. Emery, C.C. Chen, J. Gao, G. Li, Y. Yang, A polymer tandem solar cell with 10.6% power conversion efficiency, Nat. Commun., 4 (2013) 1410–1446, https://doi.org/10.1038/ncomms2411.

[20] L. Meng, Y. Zhang, X. Wan, C. Li, X. Zhang, Y. Wang, X. Ke, Z. Xiao, L. Ding, R. Xia, H.L. Yip, Y. Cao, Y. Chen, Organic and solution-processed tandem solar cells with 17.3% efficiency, Science, 361 (2018) 1094–1098, https://doi.org/10.1126/science.aat2612.

[21] V. Podzorov, V.M. Pudalov, M.E. Gershenson, Field-effect transistors on rubrene single crystals with parylene gate insulator, Appl. Phys. Lett., 82 (2003) 1739–1741, https://doi.org/10.1063/1.1560869.

[22] J.N. Hay, The physical ageing of amorphous and crystalline polymers, Pure Appl. Chem., 67 (1995) 1855–1858, https://doi.org/ /10.1351/pac199567111855.

[23] R.F. Boyer, Mechanical motions in amorphous and semi-crystalline polymers, Polymer, 17 (1976) 996–1008, https://doi.org/10.1016/0032-3861(76)90174-9.

[24] W. Brütting, Introduction to the Physics of Organic Semiconductors, ISBN: 352740550X (2006) 1–14, https://doi.org/10.1002/3527606637.ch.

[25] A.P. Demchenko, Introduction to fluorescence sensing, ISBN: 978-1-4020-9002-8, (2009) 1–586, https://doi.org/10.1007/978-1-4020-9003-5.

[26] R. Šípoš, J. Šima, Jablonski diagram revisited, Revista Cubana de Fisica. 37 (2020) 125–130.

[27] D. Frackowiak, The Jablonski diagram, J. Photochem. Photobiol., 2 (1988) 399, https://doi.org/10.1016/1011-1344(88)85060-7.

[28] A. Jabłoństski, Efficiency of anti-stokes fluorescence in dyes, Nature, 131 (1933) 839–840, https://doi.org/10.1038/131839b0.

[29] B. Valeur, M.N. Berberan-Santos, A brief history of fluorescence and phosphorescence before the emergence of quantum theory, J. Chem. Educ., 88 (2011) 731–738, https://doi.org/10.1021/ed100182h.

[30] A.T. Rhys Williams, S.A. Winfield, J.N. Miller, Relative fluorescence quantum yields using a Computer-controlled luminescence spectrometer, The Analyst, 108 (1983) 1067–1071, https://doi.org/10.1039/an9830801067.

[31] U. Wolf, V.I. Arkhipov, H. Bässler, Current injection from a metal to a disordered hopping system. I. monte carlo simulation, Phys. Rev. B Condens. Matter, 59 (1999) 7507–7513, https://doi.org/10.1103/PhysRevB.59.7507.

[32] J.C. Scott, Metal–organic interface and charge injection in organic electronic devices, J. Vac. Sci. Technol. A 21 (2003) 521–531, https://doi.org/10.1116/1.1559919.

[33] M.S. Saveleva, K. Eftekhari, A. Abalymov, T.E.L. Douglas, D. Volodkin, B. V. Parakhonskiy, A.G. Skirtach, Hierarchy of hybrid materials-the place of inorganics-in-organics in it, their composition and applications, Front. Chem., 7 (2019), https://doi.org/10.3389/fchem.2019.00179.

[34] M. Gon, K. Tanaka, Y. Chujo, Creative synthesis of organic-inorganic molecular hybrid materials, Bull. Chem. Soc. Jpn., 90 (2017) 463–474, https://doi.org/10.1246/bcsj.20170005.

[35] S.H. Mir, L.A. Nagahara, T. Thundat, P. Mokarian-Tabari, H. Furukawa, A. Khosla, Review—Organic-inorganic hybrid functional materials: An integrated platform for applied technologies, J. Electrochem. Soc., 165 (2018) B3137–B3156, https://doi.org/10.1149/2.0191808jes.

[36] G. Peng, X. Xu, G. Xu, Hybrid organic-inorganic perovskites open a new era for low-cost high efficiency solar cells, J. Nanomater., 2015 (2015), 1-10, https://doi.org/10.1155/2015/241853.

[37] P. Judeinstein, C. Sanchez, Hybrid organic-inorganic materials: a land of multidisciplinarity, J. Mater. Chem., 6 (1996) 511–525, https://doi.org/10.1039/JM9960600511.

[38] G. Kickelbick, Introduction to hybrid materials, ISBN: 978-3-527-31299-3, 2007, 1-48. https://doi.org/10.1002/9783527610495.ch1.

[39] S. Pandey, S.B. Mishra, Sol-gel derived organic-inorganic hybrid materials: Synthesis, characterizations and applications, J. Sol-Gel Sci. Technol., 59 (2011) 73–94, https://doi.org/10.1007/s10971-011-2465-0.

[40] R. Mobin, T.A. Rangreez, H.T.N. Chisti, Inamuddin, M. Rezakazemi, Organic-inorganic hybrid materials and their applications, (2019) 1135–1156, Nature, https://doi.org/10.1007/978-3-319-95987-0_33.

[41] M. Catauro, S.V. Ciprioti, Characterization of hybrid materials prepared by sol-gel method for biomedical implementations. A critical review, Materials, 14 (2021), 1788, https://doi.org/10.3390/ma14071788.

[42] V. Sharma, H. Sharma, S.K. Singh, R. Kumar, Y. Kumari, K. Sachdev, Organic-Inorganic hybrid structure as a conductive and transparent layer for energy and optoelectronic applications, ACS Appl. Electron. Mater., 3 (2021) 1601–1609, https://doi.org/10.1021/acsaelm.0c01099.

[43] D.K. Sharma, S. Shukla, K.K. Sharma, V. Kumar, A review on ZnO: Fundamental properties and applications, Mater. Today: Proc., (2020), https://doi.org/10.1016/j.matpr.2020.10.238.

[44] M.A. Borysiewicz, ZnO as a functional material, a review, Crystals, 9 (2019), https://doi.org/10.3390/cryst9100505.

[45] A. Kolodziejczak-Radzimska, T. Jesionowski, Zinc oxide-from synthesis to application: A review, Materials, 7 (2014) 2833–2881, https://doi.org/10.3390/ma7042833.

[46] Z.L. Wang, J. Song, Piezoelectric nanogenerators based on zinc oxide nanowire arrays, Science, 312 (2006) 242–246, https://doi.org/10.1126/science.1124005.

[47] A. M. Nahhas, Review of Recent Advances of ZnO Nanowires Based Sensors, American Journal of Nanomaterials, 8 (2020) 18–32, https://doi.org/10.12691/ajn-8-1-3.

[48] A. M. Nahhas, Introductory Chapter: Overview of ZnO Based Nano Materials and Devices Zinc Oxide Based Nano Materials and Devices, (2019), https://doi.org/10.5772/intechopen.85969.

[49] S. Yamaguchi, T. Iida, K. Matsui, Formation of Flower-Like Crystals of Tris(8-hydroxyquinoline)aluminum from 8-hydroxyquinoline on Anodic Porous Alumina, Adv. Mater. Sci. Eng, 2017 (2017), 1-10, https://doi.org/10.1155/2017/4150648.

[50] M. Brinkmann, G. Gadret, M. Muccini, C. Taliani, N. Masciocchi, A. Sironi, Correlation between molecular packing and optical properties in different crystalline polymorphs and amorphous thin films of mer-tris(8- hydroxyquinoline)aluminum(III), J. Am. Chem. Soc., 122 (2000) 5147–5157, https://doi.org/10.1021/ja993608k.

[51] W.B. Michael Cölle, Jürgen Gmeiner, Wolfgang Milius, Harald Hillebrecht, Preparation and Characterization of Blue-Luminescent Tris(8-hydroxyquinoline)aluminum (Alq3), Adv. Funct. Mater., 21 (2001) 1769–1773, https://doi.org/https://doi.org/10.1002/adfm.200390015.

[52] J.G. Mahakhode, B. Bahirwar, Tunable Photoluminescence from tris (8-hydroxyquinoline)aluminum (Alq_3), Proc. of ASID 06, 8-12 (2006) 237–239, http://www.iitk.ac.in/asid06/proceedings/papers/TP4_05.pdf.

[53] M. Cuba, G. Muralidharan, Enhanced luminescence properties of hybrid Alq3/ZnO (organic/inorganic) composite films, J. Lumin., 156 (2014) 1–7, https://doi.org/10.1016/j.jlumin.2014.07.008.

[54] P. Uthirakumar, E.K. Suh, C.H. Hong, Effect of zinc oxide incorporation on the morphology of tris(8-hydroxyquinoline)aluminum/zinc oxide hybrid nanomaterials, Thin Solid Films, 516 (2008) 7299–7305, https://doi.org/10.1016/j.tsf.2008.01.007.

[55] K. Thangaraju, J. Kumar, P. Amaladass, A.K. Mohanakrishnan, V. Narayanan, Study on photoluminescence from tris-(8-hydroxyquinoline)aluminum thin films and influence of light, Appl. Phys. Lett., 89 (2006), 082106, https://doi.org/10.1063/1.2338566.

[56] K. Thangaraju, R. Kumaran, T. Mohanty, K. Asokan, P. Ramamurthy, D. Kanjilal, J. Kumar, Swift heavy ion irradiation-induced modifications of tris-(8- hydroxyquinoline)aluminum thin films, Radiat. Eff. Defects Solids, 161 (2006) 695–700, https://doi.org/10.1080/10420150600909604.

[57] M. Cuba, G. Muralidharan, Effect of thermal annealing on the structural and optical properties of tris-(8-hydroxyquinoline)aluminum(III) (Alq3) films, Luminescence, 30 (2015) 352–357, https://doi.org/10.1002/bio.2738.

[58] N. Sun, C. Jiang, Q. Li, D. Tan, S. Bi, J. Song, Performance of OLED under mechanical strain: a review, J. Mater. Sci.: Mater. Electron., 31 (2020) 20688–20729, https://doi.org/10.1007/s10854-020-04652-5.

[59] A. Bernanose, Electroluminescence of organic compounds, British J. Appl. Phys., 6 (1955), S54, https://doi.org/10.1088/0508-3443/6/S4/319.

[60] R.H. Partridge, Electroluminescence from polyvinylcarbazole films: 1. Carbazole cations, Polymer, 24 (1983) 733–738,https://doi.org/10.1016/0032-3861(83)90012-5.

[61] Giulia Mattoni, The Concept System of an Organic Solar patent translators, 2015.

[62] I. Arbouch, Y. Karzazi, B. Hammouti, Organic photovoltaic cells: Operating principles, recent developments and current challenges – review, Phys. Chem. News,72 (2014) 73–84.

[63] L. Duan, A. Uddin, Progress in Stability of Organic Solar Cells, Adv. Sci., 7 (2020), https://doi.org/10.1002/advs.201903259.

[64] Q. Liu, Y. Jiang, K. Jin, J. Qin, J. Xu, W. Li, J. Xiong, J. Liu, Z. Xiao, K. Sun, S. Yang, X. Zhang, L. Ding, 18% Efficiency organic solar cells, Sci. Bull., 65 (2020) 272–275, https://doi.org/10.1016/j.scib.2020.01.001.

[65] A. Distler, C.J. Brabec, H.J. Egelhaaf, Organic photovoltaic modules with new world record efficiencies, Prog. Photovolt., 29 (2021) 24–31, https://doi.org/10.1002/pip.3336.

[66] M.B. Schubert, J.H. Werner, Flexible solar cells for clothing, Mater. Today, 9 (2006) 42–50, https://doi.org/10.1016/S1369-7021(06)71542-5.

[67] H. Chen, K. Liu, L. Hu, A.A. Al-Ghamdi, X. Fang, New concept ultraviolet photodetectors, Mater. Today, 18 (2015) 493–502, https://doi.org/10.1016/j.mattod.2015.06.001.

[68] B. Deka Boruah, Zinc oxide ultraviolet photodetectors: Rapid progress from conventional to self-powered photodetectors, Nanoscale Adv., 1 (2019) 2059–2085, https://doi.org/10.1039/c9na00130a.

[69] E. Monroy, F. Omnès, F. Calle, Wide-bandgap semiconductor ultraviolet photodetectors, Semicond. Sci. Technol., 18 (2003) 33–51, https://doi.org/10.1088/0268-1242/18/4/201.

[70] K. Liu, M. Sakurai, M. Aono, ZnO-based ultraviolet photodetectors, Sensors, 10 (2010) 8604–8634, https://doi.org/10.3390/s100908604.

[71] B. Deka Boruah, Zinc oxide ultraviolet photodetectors: Rapid progress from conventional to self-powered photodetectors, Nanoscale Adv., 1 (2019) 2059–2085, https://doi.org/10.1039/c9na00130a.

[72] I. ben Elkamel, N. Hamdaoui, A. Mezni, R. Ajjel, L. Beji, High responsivity and 1/: F noise of an ultraviolet photodetector based on Ni doped ZnO nanoparticles, RSC Adv., 8 (2018) 32333–32343, https://doi.org/10.1039/c8ra05567j.

[73] T.P. Nguyen, Polymer-based nanocomposites for organic optoelectronic devices. A review, Surf. Coat., 206 (2011) 742–752, https://doi.org/10.1016/j.surfcoat.2011.07.010.

[74] P.N. Prasad, Polymer science and technology for new generation photonics and biophotonics, Curr. Opin. Solid. State. Mater. Sci., 8 (2004) 11–19, https://doi.org/10.1016/j.cossms.2004.01.011.

[75] C.J. Wung, Y. Pang, P.N. Prasad, F.E. Karasz, Poly(p-phenylene vinylene)-silica composite: a novel sol-gel processed non-linear optical material for optical waveguides, Polymer, 32 (1991) 605–608, https://doi.org/10.1016/0032-3861(91)90471-T.

[76] Y. Li, A. Rizzo, R. Cingolani, G. Gigli, Bright white-light-emitting device from ternary nanocrystal composites, Adv. Mater, 18 (2006) 2545–2548, https://doi.org/10.1002/adma.200600181.

[77] G. Cheng, M. Mazzeo, S. D'Agostino, F. Della Sala, S. Carallo, G. Gigli, Pure white hybrid light-emitting device with color rendering index higher than 90, Opt. Lett. 35 (2010) 616, https://doi.org/10.1364/ol.35.000616.

[78] W.U. Huynh, J.J. Dittmer, A.P. Alivisatos, Hybrid nanorod-polymer solar cells, Science, 295 (2002) 2425–2427, https://doi.org/10.1126/science.1069156.

[79] J. Huang, Z. Yin, Q. Zheng, Applications of ZnO in organic and hybrid solar cells, Energy Environ. Sci., 4 (2011) 3861–3877, https://doi.org/10.1039/c1ee01873f.

[80] L. Znaidi, Sol-gel-deposited ZnO thin films: A review, Mater. Sci. Eng. B Solid State. Mater. Adv. Technol., 174 (2010) 18–30, https://doi.org/10.1016/j.mseb.2010.07.001.

[81] L. Armelao, M. Fabrizio, S. Gialanella, F. Zordan, Sol-gel synthesis and characterisation of ZnO-based nanosystems, Thin Solid Films, 394 (2001) 90–96, https://doi.org/10.1016/s0040-6090(01)01158-0.

[82] Y. Ohya, H. Saiki, Y. Takahashi, Preparation of transparent, electrically conducting ZnO film from zinc acetate and alkoxide, J. Mater. Sci., 29 (1994) 4099–4103, https://doi.org/10.1007/BF00355977.

[83] S. O'Brien, L.H.K. Koh, G.M. Crean, ZnO thin films prepared by a single step sol-gel process, Thin Solid Films, 516 (2008) 1391–1395, https://doi.org/10.1016/j.tsf.2007.03.160.

[84] J. Rao, R.J. Winfield, L.H.K. Koh, S. O'Brien, G.M. Crean, Patterned transparent zinc oxide films produced by sol-gel embossing, Phys. Status Solidi A, 205 (2008) 1938–1942, https://doi.org/10.1002/pssa.200778853.

[85] X.H. Wang, J. Shi, S. Dai, Y. Yang, A sol-gel method to prepare pure and gold colloid doped ZnO films, Thin Solid Films, 429 (2003) 102–107, https://doi.org/10.1016/S0040-6090(03)00057-9.

[86] H. Li, J. Wang, H. Liu, C. Yang, H. Xu, X. Li, H. Cui, Sol - Gel preparation of transparent zinc oxide films with highly preferential crystal orientation, Vacuum, 77 (2004) 57–62, https://doi.org/10.1016/j.vacuum.2004.08.003.

[87] G.J. Exarhos, X.D. Zhou, Discovery-based design of transparent conducting oxide films, Thin Solid Films, 515 (2007) 7025–7052, https://doi.org/10.1016/j.tsf.2007.03.014.

[88] M.D. Tyona, A theoritical study on spin coating technique, Adv. Mater. Res., 2 (2013) 195–208, https://doi.org/10.12989/amr.2013.2.4.195.

[89] D.B. Mitzi, L.L. Kosbar, C.E. Murray, M. Copel, A. Afzali, High-mobility ultrathin semiconducting films prepared by spin coating, Nature, 428 (2004) 299–303, https://doi.org/10.1038/nature02389.

[90] N. Sahu, B. Parija, S. Panigrahi, Fundamental understanding and modeling of spin coating process: A review, Indian J. Phys., 83 (2009) 493–502, https://doi.org/10.1007/s12648-009-0009-z.

[91] H.A.M. Mustafa, D.A. Jameel, Modeling and the main stages of spin coating process: A review, Journal of Applied Science and Technology Trends, 2 (2021) 91–95, https://doi.org/10.38094/jastt203109.

[92] H. Soonmin, M. Bilal Tahir, S.N. Das, M.R. Das, Preparation of Thin Films By Silar and Spin Coating Method, Eurasian J. Anal. Chem., (2019) 165–172.

[93] H. Latif, R. Zia, M. Irshad, H. Latif, Optical and Structural Properties of ZnxCd1-xS (X=0.2, 0.4, 0.6 AND 0.8), International Journal for Innovation Education and Research, 1 (2013) 30–46, https://doi.org/10.31686/ijier.vol1.iss4.124.

[94] A. Jilani, M.S. Abdel-wahab, A.H. Hammad, Advance Deposition Techniques for Thin Film and Coating, Modern Technologies for Creating the Thin-Film Systems and Coatings, (2017), https://doi.org/10.5772/65702.

[95] Dler Adil Jameel, Thin Film Deposition Processes, International Journal of Modern Physics and Applications, 1 (2015) 193–199, https://doi.org/http://www.aiscience.org/journal/paperInfo/ijmpa?paperId=1569.

[96] A.H.F. Muggleton, F.A. Howe, Crystal oscillator film thickness monitor, Nuclear Instruments and Methods, 28 (1964) 242–244, https://doi.org/10.1016/0029-554X(64)90429-X.

[97] G. Verma, M. Mishra, Development and Optimization of Uv-Vis Spectroscopy-a Review, Govinda et al., World J. Pharm. Res., 7 (2018) 1170–1180, https://doi.org/10.20959/wjpr201811-12333.

[98] D.F. Swinehart, The Beer-Lambert law, J. Chem. Educ., 39 (1962) 333–335. https://doi.org/10.1021/ed039p333.

[99] P.R. Jubu, F.K. Yam, V.M. Igba, K.P. Beh, Tauc-plot scale and extrapolation effect on bandgap estimation from UV–vis–NIR data – A case study of β-Ga2O3, J. Solid State Chem., 290 (2020) 121576, https://doi.org/10.1016/j.jssc.2020.121576.

[100] G.D. Gilliland, Photoluminescence spectroscopy of crystalline semiconductors, Mater. Sci. Eng. R Rep. 1997, https://doi.org/10.1016/s0927-796x(97)80003-4.

[101] M. Razeghi, Fundamentals of solid state engineering, 3rd Edition, (2009) 1–757, https://doi.org/10.1007/978-0-387-92168-6.

[102] A.A. Bunaciu, E. gabriela Udriştioiu, H.Y. Aboul-Enein, X-Ray Diffraction: Instrumentation and Applications, Crit. Rev. Anal. Chem., 45 (2015) 289–299, https://doi.org/10.1080/10408347.2014.949616.

[103] E.S. Ameh, A review of basic crystallography and x-ray diffraction applications, Int. J. Adv. Manuf. Technol., 105 (2019) 3289–3302, https://doi.org/10.1007/s00170-019-04508-1.

[104] N.S. Mclntyre, Quantitative Surface Analysis of Materials., ASTM Spec. Tech. Publ., 596 (1978) 1976–1977, https://doi.org/10.1016/0301-679x(79)90007-0.

[105] C.J. Powell, Quantitative Surface Analysis by X-ray Photoelectron Spectroscopy, Appl. Surf. Sci.. 1 (1978) 186–201.

[106] C.W. Oatley, The early history of the scanning electron microscope, J. Appl. Phys., 53 (1982), https://doi.org/10.1063/1.331666.

[107] H.J. Butt, B. Cappella, M. Kappl, Force measurements with the atomic force microscope: Technique, interpretation and applications, Surf. Sci. Rep., 59 (2005) 1–152, https://doi.org/10.1016/j.surfrep.2005.08.003.

[108] G. Leggett, Atomic force microscopy, Handbook of Adhesion: Second Edition. (2005) 50–52. https://doi.org/10.1002/0470014229.ch1.

[109] A.A. Ramadan, R.D. Gould, A. Ashour, On the Van der Pauw method of resistivity measurements, Thin Solid Films, 239 (1994) 272–275, https://doi.org/10.1016/0040-6090(94)90863-X.

[110] C. V. Raman, A new radiation [Reproduced from Indian J. Phys., 1928, 2,387-398], Curr. Sci., 74 (1998) 382–386, https://www.jstor.org/stable/24101519.

[111] S. Garrigues, M. de la Guardia, Vibrational spectroscopy, Handbook of Mineral Elements in Food, (2015) 301–312, https://doi.org/10.1002/9781118654316.ch15.

[112] C.J. Huang, Y.K. Su, S.L. Wu, The effect of solvent on the etching of ITO electrode, Mater. Chem. Phys., 84 (2004) 146–150, https://doi.org/10.1016/j.matchemphys.2003.11.021.

[113] Ocean Optics, USB2000+ Fiber Optic Spectrometer Installation and Operation Manual, Https://Oceanoptics.Com/Wp-Content/Uploads/USB2000-Operating-Instructions.Pdf. 38 (2010). http://www.analytik.co.uk/wp-content/uploads/2016/05/usb2000-operating-instructions.pdf?x29422.

[114] X. Li, J. Qi, Q. Zhang, Q. Wang, F. Yi, Z. Wang, Y. Zhang, Saturated blue-violet electroluminescence from single ZnO micro/nanowire and p-GaN film hybrid light-emitting diodes, Appl. Phys. Lett., 102 (2013) 221103, https://doi.org/10.1063/1.4809582.

[115] Y.S. Choi, J.W. Kang, D.K. Hwang, S.J. Park, Recent advances in ZnO-based light-emitting diodes, IEEE Trans. Electron Devices, 57 (2010) 26–41, https://doi.org/10.1109/TED.2009.2033769.

[116] A. Kolodziejczak-Radzimska, T. Jesionowski, Zinc oxide-from synthesis to application: A review, Materials, 7 (2014) 2833–2881, https://doi.org/10.3390/ma7042833.

[117] S. Pandey, S.B. Mishra, Sol-gel derived organic-inorganic hybrid materials: Synthesis, characterizations and applications, J. Sol-Gel Sci. Technol., 59 (2011) 73–94, https://doi.org/10.1007/s10971-011-2465-0.

[118] S.J. Yoo, H.J. Yun, I. Kang, K. Thangaraju, S.K. Kwon, Y.H. Kim, A new electron transporting material for effective hole-blocking and improved charge balance in highly efficient phosphorescent organic light emitting diodes, J. Mater. Chem. C, 1 (2013) 2217–2223, https://doi.org/10.1039/c3tc00801k.

[119] M.G. Shin, K. Thangaraju, S.O. Kim, J.W. Park, Y.H. Kim, S.K. Kwon, A new N-fluorenyl carbazole host material: Synthesis, physical properties and applications for highly efficient phosphorescent organic light emitting diodes, Org. Electron.,, 12 (2011) 785–793, https://doi.org/10.1016/j.orgel.2011.02.014.

[120] K. Thangaraju, J. Lee, J.I. Lee, H.Y. Chu, S.O. Kim, M.G. Shin, Y.H. Kim, K. Soon-Ki, 4,4′,4″-Tris(N-carbazolyl)-triphenylamine interlayer in highly efficient phosphorescent organic light emitting diodes based on tris[4-methyl-2-2(4′-trimethylsilylphenyl)pyridine]iridium complex, Thin Solid Films, 519 (2011) 6073–6076, https://doi.org/10.1016/j.tsf.2011.03.115.

[121] K. Thangaraju, P. Amaladass, K.S. Bharathi, A.K. Mohanakrishnan, V. Narayanan, J. Kumar, Studies on influence of light on fluorescence of Tris-(8-hydroxyquinoline)aluminum thin films, Appl. Surf. Sci., 255 (2009) 5760–5763, https://doi.org/10.1016/j.apsusc.2008.12.079.

[122] T. Earmme, E. Ahmed, S.A. Jenekhe, Solution-processed highly efficient blue phosphorescent polymer light-emitting diodes enabled by a new electron transport material, Adv. Mater, 22 (2010) 4744–4748, https://doi.org/10.1002/adma.201001585.

[123] J. Kulesza, B.S. Barros, S. Alves, Organic-inorganic hybrid materials: Metallacalixarenes. Synthesis and applications, Coord. Chem. Rev., 257 (2013) 2192–2212, https://doi.org/10.1016/j.ccr.2013.03.031.

[124] E. Holder, N. Tessler, A.L. Rogach, Hybrid nanocomposite materials with organic and inorganic components for opto-electronic devices, J. Mater. Chem., 18 (2008) 1064–1078, https://doi.org/10.1039/b712176h.

[125] M.R. Awual, M.M. Hasan, G.E. Eldesoky, M.A. Khaleque, M.M. Rahman, M. Naushad, Facile mercury detection and removal from aqueous media involving ligand impregnated conjugate nanomaterials, Chem. Eng. J., 290 (2016) 243–251, https://doi.org/10.1016/j.cej.2016.01.038.

[126] M.R. Awual, M.M. Hasan, M.M. Rahman, A.M. Asiri, Novel composite material for selective copper(II) detection and removal from aqueous media, J. Mol. Liq., 283 (2019) 772–780, https://doi.org/10.1016/j.molliq.2019.03.141.

[127] T. Sakata, K Hashimoto, M. Hiramotoff, New Aspects of Electron Transfer on Semiconductor Surface: Dye-Sensitization System, J. Phys. Chem., 94, 7, 3040–3045 1990, https://doi.org/https://doi.org/10.1021/j100370a056.

[128] J. Takada, H. Awaji, M. Koshioka, A. Nakajima, W.A. Nevin, Organic-inorganic multilayers: A new concept of optoelectronic material, Appl. Phys. Lett., 61 (1992) 2184–2186, https://doi.org/10.1063/1.108289.

[129] S. O'Brien, L.H.K. Koh, G.M. Crean, ZnO thin films prepared by a single step sol-gel process, Thin Solid Films, 516 (2008) 1391–1395, https://doi.org/10.1016/j.tsf.2007.03.160.

[130] H. Li, J. Wang, H. Liu, C. Yang, H. Xu, X. Li, H. Cui, Sol - Gel preparation of transparent zinc oxide films with highly preferential crystal orientation, Vacuum, 77 (2004) 57–62, https://doi.org/10.1016/j.vacuum.2004.08.003.

[131] G. Dasi, K. Asokan, K. Thangaraju, Studies on improved hole injection into N,N′-Bis(3-methylphenyl)-N,N′-diphenylbenzidine hole transport layer in the device by thermal annealing of indium tin oxide anode, Appl. Phys. A: Mater. Sci. Process., 123 (2017) 179, https://doi.org/10.1007/s00339-017-0778-8.

[132] J.-P. Lin, J.-M. Wu, The effect of annealing processes on electronic properties of sol-gel derived Al-doped ZnO films, Appl. Phys. Lett., 92 (2008) 134103, https://doi.org/10.1063/1.2905279.

[133] J.C. Nie, J.Y. Yang, Y. Piao, H. Li, Y. Sun, Q.M. Xue, C.M. Xiong, R.F. Dou, Q.Y. Tu, Quantum confinement effect in ZnO thin films grown by pulsed laser deposition, Appl. Phys. Lett., 93 (2008) 2006–2009, https://doi.org/10.1063/1.3010376.

[134] I. ben Elkamel, N. Hamdaoui, A. Mezni, R. Ajjel, L. Beji, High responsivity and 1/: F noise of an ultraviolet photodetector based on Ni doped ZnO nanoparticles, RSC Adv., 8 (2018) 32333–32343, https://doi.org/10.1039/c8ra05567j.

[135] K. Davis, R. Yarbrough, M. Froeschle, J. White, H. Rathnayake, Band gap engineered zinc oxide nanostructures: Via a sol-gel synthesis of solvent driven shape-controlled crystal growth, RSC Adv., 9 (2019) 14638–14648, https://doi.org/10.1039/c9ra02091h.

[136] R. Shivanna, S. Rajaram, K.S. Narayan, Interface engineering for efficient fullerene-free organic solar cells, Appl. Phys. Lett., 106 (2015) 123301, https://doi.org/10.1063/1.4916216.

[137] S.J. Kwon, J.H. Park, J.G. Park, Wrinkling of a sol-gel-derived thin film, Phys. Rev. E Stat. Nonlin. Soft Matter Phys., 71 (2005) 011604, https://doi.org/10.1103/PhysRevE.71.011604.

[138] M. Cuba, U. Rathinavalli, K. Thangaraju, G. Muralidharan, Synthesis and optical properties of ZnO incorporated Tris-(8- hydroxyquinoline)aluminum, J. Lumin., 153 (2014) 188–193, https://doi.org/10.1016/j.jlumin.2014.03.001.

[139] R.S. Sreedharan, V. Ganesan, C.P. Sudarsanakumar, K. Bhavsar, R. Prabhu, V.P.P. Mahadevan Pillai, Highly textured and transparent RF sputtered Eu_2O_3 doped ZnO films , Nano Rev., 6 (2015) 26759, https://doi.org/10.3402/nano.v6.26759.

[140] M. Caglar, Y. Caglar, S. Aksoy, S. Ilican, Temperature dependence of the optical band gap and electrical conductivity of sol-gel derived undoped and Li-doped ZnO films, Appl. Surf. Sci., 256 (2010) 4966–4971, https://doi.org/10.1016/j.apsusc.2010.03.010.

[141] M.R. Islam, M. Rahman, S.F.U. Farhad, J. Podder, Structural, optical and photocatalysis properties of sol–gel deposited Al-doped ZnO thin films, Surf. Interfaces, 16 (2019) 120–126, https://doi.org/10.1016/j.surfin.2019.05.007.

[142] J. Charlesbabu, K. Gopalakrishnan, M. Elango, K. Vasudevan, Preparation and characterization of Cd-doped ZnO thin films by spin coating method, J. Optoelectron. Adv. Mater., 10 (2008) 2578–2583, https://doi.org/10.1080/24701556.2016.1242627.

[143] J.P. Zou, P. le Rendu, I. Musa, S.H. Yang, Y. Dan, C.T. That, T.P. Nguyen, Investigation of the optical properties of polyfluorene/ZnO nanocomposites, Thin Solid Films, 519 (2011) 3997–4003, https://doi.org/10.1016/j.tsf.2011.01.205.

[144] Y. Sakurai, Y. Hosoi, H. Ishii, Y. Ouchi, G. Salvan, A. Kobitski, T.U. Kampen, D.R.T. Zahn, K. Seki, Study of the interaction of tris-(8-hydroxyquinoline)aluminum (Alq_3) with potassium using vibrational spectroscopy: Examination of possible isomerization upon K doping, J. Appl. Phys., 96 (2004) 5534–5542, https://doi.org/10.1063/1.1776626.

[145] U. Ilyas, R.S. Rawat, T.L. Tan, P. Lee, R. Chen, H.D. Sun, L. Fengji, S. Zhang, Oxygen rich p-type ZnO thin films using wet chemical route with enhanced carrier concentration by temperature-dependent tuning of acceptor defects, J. Appl. Phys., 110 (2011) 093522, https://doi.org/10.1063/1.3660284.

[146] Y. Cao, L. Miao, S. Tanemura, M. Tanemura, Y. Kuno, Y. Hayashi, Low resistivity p-ZnO films fabricated by sol-gel spin coating, Appl. Phys. Lett., 88 (2006), https://doi.org/10.1063/1.2215618.

[147] A. Kushwaha, M. Aslam, Defect controlled water splitting characteristics of gold nanoparticle functionalized ZnO nanowire films, RSC Adv., 4 (2014) 20955–20963, https://doi.org/10.1039/c4ra00782d.

[148] J. Lv, W. Wang, M. Zhao, W. Zhu, Y. Cheng, G. He, M. Zhang, X. Chen, Z. Sun, Enhanced visible light response of ZnO porous thin film by post-annealing treatment, J. Mater. Sci.: Mater. Electron., 28 (2017) 4051–4057, https://doi.org/10.1007/s10854-016-6019-7.

[149] B. Efa, M.S. Ghamsari, M.H.M. Ara, Sol – gel derived AZO thin film with unusual narrow dual emission, J. Lumin., 154 (2014) 32–35, https://doi.org/10.1016/j.jlumin.2014.03.062.

[150] P.S.G. Kim, S.J. Naftel, T.K. Sham, I. Coulthard, Y.F. Hu, A. Moewes, J.W. Freeland, Photon-in photon-out studies of Alq_3 (tris-aluminum-8-hydroxyquinolinate): Synchrotron light excited optical luminescence and X-ray emission, J. Electron Spectros. Relat. Phenomena., 144–147 (2005) 901–904, https://doi.org/10.1016/j.elspec.2005.01.242.

[151] J. Kennedy, P.P. Murmu, E. Manikandan, S.Y. Lee, Investigation of structural and photoluminescence properties of gas and metal ions doped zinc oxide single crystals, J. Alloys Compd., 616 (2014) 614–617, https://doi.org/10.1016/j.jallcom.2014.07.179.

[152] P.P. Murmu, J. Kennedy, B.J. Ruck, G.V.M. Williams, A. Markwitz, S. Rubanov, A.A. Suvorova, Effect of annealing on the structural, electrical and magnetic properties of Gd-implanted ZnO thin films, J. Mater. Sci., 47 (2012) 1119–1126, https://doi.org/10.1007/s10853-011-5883-z.

[153] F. Fang, J. Futter, A. Markwitz, J. Kennedy, UV and humidity sensing properties of ZnO nanorods prepared by the arc discharge method, Nanotechnology, 20 (2009), https://doi.org/10.1088/0957-4484/20/24/245502.

[154] D.K. Sharma, S. Shukla, K.K. Sharma, V. Kumar, A review on ZnO: Fundamental properties and applications, Mater. Today: Proc., (2020), https://doi.org/10.1016/j.matpr.2020.10.238.

[155] R. Siddheswaran, C.E. Jeyanthi, K. Thangaraju, R.V. Mangalaraja, Columnar structure growth of Mn-doped ZnO (MZO) thin films by radio frequency co-sputtering and studies on films properties, Mater. Technol., 00 (2020) 1–7, https://doi.org/10.1080/10667857.2020.1814053.

[156] G. Dasi, R. Ramarajan, D.P. Joseph, S. Vijayakumar, J.J. Shim, M. Arivananthan, R. Jayavel, K. Thangaraju, Enhanced UV emission of solution processed highly transparent Alq3/ZnO hybrid thin films, Thin Solid Films, 710 (2020) 138265, https://doi.org/10.1016/j.tsf.2020.138265.

[157] D.R. Sahu, J.L. Huang, The properties of ZnO/Cu/ZnO multilayer films before and after annealing in the different atmosphere, Thin Solid Films, 516 (2007) 208–211, https://doi.org/10.1016/j.tsf.2007.06.124.

[158] S. Dhara, P.K. Giri, ZnO/anthracene based inorganic/organic nanowire heterostructure: Photoresponse and photoluminescence studies, J. Appl. Phys., 111 (2012) 1–8, https://doi.org/10.1063/1.3687936.

[159] Y. Zhu, A. Apostoluk, P. Gautier, A. Valette, L. Omar, T. Cornier, J.M. Bluet, K. Masenelli-Varlot, S. Daniele, B. Masenelli, Intense visible emission from ZnO/PAAX (X = H or Na) nanocomposite synthesized via a simple and scalable sol-gel method, Sci. Rep., 6 (2016) 1–11, https://doi.org/10.1038/srep23557.

[160] K. Thangaraju, R. Kumaran, P. Ramamoorthy, V. Narayanan, J. Kumar, Study on photoluminescence from tris-(8-hydroxyquinoline)indium thin films and influence of light, Optik. 123 (2012) 1393–1396, https://doi.org/10.1016/j.ijleo.2011.08.018.

[161] V. Sharma, H. Sharma, S.K. Singh, R. Kumar, Y. Kumari, K. Sachdev, Organic-Inorganic Hybrid Structure as a Conductive and Transparent Layer for Energy and Optoelectronic Applications, ACS Appl. Electron. Mater., 3 (2021) 1601–1609, https://doi.org/10.1021/acsaelm.0c01099.

[162] S.H. Mir, L.A. Nagahara, T. Thundat, P. Mokarian-Tabari, H. Furukawa, A. Khosla, Review—Organic-Inorganic Hybrid Functional Materials: An Integrated Platform for Applied Technologies, J. Electrochem. Soc., 165 (2018) B3137–B3156, https://doi.org/10.1149/2.0191808jes.

[163] D. Shao, M. Yu, H. Sun, G. Xin, J. Lian, S. Sawyer, High-performance ultraviolet photodetector based on organic-inorganic hybrid structure, ACS Appl. Mater. Interfaces, 6 (2014) 14690–14694, https://doi.org/10.1021/am504090e.

[164] F. Cao, W. Tian, B. Gu, Y. Ma, H. Lu, L. Li, High-performance UV–vis photodetectors based on electrospun ZnO nanofiber-solution processed perovskite hybrid structures, Nano Res., 10 (2017) 2244–2256, https://doi.org/10.1007/s12274-016-1413-2.

[165] Z. Jin, J. Wang, High-responsivity solution-processed organic-inorganic hybrid bilayer thin film photoconductors, J. Mater. Chem. C, 1 (2013) 7996–8002, https://doi.org/10.1039/c3tc31143k.

[166] J. Kennedy, B. Sundrakannan, R.S. Katiyar, A. Markwitz, Z. Li, W. Gao, Raman scattering investigation of hydrogen and nitrogen ion implanted ZnO thin films, Can. J. Chem., 8 (2008) 291–294, https://doi.org/10.1016/j.cap.2007.10.018.

[167] F. Decremps, J. Pellicer-Porres, A.M. Saitta, J.C. Chervin, A. Polian, High-pressure Raman spectroscopy study of wurtzite ZnO, Phys. Rev. B Condens. Matter Mater. Phys., 65 (2002) 921011–921014, https://doi.org/10.1103/PhysRevB.65.092101.

[168] L. Bergman, X.B. Chen, J. Huso, J.L. Morrison, H. Hoeck, Raman scattering of polar modes of ZnO crystallites, J. Appl. Phys., 98 (2005) 093507, https://doi.org/10.1063/1.2126784.

[169] Y. Zhang, H. Jia, R. Wang, C. Chen, X. Luo, D. Yu, C. Lee, Low-temperature growth and Raman scattering study of vertically aligned ZnO nanowires on Si substrate, Appl. Phys. Lett., 83 (2003) 4631–4633, https://doi.org/10.1063/1.1630849.

[170] S. ben Yahia, L. Znaidi, A. Kanaev, J.P. Petitet, Raman study of oriented ZnO thin films deposited by sol-gel method, Spectrochim. Acta A Mol. Biomol. Spectrosc., 71 (2008) 1234–1238, https://doi.org/10.1016/j.saa.2008.03.032.

[171] K.A. Alim, V.A. Fonoberov, A.A. Balandin, Origin of the optical phonon frequency shifts in ZnO quantum dots, Appl. Phys. Lett., 86 (2005) 1–3, https://doi.org/10.1063/1.1861509.

[172] E. Nowak, M. Szybowicz, A. Stachowiak, W. Koczorowski, D. Schulz, K. Paprocki, K. Fabisiak, S. Los, A comprehensive study of structural and optical properties of ZnO bulk crystals and polycrystalline films grown by sol-gel method, Appl. Phys. A: Mater. Sci. Process., 126 (2020) 1–12, https://doi.org/10.1007/s00339-020-03711-2.

[173] M.D. Halls, R. Aroca, Vibrational spectra and structure of tris (8-hydroxyquinoline) aluminum (III), Can. J. Chem., 1736 (1998) 1730–1736, https://doi.org/https://doi.org/10.1139/v98-182.

[174] R. Zamiri, A. Rebelo, G. Zamiri, A. Adnani, A. Kuashal, M.S. Belsley, J.M.F. Ferreira, Far-infrared optical constants of ZnO and ZnO/Ag nanostructures, RSC Adv., 4 (2014) 20902–20908, https://doi.org/10.1039/c4ra01563k.

[175] N.B. Patil, A.R. Nimbalkar, M.G. Patil, ZnO thin film prepared by a sol-gel spin coating technique for NO_2 detection, Mater. Sci. Eng. B Solid State. Mater. Adv. Technol., 227 (2018) 53–60, https://doi.org/10.1016/j.mseb.2017.10.011.

[176] M. Chen, X. Wang, Y.H. Yu, Z.L. Pei, X.D. Bai, C. Sun, R.F. Huang, L.S. Wen, X-ray photoelectron spectroscopy and auger electron spectroscopy studies of Al-doped ZnO films, Appl. Surf. Sci., 158 (2000) 134–140, https://doi.org/10.1016/S0169-4332(99)00601-7.

[177] K. Kotsis, V. Staemmler, Ab initio calculations of the O1s XPS spectra of ZnO and Zn oxo compounds, Phys. Chem. Chem. Phys., 8 (2006) 1490–1498, https://doi.org/10.1039/b515699h.

[178] M. Wang, W. Li, Y. Ma, H. Guan, C. Cheng, G. Du, Photoelectron spectroscopy study of the interactions between ErF 3 dopants and Alq_3 hosts for near-infrared organic light-emitting diodes, Appl. Surf. Sci., 309 (2014) 22–26. https://doi.org/10.1016/j.apsusc.2014.04.115.

[179] T.P. Nguyen, J. Ip, P. Jolinat, P. Destruel, XPS and sputtering study of the Alq_3/electrode interfaces in organic light emitting diodes, Appl. Surf. Sci., 172 (2001) 75–83, https://doi.org/10.1016/S0169-4332(00)00826-6.

[180] Q.T. Le, L. Yan, V.E. Choong, E.W. Forsythe, M.G. Mason, C.W. Tang, Y. Gao, Photoemission study of interfaces in organic light-emitting diodes, Synth. Met., 102 (1999) 1014–1015, https://doi.org/10.1016/S0379-6779(98)01263-6.

[181] M.R. Awual, M.M. Hasan, A. Islam, M.M. Rahman, A.M. Asiri, M.A. Khaleque, M.C. Sheikh, Introducing an amine functionalized novel conjugate material for toxic nitrite detection and adsorption from wastewater, J. Clean. Prod., 228 (2019) 778–785, https://doi.org/10.1016/j.jclepro.2019.04.280.

[182] F. Khan, W. Khan, J.H. Kim, N. ul Huda, H.M. Salman Ajmal, S.D. Kim, Oxygen desorption kinetics of ZnO nanorod-gated AlGaN/GaN HEMT-based UV photodetectors, AIP Adv. , 8 (2018) 075225, https://doi.org/10.1063/1.5040295.

[183] S. Dhara, P.K. Giri, ZnO Nanowire Heterostructures: Intriguing Photophysics and Emerging Applications, Rev. Nanosci. Nanotechnol., 2 (2013) 147–170, https://doi.org/10.1166/rnn.2013.1032.

[184] Y.Y. Lin, C.W. Chen, W.C. Yen, W.F. Su, C.H. Ku, J.J. Wu, Near-ultraviolet photodetector based on hybrid polymer/zinc oxide nanorods by low-temperature solution processes, Appl. Phys. Lett., 92 (2008) 233301, https://doi.org/10.1063/1.2940594.

[185] G.M. Ali, P. Chakrabarti, Performance of ZnO-based ultraviolet photodetectors under varying thermal treatment, IEEE Photonics J., 2 (2010) 784–793, https://doi.org/10.1109/JPHOT.2010.2054070.

[186] A.B. Djurišić, T.W. Lau, L.S.M. Lam, W.K. Chan, Influence of atmospheric exposure of tris (8-hydroxyquinoline) aluminum (Alq_3): A photoluminescence and absorption study, Appl. Phys. A: Mater. Sci. Process., 78 (2004) 375–380, https://doi.org/10.1007/s00339-002-1915-5.

[187] K. Charipar, H. Kim, A. Piqué, N. Charipar, ZnO nanoparticle/graphene hybrid photodetectors via laser fragmentation in liquid, Nanomaterials, 10 (2020) 1–12, https://doi.org/10.3390/nano10091648.

[188] H.K. Yadav, K. Sreenivas, V. Gupta, Study of metal ZnO based thin film ultraviolet photodetectors: The effect of induced charges on the dynamics of photoconductivity relaxation, J. Appl. Phys., 107 (2010) 044507, https://doi.org/10.1063/1.3291133.

[189] D.C. Agarwal, A. Kumar, S.A. Khan, D. Kabiraj, F. Singh, A. Tripathi, J.C. Pivin, R.S. Chauhan, D.K. Avasthi, SHI induced modification of ZnO thin film: Optical and structural studies, Nucl Instrum Methods Phys Res B, 244 (2006) 136–140, https://doi.org/10.1016/j.nimb.2005.11.077.

[190] S.K. Sahoo, S. Mangal, D.K. Mishra, U.P. Singh, P. Kumar, 100 keV H+ ion irradiation of as-deposited Al-doped ZnO thin films: An interest in tailoring surface morphology for sensor applications, Surf. Interface. Anal., 50 (2018) 705–712, https://doi.org/10.1002/sia.6461.

[191] P.M.R. Kumar, C.S. Kartha, K.P. Vijayakumar, F. Singh, D.K. Avasthi, T. Abe, Y. Kashiwaba, G.S. Okram, M. Kumar, S. Kumar, Modifications of ZnO thin films under dense electronic excitation, J. Appl. Phys., 97 (2005), https://doi.org/10.1063/1.1823574.

[192] R. Krishna, D.C. Agarwal, D.K. Avasthi, Synthesis and modification of ZnO thin films by energetic ion beams, Radiat. Eff. Defects Solids, 176 (2021) 145–166, https://doi.org/10.1080/10420150.2021.1891065.

[193] S. Mal, S. Nori, J. Narayan, J.T. Prater, D.K. Avasthi, Ion-irradiation-induced ferromagnetism in undoped ZnO thin films, Acta Mater., 61 (2013) 2763–2768, https://doi.org/10.1016/j.actamat.2012.09.071.

[194] H.A. Khawal, B.N. Dole, A study of the 160 MeV Ni7+swift heavy ion irradiation effect of defect creation and shifting of the phonon modes on Mn: XZn1-xO thin films, RSC Adv., 7 (2017) 34736–34745, https://doi.org/10.1039/c7ra01809f.

[195] S.K. Sahoo, S. Mangal, D.K. Mishra, U.P. Singh, P. Kumar, 50 keV H+ ion beam irradiation of Al doped ZnO thin films: Studies of radiation stability for device applications, Surf. Interface. Anal , 49 (2017) 1279–1286, https://doi.org/10.1002/sia.6328.

[196] K. Thangaraju, R. Kumaran, K. Asokan, P. Ramamoorthy, D. Kanjilal, J. Kumar, Photoluminescence of Tris-(8-hydroxyquinoline)aluminum thin films and influence of swift heavy ion irradiation, Polym. Plast. Technol. Eng., 47 (2008) 479–482, https://doi.org/10.1080/03602550801952003.

[197] G. Dasi, T. Lavanya, S. Suneetha, S. Vijayakumar, J.J. Shim, K. Thangaraju, Raman and X-ray photoelectron spectroscopic investigation of solution-processed Alq_3/ZnO hybrid thin films, Spectrochim. Acta. A Mol. Biomol. Spectrosc., 265 (2022) 120377, https://doi.org/10.1016/j.saa.2021.120377.

[198] J.F. Ziegler, J.M. Manoyan, The stopping of ions in compounds, Nucl. Instrum. Methods Phys. Res. B, 35 (1988) 215–228, https://doi.org/10.1016/0168-583X(88)90273-X.

[199] N. Srinatha, P. Raghu, H.M. Mahesh, B. Angadi, Spin-coated Al-doped ZnO thin films for optical applications: Structural, micro-structural, optical and luminescence studies, J. Alloys Compd., 722 (2017) 888–895, https://doi.org/10.1016/j.jallcom.2017.06.182.

[200] G.K. Williamson, W.H. Hall, X-ray line broadening from filed aluminium and wolfram, Acta Metallurgica, 1 (1953) 22–31, https://doi.org/10.1016/0001-6160(53)90006-6.

[201] L. Mishra, V. Kumar, U.P. Singh, Impact of swift heavy ion (120 MeV , Ag 9 +) on doped ZnO : Al thin film, Materials, (2019), https://doi.org/10.20944/preprints201910.0310.v1.

[202] B. Lin, Z. Fu, Y. Jia, Green luminescent center in undoped zinc oxide films deposited on silicon substrates, Appl. Phys. Lett., 79 (2001) 943–945, https://doi.org/10.1063/1.1394173.

[203] F. Yu, T. Song, B. Wang, B. Xu, H. Li, H. Hu, L. He, H. Duan, S. Wang, X. Tang, The effects of intrinsic defects on the structural and optical properties of ZnO thin film prepared via a sol-gel method, Materials Research Express, 6 (2019) 0–8, https://doi.org/10.1088/2053-1591/ab4394.

[204] S. Mal, S. Nori, J. Narayan, J.T. Prater, D.K. Avasthi, Ion-irradiation-induced ferromagnetism in undoped ZnO thin films, Acta Mater., 61 (2013) 2763–2768, https://doi.org/10.1016/j.actamat.2012.09.071.

[205] D.C. Agarwal, D.K. Avasthi, F. Singh, D. Kabiraj, P.K. Kulariya, I. Sulania, J.C. Pivin, R.S. Chauhan, Swift heavy ion induced structural modification of atom beam sputtered ZnO thin film, Surf. Coat., 203 (2009) 2427–2431, https://doi.org/10.1016/j.surfcoat.2009.02.109.

[206] D. Ranjith Kumar, K.S. Ranjith, L.R. Nivedita, K. Asokan, R.T. Rajendra Kumar, Swift heavy ion induced effects on structural, optical and photo-catalytic properties of Ag irradiated vertically aligned ZnO nanorod arrays, Nucl Instrum Methods Phys Res B, 450 (2019) 95–99, https://doi.org/10.1016/j.nimb.2018.03.015.

[207] K. Thangaraju, R. Kumaran, T. Mohanty, K. Asokan, P. Ramamurthy, D. Kanjilal, J. Kumar, Swift heavy ion irradiation-induced modifications of tris-(8- hydroxyquinoline)aluminum thin films, Radiat. Eff. Defects Solids, 161 (2006) 695–700, https://doi.org/10.1080/10420150600909604.

[208] J. Singh, R.G. Singh, S.K. Gautam, H. Gupta, S. Ojha, F. Singh, Swift heavy ion irradiation induced negative differential resistance and transport of charge carriers in conducting polymer-metal oxide hybrids, Radiat. Phys. Chem., 179 (2021) 109211, https://doi.org/10.1016/j.radphyschem.2020.109211.

[209] K.K. Lee, D. Wang, O. Shinobu, T. Ohshima, Reliability of gamma-irradiated n-channel ZnO thin-film transistors: electronic and interface properties, Radiat. Eff. Defects Solids, 173 (2018) 250–260, https://doi.org/10.1080/10420150.2018.1427093.

[210] J.H. Burroughes, D.D.C. Bradley, A.R. Brown, R.N. Marks, K. Mackay, R.H. Friend, P.L. Burns, A.B. Holmes, J.H. Burroughes, Nature, 347 (1990) 539–541, https://doi.org/10.1038/347539a0.

[211] Z. Shen, P.E. Burrows, V. Bulović, S.R. Forrest, M.E. Thompson, Three-color, tunable, organic light-emitting devices, Science, 276 (1997) 2009–2011, https://doi.org/10.1126/science.276.5321.2009.

[212] J.R. Sheats, H. Antoniadis, M. Hueschen, W. Leonard, J. Miller, R. Moon, D. Roitman, A. Stocking, Organic electroluminescent devices, Science, 273 (1996) 884–888, https://doi.org/10.1126/science.273.5277.884.

[213] M.G. Shin, S.O. Kim, H.T. Park, S.J. Park, H.S. Yu, Y.H. Kim, S.K. Kwon, Synthesis and characterization of ortho-twisted asymmetric anthracene derivatives for blue organic light emitting diodes (OLEDs), Dyes Pigm., 92 (2012) 1075–1082, https://doi.org/10.1016/j.dyepig.2011.03.002.

[214] S.J. Yoo, H.J. Yun, I. Kang, K. Thangaraju, S.K. Kwon, Y.H. Kim, A new electron transporting material for effective hole-blocking and improved charge balance in highly efficient phosphorescent organic light emitting diodes, J. Mater. Chem. C, 1 (2013) 2217–2223, https://doi.org/10.1039/c3tc00801k.

[215] S.O. Kim, Q. Zhao, K. Thangaraju, J.J. Kim, Y.H. Kim, S.K. Kwon, Synthesis and characterization of solution-processable highly branched iridium (III) complex cored dendrimer based on tetraphenylsilane dendron for host-free green phosphorescent organic light emitting diodes, Dyes Pigm., 90 (2011) 139–145, https://doi.org/10.1016/j.dyepig.2010.10.005.

[216] J. He, M. Lu, X. Zhou, J.R. Cao, K.L. Wang, L.S. Liao, Z.B. Deng, X.M. Ding, X.Y. Hou, S.T. Lee, Damage study of ITO under high electric field, Thin Solid Films, 363 (2000), https://doi.org/10.1016/S0040-6090(99)01066-4.

[217] J.C. Scott, J.H. Kaufman, P.J. Brock, R. DiPietro, J. Salem, J.A. Goitia, Degradation and failure of MEH-PPV light-emitting diodes, J. Appl. Phys., 79 (1996) 2745–2751, https://doi.org/10.1063/1.361096.

[218] C.I. Chao, K.R. Chuang, S.A. Chen, Failure phenomena and mechanisms of polymeric light-emitting diodes: Indium-tin-oxide damage, Appl. Phys. Lett., 69 (1996) 2894–2896, https://doi.org/10.1063/1.117354.

[219] Y.N. Kim, H.G. Shin, J.K. Song, D.H. Cho, H.S. Lee, Y.G. Jung, Thermal degradation behavior of indium tin oxide thin films deposited by radio frequency magnetron sputtering, J. Mater. Res., 20 (2005) 1574–1579, https://doi.org/10.1557/JMR.2005.0199.

[220] H. Ohsaki, Y. Kokubu, Global market and technology trends on coated glass for architectural, automotive and display applications, Thin Solid Films, 351 (1999) 1–7, https://doi.org/10.1016/S0040-6090(99)00147-9.

[221] C.C. Wu, C.I. Wu, J.C. Sturm, A. Kahn, Surface modification of indium tin oxide by plasma treatment: An effective method to improve the efficiency, brightness, and reliability of organic light emitting devices, Appl. Phys. Lett., 70 (1997) 1348–1350, https://doi.org/10.1063/1.118575.

[222] I.D. Parker, Carrier tunneling and device characteristics in polymer light-emitting diodes, J. Appl. Phys., 75 (1994) 1656–1666, https://doi.org/10.1063/1.356350.

[223] Y. Yang, E. Westerweele, C. Zhang, P. Smith, A.J. Heeger, Enhanced performance of polymer light-emitting diodes using high-surface area polyaniline network electrodes, J. Appl. Phys., 77 (1995) 694–698, https://doi.org/10.1063/1.359056.

[224] S.Y. Kim, J.L. Lee, K.B. Kim, Y.H. Tak, Effect of ultraviolet-ozone treatment of indium-tin-oxide on electrical properties of organic light emitting diodes, J. Appl. Phys., 95 (2004) 2560–2563, https://doi.org/10.1063/1.1635995.

[225] C.N. Li, C.Y. Kwong, A.B. Djurišić, P.T. Lai, P.C. Chui, W.K. Chan, S.Y. Liu, Improved performance of OLEDs with ITO surface treatments, Thin Solid Films, 477 (2005) 57–62, https://doi.org/10.1016/j.tsf.2004.08.111.

[226] J.S. Kim, P.K.H. Ho, D.S. Thomas, R.H. Friend, F. Cacialli, G.W. Bao, S.F.Y. Li, X-ray photoelectron spectroscopy of surface-treated indium-tin oxide thin films, Chem. Phys. Lett., 315 (1999) 307–312, https://doi.org/10.1016/S0009-2614(99)01233-6.

[227] C. Suresh Kumar, A. Subrahmanyam, J. Majhi, Automated reedtype Kelvin probe for work function and surface photovoltage studies, Rev. Sci. Instrum., 67 (1996) 805–808, https://doi.org/10.1063/1.1146813.

[228] J.F. Smith, A.J. Aronson, D. Chen, W.H. Class, Reactive magnetron deposition of transparent conductive films, Thin Solid Films, 72 (1980) 469–474, https://doi.org/10.1016/0040-6090(80)90533-7.

[229] M.J. Alam, D.C. Cameron, Optical and electrical properties of transparent conductive ITO thin films deposited by sol-gel process, Thin Solid Films, 377–378 (2000) 455–459, https://doi.org/10.1016/S0040-6090(00)01369-9.

[230] Y.D. Glinka, S.H. Lin, L.P. Hwang, N.H. Tolk, Size effect in self-trapped exciton photoluminescence from SiO2-based nanoscale materials, Phys. Rev. B Condens. Matter Mater. Phys., 64 (2001) 854211–8542111, https://doi.org/10.1103/PhysRevB.64.085421.

[231] and S.T.L. Y. K. Chang, H. H. Hsieh, W. F. Pong, M.-H. Tsai, F. Z. Chien, P. K. Tseng, L. C. Chen, T. Y. Wang, K. H. Chen, D. M. Bhusari, J. R. Yang, quantum confinement effect in diamond nanocrystals studied by X-ray-absorption spectroscopy, Phys. Rev. Lett.. 82 (1999) 5377. https://doi.org/https://doi.org/10.1103/PhysRevLett.82.5377.

[232] O.P. Agnihotri, A.K. Sharma, B.K. Gupta, R. Thangaraj, The effect of tin additions on indium oxide selective coatings, J. Phys. D: Appl. Phys., 11 (1978) 643–647, https://doi.org/10.1088/0022-3727/11/5/008.

[233] J. Bhattacharyya, D.De, A.K. Pal, S. Chaudhuri, Preparation and Characterization of indium tin oxide films produced by the D.C. Sputtering Technique, Thin Solid Films, 128 (1985) 231–239, https:// doi:10.1016/0040-6090(85)90075-6.

[234] G. Frank, H. Kostlin, Electrical Properties and Defect Model of Tin-Doped Indium Oxide Layers, Appl.Phys.A, 27 (1982) 197-206, https://doi.org/https://doi.org/10.1007/BF00619080.

[235] G.B. González, T.O. Mason, J.P. Quintana, O. Warschkow, D.E. Ellis, J.H. Hwang, J.P. Hodges, J.D. Jorgensen, Defect structure studies of bulk and nano-indium-tin oxide, J. Appl. Phys., 96 (2004) 3912–3920, https://doi.org/10.1063/1.1783610.

[236] T. Minami, New n-Type Transparent Conducting Oxides, MRS Bulletin, 25 (2000) 38, https://doi.org/https://doi.org/10.1557/mrs2000.149.

[237] K. Adachi, T. Hirayama, H. Sakata, The effect of gas atmospheres on resistivity of indium tin oxide films at high temperature, J. Mater. Sci., 25 (1990) 1403-1406, https://doi.org/https://doi.org/10.1007/BF00585457.

[238] D. Raoufi, A. Kiasatpour, H.R. Fallah, A.S.H. Rozatian, Surface characterization and microstructure of ITO thin films at different annealing temperatures, Appl. Surf. Sci., 253 (2007) 9085–9090, https://doi.org/10.1016/j.apsusc.2007.05.032.

[239] M. Gulen, G. Yildirim, S. Bal, A. Varilci, I. Belenli, M. Oz, Role of annealing temperature on microstructural and electro-optical properties of ITO films produced by sputtering, J. Mater. Sci.: Mater. Electron., 24 (2013) 467–474, https://doi.org/10.1007/s10854-012-0768-8.

[240] S.J. Kwon, J.H. Park, J.G. Park, Wrinkling of a sol-gel-derived thin film, Phys. Rev. E Stat. Nonlin. Soft Matter Phys., 71 (2005), https://doi.org/10.1103/PhysRevE.71.011604.

[241] M. Castellani, I. Salzmann, P. Bugnon, S. Yu, M. Oehzelt, N. Koch, Structural and electronic implications for carrier injection into organic semiconductors, Appl. Phys. A: Mater. Sci. Process., 97 (2009) 1–9, https://doi.org/10.1007/s00339-009-5336-6.

[242] K. Thangaraju, P. Amaladass, K.S. Bharathi, A.K. Mohanakrishnan, V. Narayanan, J. Kumar, Studies on influence of light on fluorescence of Tris-(8-hydroxyquinoline)aluminum thin films, Appl. Surf. Sci., 255 (2009) 5760–5763, https://doi.org/10.1016/j.apsusc.2008.12.079.

[243] M.C. Hwang, K. Thangaraju, K.H. So, S.C. Shin, S.K. Kwon, Y.H. Kim, A new bulky trymethylsilylxylene substituted iridium(III) complex with picolinic acid as ancillary ligand: Synthesis; Characterization and applications for efficient yellow-green emitting phosphorescent organic light emitting diodes, Synth. Met., 162 (2012) 391–397, https://doi.org/10.1016/j.synthmet.2011.12.026.

[244] S.O. Kim, K. Thangaraju, S. Jung, W. Lu, S.M. Park, J. Lee, J.I. Lee, H.Y. Chu, Y.H. Kim, S.K. Kwon, Highly efficient phosphorescent organic light emitting diodes based on Iridium(III) complex with bulky substituent spacers, in: J. Nanosci. Nanotechnol., 2012: pp. 4375–4378, https://doi.org/10.1166/jnn.2012.5911.

[245] J. He, M. Lu, X. Zhou, J.R. Cao, K.L. Wang, L.S. Liao, Z.B. Deng, X.M. Ding, X.Y. Hou, S.T. Lee, Damage study of ITO under high electric field, Thin Solid Films, 363 (2000) 240–243, https://doi.org/10.1016/S0040-6090(99)01066-4.

[246] V.S. Reddy, K. Das, A. Dhar, S.K. Ray, The effect of substrate temperature on the properties of ITO thin films for OLED applications, Semicond. Sci. Technol., 21 (2006) 1747–1752, https://doi.org/10.1088/0268-1242/21/12/043.

[247] D.A. Rider, R.T. Tucker, B.J. Worfolk, K.M. Krause, A. Lalany, M.J. Brett, J.M. Buriak, K.D. Harris, Indium tin oxide nanopillar electrodes in polymer/fullerene solar cells, Nanotechnology, 22 (2011) 085706, https://doi.org/10.1088/0957-4484/22/8/085706.

[248] E.I. Aminaka, T. Tsutsui, S. Saito, Effect of layered structures on the location of emissive regions in organic electroluminescent devices, J. Appl. Phys., 79 (1996) 8808–8815, https://doi.org/10.1063/1.362475.

[249] D.K. Maurya, Effects of post-thermal treatment on the properties of rf reactive sputtered ITO films, Microelectronics Journal, 38 (2007) 76–79, https://doi.org/10.1016/j.mejo.2006.09.009.

[250] B.R. Cho, I.Y. Park, Effect of post-annealing on the formation of ITO thin films, J.Korean Phys. Soc., 53 (2008) 19–22, https://doi.org/10.3938/jkps.53.19.

[251] Y.N. Kim, H.G. Shin, J.K. Song, D.H. Cho, H.S. Lee, Y.G. Jung, Thermal degradation behavior of indium tin oxide thin films deposited by radio frequency magnetron sputtering, J. Mater. Res., 20 (2005) 1574–1579, https://doi.org/10.1557/JMR.2005.0199.

[252] Z. Su, L. Wang, Y. Li, H. Zhao, B. Chu, W. Li, Ultraviolet-ozone-treated PEDOT: PSS as anode buffer layer for organic solar cells, Nanoscale Res. Lett., 7 (2012) 1–6, https://doi.org/10.1186/1556-276X-7-465.

[253] S.W. Baek, J. Noh, C.H. Lee, B. Kim, M.K. Seo, J.Y. Lee, Plasmonic forward scattering effect in organic solar cells: A powerful optical engineering method, Sci. Rep., 3 (2013) 1–7, https://doi.org/10.1038/srep01726.

[254] M.P. de Jong, L.J. van Ijzendoorn, M.J.A. de Voigt, Stability of the interface between indium-tin-oxide and poly(3,4-ethylenedioxythiophene)/poly(styrenesulfonate) in polymer light-emitting diodes, Appl. Phys. Lett., 77 (2000) 2255–2257, https://doi.org/10.1063/1.1315344.

[255] J.Y. Kim, K. Lee, N.E. Coates, D. Moses, T.Q. Nguyen, M. Dante, A.J. Heeger, Efficient tandem polymer solar cells fabricated by all-solution processing, Science, 317 (2007) 222–225, https://doi.org/10.1126/science.1141711.

[256] P. Dhamodharan, C. Manoharan, M. Bououdina, R. Venkadachalapathy, S. Ramalingam, Al-doped ZnO thin films grown onto ITO substrates as photoanode in dye sensitized solar cell, Sol Energy, 141 (2017) 127–144, https://doi.org/10.1016/j.solener.2016.11.029.

[257] R.H. Fowlder, L. Nordheim, Feldemission – Wikipedia, Proc. R. Soc. A, 125 (2010) 5–6, https://doi.org/10.1098/rspa.1928.0091.

[258] N. Koch, A. Elschner, J.P. Rabe, R.L. Johnson, Work function independent hole-injection barriers between pentacene and conducting polymers, Adv. Mater., 17 (2005) 330–335, https://doi.org/10.1002/adma.200400697.

[259] A. Srivastava, R. Singh, S. Jit, S. Tripathi, Fabrication of MoS_2/ZnO Hybrid Nanostructures for Enhancing Photodetection, IEEE Photonics Technol. Lett., 32 (2020) 1527–1530, https://doi.org/10.1109/LPT.2020.3039299.

[260] Y. Fang, Z. Zhao, M. Zhu, Z. Weng, C. Fang, X. Jia, High-Responsivity Solar-Blind Ultraviolet Photodetectors Based on Carbon Nanodots/Graphene Hybrids, IEEE Trans. Electron Devices, 68 (2021) 1101–1106, https://doi.org/10.1109/TED.2021.3051111.

[261] L.W.* and Y.T. Xiaoyan Liu, Optoelectronic Properties of Ultrathin Indium Tin Oxide Films , Crystals Article, 11 (2021) 1–13, https://doi.org/https://doi.org/10.3390/cryst11010030.

[262] Q. Wang, G. Williams, H. Aziz, Photo-degradation of the indium tin oxide (ITO)/organic interface in organic optoelectronic devices and a new outlook on the role of ITO surface treatments and interfacial layers in improving device stability, Org. Electron., 13 (2012) 2075–2082, https://doi.org/10.1016/j.orgel.2012.06.017.

[263] E.L. Hanson, J. Guo, N. Koch, J. Schwartz, S.L. Bernasek, Advanced surface modification of indium tin oxide for improved charge injection in organic devices, J. Am. Chem. Soc., 127 (2005) 10058–10062, https://doi.org/10.1021/ja050481s.

[264] T. Yamada, H. Makino, N. Yamamoto, T. Yamamoto, Ingrain and grain boundary scattering effects on electron mobility of transparent conducting polycrystalline Ga-doped ZnO films, J. Appl. Phys., 107 (2010) 123534, https://doi.org/10.1063/1.3447981.

[265] J.G. Lu, Z.Z. Ye, Y.J. Zeng, L.P. Zhu, L. Wang, J. Yuan, B.H. Zhao, Q.L. Liang, Structural, optical, and electrical properties of (Zn,Al)O films over a wide range of compositions, J. Appl. Phys., 100 (2006), https://doi.org/10.1063/1.2357638.

[266] E.M. Mkawi, K. Ibrahim, M.K.M. Ali, M.A. Farrukh, A.S. Mohamed, The effect of dopant concentration on properties of transparent conducting Al-doped ZnO thin films for efficient Cu_2ZnSnS_4 thin-film solar cells prepared by electrodeposition method, Appl. Nanosci. (Switzerland), 5 (2015) 993–1001, https://doi.org/10.1007/s13204-015-0400-3.

[267] N. Hernandez-Como, G. Rivas-Montes, F.J. Hernandez-Cuevas, I. Mejia, J.E. Molinar-Solis, M. Aleman, Ultraviolet photodetectors based on low temperature processed ZnO/PEDOT:PSS Schottky barrier diodes, Mater. Sci. Semicond. Process. , 37 (2015) 14–18, https://doi.org/10.1016/j.mssp.2014.12.063.

[268] S. Nandi, S. Kumar, A. Misra, Zinc oxide heterostructures: Advances in devices from self-powered photodetectors to self-charging supercapacitors, Mater. Adv., 2 (2021) 6768–6799, https://doi.org/10.1039/d1ma00670c.

[269] F. Tian, Q. Lei, X. Wang, Y. Wang, Effect of deep trapping states on space charge suppression in polyethylene/ZnO nanocomposite, Appl. Phys. Lett., 99 (2011) 2009–2012, https://doi.org/10.1063/1.3646909.

[270] M.S. Gaur, B.S. Rathore, Structural and thermal properties of swift heavy ion beam irradiated polycarbonate/zinc oxide nanocomposites, J. Therm. Anal. Calorim., 119 (2015) 1105–1112, https://doi.org/10.1007/s10973-014-4248-7.

[271] W.C. Lai, K.W. Lin, T.F. Guo, P. Chen, Y.Y. Liao, Perovskite-based solar cells with inorganic inverted hybrid planar heterojunction structure, AIP Adv., 8 (2018) 015109(1–8), https://doi.org/10.1063/1.5010951.

[272] P. Juhasz, J. Nevrela, M. Micjan, M. Novota, J. Uhrik, L. Stuchlikova, J. Jakabovic, L. Harmatha, M. Weis, Charge injection and transport properties of an organic light-emitting diode, Beilstein J. Nanotechnol., 7 (2016) 47–52, https://doi.org/10.3762/bjnano.7.5.

[273] U.B. Sharopov, B.G. Atabaev, R. Djabbarganov, Defect Formation on the Surface of ZnO Using Low-Energy Electrons, J. Surf. Investig., 14 (2020) 101–104, https://doi.org/10.1134/S1027451020010164.

[274] G. Dasi, T. Lavanya, G. Sathiyan, R.K. Gupta, A. Garg, P. Amaladass, K. Thangaraju, Improved hole injection/extraction using PEDOT:PSS interlayer coated onto high temperature annealed ITO electrode for efficient device performances, Superlattices and Microstructures, 156 (2021) 106953,https://doi.org/10.1016/j.spmi.2021.106953.

List of publications

Journals published

1. Gnyaneshwar Dasi, K. Asokan, and Kuppusamy Thangaraju*, Studies on improved hole injection into N,N′-Bis(3-methylphenyl)- N,N′- diphenylbenzidine hole transport layer in the device by thermal annealing of indium tin oxide anode, **Appl. Phys. A 123 (2017) 179**, https://doi.org/10.1007/s00339-017-0778-8.
2. Gnyaneshwar Dasi, R. Ramarajan, D. Paul Joseph, S. Vijayakumar, Jae-Jin Shim, M. Arivananthan, R. Jayavel, Kuppusamy Thangaraju*, Enhanced UV emission of solution processed highly transparent Alq_3/ZnO hybrid thin films, **Thin Solid Films 710 (2020) 138265**, https://doi.org/10.1016/j.tsf.2020.138265.
3. Gnyaneshwar Dasi, Thyda Lavanya, Govindasamy Sathiyan, Raju Kumar Gupta, Ashish Garg, P. Amaladass, and Kuppusamy Thangaraju* Improved hole injection/extraction using PEDOT:PSS interlayer coated onto high temperature annealed ITO electrode for efficient device performances, **Superlattices and Microstructures 156 (2021) 106953**, https://doi.org/10.1016/j.spmi.2021.106953.
4. Gnyaneshwar Dasi, Thyda Lavanya, S. Suneetha, S. Vijayakumar, Jae-Jin Shim, Kuppusamy Thangaraju* Raman and X-ray photoelectron spectroscopic investigation of solution processed Alq_3/ZnO hybrid thin films, **Spectrochimica Acta Part A: Molecular and Biomolecular Spectroscopy, 262 (2022) 120377,** https://doi.org/10.1016/j.saa.2021.120377.

Full Length Paper Published in International Proceedings

1. Gnyaneshwar Dasi, R. Ramarajan, R. Thangappan, R. Jayavel, and K. Thangaraju*, Improved electroluminescence in organic light emitting diodes by thermal annealing of indium tin oxide anode, AIP Conference Proceedings 1832, 060017 (2017), https://doi.org/10.1063/1.4980422.

2. Gnyaneshwar Dasi, R. Ramarajan, and Kuppusamy Thangaraju*, Improved electron injection in spin coated Alq_3 incorporated ZnO thin film in the device for solution processed OLEDs, AIP Conference Proceedings 1942, 060015 (2018), https://doi.org/10.1063/1.5028785.
3. Gnyaneshwar Dasi, R. Ramarajan, and Kuppusamy Thangaraju*, Improved performance in the aged electron-only devices based on tris-(8- hydroxyquinoline)aluminum thin film as electron transport layer for OLED applications, AIP Conference Proceedings 2115, 030211 (2019), https://doi.org/10.1063/1.5113050.
4. Gnyaneshwar Dasi and Kuppusamy Thangaraju*, ZnO/Tris-(8-hydroxyquinoline)aluminum (Alq_3) bilayer structure based ultraviolet photodetector with improved recovery time, AIP Conference Proceedings, 2265, 030217 (2020), https://doi.org/10.1063/5.0017062.

Manuscripts to be communicated

1. Gnyaneshwar Dasi, Thyda Lavanya, S. Suneetha, Kuppusamy Thangaraju*, Influence of Ni^{7+} swift heavy ion (SHI) irradiation on Alq_3/ZnO hybrid thin film for UV photodetector applications.
2. Gnyaneshwar Dasi, Thyda Lavanya, S. Suneetha, Kuppusamy Thangaraju*, Improved performance of UV Photodetectors based on Organic/Inorganic- Alq_3/ZnO hybrid thin films.
3. Gnyaneshwar Dasi, Thyda Lavanya, S. Suneetha, Meenakumari, D. Dinakar, Kuppusamy Thangaraju* Thickness effect of Alq_3/ZnO hybrid thin films on UV photodetectors performance.